A Nuclear Magnetic Resonance Study of Hydrous Layer Silicates

Graham G. Almond B.Sc. (Hons.)

A thesis submitted in partial fulfilment of the requirements for the degree of Doctor of Philosophy at the University of Durham

Department of Chemistry
University of Durham

1995

Abstract

This is a study of five silicates, namely makatite, kanemite, octosilicate, magadiite and kenyaite. The silicates have been analysed using a range of techniques, principally solid-state NMR spectroscopy.

High-quality ^{29}Si NMR spectra have been obtained for samples of all five layered sodium polysilicate hydrates. Amongst other findings, these have revealed four crystallographically distinct sites in makatite and a Q^4:Q^4 site ratio in kenyaite of *ca.* 5. Proton MAS NMR studies can produce well-resolved spectra, particularly for carefully-dried samples. Distinct water and strongly hydrogen-bonded proton species have been detected. The latter are particularly noteworthy and they are present in kanemite, octosilicate, magadiite and kenyaite, but not in makatite or layered silicic acids. Interactions between the resolved proton species have been investigated with a series of 1- and 2-dimensional experiments resulting in the detection of mixing, *via* spin-diffusion or chemical exchange. Sodium-23 NMR studies were complicated by second-order effects from strong quadrupolar interactions and the presence of a significant signal from a sodium chloride contamination in many samples. The latter had fooled previous authors. Acidification products of kanemite, octosilicate and magadiite were characterised by ^{29}Si CP NMR, thermogravimetric analysis, ^{1}H MAS NMR and powder X-ray diffraction. A single H-kanemite sample proved to be $H_2Si_2O_5$, but two types of H-octosilicate and H-magadiite sample were prepared. These differed in the presence of interlayer water. Several CP experiments were used to investigate the relationship between ^{29}Si and ^{23}Na nuclei and protons in the silicates. Cross-polarisation mechanisms tended to involve magnetisation transfer from the H-bonded protons only. Their determination was possible with a consideration of the extent of spin-diffusion or chemical exchange over the time-scale of the relevant experiments. Finally, new model structures for kanemite and the interlayer space in kanemite, octosilicate, magadiite and kenyaite have been suggested, while previously-proposed silicate layers have been reconsidered.

Memorandum

The research presented in this thesis has been carried out in the Department of Chemistry, University of Durham, between October 1991 and October 1994. Unless otherwise stated, it is the original work of the author. None of this work has been submitted for any other degree.

Acknowledgements

There are many people who I would like to thank for their help during my research.

Firstly, my supervisor Professor Robin Harris has been a source of ideas and encouragement. Barry Say, Dr. David Apperley and Nicola Davies have provided spectrometers and spectra. At Unilever, I am grateful to Drs. Peter Graham and Kevin Franklin for their supervision, Dr. Steve Loades, for the molecular modelling, and Ian Crone, for providing numerous samples.

My abiding memories of Durham will be the good times I have had with other members of the NMR group. They are too numerous for a complete list of names, but Abdul Khaliq was an entertaining and tolerant colleague for more than three years, while it was fun to share an office with Elke Bahlmann, Stefan Friebel and Anna Minoja.

Pride of place in these acknowledgements must go to Danita Pearson, who has provide love and support all the way through my higher education.

Abbreviations

$\mathbf{B_0}$	The static magnetic field of a spectrometer.
$\mathbf{B_1}$	An applied radiofrequency magnetic field.
CP	Cross-polarisation (with magic-angle spinning in this work).
d(O-H···O)	The oxygen-oxygen separation in a hydrogen-bond.
$\Delta_{1/2}$	Full peak width at half height.
δ_{Na}*	The *apparent* chemical shift for resonance of a sodium-23 nucleus.
δ_X	The chemical shift for resonance of a nucleus of element X.
FTIR	Fourier-transform infrared (spectroscopy).
γ_X	The gyromagnetic ratio of a nucleus X.
MAS	Magic-angle spinning.
M_t	Observed signal intensity at time, t.
NMR	Nuclear magnetic resonance (spectroscopy).
PDMSO	Polydimethylsiloxane.
pXRD	Powder X-ray diffraction.
r^2	The correlation coefficient from regression analysis.
SP/MAS	Single-Pulse with magic-angle spinning.
τ	The delay between radiofrequency pulses.
T_1	Spin-lattice relaxation time.
t_1,t_2	The acquisition periods in a 2-dimensional pulse sequence.
$T_{1\rho}$	Spin-lattice relaxation time in the rotating frame of reference.
T_2	Spin-spin relaxation time.
TGA	Thermogravimetric analysis.
TMS	Tetramethylsilane.

Contents

Chapter One Introduction

1.1 The Aim of the Project

This is a nuclear magnetic resonance study of layer silicates. A group of five silicates have been investigated, namely makatite, kanemite, octosilicate (or ilerite), magadiite and kenyaite.

The five silicates form a series of layered systems of apparently increasing structural complexity. The structure of makatite has been fully resolved by single-crystal X-ray diffraction and it contains silicate layers separated by aqueous sodium and proton species. It is expected that the other members of the group are structurally similar, differing in the thickness of the silicate layers. The interlayer species are highly reactive and it is this property which is potentially useful. Catalytic and ion-exchange properties for the silicates have been reported as well as potential applications as additives in the rubber and detergent industries.

The aim of this work was to use a range of analytical techniques (principally solid-state NMR) to further characterise makatite, kanemite, octosilicate, magadiite and kenyaite. Supporting evidence has been provided by thermal analysis and powder X-ray diffraction.

1.2 Nomenclature

For the purposes of this research, it has been assumed that the five silicates form a closed, related set. (The work has shown whether this was a valid assumption.) They had been known collectively as the Layered Alkali Metal Silicates. However, this name is ambiguous as it would also include at least three other classes of silicate: the disilicates, α-, β-, γ- & δ-$Na_2Si_2O_5$ and $KHSi_2O_5$; ion-exchanged forms of makatite, kanemite, octosilicate, magadiite and kenyaite; and the potassium silicates discovered by Beneke, Lagaly and co-workers. A better name can be coined by considering the characteristic stoichiometric and structural features of these five silicates.

Makatite	$Na_2O.4SiO_2.5H_2O$
Kanemite	$Na_2O.4SiO_2.7H_2O$
Octosilicate	$Na_2O.8SiO_2.9H_2O$
Magadiite	$Na_2O.14SiO_2.10H_2O$
Kenyaite	$Na_2O.22SiO_2.10H_2O$

Table 1.1 Typical formulae.

Table 1.1 lists formulae for makatite, kanemite, octosilicate, magadiite and kenyaite. There is some variation in reported formulae, but these are typical values.[1] Primarily, these are silicates rather than silicic acids or silica. The more specific term, "silicate mineral" can not be used as octosilicate can only be obtained synthetically. They are certainly alkali metal silicates, but it is the sodium forms which occur naturally and are prepared by most syntheses. Related potassium silicates have been reported,[2,3] but these have slightly different acidification properties, and they have not been considered in this work. Makatite, kanemite, octosilicate, magadiite and kenyaite contain a large amount of structural water. This is an important feature with respect to reactivity and NMR spectroscopy. The hydrous character also distinguishes them

from the disilicates. The history of makatite, kanemite, octosilicate, magadiite and kenyaite started with a search for polysilicates:[4] those with a high silica:soda ratio. The prefix poly- describes silicates which are highly-siliceous, SiO_2:$Na_2O \geq 4$; in disilicates the ratio is obviously two ($Na_2Si_2O_5 \equiv Na_2O{:}2SiO_2$).

The layer or sheet structure of these compounds is well established from X-ray diffraction data. The resolved unit cell of makatite[5] and strong powder-pattern basal reflections for all five silicates indicate that this is the case. The term phyllosilicate describes this lamellar nature,[6] where the layers form the ab plane of a lattice with a fundamental repeat distance in the c direction. The crystallinity of the five silicates (particularly after acidification) has often be emphasised.

The silicate, sodium-containing, hydrous, siliceous, lamellar and crystalline nature means that makatite, kanemite, octosilicate, magadiite and kenyaite can collectively be known as:

Layered Crystalline Sodium Polysilicate Hydrates;
or Highly Siliceous Crystalline Sodium Phyllosilicate Hydrates.

Previous authors have used a few of the characteristics to provide a descriptive term. For example, Yanagisawa *et al.*[7] described kanemite as "one of the layered polysilicates." Two previous Ph.D. theses have covered all five silicates exclusively and used the following terms as chapter headings:

Crystalline Sodium Polysilicate Hydrates, Smith, 1982;[4]
Layered Sodium Phyllosilicate Hydrates, Nesbitt, 1986.[1]

The two titles show the different emphases of each project. Smith was involved in synthesis and XRD characterisation, so crystallinity was important. Nesbitt analysed samples by NMR and formed model structures so the layer nature was (tautologically) emphasised. It is structural rather than synthetic characteristics that have been

important in this work, so the following name will be used to describe makatite, kanemite, octosilicate, magadiite and kenyaite:

Layered Sodium Polysilicate Hydrates

1.3 Layered Sodium Polysilicate Hydrates

The early history of the layered sodium polysilicate hydrates was elegantly reviewed by Smith in his 1982 Ph.D. thesis.[4] Between 1948 and 1964, makatite, kanemite, octosilicate and magadiite were probably all synthesised. However, they were not named until the natural discovery of makatite, kanemite, magadiite and kenyaite between 1967 and 1972. Therefore, there is some uncertainty in the retrospective assignment of modern names to earlier synthetic discoveries. Smith indicated that some of the reviewed information was contradictory; this is certainly the case for the reported formulae.

The early studies investigated the siliceous part of the Na_2O:SiO_2:H_2O ternary system. It had been believed that crystalline polysilicates would not be formed until Wegst and Wills[8] reported the formation of a tetrasilicate in 1948. Two years later, the same compound was reported by Baker *et al.* with the formula $3Na_2O:13SiO_2:11H_2O$ and it is probably makatite.[9] Natural makatite $Na_2O:4SiO_2:5H_2O$ was found by Hay in 1968 in Lake Magadi, Kenya.[10] Its name comes from the Masai word, *emakat* or soda. Khomiakov *et al.* reported a first Soviet occurrence of makatite in 1980, giving it the formula, $Na_2Si_4O_9.5H_2O$.[11]

In 1952, McCulloch reported that a different tetrasilicate precipitated from a commercial silicate solution liquor after several years.[12] This was probably kanemite, which gives a silicic acid $H_2Si_2O_5$ on treatment with acid. Kalt and Wey reported a successful reverse reaction in 1968.[13] Johan and Maglione found natural kanemite in the Kanem region of Lake Chad in 1972.[14]

McCulloch produced two other polysilicates with silica:soda ratios of 1:9.4 and 1:13.1. The former was later prepared by Iler with a formula $Na_2O:8SiO_2:9H_2O$.[15] It has since been called ilerite or more commonly (sodium) octosilicate: neither are particularly good names. Iler demonstrated the considerable ion-exchange potential of the silicate and showed that copper leached out of the edges of a heated copper octosilicate crystal, implying a layer structure.

The 1:13.1 compound proved to have the same powder X-ray diffraction pattern as natural magadiite, $Na_2O:14SiO_2:9H_2O$, which Eugster obtained from Lake Magadi, Kenya in 1967.[16] This periodically-dry soda lake also provided kenyaite, $Na_2O:22SiO_2:10H_2O$, which has since been synthesised by Beneke and Lagaly[3] and Bapst *et al.*[17] Magadiite has also been found in two American locations.[18,19]

It is unlikely that there are more layered sodium polysilicate hydrates to be discovered. Smith's work showed that using more or less extreme synthesis conditions results in the formation of SiO_2 and disilicates, respectively.[4] Rowe *et al.* formed trisilicates by storing siliceous $Na_2O:SiO_2:H_2O$ solutions at 200 to 300 °C.[20]

Until the early eighties most of the work on layered sodium polysilicate hydrates had been concerned with their synthesis and reactivity. In the last ten years, two factors have meant that the structures of these silicates can be researched. The first is that Annehed *et al.* obtained the crystal structure of makatite by single-crystal X-ray diffraction.[5] A suitable crystal was formed by using triethanolamine in the reaction mixture. The second factor is the availability of high-resolution solid-state nuclear magnetic resonance spectroscopy.

References

1 G.J. Nesbitt, Ph.D. Thesis, University of Durham, 1986.

2 K. Beneke and G. Lagaly, *Am. Mineral.*, 1989, **74**, 224-229.

3 K. Beneke and G. Lagaly, *Am. Mineral.*, 1983, **68**, 818-826.

4 D.N. Smith, Ph.D. Thesis, University of Aberdeen, 1981.

5 H. Annehed, L. Fälth and F.J. Lincoln, *Zeitschrift für Kristallographie*, 1982, **159**, 203-210.

6 F. Liebau, *Structural Chemistry of Silicates*, Springer-Verlag, Berlin, 1985, p.70.

7 T. Yanagisawa, T. Schimizu, K. Kuroda and C. Kato, *Bull. Chem. Soc. Japan*, 1990, **63**, 988-992.

8 W.F. Wegst and J.H. Wills, U.S. Reissue, 23043, 1948.

9 C.L. Baker, L.R. Jue and J.H. Wills, *J. Am. Chem. Soc.*, 1950, **72**, 5369.

10 R.L. Hay, *Contrib. Min. Petr.*, 1968, **17**, 225.

11 A.P. Khomiakov, V.I. Stepanov, A.V. Bykova and I.S. Naumova, *Doklody Akademii Nauk SSSR*, 1980, **225**, 971-976.

12 L. McCulloch, *J. Am. Chem. Soc.*, 1952, **74**, 2453.

13 A. Kalt and R. Wey, *Bull. Groupe fr. Argiles*, 1968, **20**, 205.

14 Z. Johan and G.F. Maglione, *Bull. Soc. fr. Mineral. Cristallogr.*, 1972, **95**, 371.

15 R.K. Iler, *J. Coll. Sci.*, 1964, **19**, 648-657.

16 H.P. Eugster, *Science*, 1967, **157**, 1177.

17 G. Bapst, L. Delmotte, J.L. Guth and A. Kalt, *Fortschrift Mineral.*, 1983, **61**, 11-12.

18 H.P. Eugster, B.F. Jones and R.A. Sheppard, *Geol. Soc. Am. Annual Meetings*, 1967, 60.

19 T.P. Rooney, B.F. Jones and J.T. Neal. *Am. Mineral.*, 1969, **54**, 1034.

20 J.J. Rowe, R.O. Fournier and G.W. Moray, *Inorg. Chem.*, 1967, **6**, 1967.

Chapter Two General NMR Theory

2.1 Nuclear Magnetic Resonance

Nuclear Magnetic Resonance (NMR) is the absorption of radiofrequency radiation caused by transitions between the spin-states of certain nuclei. NMR spectroscopy can measure the frequency and quantity of radiation that is absorbed. A recently published text book[1] claims to explain the physical and mathematical basis behind the subject, simply but exactly; it takes 288 pages. Clearly there is only room for an elementary account in this thesis. More information can be found in any of the many available NMR text-books, which have been the source for this chapter.[1-8]

The nuclei of many isotopes possess nuclear spin, characterised by a quantum number, I. This number determines the magnitude of the spin angular momentum, P, and the number of possible spin states, m_I, for each nucleus (2I + 1).

$$P = \hbar\sqrt{I(I+1)} \qquad \text{Eq. 2.1}$$

$$m_I = -I, -I+1, \cdots I-1, I \qquad \text{Eq. 2.2}$$

Nuclear magnetic resonance spectroscopy detects transitions between these spin-states. Therefore, all the nuclei in the periodic table can be divided into three groups on the basis of their spin-quantum number. For those with I=0, NMR spectroscopy is impossible– there is only one spin-state and transitions can not occur. For those with I=½, NMR spectroscopy can be straightforward– there are two spin-states and one possible transition. The spectroscopy of "quadrupolar" nuclei with I>½ is less simple because there are many spin-states and more than one transition; additional complications arise because the nuclei have an electric quadrupole moment. The most abundant isotopes of carbon, oxygen and silicon are NMR-inactive (I=0), though in each case there is a rarer isotope with non-zero spin, ^{13}C, ^{17}O and ^{29}Si.

Since nuclei are charged and spinning they have a magnetic moment, μ. This is proportional to the angular momentum, with a constant of proportionality, γ, that is specific to each nucleus. The gyromagnetic ratio, γ, can be positive or negative depending on whether the spin magnetic moment is parallel or anti-parallel to the spin angular momentum.

$$\mu = \gamma \mathbf{P} \qquad \text{Eq. 2.3}$$

$$\mu = \gamma \hbar \sqrt{I(I+1)} \qquad \text{Eq. 2.4}$$

The 2I+1 spin-states, m_I, are degenerate unless a magnetic field, $\mathbf{B_0}$, is applied. The energy, U, of each spin-state depends on the orientation, θ, of the spin magnetic moment relative to the magnetic field.

$$U = -\mu.\mathbf{B_0} = -\mu \cos\theta B_0 \qquad \text{Eq. 2.5}$$

$$\cos\theta = m_I / \sqrt{I(I+1)} \qquad \text{Eq. 2.6}$$

$$U = -\gamma \hbar m_I B_0 \qquad \text{Eq. 2.7}$$

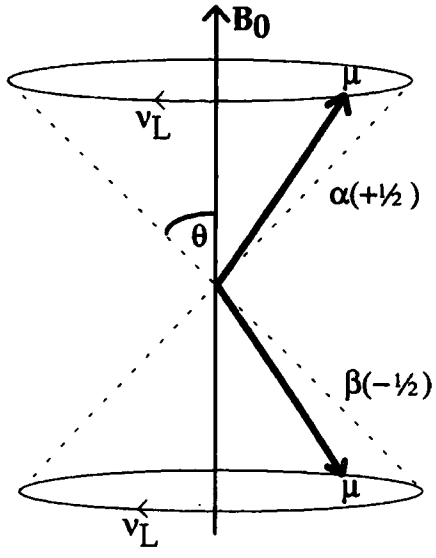

Figure 2.1 The precession of the magnetic moments corresponding to the α and β spin-states of an I = ½ nucleus at the Larmor frequency ν_L about an external magnetic field $\mathbf{B_0}$.

In a classical treatment of resonance, the magnetic moments, μ, experience a torque from $\mathbf{B_0}$. This causes them to precess around $\mathbf{B_0}$ with a frequency, $|\gamma|B_0/2\pi$, known as the Larmor frequency, ν_L. Figure 2.1 is an explanatory diagram.

The 2I + 1 energy levels are clearly separated by an energy $|\gamma\hbar B_0|$ and electromagnetic radiation of an appropriate frequency, ν, will cause transitions. The selection rule governing such transitions is $\Delta m_I = \pm 1$. Nuclear magnetic resonance occurs when the conditions in equation 2.9 are met and energy is absorbed.

$$\Delta E = h\nu = |\gamma\hbar B_0 \Delta m_I| \qquad \text{Eq. 2.8}$$

$$\nu = |\gamma / 2\pi| B_0 \qquad \text{Eq. 2.9}$$

2.2 Bulk Magnetisation and the Rotating Frame of Reference

In a sample at equilibrium, there will be a slight excess of spins in the low energy state(s), giving a resultant magnetic moment parallel to the magnetic field. Therefore, the equilibrium bulk magnetisation of a sample can be represented as a vector parallel to the magnetic field (for $\gamma>0$).

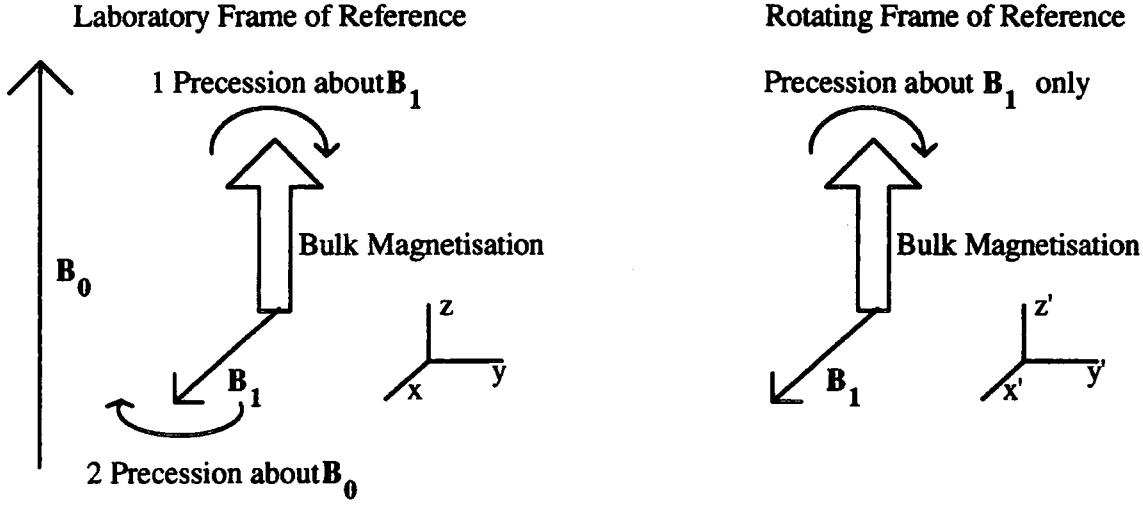

Figure 2.2 The bulk magnetisation vector of a sample lies parallel to the external magnetic field at equilibrium. On resonance, it precesses about both $\mathbf{B_0}$ and $\mathbf{B_1}$. This motion is simpler when considered in the rotating frame of reference.

Electromagnetic radiation is applied for resonance. This acts as a second magnetic field, $\mathbf{B_1}$, perpendicular to and rotating about $\mathbf{B_0}$. On resonance, the bulk magnetisation will precess about $\mathbf{B_1}$. In the laboratory frame of reference, this motion is a complex spiralling. However, the picture can be simplified by considering the motion of the bulk magnetisation relative to $\mathbf{B_1}$. The bulk magnetisation of a sample and the "rotating frame of reference" are useful and common conventions in NMR. Figure 2.2 is an explanatory diagram.

2.3 The Single Pulse Experiment

A classical treatment of the simplest NMR method is very informative. The timing of this experiment can be divided into four regions: a pulse to excite the nuclei, a pause for the electronics in the spectrometer to recover; detection of any magnetisation perpendicular to the external magnetic field; and a delay for the sample to return to equilibrium. This information can be represented as a pulse sequence which shows when the transmitter is switched on and when magnetisation is detected (figure 2.3).

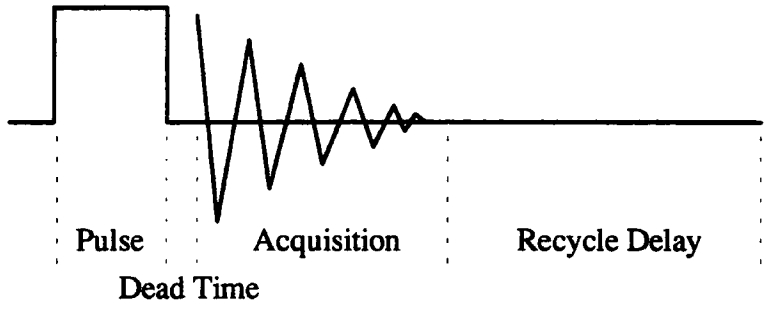

Figure 2.3 Pulse sequence for a Single Pulse experiment.

Because of uncertainty, a pulse can only be monochromatic if it is of infinite duration. The excitation envelope of a finite pulse is sinc shaped around the central frequency, ν_C. The spread of the excitation is larger for shorter pulses. The duration of the pulse, τ_p, and its intensity, B_1, determine the exact position of the bulk magnetisation vector after its application. Excitation of the spins in a sample causes precession of the spin magnetisation vector by an angle $\gamma B_1 \tau_p$ in the rotating frame of reference. Since the magnetisation is detected in the xy-plane, the optimum pulse duration corresponds to 90° of precession– a 90° or $\pi/2$ pulse. A 180° pulse inverts the spins but would give no detectable signal.

The signal is detected in the form of an interferogram or free-induction decay, FID, and follows the decay of magnetisation back to its equilibrium (zero) value in the

xy-plane. This relaxation is caused by a loss of coherence between the individual spins in the sample. The signal is sampled a number of times, TD, during the acquisition time, AQ, with a constant interval– the dwell time, DW. In some spectrometer systems, detectors simultaneously measure at two directions that are 90° out of phase with each other (nominally real and imaginary) so the acquisition time is half the product of DW and TD. The value of DW determines the width of the spectrum, SW, after fourier-transformation– conversion of the time-domain FID into a frequency domain spectrum. The digital-resolution of the spectrum is determined by the number of points that are fourier-transformed and can be increased by zero-filling– addition of zeros after the detected FID.

$$AQ = DW \times TD/2 \qquad \text{Eq. 2.10}$$

$$SW = 1 / DW \qquad \text{Eq. 2.11}$$

The pulse/detect sequence can be repeated many times while the FID's after each pulse are summed to produce a better spectrum. The resultant signal to noise is proportional to $N^{1/2}$, the square root of the number of repetitions, or transients– signal is proportional to N, but noise is proportional to $N^{1/2}$. A recycle delay is necessary in the single pulse sequence to allow the bulk magnetisation of the sample to return to equilibrium between each pulse. The return to equilibrium occurs *via* spin-spin relaxation and spin-lattice relaxation. An adequate acquisition time should be allowed for the former to occur, while five times the spin-lattice relaxation time is necessary for the total inter-pulse time.

2.4 Spin-Lattice and Spin-Spin Relaxation

At equilibrium, the bulk magnetisation vector of a sample lies parallel to the applied magnetic field, along the z-axis, say. During a typical single-pulse NMR experiment, a pulse of the correct intensity, frequency and duration places bulk magnetisation into a plane perpendicular to the external magnetic field. To return to equilibrium, the xy-plane magnetisation must decay to zero and z-axis magnetisation must be recovered. These distinct processes are shown in figure 2.4.

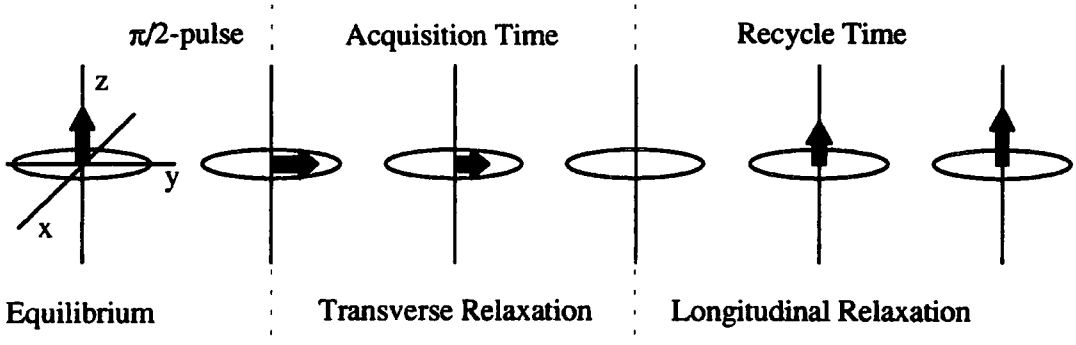

Figure 2.4 The behaviour of the bulk magnetisation in the rotating frame of reference after a $\pi/2$ pulse. Longitudinal and transverse relaxation do in fact occur simultaneously. However, the choice of acquisition time depends on the former while the choice of the recycle time depends on the latter. Longitudinal relaxation is substantially slower than transverse relaxation in solids.

Longitudinal or spin-lattice relaxation usually occurs exponentially with a time constant, T_1, the spin-lattice relaxation time. It can be measured by a simple experiment– inversion recovery (figure 2.5). After a 180° pulse the magnetisation is allowed to relax back to equilibrium for a variable time τ. The extent of the relaxation can be measured with a 90° pulse. A curve of signal against τ for several values of τ can be fitted to equation 2.12 to obtain a value of T_1. Signal intensities, M_0, M_∞ and M_τ, refer to zero, infinite time and τ, respectively.

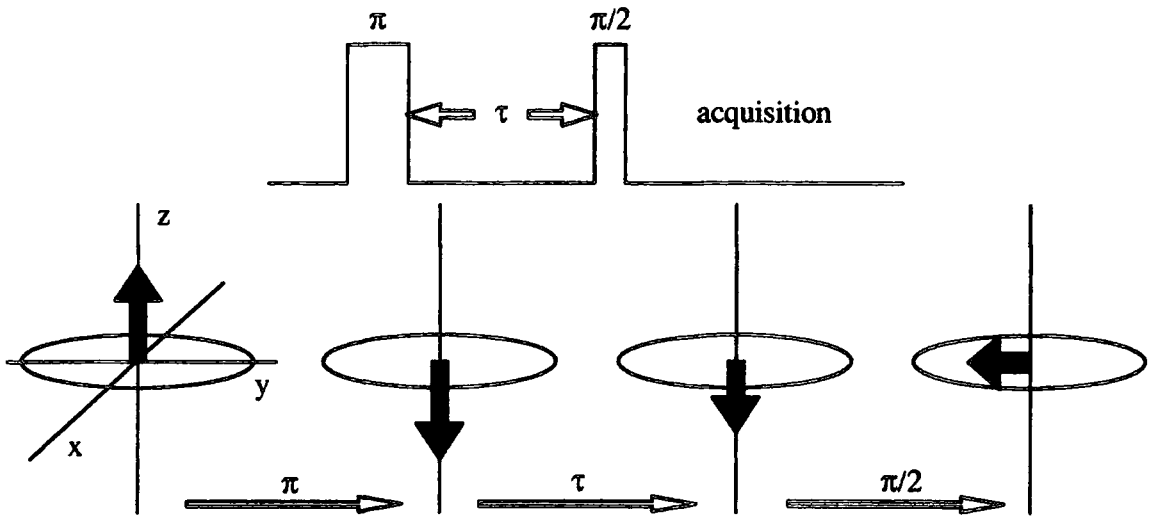

Figure 2.5 The inversion-recovery pulse sequence and its effect on the bulk magnetisation in the rotating frame of reference.

$$M_\tau = M_\infty - (M_\infty - M_0)\exp(-\tau / T_1) \qquad \text{Eq. 2.12}$$

Spin-lattice relaxation occurs through transitions which are caused by oscillating magnetic fields– the opposite of resonance. The value of T_1 can depend on the mobility of the environment of the nucleus or on factors which cause magnetic fields– neighbouring dipoles or paramagnetics, for instance.

The decay of xy-plane magnetisation is monitored by the FID. For a single species on resonance, exponential decay is normally observed. Away from resonance, there will be an additional oscillating component to the decay. In both cases fourier-transformation of the FID gives a spectrum with a line-width at half height of $1/\pi T_2^*$, where T_2^* is the time-constant of the (assumed) exponential decay. Experimental imperfections, such as magnetic field inhomogeneities, have a large effect on the value of T_2^*. A time constant, T_2, the spin-spin relaxation time, can often be measured for the intrinsic transverse decay– that from the sample. Spin-spin relaxation can be regarded as a loss of phase coherence between individual spins in a sample– an entropy phenomenon as well as one of energy. In solids, T_2 is not necessarily well defined.

2.5 Spin-Locking and $T_{1\rho}$

Spin-locking is an important phenomenon in NMR and introduces a third time constant, $T_{1\rho}$, the spin-lattice relaxation time in the rotating frame of reference. The magnetisation created by a 90° pulse can be locked in the x-y plane by applying a second longer pulse, 90° out of phase with the initial one. Since B_1 is the effective static field experienced by the nucleus in the rotating frame, the magnetisation will relax longitudinally with respect to this. Therefore, it is referred to as spin-lattice relaxation, but, since $T_{1\rho}$ involves relaxation in the transverse plane to $\mathbf{B_0}$, it has much in common with T_2. In cases of simple exponential decay, $T_{1\rho}$ can be measured by fitting signal intensities, M_τ, obtained with many spin-lock times, τ, to equation 2.13.

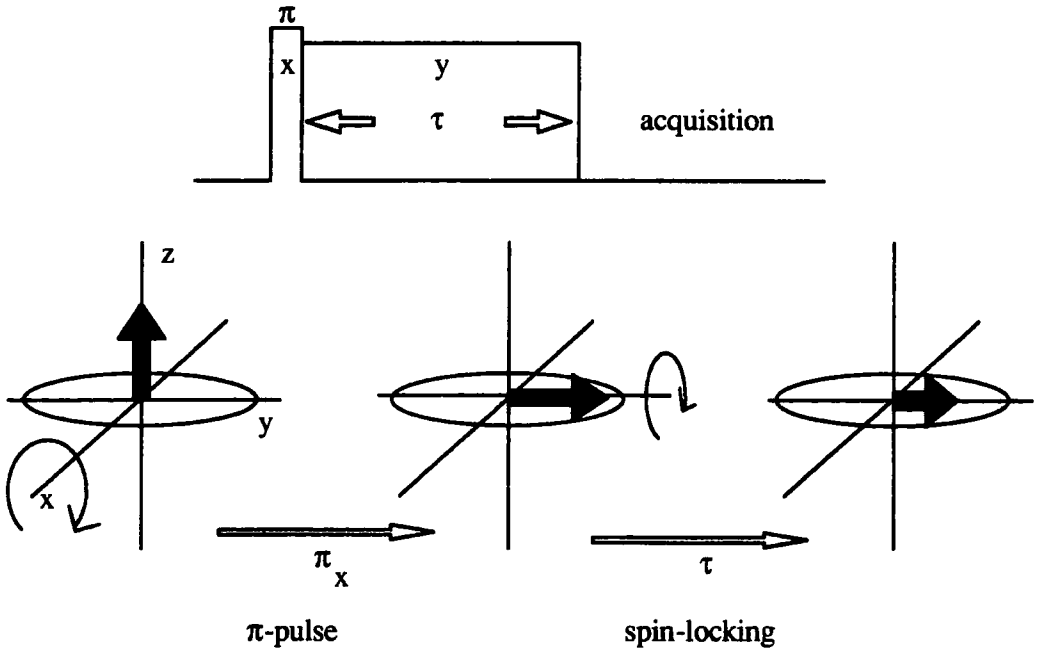

Figure 2.6 A pulse sequence involving spin-locking and its effect on the net magnetisation in the rotating frame of reference.

$$M_\tau = M_0 \exp\left(-\tau / T_{1\rho}\right) \qquad \text{Eq. 2.13}$$

2.6 Hamiltonians

A classical formalism approach to NMR theory is very useful for the consideration of simple experiments. Consideration of bulk magnetisation vectors is adequate for an explanation of the single-pulse and inversion-recovery pulse sequences, for example, but a more rigorous quantum-mechanical treatment is needed for more complicated experiments.

A central postulate of quantum mechanics is that all observables have operators. Since NMR is concerned with resonance lines, corresponding to gaps in energy levels it is energy operators which are relevant. Such an energy operator is referred to as a Hamiltonian operator or Hamiltonian, H. Several Hamiltonians are needed to account for all the internal and external interactions in a given spin system; collectively these are known as the nuclear spin Hamiltonian (equation 2.14).[7]

$$H = H_Z + H_{rf} + H_{CS} + H_Q + H_{SR} + H_D + H_J \qquad \text{Eq. 2.14}$$

H_Z external magnetic fields (the Zeeman term).

H_{rf} external radiofrequency magnetic fields.

H_{CS} induced magnetic fields due to orbital electronic motions (chemical shift).

H_Q electric field gradients (quadrupolar coupling).

H_{SR} associated with molecular angular momentum (spin rotation).

H_D magnetic dipolar coupling.

H_J indirect coupling through electron spins ("scalar" or J coupling).

H_{SR} is scarcely ever encountered in the solid state, so it will not be further discussed here. The four terms, H_{CS}, H_Q, H_J and H_D are reduced to isotropic average values in the solution state. For H_{CS}, this is related to δ, the chemical shift, and for H_J, this is the coupling constant, J. H_Q and H_D are both averaged to zero and therefore have no effect on the transition frequencies observed in solution-state NMR.

The reason for this averaging is that all these terms have an orientation dependence which is averaged by "molecular tumbling" in liquids. Solution-state spectra tend to have sharp, "isotropic" lines, which can be split by scalar coupling, only. In the solid-state, absorptions can cover a range of chemical shift values and be further broadened by dipolar and quadrupolar interactions.

The extra broadening interactions provide the solid-state NMR spectroscopist with additional information that is not available from solution work. Alternatively, several techniques have been devised to remove the line-broadening effects and produce high-resolution solid-state NMR spectra.

2.7 Problems in Solid-State NMR and their Solutions

2.7.1 Solid-State NMR

A perfect NMR experiment would give a spectrum with sharp lines in a short time. There are several ways in which solid-state NMR does not match this ideal. Firstly, anisotropic interactions, which are averaged by molecular tumbling in solutions, tend to have line-broadening effects in the solid-state. Secondly, many useful nuclei are rare. For example, ^{29}Si and ^{13}C are 5 % and 1 % abundant, respectively, so many repetitions would be necessary to acquire a spectrum with reasonable signal to noise. Finally, spin-lattice relaxation times can be large and correspondingly long recycle delays might be necessary. Thankfully, a suite of techniques has been developed for the rapid acquisition of sharp ^{13}C or ^{29}Si spectra: magic-angle spinning (MAS) can average lines broadened by chemical-shift anisotropy; dipolar heteronuclear broadening can be removed by high-power proton decoupling; and cross-polarisation (CP) can give spectra with better signal to noise using short recycle times. These techniques are by no means limited to the acquisition of dilute, spin-½ nuclei, such as ^{13}C or ^{29}Si. Decoupling can narrow spectra for any proton-containing samples, while in favourable cases, magic-angle spinning can average quadrupolar and homonuclear dipolar interactions.

2.7.2 Shielding Anisotropy and Magic-Angle Spinning

The exact frequency, ω, for resonance of a particular nuclear site depends on the gyromagnetic ratio, γ, of the nucleus and the degree to which the nucleus is screened from the external magnetic field (equation 2.15).

$$\omega = \gamma (B_0 - \sigma B_0) \qquad \text{Eq. 2.15}$$

The shielding constant, σ, is anisotropic, *i.e.* its value can differ with the orientation of the nucleus with respect to $\mathbf{B_0}$. It is therefore a tensor with diagonal elements σ_{11}, σ_{22} and σ_{33}, the principal components. The observed shielding, σ_{zz}, which corresponds to the chemical shift, is the combination of the principal components given by equation 2.16, where θ_j is the angle between σ_{jj} and the applied magnetic field. In isotropic solution an average value, σ_{iso}, is seen due to molecular tumbling (equation 2.17). The screening observed in solids can be related to σ_{iso} by equation 2.18.

$$\sigma_{zz} = \sum_{j=1}^{3} \sigma_{jj} \cos^2 \theta_j \qquad \text{Eq. 2.16}$$

$$\sigma_{iso} = \tfrac{1}{3}(\sigma_{11} + \sigma_{22} + \sigma_{33}) \qquad \text{Eq. 2.17}$$

$$\sigma_{zz} = \tfrac{1}{3}\sigma_{iso} + \tfrac{1}{3}\sum_{j=1}^{3}\left(3\cos^2 \theta_j - 1\right)\sigma_{jj} \qquad \text{Eq. 2.18}$$

Since a powder sample will contain nuclei with range of orientations, θ, a spectrum influenced by chemical-shift anisotropy, will have a range of chemical shifts. The pattern of this broadening will depend on the values of the principal components and a single line will only be seen for the case where $\sigma_{11}=\sigma_{22}=\sigma_{33}$, *i.e.* cubic symmetry.

Magic-angle spinning can be used to remove the effects of chemical shift anisotropy. If a sample is rotated at an angle, β, to the applied magnetic field, equation 2.19 describes the relationship between β, θ_j and χ, the angle between σ_{jj} and the axis of rotation.

$$\left\langle 3\cos^2 \theta_j - 1 \right\rangle = (3\cos^2 \beta - 1)(3\cos^2 \chi - 1) \qquad \text{Eq. 2.19}$$

At an angle $\beta=\cos^{-1}(3^{-1/2})$, the average value of $(3\cos^2\theta_j-1)$ is zero. This angle, 54.7°, is known as the "magic-angle". Thus, rapid magic-angle sample-spinning (figure 2.7) can average the effects of chemical shift anisotropy to give a spectrum with a single isotropic line. A spinning rate greater then the width of the powder pattern is necessary for complete averaging. At rates less than this value, and greater than the intrinsic line-width, the powder pattern will break up into a manifold of spinning side-bands– a central line at the isotropic chemical shift and satellites at multiples of the spinning rate from the centre.

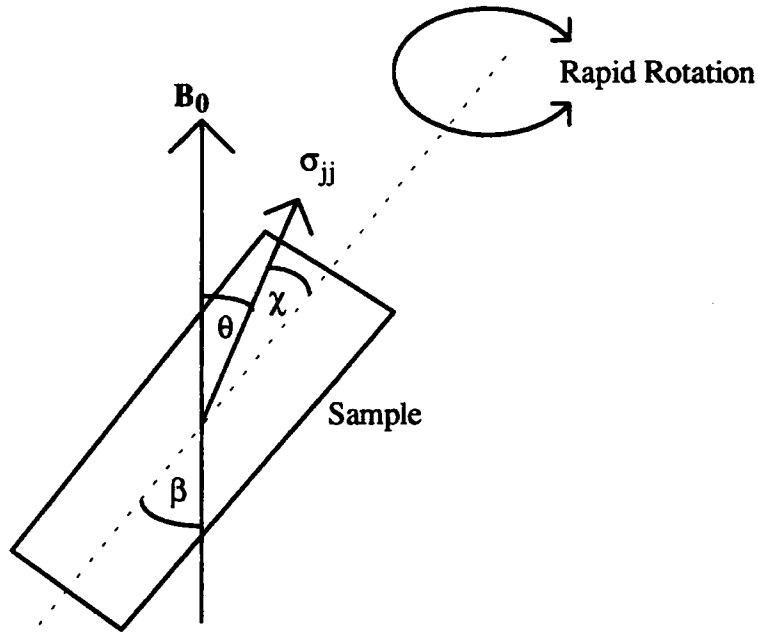

Figure 2.7 Magic-angle spinning.

2.7.3 Dipolar Broadening and High-Power Proton Decoupling

The dipolar interaction is responsible for cross-polarisation and spin-diffusion, which will be further considered later in this work. It is also responsible for the broadening of ^1H spectra (homonuclear dipole-dipole coupling, protons interacting with other protons in a sample) and spectra of other nuclei (heteronuclear dipole-dipole coupling, the interaction of protons with ^{29}Si or ^{13}C, say).

The simplest hetero– and homonuclear systems to consider are those containing just two spins. Though this is an ideal case, it is approached in real samples where two interacting species are isolated. For a heteronuclear system, IS, the transition frequency, $\nu_{obs.}$, of the non-proton nucleus, S, is given by equation 2.20, where θ is the angle between the internuclear vector, r_{IS}, and the applied magnetic field. D is the dipolar coupling constant– a useful value to measure because it can be related to r_{IS}.

$$\nu_{obs.} = \nu_S \pm \tfrac{1}{2} D(1 - 3\cos^2\theta) \qquad \text{Eq. 2.20}$$

$$D = \gamma_I \gamma_S \frac{\hbar}{2\pi} \frac{\mu_0}{4\pi r_{IS}^3} \qquad \text{Eq. 2.21}$$

In a powder, there will be many values of θ and the observed spectrum will be a powder pattern, with a characteristic shape. Rapid magic-angle spinning can average the orientation term in equation 2.20 to zero. However, the rate of rotation would have to be of the same order as the dipolar coupling. Alternatively, the protons can be decoupled by irradiation of the sample at the proton resonance frequency during acquisition. This technique, high-power proton decoupling, is similar to the decoupling used in solution-state NMR to remove the effects of scalar coupling. However, much higher power is necessary in the solid-state as D_{SiH} can be around three orders of magnitude larger than J_{SiH}.

Similar broadening is observed in ^1H NMR, where decoupling is clearly not possible. Some line-narrowing can be achieved by magic-angle spinning, and more elaborate techniques are available for the acquisition of high-resolution spectra, such as CRAMPS.

2.7.4 Cross-Polarisation

Acquisition of ^{13}C or ^{29}Si spectra is encumbered by the low natural abundance of these nuclei and long spin-lattice relaxation times. However, many samples contain protons which are 100 % abundant and have short values of T_1. Cross-polarisation (CP) is a method which uses the desirable properties of protons to obtain spectra for other nuclei. The resultant ^{13}C or ^{29}Si CP spectra can be acquired more quickly and with better signal to noise than with the SP technique.

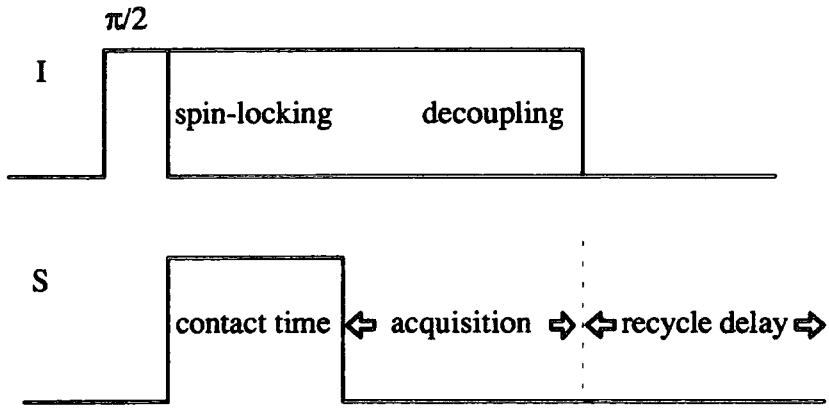

Figure 2.8 A standard cross-polarisation sequence.

Cross-polarisation occurs *via* a transfer of magnetisation in the rotating frame of reference from excited protons, I, to rare nuclei, S. The sequence in figure 2.8 starts with a 90° pulse in the proton channel. The resultant magnetisation is then spin-locked and the rare-spin transmitter is switched on for a period known as the contact time. Under favourable conditions, magnetisation can be transferred to the S-spins. A rare-nucleus spectrum can then be acquired, with decoupling, if necessary.

The Hartmann-Hahn matching condition is favourable for magnetisation transfer. At this condition (equation 2.22), the energy level separations of the spin-locked I-spins and S-spins are the same and magnetisation transfer is energy-neutral

and efficient. The heteronuclear dipolar interaction is responsible for this process and it occurs *via* "flip-flops"– $\alpha\beta$ to $\beta\alpha$.

$$\gamma_I B_{1I} = \gamma_S B_{1S} \qquad \text{Eq. 2.22}$$

The CP recycle delay is chosen on the basis of the proton spin-lattice relaxation time, so a faster rate of repetition is usually possible for CP. The signal enhancement inherent in this experiment can be derived with a thermodynamic treatment of the cross-polarisation process for a system of abundant I-spins and dilute S-spins.[3] Equations 2.23 and 2.24 show that the equilibrium magnetisation of the I and S spins, $M_I^{(0)}$ and $M_S^{(0)}$, is proportional to the quotient of the external magnetic field, B_0, and the temperature of the whole system, or lattice temperature, T_L. In these equations, k is the Boltzmann constant and N_I and N_S are the numbers of I and S-spins respectively.

$$M_I^{(0)} = \frac{\hbar}{kT_L}\left(\tfrac{1}{3}\gamma_I^2\hbar I(I+1)N_I\right)B_0 = \beta_L C_I B_0 \qquad \text{Eq. 2.23}$$

$$M_S^{(0)} = \frac{\hbar}{kT_L}\left(\tfrac{1}{3}\gamma_S^2\hbar S(S+1)N_S\right)B_0 = \beta_L C_S B_0 \qquad \text{Eq. 2.24}$$

The bracketed terms are Curie constants, C_I and C_S, while $\hbar/kT_L$ is the inverse lattice temperature, β_L. When the proton magnetisation is spin locked, the spin-temperature, β_0, is much greater as the apparent field, B_{1I}, is smaller than B_0. Equation 2.26 relates the energy of the spin-system, E, to the inverse spin temperature of the abundant spins.

$$M_I^{(0)} = \beta_0 C_I B_{1I} \qquad \text{Eq. 2.25}$$

$$E = -\beta_0 C_I B_{1I}^2 \qquad \text{Eq. 2.26}$$

During the contact time, the I and S spins reach thermal equilibrium with a common spin-temperature, β_1. After the contact time the energy of the system can be rewritten in terms of β_1. Equation 2.27 is correct since energy is conserved.

$$E = -\beta_1 C_I B_{II}^2 - \beta_1 C_S B_{IS}^2 = -\beta_0 C_I B_{II}^2 \qquad \text{Eq. 2.27}$$

The resultant inverse spin-temperature can be calculated with a substitution of terms for the Hartmann-Hahn conditions and the definition of the Curie constant into equation 2.27.

$$\beta_1 = \beta_0 \left(1 + \frac{\gamma_I^2 C_S}{\gamma_S^2 C_I}\right)^{-1} = \beta_0 \left(1 + \frac{S(S+1)N_S}{I(I+1)N_I}\right)^{-1} = \beta_0 (1+\varepsilon)^{-1} \qquad \text{Eq. 2.28}$$

Equation 2.29 shows that the S magnetisation after the contact time, $M_S^{(1)}$, can be obtained from β_1. The enhancement, η, with respect to the equilibrium value can be calculated. This is the enhancement that might be expected with cross-polarisation compared to single-pulse methods (equation 2.30).

$$M_S^{(1)} = \beta_1 C_S B_{1S} = \frac{\gamma_I}{\gamma_S}(1+\varepsilon)^{-1} \beta_L C_S B_0 \qquad \text{Eq. 2.29}$$

$$\eta = \frac{M_S^{(1)}}{M_S^{(0)}} = \frac{\gamma_I}{\gamma_S}(1+\varepsilon)^{-1} = \frac{M^{CP}}{M^{SP}} \qquad \text{Eq. 2.30}$$

For cross-polarisation between abundant and rare spin-½ nuclei, the value of ε is small and the enhancement is simply the ratio of the gyromagnetic ratios. Thus the signal for ^{13}C and ^{29}Si CP might be increased with respect to that for SP by factors of 27/7 and 27/5, respectively. This is the maximum possible enhancement for a single cycle of the pulse sequence and there are several factors which might make the observed signal enhancement less than this (see chapter 7).

References

1 J.W. Hemmel and J. Klinowski, *Fundamentals of Nuclear Magnetic Resonance*, Longman Scientific and Technical, Harlow, 1993.

2 A.E. Derome, *Modern NMR Techniques for Chemistry Research*, Pergamon Press, Oxford, 1987.

3 R.R. Ernst, G. Bodenhausen and A. Wokaun, *Principles of Nuclear Magnetic Resonance in One and Two Dimensions*, Clarendon Press, Oxford, 1987.

4 B.C. Gerstein and C.R. Dybowski, *Transient Techniques in NMR of Solids*, Academic Press Inc., Orlando, 1985.

5 P. Granger and R.K. Harris, eds., *Multinuclear Magnetic Resonance in Liquids and Solids– Chemical Applications*, Kluwer Academic Publishers, Dordrecht, 1990.

6 R.K. Harris, *Nuclear Magnetic Resonance Spectroscopy: A Physiochemical View*, Longman Scientific and Technical, Harlow, 1987.

7 S.W. Homans, *A Dictionary of Concepts in NMR*, Clarendon Press, Oxford, 1989.

8 J.K.M. Sanders and B.K. Hunter, *Modern NMR Spectroscopy*, Oxford University Press, Oxford, 1987.

Chapter Three Literature Review

3.1 Classification of Silicate Atom Types and their Detection by ^{29}Si NMR

Though coordination numbers one to six have been assigned to silicon, the only relevant values in silicates are four and six.[1] These correspond to SiO_4 tetrahedra and SiO_6 octahedra. However, octahedral coordination is observed in few silicates (for example, thaumasite and stishovite) and the remainder of this discussion can be restricted to the tetrahedral case. The oxygen atoms in an $[SiO_4]^{4-}$ tetrahedron can either form bridges to other silicon atoms or remain as anions; the charge being balanced by cations.

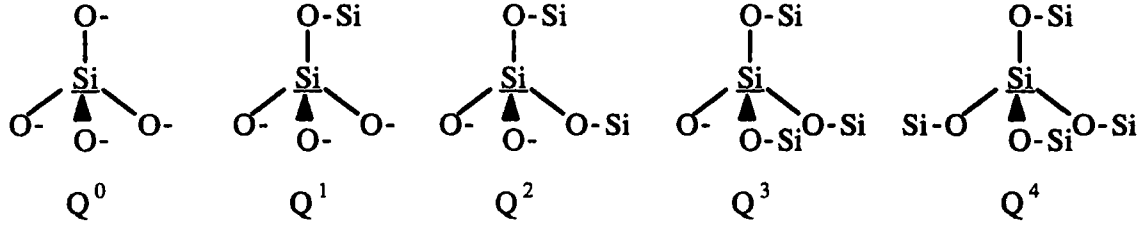

Figure 3.1 The Q^s nomenclature for silicon atom types. In each case, the underlined atom in the centre of the polyhedra can be described by the number of bridging oxygen atoms to which it is bonded.

Liebau has classified silicate silicon atoms by the number of bridging oxygen atoms or connectedness, s, and the Q^s nomenclature is commonly used (see figure 3.1).[2] Values of n between 0 and 4 are possible in this very useful convention. The isolated monomeric anion in the nesosilicate, olivine (Mg_2SiO_4) is designated Q^0.[2] Dimeric and trimeric sorosilicate structures, such as hemimorphite, $Zn_4Si_2O_7(OH)_2$, and aminoffite, $Ca_3(BeOH)_2Si_3O_{10}$, can contain Q^1 and Q^2 silicon atoms. The latter are also found in rings or cyclosilicates, such as pseudowollastonite, $CaSi_3O_9$, and infinite chains or inosilicates, such as enstatite, $Mg_2Si_2O_6$. Two-dimensional silicate sheets are known as phyllosilicates. These include the layered sodium polysilicate

hydrates and contain Q^3 and Q^4 units, depending on the sheet-thickness. Makatite, $Na_2O{:}4SiO_2{:}5H_2O$, is a single-sheet silicate and contains Q^3 atoms only. Three-dimensional frameworks, such as quartz and other silica polymorphs, $(SiO_2)_x$, contain Q^4 atoms only. Figure 3.2 shows some examples.

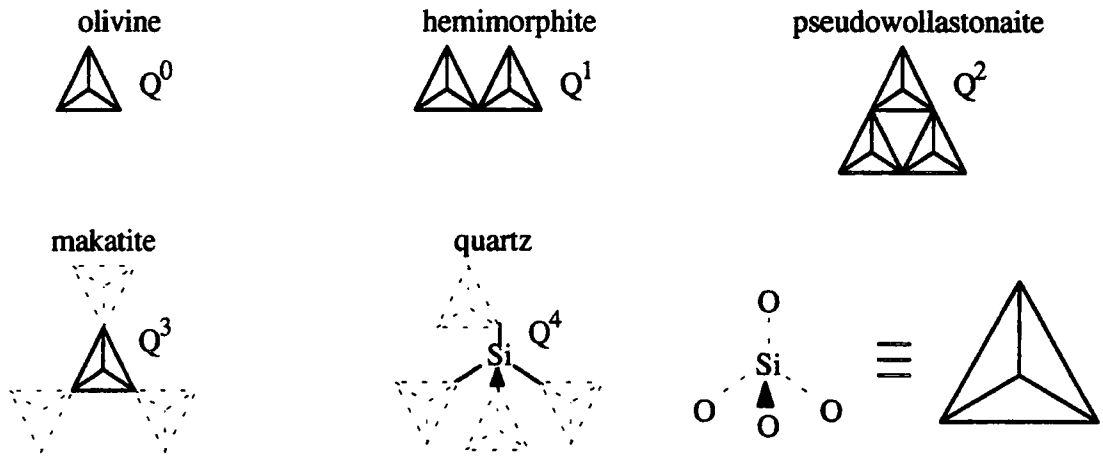

Figure 3.2 Examples of silicates containing different types of silicon atom.

In many cases, the connectedness of a silicon atom can be determined from the chemical shift of its ^{29}Si NMR signal. Several authors have reported tables relating δ_{Si} ranges to Q^s.[3,4,5] These have been obtained by considering many silicates where structures are known. Figure 3.3 combines the data from Engelhardt and Michel[2] and Mägi *et al.*[5]

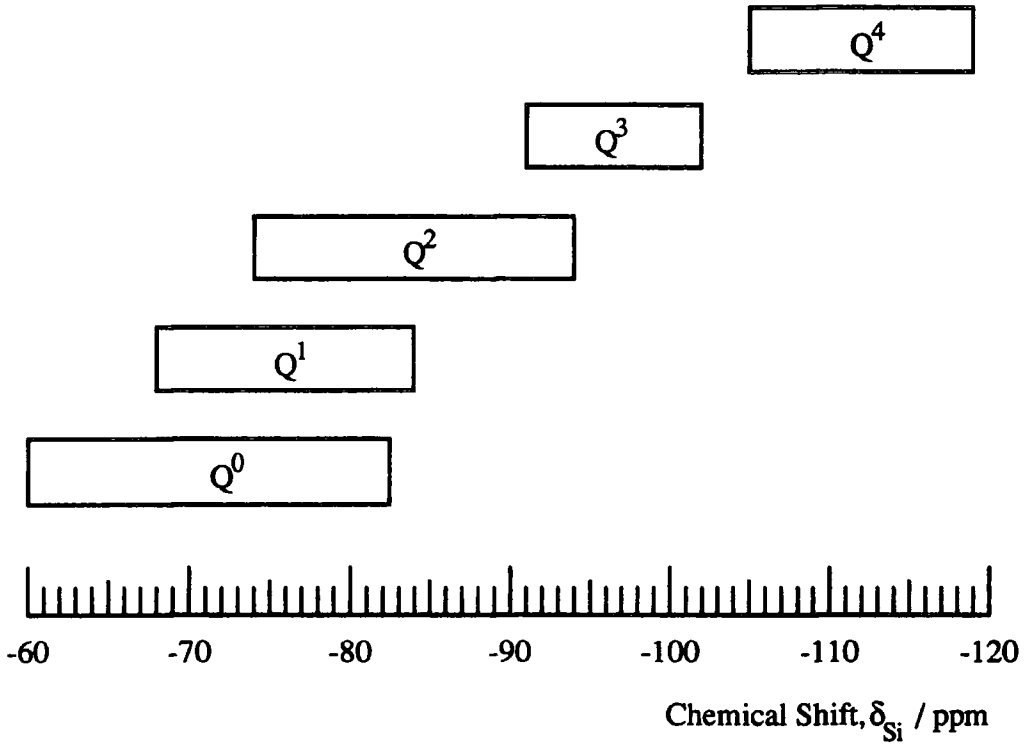

Figure 3.3 The relationship between ^{29}Si chemical shift and connectedness.

3.2 Previous NMR Studies of the Layered Sodium Polysilicate Hydrates

The first ^{29}Si NMR spectra of layered sodium polysilicate hydrates were reported by Schwieger *et al.* in 1985.[6] The authors acquired single-pulse spectra for octosilicate, magadiite and a "kenyaite-like structure." Separate signals could be resolved for silicon species of type Q^3 and Q^4. The Q^4 chemical shifts of the single signal in octosilicate and the overlapping signals in magadiite and kenyaite were related to mean Si-O-Si bond angles using the relationship of Smith and Blackwell.[7] Successful cross-polarisation spectra were acquired for octosilicate and magadiite, only. The enhancement of the Q^3 signals with respect to the Q^4 signals in these spectra was related to the stronger interaction between proton and silicon nuclei in a silanol silicon atom, ≡Si-OH. The authors measured the ratios of Q^3 and Q^4 peak areas for octosilicate, magadiite and kenyaite as 1:0.89, 1:2.07 and 1:4.07, respectively. These values were used to form hypothetical model structures for the layered sodium polysilicate hydrates by condensation of two, three or five layers of the known makatite structure.[8] Similar models were related to thermal behaviour and powder X-ray diffraction results by Brandt and co-workers.[9,10,11]

Pinnavaia *et al.* used ^{29}Si NMR to study tetrahedral site distributions in magadiite and its layered silicic acid.[12] Two signals were visible in a ^{29}Si SP spectrum of magadiite. These were assigned with respect to the chemical shift of kanemite which was assumed to contain Q^3 silicon atoms only. Since the high-frequency signal of magadiite shared this chemical shift, it was assigned to Q^3 silicon atoms while the other signal was assigned to Q^4 silicon atoms. The integrated Q^3:Q^4 ratios of the two signals was 0.25:0.75 in magadiite and 0.24:0.76 in H-magadiite. These values were used to form a simple hypothetical model of the H-magadiite silicate layer. The spectrum of kanemite also contained a small Q^4 absorption, due to hydrolysis and condensation of the Q^3 units.

Rojo *et al.* used ^{29}Si NMR to study the thermal behaviour of H-magadiite and the formation of a silyl derivative.[13] After heating at 200 °C, the silicic acid gives a

spectrum containing two broad lines which were assigned to Q^3 and Q^4 silicon sites. There was an increase in the relative Q^4 intensity after heating at 500 °C. This is characteristic of condensation processes which were complete after heating to 800 °C, where a single Q^4 line was observed. The initial heating resulted in a sharpening of the two signals and a divergence of their chemical shifts. This was attributed to a decrease in interactions between the Q^3 silanol protons and bridging oxygen atoms. The ^{29}Si NMR spectrum of a trimethylsilyl derivative contained similar signals to the original H-magadiite sample, indicating that many structural features were retained after the silylation procedure. Rojo *et al.* proposed a simple structure for the H-magadiite silicate layer using the same method as Pinnavaia *et al.* and their own Q^3:Q^4 site ratio (0.33:0.67).

The work of Nesbitt included ^{29}Si, ^{23}Na and ^{1}H NMR spectra of several makatite, kanemite, octosilicate, magadiite and kenyaite samples.[14] The ^{29}Si spectra of makatite and kanemite contained two Q^3 signals. In both cases, these were assigned with respect to the known crystal structure of makatite.[8] The two types of silicon atom can be differentiated with respect to bonding to sodium, *via* oxygen. Nesbitt also acquired ^{23}Na NMR and ^{1}H CRAMPS spectra. A notable conclusion from the former was the presence of an isolated sodium site in some magadiite and kenyaite samples.[15] This sodium site produced no signal on ^{23}Na cross-polarisation and a high-frequency Q^4 signal in kenyaite behaved similarly on ^{29}Si cross-polarisation. For octosilicate, magadiite and kenyaite, ^{29}Si SP site ratios, Q^3:Q^4, were used to form hypothetical model structures in the same way as Schwieger *et al.*[6] Thus, the structure of all the other layered sodium polysilicate hydrates could be related to that of makatite. The average measured Q^3:Q^4 ratios in his work were 1:1 for octosilicate, 1:1.5 for magadiite and 1:2.7 for kenyaite. Unlike Schwieger *et al.*, Nesbitt saw that the sheets could be condensed in two ways. One of these methods of "lamination" left Q^3 silicon atoms within the silicate layers, providing a plausible site for isolated sodium species.

Garces *et al.*[16] based model structures for magadiite and octosilicate on known zeolite structures using scant evidence from infrared and ^{29}Si NMR spectroscopy. The FTIR spectra of octosilicate and magadiite contain peaks at 1225 cm^{-1}, shoulders at 1210 cm^{-1} and 1175 cm^{-1} and absorptions in the region 650-500 cm^{-1}. Such features are typical of five-membered rings of silicon atoms (as in sepiolite), blocks of four five-membered rings (dachiardite and epistilbite) and chains of blocks of four five-membered rings, respectively. The ^{29}Si NMR spectra contained Q^3 and Q^4 silicon sites, with the former being lost on heating the samples. The Q^3 chemical shifts were similar to that observed in zeolite ZSM-5 and the Q^4 chemical shifts were in the region of silicalite absorptions. With this spectroscopic evidence, the authors proposed new hypothetical structures for magadiite and octosilicate which were based on those of the mordenite and pentasil group zeolites, which also contain 5-membered rings.

Yanagisawa *et al.* prepared trimethylsilyl, diphenylmethylsilyl, allyldimethylsilyl and dodecyltrimethyl ammonium derivatives of kanemite, magadiite and K-kenyaite.[17-20] A microporous product was prepared by calcination of the latter. Several techniques were used in the characterisation of these reactions, including ^{29}Si NMR spectroscopy. By making organic derivatives of the surface silanol groups of the layered sodium polysilicate hydrates, the authors hoped to "design the interlayer space."

Rojo *et al.* reported a spectroscopic study of the formation of H-magadiite by proton-sodium exchange.[21] Two end-points were visible in curves for the titration of their magadiite sample with acid. These correspond to exchange of the two types of sodium species that are visible in the ^{23}Na NMR spectra. The authors investigated this reaction with a variable temperature static ^1H NMR and infrared study and measured the basal spacings of their silicic acid products using powder X-ray diffraction. The silicic acid from natural magadiite (basal spacing, d_{001} = 11.2 Å) was different to that from a synthetic sample (d_{001} = 13.2 Å). Using their results, the authors were able to propose a schematic interlayer space (figure 3.4) There are two

sites for the sodium ions in magadiite together with water molecules, hydroxyl groups and oxide ions. The H-magadiite interlayer space consists solely of two types of hydroxyl groups– as previously predicted by Rojo *et al.*[22] Thermogravimetric analysis showed that the silicic acids contain less water than their parent sodium form. On heating Na-magadiite, water molecules are lost below 250 °C; above this temperature, silanol groups condense with the loss of further water molecules.

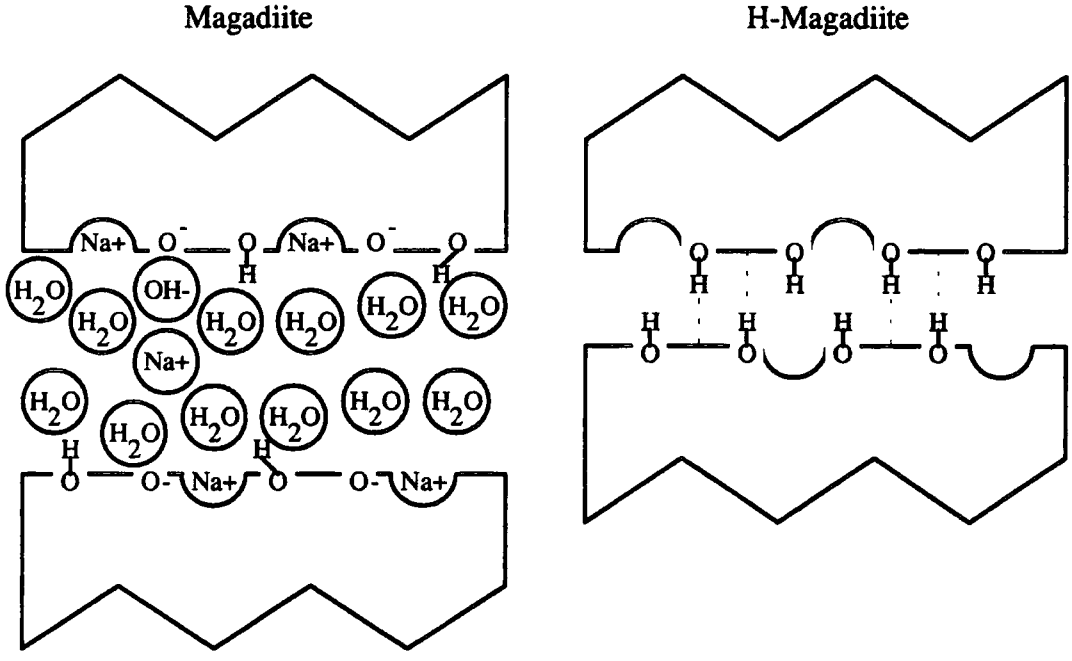

Figure 3.4 Schematic representations of the interlayer spaces in magadiite (d_{001} = 15.5 Å) and H-magadiite (d_{001} = 11.2 Å), after Rojo *et al.*[21]

Sprung *et al.* produced a microporous pillared magadiite sample, by the reaction of H-magadiite with polymers of phenyltrichlorosilane and cyclohexyltrichlorosilane.[23] Powder X-ray diffraction, surface area measurements, scanning electron micrography, thermogravimetric analysis, infrared spectroscopy and ^{29}Si and ^{13}C NMR were used as analytical methods during this work. Single-pulse ^{29}Si spectra were shown for the original magadiite sample, its silicic acid and a pillared derivative. The structure of the silicate layer was probably retained after reaction with the

organosilicon polymer since all three spectra show similar Q^3 and Q^4 peaks. Cross-polarisation ^{29}Si spectra were reported for the pillared product even after calcination at 550 °C, indicating that the sample still contained some protons after extreme heat treatment.

Schwieger *et al.* studied the acidification of makatite.[24] The ^{29}Si NMR spectra of makatite and H-makatite would be expected to have Q^3 peaks only. This was the case in their cross-polarisation spectra, but a second peak was visible at δ_{Si} -107.5 in the single-pulse spectra. This was assigned to an α-quartz impurity on the basis of its chemical shift.[25] H-Makatite had a main peak at a lower-frequency than its parent sodium form, by *ca.* 7 ppm. Slightly shifted signals had been observed in the silicic acid spectra of octosilicate, magadiite and kenyaite: the difference in chemical shifts covered a range of -0.1 ppm to 2.0 ppm. The shift change for makatite and H-makatite was similar to that observed for α-$Na_2Si_2O_5$ and $H_2Si_2O_5$-I (δ_{Si} -94.4 and -101.6, respectively). These observations were explained with respect to structural effects– for example, changes in bond-angle.

Scholzen *et al.*[26] published a paper entitled "Diversity of Magadiite." Several samples of magadiite and a related potassium silicate were analysed using powder X-ray diffraction, FTIR spectroscopy and ^{29}Si NMR. The related potassium silicates could be prepared from magadiite by treating the silicic acid with aqueous potassium hydroxide. Though other methods showed that there was some diversity in these samples, they all had similar basal spacings in the region 15.0-15.2 Å. The powder X-ray diffraction patterns could be sharpened by refluxing the silicates in aqueous Na_2CO_3 solution. The ^{29}Si NMR spectra contained Q^3 signals over a range of 0.4 ppm and the Na_2CO_3-treatment shifted the ^{29}Si NMR signals to lower frequencies by *ca.* 2 ppm, sharpening the lines of the Na-magadiite samples, considerably. The main manifestation of the diversity is in the measured Q^4:Q^3 ratios. These varied between 1 and 2.7. The authors related these ratios to formulae and noted that the values were heavily dependent on pulse repetition times.

Borbély *et al.* studied the characterisation and structural features of octosilicate and H-octosilicate.[27] They used a combination of thermogravimetric analysis and Karl Fischer titrations to determine the water contents of their samples. The method allowed molecular water and structural water (from silanol groups) to be distinguished. A small amount of aluminium contamination was detected in octosilicate by ^{27}Al NMR; this was used to assign the small shoulder in a ^{29}Si NMR spectrum to Si{3Si,Al}. Acidification of octosilicate produced a silicic acid with a Q^3 signal at δ_{Si} -99. On mild heating this shifted to δ_{Si} -103; this change was accompanied by a sharp DTA endotherm at *ca.* 360 K. The powder X-ray diffraction pattern of H-octosilicate was tentatively indexed using the a and b parameters of octosilicate; with a smaller value for c (corresponding to a shorter basal spacing) and a 119.8° value for β– indicating that acidification results in a shearing of the silicate layers.

Dailey and Pinnavaia reported an intercalative reaction of a cobalt(III) cage complex with magadiite[28] and the formation of a silica-pillared derivative of H-magadiite.[29] The cationic metal cage complex was (1,3,6,8,10,13,16,19-octaazabicyclo[6,6,6]eicosane)cobalt(III) and the silica-pillared derivative was formed by reaction with octylamine and tetraethylorthosilicate. Several analytical methods were used in their work, including some highly-significant ^{29}Si NMR measurements. Previously, there had been great variety in the reported Q^3:Q^4 ratios for magadiite. This was assumed to be due to selective saturation of some of the signals because a short repetition time ($<5T_1^{Si}$) had been used. Dailey and Pinnavaia calculated ^{29}Si spin-lattice relaxation times and determined an accurate Q^3:Q^4 ratio of 0.35:1 for Na-magadiite. The T_1-values were 180 s and 280 s for the Q^3 and Q^4 sites, respectively in magadiite and 95 s for all peaks in H-magadiite.

Wong and Cheng prepared pillared magadiite by ion-exchange with Keggin ion solution.[30] The sample was used as a catalyst in an attempted dehydration of propan-2-ol and the ^{29}Si SP spectrum was fairly similar to that of H-magadiite after calcination in air at 300 °C.

Hauck used octosilicate as a standard sample to test spectrometer procedures for measuring relaxation times.[31] The results include spin-lattice relaxation times of 60 s and 117 s for the Q^3 and Q^4 signals in octosilicate and an accurate Q^3:Q^4 ratio which was close to unity.

Heidemann also measured ^{29}Si spin-lattice relaxation times for magadiite and calculated Q^3:Q^4 ratios.[32] In his work T_1-values were even larger 156 s and 500 s to 610 s for the Q^3 and Q^4 signals, respectively, in a synthetic sample and 274 s and 784 s to 915 s in a natural sample. The Q^3:Q^4 ratios in both samples was around 1:3.

Many authors have acquired ^{29}Si NMR spectra of the layered sodium polysilicate hydrates. Table 3.1 lists chemical shifts and there is clearly some variation.

Silicate	Silicon Chemical Shift, δ_{Si} / ppm		Reference
	Q^3	Q^4	
Makatite	-93.5		Nesbitt[14]
Makatite	-93.6		Schwieger *et al.* [24]
Kanemite	-101		Pinnavaia *et al.*[12]
Kanemite	-95.9 -97.8		Nesbitt[14]
Kanemite	-97.2		Yanagisawa *et al.*[20]
Octosilicate	-101.8	-111.2	Schwieger *et al.* [6]
Octosilicate	-100.2	-111.3	Nesbitt[14]
Octosilicate	-100	-111	Garces *et al.*[16]
Octosilicate	-100.5	-111.7	Borbély *et al.*[27]
Octosilicate	-99.9	-111.1	Hauck[31]
Magadiite	-101.0	-112.2 -114.8 -117.5	Schwieger *et al.*[6]
Magadiite	-102	-113	Pinnavaia *et al.*[12]
Magadiite	-99.5	-109.6 -111.3 -114.0	Nesbitt[14]
Magadiite	-99.5	-109.5 -111.3 -114.0	Nesbitt[14]
Magadiite	-99.1	-109.3 -111.3 -113.6	Nesbitt[14]
Magadiite	-99.5	-111.3 -114.0	Nesbitt[14]
Magadiite	-99.5	-109.0 -111.3 -114.0	Nesbitt[14]
Magadiite	-99.5	-109.0 -111.3 -114.0	Nesbitt[14]

Silicate	Silicon Chemical Shift, δ_{Si} / ppm		Reference
	Q^3	Q^4	
Magadiite	-99.7	-109.5 -111.2 -113.6	Garces *et al.*[16]
Magadiite	-99.0	-110.7 -113.2	Yanagisawa *et al.*[17,18,19]
Magadiite	-99.1	-109.7 -111.0 -113.7	Sprung *et al.*[23]
Magadiite	-99.2	-110.0 -111.0 -113.5	Scholzen *et al.*[26]
Magadiite	-99.3	-110.0 -111.2 -113.9	Scholzen *et al.*[26]
Magadiite	-99.8	-110.7 -111.7 -114.2	Dailey and Pinnavaia[28]
"Kenyaite" – a kenyaite-like structure	-101.0	-109.7 -112.2 -114.1 -117.0 -120.5	Schwieger *et al.*[6]
Kenyaite	-99.5	-108.2 -110.6 -111.2 -114.0 -118.5	Nesbitt[14]
Kenyaite	-99.1	-109.5 -111.3 -113.6 -118.5	Nesbitt[14]
K-Kenyaite	-98.5	-109.7	Yanagisawa *et al.*[17,18,19]

Table 3.1 Literature ^{29}Si chemical shifts for layered sodium polysilicate hydrates.

3.3 Layered Sodium Polysilicate Hydrate Structures

3.3.1 Known Structures of Potentially-Related Silicates

Makatite is the only layered sodium polysilicate hydrate with a known structure. This was reported by Annehed *et al.* in 1982.[8] Single crystals of an adequate size for X-ray diffraction were grown from a solution containing the complexing agent, triethanolamine.[33] The structure consists of single silicate layers separated by hydrated sodium ions. Figure 3.5 shows that each $[Si_2O_4(OH)]_n^{n-}$ layer consists of six-membered rings of corner-sharing SiO_4 tetrahedra. Figure 3.6 shows the co-ordination of water and oxide ions around the sodium ions.

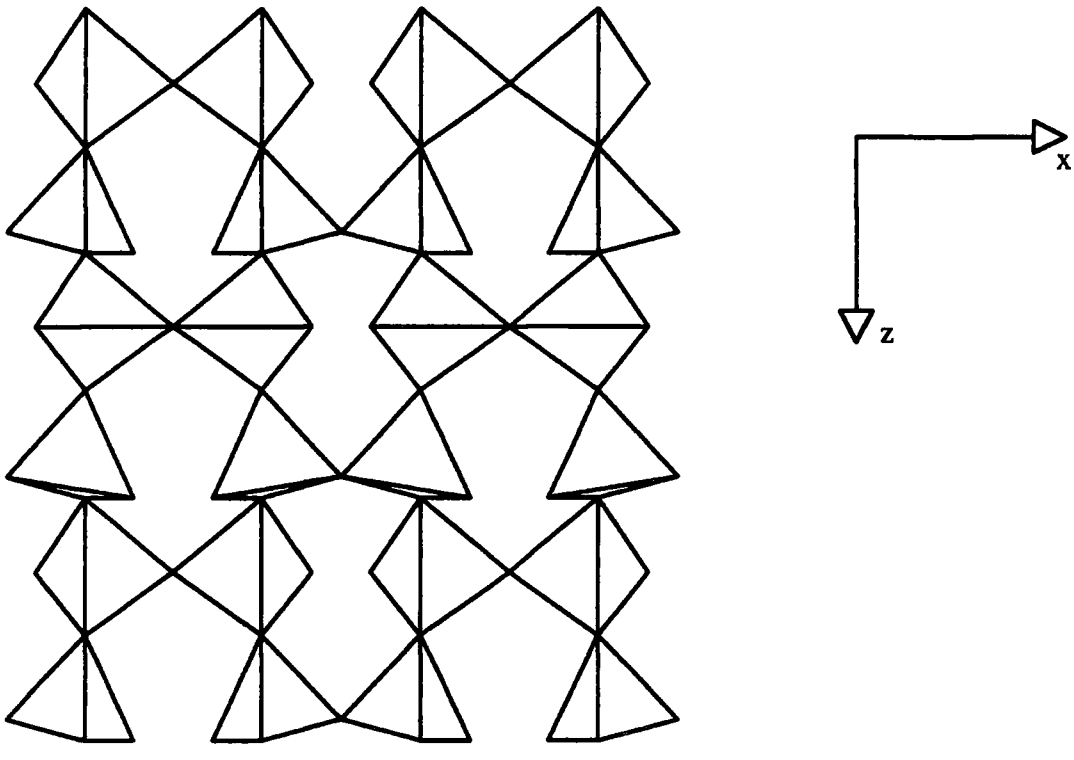

Figure 3.5 A schematic diagram of one makatite $[Si_2O_4(OH)]_n^{n-}$ layer. Using the notation of Annehed *et al.* this is a projection parallel to [010].[8] Tetrahedra represent SiO_4.

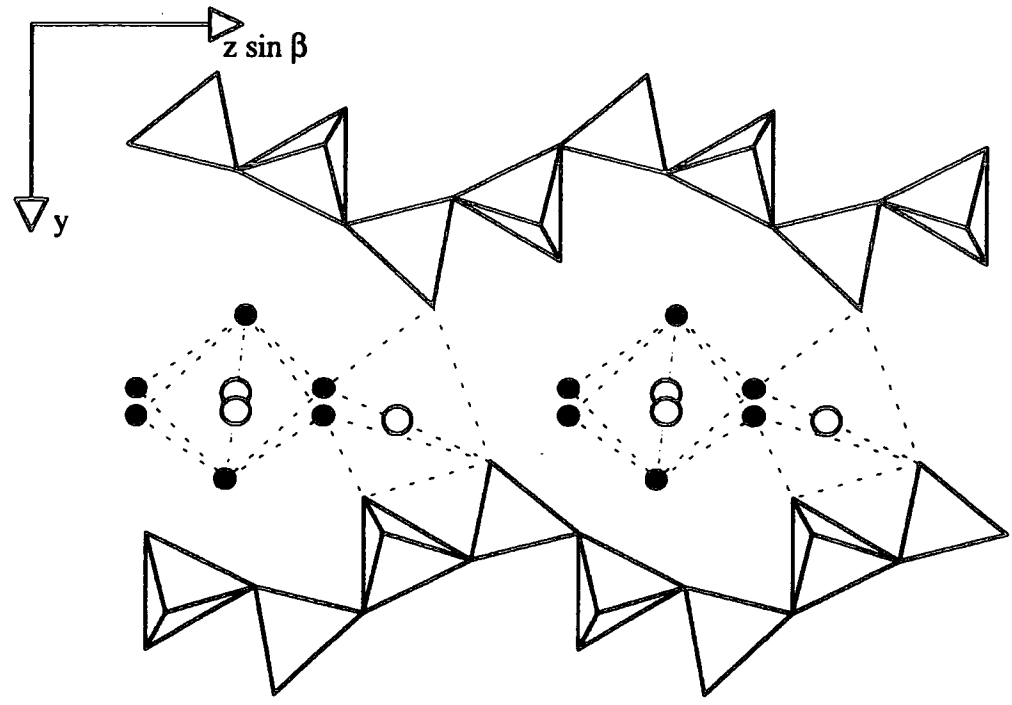

Figure 3.6 A schematic diagram of the makatite structure showing SiO_4 tetrahedra, water oxygen atoms (small filled circles) and sodium ions (large unfilled circles). According to the notation of Annehed *et al.*, this is a projection along the a crystallographical axis.[8]

Kanemite shares the same silicic acid as $KHSi_2O_5$. The structure of this silicate has been reported by Le Bihan *et al.*[34] As with makatite, the structure consists of single silicate layers containing six-membered rings of corner-sharing SiO_4 tetrahedra (figure 3.7).

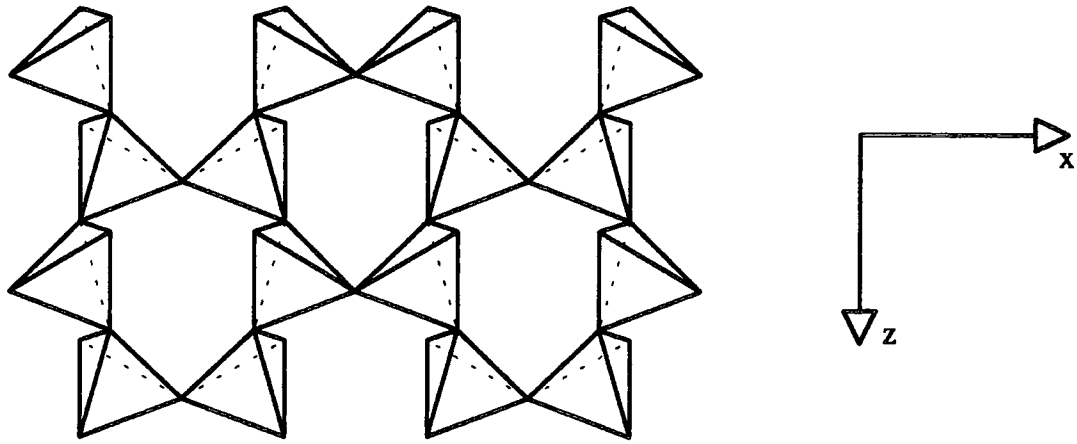

Figure 3.7 A schematic diagram of the silicate layer in $KHSi_2O_5$.[35]

The structural differences between makatite and $KHSi_2O_5$ can be emphasised by considering simplified versions of the projections in figure 3.6. In figure 3.8, SiO_4 tetrahedra are represented as triangles. This is a closer approximation for makatite than in $KHSi_2O_5$, where there is considerably more puckering of the SiO_4 tetrahedra. This extra puckering is responsible for the ^{29}Si chemical shift of $KHSi_2O_5$ (*ca.* -90 ppm) being less negative than that of makatite.[36]

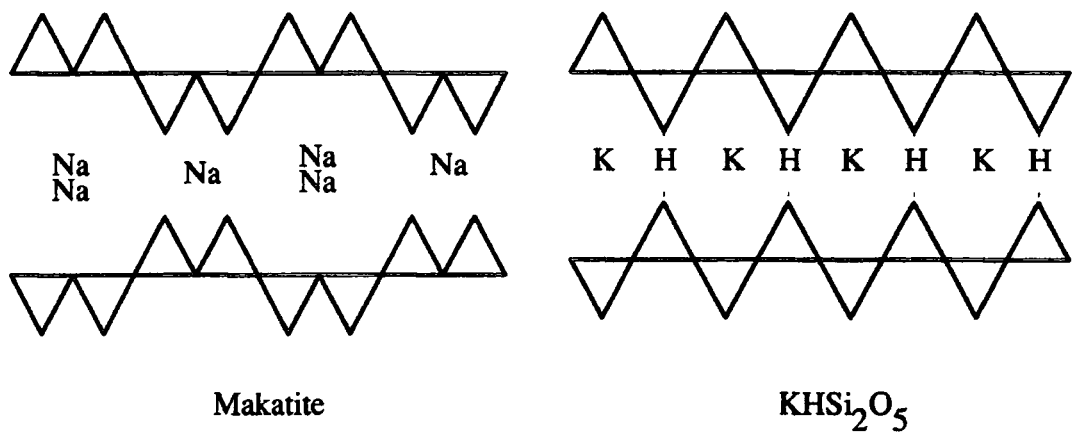

Figure 3.8 Schematic projections of the structures of makatite and $KHSi_2O_5$.

Other than the presence of a different alkali metal ion, there are two important structural differences between makatite and $KHSi_2O_5$. The periodicities of these projections are different: the makatite layer is a combination of *vierer* chains while the $KHSi_2O_5$ layer is a combination of *zweier* chains.[37] More importantly, the layers in $KHSi_2O_5$ only are connected by hydrogen bonds. Deng *et al.* have shown that the H-bonded protons give a high-frequency ^1H MAS NMR signal,[36] which is not present in the spectrum of makatite.

Makatite and $KHSi_2O_5$ are single-sheet silicates which only contain Q^3 silicon atoms. Octosilicate, magadiite and kenyaite contain Q^4 silicon atoms and are likely to have structures with multiple sheets. An interesting example of such a silicate is piperazine silicate (EU19).[38] Though only very small crystals were available, structural determination was possible using synchrotron radiation.[39] EU19 consists of

double silicate layers, held together by hydrogen bonds with piperazinium cations. The double silicate layer contains silicate sheets of eight-membered rings of SiO_4 tetrahedra (figure 3.9a). The linking between these sheets constitutes five-membered rings (figure 3.9b).

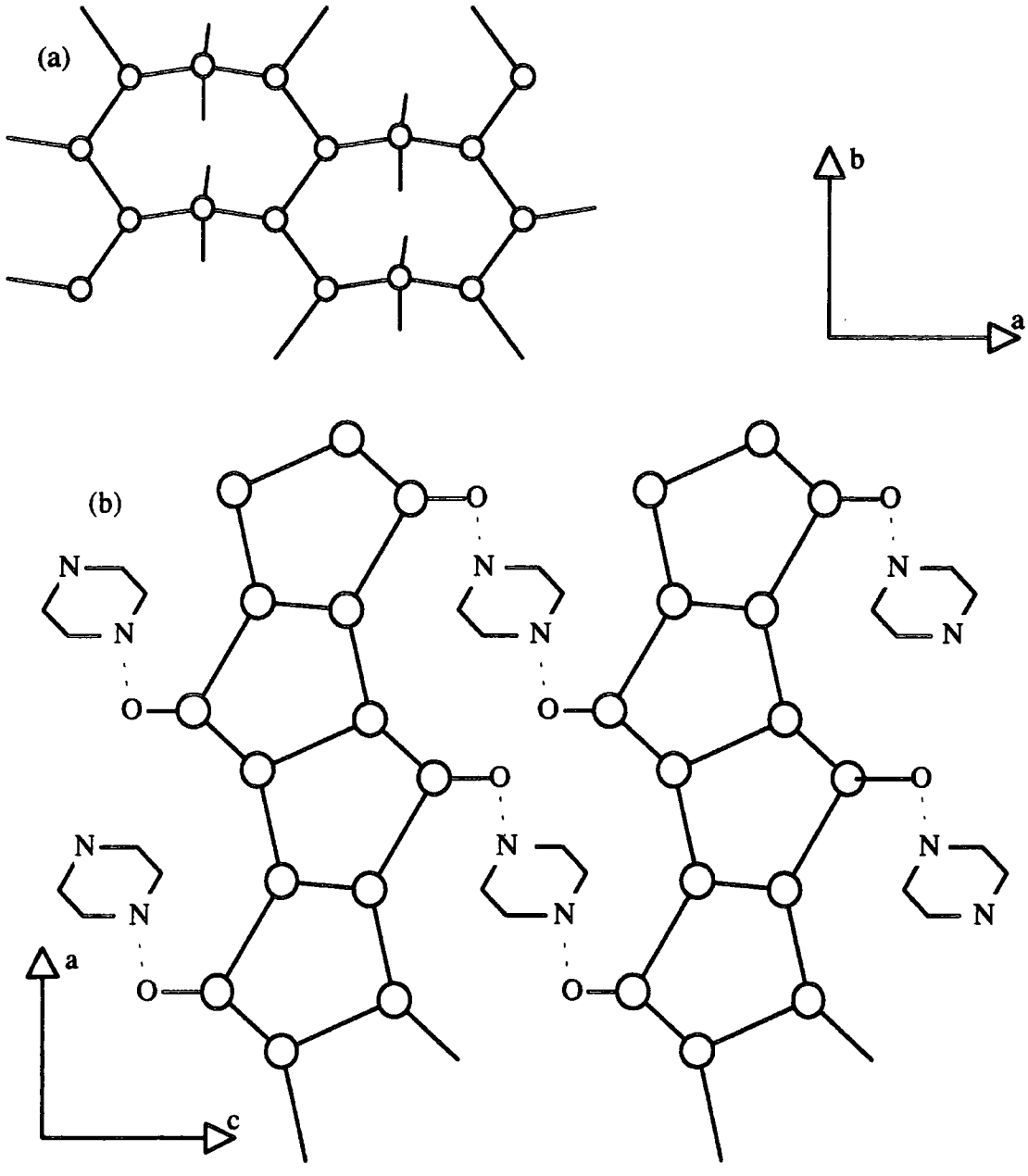

Figure 3.9 The structure of EU19;[39] a) a component of the double silicate layer in projection along c; and B) a b-axis view, showing double silicate layers held together by H-bonding interactions with piperazinium cations. In each diagram, circles represent silicon atoms; these are separated by oxygen atoms (not shown).

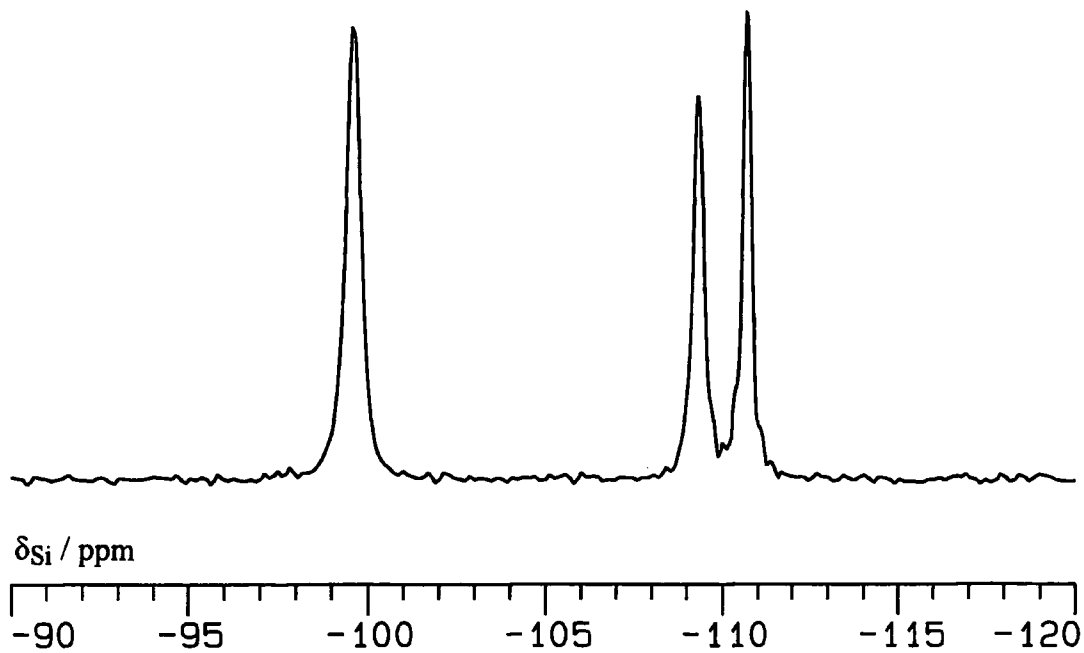

Figure 3.10 A ^{29}Si CP spectrum of EU19. The conditions used were: recycle time = 10 s, 256 transients, spinning rate = 1.97 kHz; and contact time = 5 ms. The sample was kindly prepared by Dr. Kevin Franklin and I.A. Crone at Unilever Research Port Sunlight Laboratory.

Figure 3.10 shows a ^{29}Si cross-polarisation spectrum of EU19. This contains three signals which correspond to the three silicon atoms in the asymmetric unit of the compound. A Q^3:Q^4 ratio of 1:2 would be expected from a quantitative ^{29}Si NMR spectrum.

The silica polymorph, tridymite has a ^{29}Si NMR spectrum with signals at δ_{Si} -109, -111 and -114.0.[7] These are very similar Q^4 chemical shifts to those of magadiite. Therefore, the structure of magadiite might be similar to that of tridymite. Tridymite has a regular 3-dimensional structure (figure 3.11);[40] variations in bond angles and bond length must be responsible for the ^{29}Si chemical shift range in the spectrum of Smith and Blackwell.[7]

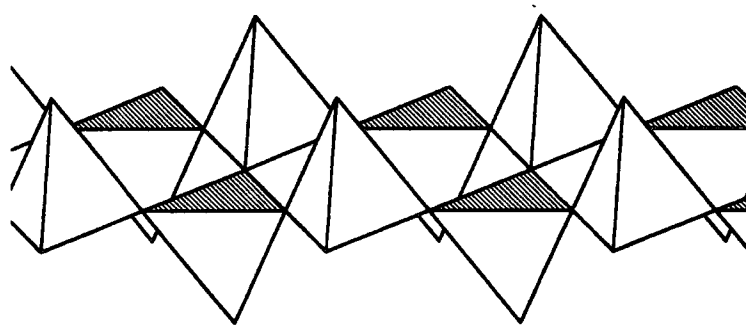

Figure 3.11 Part of a silicate sheet from the 3-dimensional structure of tridymite.

3.3.2 Previously-Proposed Structures

Several authors have proposed hypothetical silicate layers for octosilicate, magadiite and kenyaite. Pinnavaia *et al.*[12] and Rojo *et al.*[13] proposed simple models for H-magadiite. These were based solely on values of the Q^3:Q^4 ratio, measured from ^{29}Si SP spectra. The models were both double-sheet layers and are shown in figure 3.12. The model of Pinnavaia *et al.* is more likely to be accurate because it is based on the correct value of the site ratio (that measured with an adequate recycle time by Dailey and Pinnavaia[28,29]).

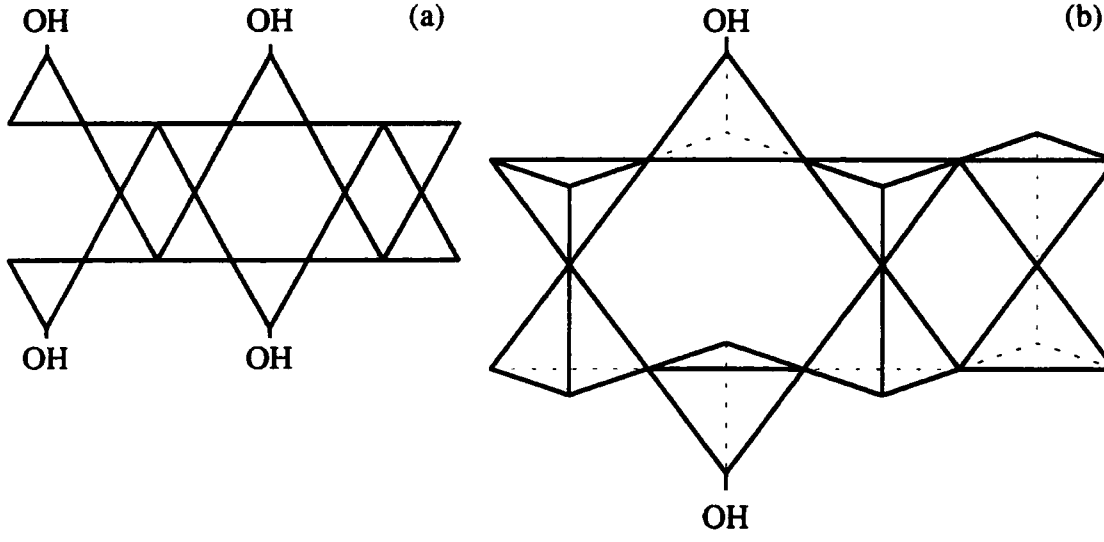

Figure 3.12 Hypothetical H-magadiite structures: (a) Rojo *et al.*,[13] Q^4:Q^3 = 2; and (b) Pinnavaia *et al.*,[12] Q^4:Q^3 = 3. In both cases, the schematic diagrams represent a layer of H-magadiite along a direction normal to the layer plane.

Schwieger *et al.*[6] and Nesbitt[14] showed that hypothetical layer structures for octosilicate, magadiite and kenyaite could be formed by condensation of sheets of makatite. Figure 3.13 shows the way Schwieger *et al.* represented models for octosilicate, magadiite and kenyaite, with Q^4:Q^3 ratios of 1, 2 and 4, respectively. Nesbitt showed that there were two ways of joining two makatite sheets together: these were denoted A- and B-lamination (Figure 3.14).

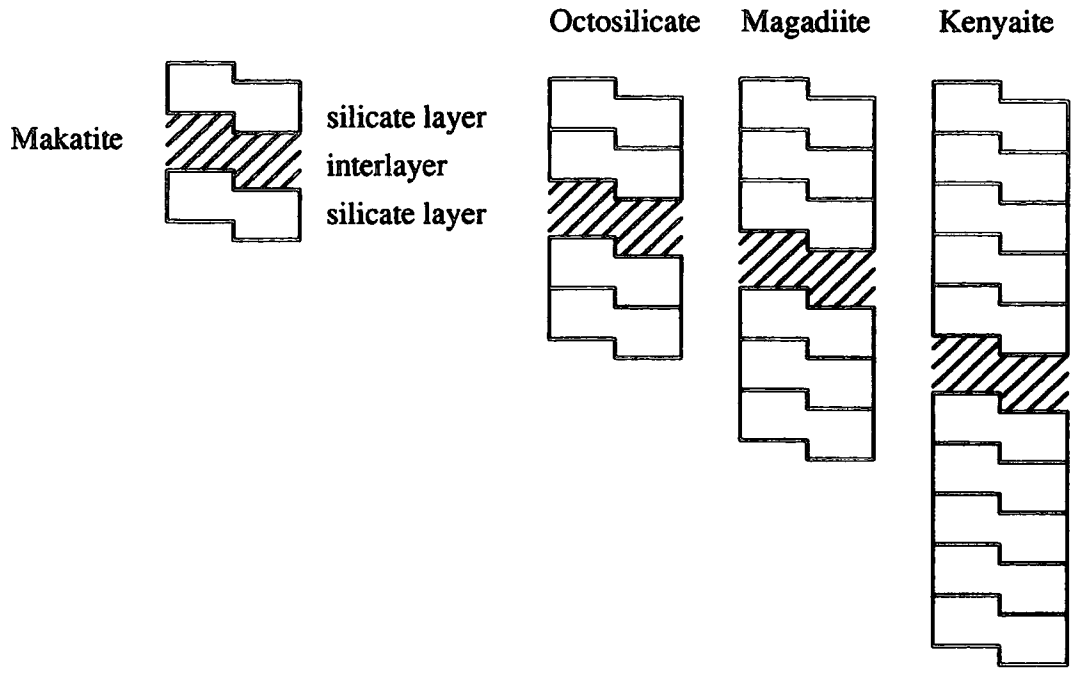

Figure 3.13 The hypothetical structures of Schwieger *et al.*,[6] based on the condensation of makatite sheets.

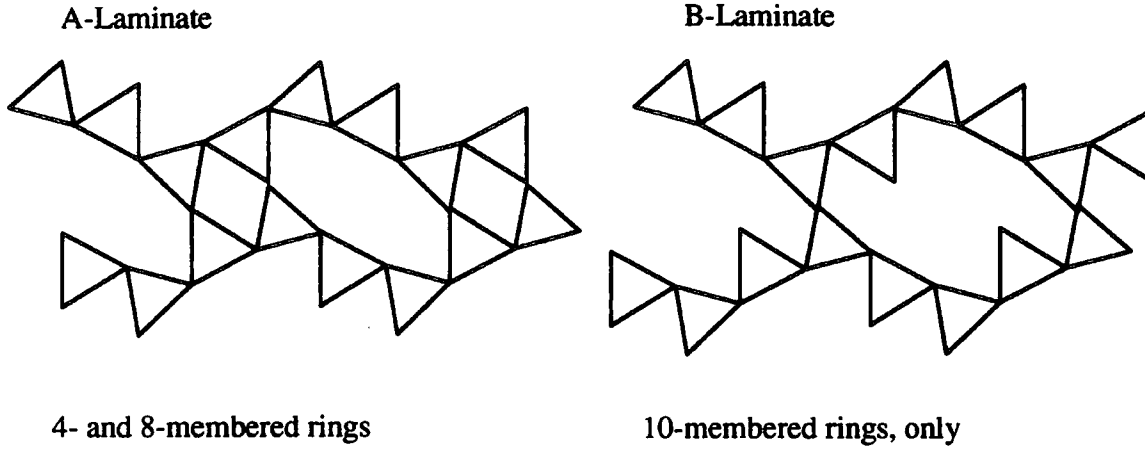

Figure 3.14 Two methods of forming more condensed layers from sheets of makatite.[14]

Nesbitt obtained Q^4:Q^3 ratios of 1.0, 1.5 and 2.7 for octosilicate, magadiite and kenyaite, respectively. Plausible hypothetical layers were proposed on the basis of these values: octosilicate, 1 A-laminate; magadiite, 2A and 1B; and kenyaite, 3A and 1B or 4A and 1B. The magadiite and kenyaite structures have Q^3 sites within the

layer. This fitted the conclusion that there were intra- and interlayer sodium sites. Figure 3.15 depicts molecular models of several layers formed from condensed makatite sheets.

Overleaf

Figure 3.15 Molecular models of several hypothetical silicate layers. The models were formed by manipulating and joining makatite silicate sheets[8] using Biosymm Catalysis Software. Silicon atoms are shown in yellow, oxygen atoms in red and protons in white. All terminal oxygen atoms have been capped by protons.

a) Two makatite sheets, one A-laminate: $Q^4:Q^3 = 1$; Nesbitt[14] and Schwieger *et al.*[6] models for octosilicate.

b) Three makatite sheets, two A-laminates: $Q^4:Q^3 = 2$; Schwieger *et al.* model for magadiite.

c) Four makatite sheets, three A-laminates: $Q^4:Q^3 = 3$; Correct site ratio for magadiite.[28]

d) Four makatite sheets, two A-laminates and one B-laminate: $Q^4:Q^3 = 5/3$; Nesbitt model for magadiite.

e) Six makatite sheets, four A-laminates and one B-Laminate: $Q^4:Q^3 = 3$; correct site ratio for magadiite.

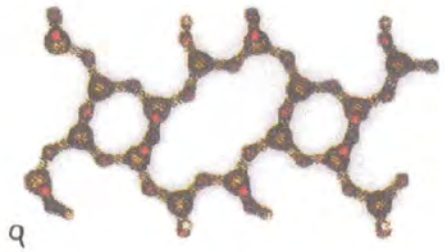

a

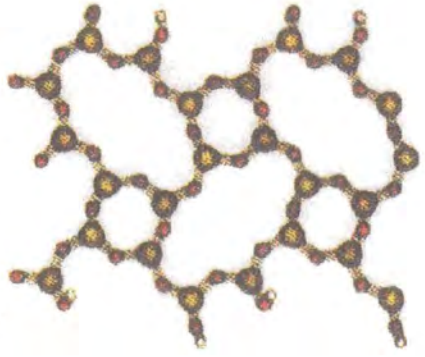

b

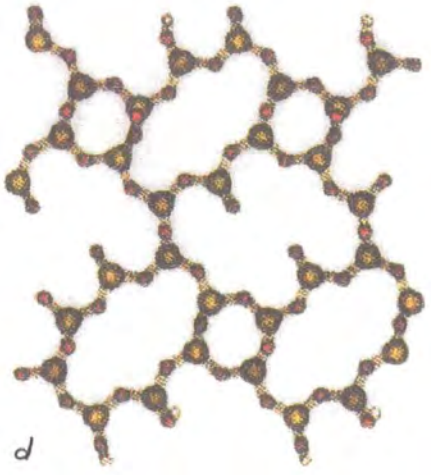

d

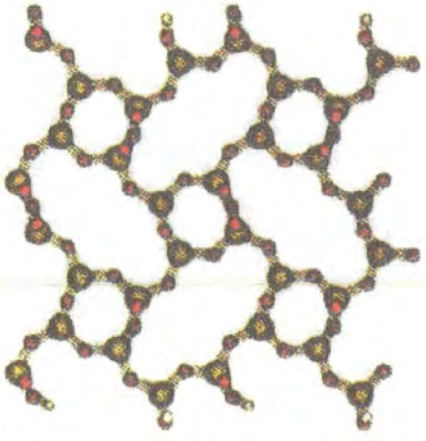

c

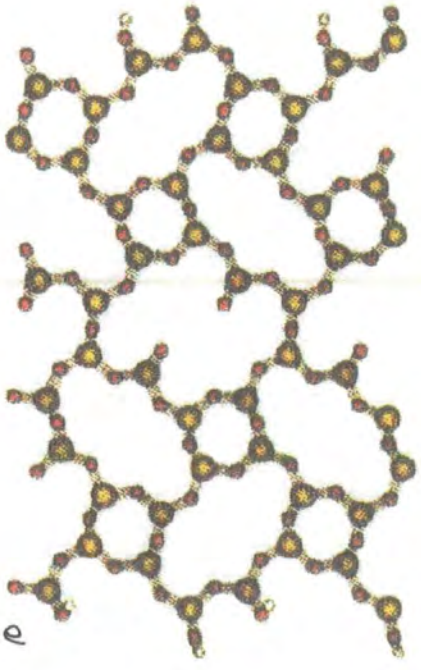

e

In a series of papers, Brandt and co-workers showed that the model structures of Schwieger *et al.* were consistent with known X-ray diffraction and NMR measurements[9,10] as well as explaining the thermal behaviour of magadiite.[11] This work included a new proposal for a kenyaite layer structure (figure 3.16). This was smaller in the b-direction than a condensed makatite structure, yet it still corresponded to a Q^4:Q^3 ratio of 4.

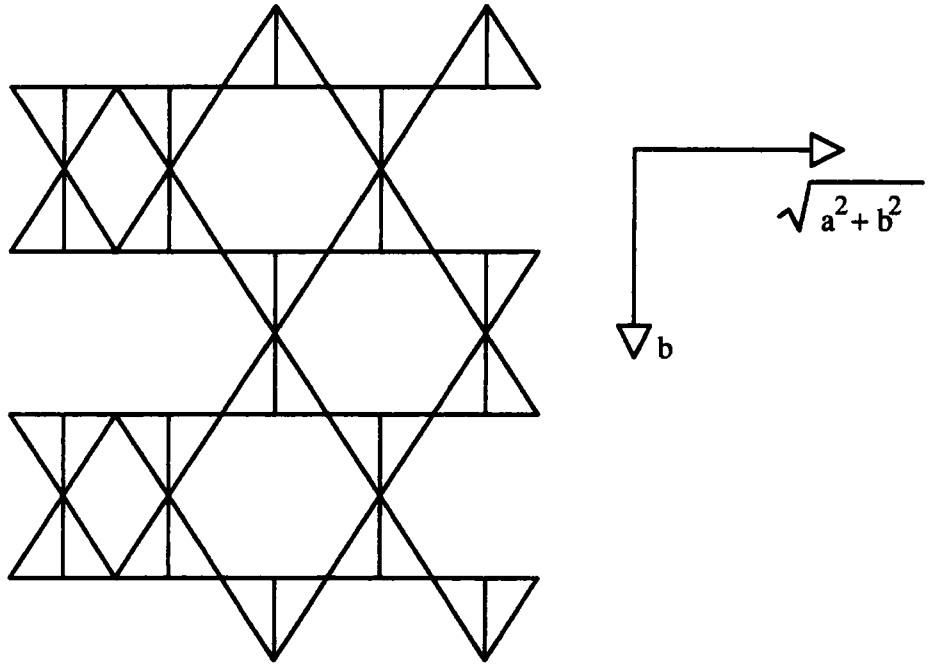

Figure 3.16 The hypothetical structure of Brandt and co-workers for kenyaite.[9,10]

3.4 Potential Uses for the Layered Sodium Polysilicate Hydrates

The layered sodium polysilicate hydrates are porous, absorbent materials with considerable inner-crystalline reactivity. Therefore, they have several potential uses where such properties are desirable. Their ion-exchange capacity means that many modified silicates can be designed. Sodium ions can be replaced with metals, including those with catalytic properties, such as nickel. Such exchange reactions can also be performed with large quaternary ammonium compounds, forming phases with increased layer separations. The layered nature is retained after such reactions and further modifications can be attempted to form pillared materials, where the silicate layers are separated by stable silicate or polymeric pillars. Many applications have been patented, particularly for magadiite. These have tended to be for potential use as catalysts or in the rubber and detergent industries.

Schwieger *et al.*[41] used nickel treated Na-, H-, NH_4- and Ca-magadiite samples as dehydrogenation catalysts. In favourable cases, 90 minutes of stable catalytic activity were observed with cyclohexane and n-hexane. Catalysts with several active sites can be prepared by inserting a polymeric oxide between silicate layers and incorporating metals. In a patented example,[42] magadiite or kenyaite, impregnated with tetraethyl orthosilicate can be swelled by cetylethyldimethyl ammonium bromide and an aromatisation catalyst can be formed with gallium, zinc, group VIIIa or group VIa metals. Magadiite is also named in a patent for the cracking of hydrocarbons.[43] In this case, the catalyst was prepared with polymeric silica between the layers. Wong and Cheng prepared a pillared magadiite sample by intercalation of a Keggin ion between the silicate layers.[30] The potential catalytic activity of this sample was tested in a propan-2-ol dehydration reaction.

There are many patented applications for the use of layered sodium polysilicate hydrates in the rubber industry. In general, magadiite is used as a support for agents which can improve certain properties: magadiite-supported amines accelerate vulcanisation and produce a more stable product;[44] colouring agents can be prepared

by supporting pigments;[45] when flame retardants are adsorbed on magadiite, flame-proofing is improved because retardant desorption decreases;[46] supported silicone oil, a moulding additive, is more easily incorporated into solid rubber or latex;[47] and excellent rubber crumbs can be prepared with the addition of magadiite (7 %).[48]

The layered sodium polysilicate hydrates have potential uses in the detergent industry. As with zeolites, they can be used in formulations with low concentrations of phosphates. Bergk *et al.* reported that magadiite could replace a quarter of the sodium tripolyphosphate in laundry formulations.[49] Several other potential applications for magadiite have been patented: a detergent raw material;[50] a high-whiteness detergent ingredient;[51] a hand cleaner ingredient;[52] a fluorescent brightener;[53] and a phenol removal adsorbent.[54]

References

1 F. Liebau, *Structural Chemistry of Silicates*, Springer-Verlag, Berlin, 1985, p.53.

2 G. Engelhardt and D. Michel, *High-Resolution Solid-State NMR of Silicates and Zeolites*, J. Wiley and Sons, Chichester, 1987.

3 K.A. Smith, R.J. Kirkpatrick, E. Oldfield and D.M. Henderson, *Am. Mineral.*, 1983, **68**, 1206-1215.

4 J.M. Thomas, J. Klinowski, S. Ramdas, M.W. Anderson, C.A. Fyfe and G.C. Gobi, in G.D. Stucky and F.G. Dwyer, Eds., *Intrazeolite Chemistry*, American Chemical Society, Washington DC, 1983, p. 159-180.

5 M. Mägi, A. Lippmaa, A. Samoson, G. Engelhardt and A. Grimmer, *J. Phys. Chem.*, 1984, **88**, 1518-1522.

6 W. Schwieger, D. Heidemann and K.-H. Bergk, *Rev. Chim. Minérale*, 1985, **22**, 639-650.

7 J.V. Smith and C.S. Blackwell, *Nature*, 1983, **303**, 223-225.

8 H. Annehed, L. Fälth and F.J. Lincoln, *Zeitschrift für Kristallographie*, 1982, **159**, 203-210.

9 A. Brandt, W. Schwieger and K.-H. Bergk, *Cryst. Res. Technol.*, 1988, **23**, 1201-1203.

10 A. Brandt, W. Schwieger and K.-H. Bergk, *Rev. Chim. Minérale*, 1987, **24**, 564-571.

11 A. Brandt, W. Schwieger, K.-H. Bergk, P. Grabner and M. Porsch, *Cryst. Res. Technol.*, 1989, **24**, 47-54.

12 T.J. Pinnavaia, I.D. Johnson and M. Lipsicas, *J. Solid State Chem.*, 1986, **63**, 118-121.

13 J.M. Rojo, J. Sanz, E. Ruiz-Hitzky and J.M. Serratosa, *Z. anorg. allg. Chem.*, 1986, **540/541**, 227-233.

14 G.J. Nesbitt, Ph.D. Thesis, University Of Durham, !986.

15 R.K. Harris and G.J. Nesbitt, *J. Magn. Reson.*, 1988. **78**, 245.

16 J.M. Garces, C.R. Rocke, C.E. Crowder and D.L Hasha, *Clays and Clay Minerals*, 1988, **36**, 409-418.

17 T. Yanagisawa, K.Kuroda and C. Kato, *Reactivity of Solids*, 1988, **5**, 167-175.

18 T. Yanagisawa, K.Kuroda and C. Kato, *Bull. Chem. Soc. Japan*, 1988, **61**, 3743-3745.

19 T. Yanagisawa, M. Harayama, K.Kuroda and C. Kato, *Solid State Ionics*, 1990, **42**, 15-19.

20 T. Yanagisawa, K. Schimizu, K.Kuroda and C. Kato, *Bull. Chem. Soc. Japan*, 1990, **63**, 988-992.

21 J.M. Rojo, E. Ruiz-Hitzky and J. Sanz, *Inorg. Chem.*, 1988, **27**, 2785-2790.

22 J.M. Rojo, E. Ruiz-Hitzky, J. Sanz and J.M. Serratosa, *Rev. Chim. Minérale*, 1983, **20**, 207.

23 R. Sprung and M.E. Davies, *Ind. Eng. Chem. Res.*, 1990, **29**, 213-220.

24 W. Schwieger, K.-H. Bergk, D. Heidemann, G. Lagaly and K. Beneke, *Zeitschrift für Kristallographie*, 1991, **197**, 1-12.

25 E. Lippmaa, A. Samoson, G. Engelhardt and A.-R. Grimmer, *J. Am. Chem. Soc.*, 1980, **102**, 4889-4893.

26 G. Scholzen, K. Beneke and G. Lagaly, *Z. anorg. allg. Chem.*, 1991, **597**, 183-196.

27 G. Borbély, H.K. Beyer and H.G. Karge, *Clays and Clay Minerals*, 1991, **39**, 490-497.

28 J.S. Dailey and T.J. Pinnavaia, *Journal of Inclusion Phenomena and Molecular Recognition in Chemistry*, 1992, **13**, 47-61.

29 J.S. Dailey and T.J. Pinnavaia, *Chem. Mater.*, 1992, **4**, 855-863.

30 S.T. Wong and S. Cheng , *Chem. Mater.*, 1993, **5**, 770-777.

31 D.S.B. Hauck, Diplomarbeit, Heinrich-Heine Universität, Düsseldorf, 1993.

32 D. Heidemann, Poster, Eleventh International Meeting on NMR Spectroscopy, 1993.

33 J.F. Charnell, *J. Cryst. Growth*, 1971, **8**, 291-294.

34 M.T. Le Bihan, A. Kalt and R. Wey, *Bull. Soc. Fr. Minéral. Cristallogr.*, 1971, **94**, 15.

35 A. Kalt, B. Perati and R. Wey in M.M. Mortland and V.Farmer (Eds.), *International Clay Conference*, 1977, Elsevier, Amsterdam, 1979, 509-516.

36 Z.Q. Deng, J.F. Lambert and J.J. Fripiat, *Chemistry of Materials*, 1989, **1**, 375-380.

37 F. Liebau, *Structural Chemistry of Silicates*, Springer-Verlag, Berlin, 1985, p. 55.

38 A.J. Blake, K.R. Franklin and B.M. Lowe, *J. Chem. Soc. Dalton Trans.*, 1988, 2513-2517.

39 S.J. Andrews, M.Z. Papiz, R. McMeeking, A.J. Blake, K.R. Franklin, B.M. Lowe, J.R. Helliwell and M.M. Harding, *Acta. Cryst.*, 1988, **B44**, 73-77.

40 F. Liebau, *Structural Chemistry of Silicates*, Springer-Verlag, Berlin, 1985, p. 127.

41 W. Schwieger, K.-H. Bergk, Wendtlandt and Reschetilowski, *Z. Chem.*, 1985, **25**, 228-230.

42 P. Chu, M.E. Landis, G.W. Kirker, *Catalytically active layered oxides containing interlayer polymeric oxides and their synthesis*, **Patent Can. CA 1,251,432**, 1989.[CA111(4)29059]

43 P. Chu, T.F. Degnan Jr., I.D. Johnson and C.T. Kresge, *Aromatisation process utilizing a pillared layer silicate plus a base metal or noble metal*, **Patent Eur. Pat. Appl. EP 434,462**, 1991. [CA115(13)135664]

44 K. Giessmann, R. Sourisseau, G. Merkmann, H. Knoll, S. Borgmann, P. Knop, W. Hoese and U. Harms, *Adducts of amines with layered silicates as vulcanisation accelerators*, **Patent Ger. (East) DD 251,764**, 1987. [CA109(16130637]

45 K. Giessmann, R. Sourisseau, W. Mueller, G. Merkmann, H. Knoll, S. Borgmann, P. Knop, W. Hoese and K. Kaesebier, *Coloring agent-layered*

silicate adducts for use in rubbers, **Patent Ger. (East) DD 251,769**, 1987. [CA109(16)130620]

46 K. Giessmann, R. Sourisseau, G. Merkmann, G. Grosskreuz, J. Hopfe, H. Knoll, S. Borgmann, P. Knop, W. Hoese *et al.*, *Layered silicates as carriers for fireproofing agents for rubbers*, **Patent Ger. (East) DD 251.768**, 1987. [CA109(16)130618]

47 K. Giessmann, R. Sourisseau, M. Foertsch, W. Hoese, H. Knoll and S. Borgmann, *Additives for moulding of solid rubbers or rubber latexes*, **Patent Ger. (East) DD 251,766**, 1987. [CA109(16)130617]

48 H. Knoll, U. Harms, S. Borgmann, P. Knop, W. Hoese, G. Merkmann, K. Giessmann, K. Kaesebier and H. Hoelzel, *Preparation of storage-stable free-flowing rubber crumbs*, **Patent Ger. (East) DD 266,577**, 1989. [CA111(24)215828]

49 K.-H. Bergk, D. Kauffman, M. Porsch and W. Schwieger, *Seifen, Oele, Fette, Wachse*, 1987, **113**, 555-561.

50 K.H. Bergk, M. Porsch, W. Schwieger, D. Kaufmann and P. Renger, *Preparation of raw material mixtures for detergents*, **Patent Ger. (East) DD 234,878**, 1986. [CA105(20)174849]

51 K.H. Bergk, M. Porsch, W. Schwieger, D. Kaufmann, P. Renger, F. Janowski, K.H. Neumann and R. Almeroth, *Preparation of water-insoluble alkali metal layered silicates with high whiteness*, **Patent n**, d. [CA105(16)136442]

52 P. Knop, K. Kaesebier, G. Nemitz, S. Borgmann, W. Roscher, H. Schurig, H.G. Bromann, W. Hoese and H. Fuertig, *Skin-compatible paste for cleaning of heavily soiled hands*, **Patent Ger. (East) DD 265,160**, 1989. [CA111(18)156523]

53 K.H. Bergk, W. Heyer, W. Schwieger, F. Wolf, D. Kaufmann, D. Muth, H. Fuertig, W. Hoese, P. Knop *et al.*, *Washing and cleaning agent for solid surfaces*, **Patent Ger. (East) DD 161,180**, 1985. [CA104(2)7519]

54 S. Lindau, F. Wolf and F. Frahm, *Absorbent for removal of phenols*, **Patent Ger. (East) DD 219,678**, 1985. [CA103(16)128580]

Chapter Four Experimental

4.1 NMR Spectrometers

Three different spectrometers have been used for this work. During the first two years most research was done using a Bruker CXP200. This was replaced by a Chemagnetics CMX200 for the final year. Throughout the work, occasional spectra were acquired with a Varian VXR300. This was replaced in July 1994 with a Varian Unity Plus 300, which was used to acquire a few spectra.

The CXP200 and CMX200 spectrometers used the same Oxford Instruments wide-bore (89.5 mm) superconducting magnet with a magnetic field strength of 4.7 T. This gives resonance frequencies of 200.13, 52.938, 50.323 and 39.760 MHz for ^{1}H, ^{23}Na, ^{13}C and ^{29}Si respectively. The magnet was refurbished before the installation of the CMX200 with no change in magnetic field or resonance frequencies.

The CXP200 was a dual-channel spectrometer, capable of simultaneous irradiation at a high frequency (corresponding to protons) and a low frequency (corresponding to ^{29}Si, say). The radiofrequency pulses were controlled by separate frequency synthesisers and a 16-step pulse programmer. The Aspect 3000 software had been upgraded to virtually the equivalent of a Bruker MSL spectrometer. Acquisition, file-storage and retrieval, automation and plotting were enabled *via* a BBC microcomputer interface.

The CMX200 is a three-channel spectrometer; these are nominally equivalent and capable of irradiation over all possible resonance frequencies. Digital pulse generation and phasing make many sophisticated experiments possible. Two software packages, CMXW and Spinsight, were used for acquisition, file-storage and retrieval, automation and plotting, and the system was controlled by a Sun work-station interface. Transmitter power levels could be set manually by dials on the spectrometer, through the keyboard or from within a pulse programme. Efficient operation was possible with the implementation of macros– for setting tuning

conditions, running variable parameter experiments or contiguous plotting, for example.

Two commercial Doty probes were used for all the work on the CXP200 spectrometer. These were broad-band, dual-channel, double-bearing probes covering, between them, the tuning range 20 to 90 MHz. Though each probe only covered half this range, ^{15}N to ^{13}C and ^{13}C to ^{31}P, both could be successfully tuned to silicon and ^{1}H spectra could be obtained through the decoupling channels. It was generally the higher frequency probe that was used for ^{29}Si. The zirconia rotors were cylindrical with a 7 mm outside diameter and capable of holding *ca.* 0.25 g of a layered sodium polysilicate hydrate sample. Kel-F caps were used and inserts of the same material were available for running liquids or air-sensitive materials. Stable spinning rates between 100 Hz and 5 kHz were achievable.

Several probes are available for use with the CMX200 spectrometer including the two Doty probes mentioned above. A Chemagnetics "HX" dual-channel double-bearing probe was used for acquisition over the whole frequency range. Tuning to a particular nucleus merely required the insertion of particular capacitors. The zirconia Pencil rotors are larger than those for the CXP200 with a 7.5 mm outside diameter and a capacity of *ca.* 0.4 g of a layered sodium polysilicate hydrate. Samples were packed between a PTFE end-cap and spacer; the bottom of the rotor was grooved to enable spinning and made of Kel-F. Spinning rates of up to 6 kHz were possible and an automatic speed controller was available to keep these constant to within ±1 Hz. A Chemagnetics "HF" probe was used for fast spinning experiments. The small 4 mm zirconia rotors could be used with PTFE or polymethylmethacrylate spacers and end-caps. Spinning-rates of up to 18 kHz were possible.

4.2 The Optimisation Procedure

Before the acquisition of spectra, several tuning procedures have to be undertaken to optimise the performance of the spectrometer: setting the magic-angle; shimming; getting a 90° pulse of the correct duration; Hartmann-Hahn matching; and referencing the chemical shift. Many methods have been used in the course of this work.

Shimming involves the fine adjustment of coils within the magnet to ensure a homogenous magnetic field. Setting shims from scratch can be a lengthy process for which there are well-established procedures;[1] this is normally only necessary when introducing new probes into a spectrometer system. Some small amount of adjustment to the existing shim values was sometimes necessary before acquiring spectra. This was achieved by optimising the single line observed in the ^{1}H spectrum of silica gum, in terms of line-width and shape (for the CXP200) or by maximising the FID observed from adamantane or PDMSO (for the CMX200).

The orientation of a rotor relative to the magnetic field was set to the magic-angle using one of two methods: maximising the rotational echoes in the ^{79}Br FID of KBr or optimising the shape of the NO_3 resonance in the ^{15}N spectrum of an NH_4NO_3 sample (20 % enriched in ^{15}N). Since small deviations from the magic angle would have little effect on the spectra acquired for this work, it was not necessary to set the magic-angle prior to each spectrometer session.

With a simple single pulse sequence, optimum signal intensity is observed when the pulse induces a 90° nutation of the sample's bulk magnetisation. Therefore, approximate calibration of the pulse duration is necessary to ensure reasonable signal to noise. This can be achieved through obtaining a null signal corresponding to a 180° pulse, by varying the intensity or duration of the pulse. More complex pulse sequences (*e.g.* CRAMPS) depend more heavily on the precision of the pulse-duration calibrations, and special pulse sequences exist to do this. If a ^{1}H 90° pulse is correctly

set, then achieving a Hartmann-Hahn match effectively calibrates the 90° pulse duration of the dilute-spin nucleus.

Hartmann-Hahn matching is necessary for successful cross-polarisation. This involves equalisation of the gap between the rare and abundant spin energy levels so that $\gamma_I B_{1I} = \gamma_S B_{1S}$ (see section 2.7). The power of the proton transmitter is generally the limiting factor in tuning for this experiment as it is on for the longer fraction of the pulse sequence. Therefore, a maximum ^1H power is generally fixed and the power of the dilute-spin transmitter varied until optimum signal intensity is observed. For such a procedure to be feasible, a suitable sample is necessary. Adamantane is an excellent compound for obtaining the Hartmann-Hahn match for ^{13}C CP. Several samples have been used throughout his work for ^{29}Si CP: Gasil 200; H-kanemite, tetra(*tert*-butyl)silane and tetrakis(trimethylsilyl)silane. Of these, the last-mentioned is certainly the best. For ^{23}Na CP no suitable sample has been obtained and octosilicate has been used to find an approximate match ($NaBH_4$ has been recommended in the literature).[2]

Several secondary references have been used to set chemical shifts to widely accepted values (See table 4.1). For this work, the chemical shifts of silica gum, tetrakis(trimethylsilyl)silane, polydimethylsiloxane and adamantane have been measured relative to the widely accepted reference of tetramethylsilane ($\delta_{Si} = \delta_H = \delta_C = 0$ ppm). The use of a sodium chloride solution at a finite (but consistent) concentration might give reported ^{23}Na chemical shift values that differ from those measured relative to the more widely-accepted standard. It was judged that any trouble taken for better referencing would have been out of proportion to the usefulness of exact δ_{Na} measurement in the solid-state.

A typical CXP200 spectrometer session involved tuning the proton channel with silica gum– checking the shimming and adjusting the intensity for a 4 μs 90° pulse; obtaining a Hartmann-Hahn match for ^{13}C CP with adamantane; and then tuning to silicon, referencing with silica gum and obtaining a Hartmann-Hahn match with H-kanemite. With the CMX200 spectrometer, most of the tuning could be achieved by obtaining a ^{13}C CP Hartmann-Hahn match for adamantane: the state of

the shimming and the magic-angle would be apparent from the width and shape of the lines, and the proton 90° pulse duration could be obtained by looking for zero signal from a 180° pulse. The spectrometer was then tuned for ^{29}Si, ^{23}Na, or ^{1}H with tetrakis(trimethylsilyl)silane, NaCl solution (1 mol dm^{-3}) or PDMSO, respectively.

Nucleus	Secondary References	Chemical Shift, δ / ppm	Primary Reference, $\delta = 0$ ppm
^{29}Si	Silica Gum tetrakis(trimethylsilyl)silane	-22.74 -9.5	Tetramethyl Silane (TMS)
^{1}H	Silica Gum Polydimethylsiloxane	0.06 0.08	Tetramethyl Silane (TMS)
^{23}Na	Aqueous NaCl (1 mol dm^{-3})	0	Aqueous NaCl (0 mol dm^{-3})
^{13}C	Adamantane	28.4(CH)	Tetramethyl Silane (TMS)

Table 4.1 Compounds for chemical shift referencing.

4.3 Acquiring Spectra

The possible nuclei for study in this work were clearly restricted to those present in the layered sodium polysilicate hydrates, ^{29}Si, ^{1}H, ^{23}Na and ^{17}O. In addition, ^{13}C NMR was used to tune the spectrometer. Table 4.2 lists relevant spectroscopic data for these nuclei.[3]

Nucleus	Spin, I	Natural Abundance / %	Gyromagnetic ratio, γ / 10^7 rad T^{-1} s^{-1}	Relative Receptivity: to ^{1}H	Relative Receptivity: to ^{13}C
^{29}Si	$\frac{1}{2}$	4.70	-5.3188	3.69 x10-4	2.10
^{1}H	$\frac{1}{2}$	99.985	26.7519	1	5670
^{23}Na	$\frac{3}{2}$	100	7.08013	9.27 x 10-2	526
^{13}C	$\frac{1}{2}$	1.108	6.7283	1.76 x 10-4	1
^{17}O	$\frac{5}{2}$	0.037	-3.6279	1.08 x 10-5	0.0611

Table 4.2 Spin properties of the nuclei available for study in this work.

Because of low natural abundance and a small gyromagnetic ratio, no spectra were acquired for ^{17}O; enriched samples would have been necessary to have obtained spectra in a reasonable time.

Single-pulse and cross-polarisation experiments have been used for the acquisition of single 1-dimensional spectra. Pulse sequences for these are shown in figures 2.3 and 2.8, respectively. Standard programs were supplied with each spectrometer for the acquisition of single pulse without decoupling, decoupled single pulse and cross-polarisation spectra– DURHSPND, DURHSPDE and DURHCPMA, respectively for the CXP200 and 1pulse, 1pda and cp, respectively for the CMX200. Many additional standard experiments were available: DURHSPT1 and t1ir for inversion-recovery; DURHCPVC for variable contact time cross-polarisation; t1rho and t1rhox for measuring proton $T_{1\rho}$-values directly or by CP. The CMX200 cross-

polarisation with flip-back pulse-sequence, cpflip, was also commonly used. It should be noted that CXP200 pulse sequence names have been written in upper-case with the prefix, DURH-, while CMX200 pulse sequence names have been written in lower-case with no prefix. In this work, some CMX200 pulse sequences were specially written: for 2-dimensional $^{1}H,^{1}H$ exchange; selective-inversion; and 2-dimensional cross-polarisation correlation spectroscopy.

Some spectral parameters are listed for each spectrum in this thesis, particularly the spinning rate, recycle time, contact time and number of transients, as these were liable to vary greatly for each spectrum. Typical values of the other parameters deserve recording here. With all machines, 90° pulses were tuned to *ca.* 4 μs for all nuclei except ^{23}Na, where the quadrupolar nature of the nuclei meant that the choice of pulse-duration was more variable. This value is particularly relevant to measurements of $T_{1\rho}$, which is dependent of the spin-locking frequency (62.5 kHz, in this case). The dwell time and number of points acquired for each spectrum were chosen to provide adequate spectral widths and acquisition times.

4.4 Calculation of Relaxation Times

This work contains many experiments that give rate constants. Spin-lattice relaxation times have been obtained using the inversion-recovery pulse sequence. Variable contact time experiments allow T_{IS} and proton $T_{1\rho}$ values to be calculated. Proton spin-lattice relaxation times in the rotating frame of reference have also been determined with variable spin-locked delay experiments, either directly or indirectly (*via* CP). In general, one pulse program will be used in each experiment, while a macro or automation program acquires several FID's, each with a different value for one of the parameters. Spectra are then obtained using constant apodisation, zero-filling, fourier-transformation, baseline-correction and phasing. Peak-picking can then provide lists of signal intensity against the varied time parameter. This information can be fitted to an equation giving values of the rate constants. Table 4.3 provides a summary of the experiments and equations that have been used.

SPSS for MS Windows version 6.0 has been used for all fitting procedures at its default settings– the Levenberg-Marquardt estimation method minimising the sum of squared residuals with no constraints. This method results in values for the parameter estimates, an asymptotic standard error, asymptotic 95 % confidence limits and a correlation coefficient, r^2. For each value determined, the parameter estimate has been quoted with an error calculated from the 95 % confidence limits and not the standard error (which would be at 50 % confidence). The r^2 parameter has been used as a measure of fit between the data and the model equation. Where graphs are shown, the fitted lines have been simulated by determining signal intensities from the fitted values for at least a hundred time values spread equally over the time range, using Microsoft Excel for Windows version 4.0.

Experiment	Equation	Relaxation Time(s)
Inversion-Recovery	2.12	T_1
Variable Contact Time	7.17	$T_{1\rho}$ and T_{IS}
Variable Spin-Locked Delay	2.13	$T_{1\rho}$

Table 4.2 Experiments and equations for determining relaxation times.

4.5 Origin of Samples

Layered sodium polysilicate hydrates samples have been obtained from three sources. Five samples have been donated by Prof. R.K. Harris of Durham University (table 4.3). It is highly likely that most of these samples had been previously analysed by Nesbitt,[4] while the octosilicate sample was prepared by Smith.[5] Many samples have been prepared at Unilever Research Port Sunlight Laboratories by Ian. A. Crone or Dr. Peter Graham (table 4.3). An additional three samples were synthesised; details can be found in section 4.6. In many cases these samples have been further modified by chemical or physical treatment, but the following tables list the untreated samples that were available for this work.

Silicate	Sample	Synthetic or Natural?	Source
Makatite	mka	Synthetic	Nesbitt[4]*
Kanemite	kna	Synthetic	Nesbitt*
Octosilicate	oca	Synthetic	Smith, 1982[5]
Magadiite	mga	Natural	Cureton Mineral Co., Tucson, Arizona, USA.*
Kenyaite	kya	Natural	Cureton Mineral Co., Tucson, Arizona, USA.*

Table 4.3 Layered sodium polysilicate hydrate samples received from Prof. R.K. Harris, Durham University. *These have probably been previously tested by Nesbitt.

Silicate	Sample	Source
Kanemite	knb	Synthesised
Kanemite	knc	Synthesised
Octosilicate	ocb	Unilever
Octosilicate	occ	Unilever
Magadiite	mgb	Synthesised
Magadiite	mgc	Unilever
Magadiite	mgd	Unilever
Magadiite	mge	Unilever
Magadiite	mgf	Unilever
Kenyaite	kyb	Unilever

Table 4.3 Layered polycrystalline silicate hydrate samples synthesised at Unilever Research Port Sunlight Laboratories.

4.6 Syntheses

Three layered sodium polysilicate hydrate samples were synthesised for this work. The following methods were used.

Magadiite (sample mgb) was synthesised using a method, IAC7, which was devised by I.A. Crone at Unilever Research Port Sunlight Laboratories and is based on the work of Fletcher & Bibby.[6] Distilled water (89.25 g), precipitated silica (18.02 g), sodium hydroxide (1.39 g) and sodium carbonate (7.07 g) were weighed into a Teflon cup (capacity 150 cm^3). This was sealed into a Berghof high temperature autoclave and heated at 150-160 °C. for 40 hours. After cooling, the contents were filtered, washed with a little distilled water and allowed to dry overnight. The synthesis yielded 18.85 g of a white powder, which X-ray diffraction showed to be magadiite.

Kanemite (sample knb) was prepared using the method of Beneke and Lagaly.[7] A methanolic silica slurry was prepared by stirring precipitated silica (60 g) in methanol (200 cm^3) with a Teflon-blade mixer in an open vessel (capacity 400 cm^3). An aqueous sodium hydroxide solution (40 g in 35 cm^3) was slowly added over thirty minutes. The rate of this addition was regulated so that the temperature did not exceed 30 °C. During this period, more methanol (100 cm^3) was added to replace what was lost by evaporation. The resulting slurry was then dried at 90 °C. overnight, expanding to give a sponge-like solid. This was broken up and placed in crucibles to be heated at 700 °C. for 5½ hours. The resulting solid was ground and weighed (38 g). The powder was dispersed in a large volume of distilled water (2000 cm^3) and filtered overnight. The residue was washed with a little distilled water and allowed to dry. The final yield was 18.9 g of fine white powder which XRD showed to be kanemite.

This method was repeated using a large sealed vessel for the preparation of kanemite (sample knc). This prevented the evaporation of methanol so no further addition was necessary. The temperature was more easily monitored and never rose above 20 °C. The product was shown to be kanemite by powder X-ray diffraction.

References

1 A.E. Derome, *Modern NMR Techniques for Chemistry Research*, Pergamon Press, Oxford, 1987.

2 R.K. Harris and G.J. Nesbitt, *J. Magn. Reson.*, 1988. **78**, 245.

3 R.K. Harris, *Nuclear Magnetic Resonance Spectroscopy: A Physiochemical View*, Longman Scientific and Technical, Harlow, 1987.

4 G.J. Nesbitt, Ph.D. Thesis, University of Durham, 1986.

5 D.N. Smith, Ph.D. Thesis, University of Aberdeen, 1981.

6 R.A. Fletcher and D.M. Bibby, *Clays and Clay Minerals*, 1987, **35**, 318-320.

7 K. Beneke and G. Lagaly, *Am. Mineral.*, 1977, **62**, 763-771.

5 Silicon-29, Hydrogen-1 and Sodium-23 NMR

5.1 Silicon-29 NMR

5.1.1 Introduction

Over the last ten years the layered sodium polysilicate hydrates have been extensively studied by silicon-29 NMR. Though much of the work has been concentrated on magadiite, single-pulse and cross-polarisation spectra have been reported for all five silicates– the work of Nesbitt[1] and Heidemann, Schwieger and co-workers[2,3] has been particularly comprehensive. Therefore, much of the work in this section will be a confirmation of previously-published results. Nevertheless, it has been essential because ^{29}Si NMR has been used as the primary method of sample characterisation. An NMR spectrum could quickly show whether the contents of a sample bottle correspond to its labelling. This has been particularly useful as samples have been obtained from many sources. In addition to its essential analytical role, this ^{29}Si NMR study has provided some discoveries leading to new conclusions while existing findings can be reconsidered.

Layered sodium polysilicate hydrate ^{29}Si NMR spectra contain sharp lines within the region, δ_{Si} -90 to -120. The signals can be assigned to silicon atoms of type Q^3 or Q^4, with some confidence. Makatite and kanemite contain silicon atoms of type Q^3 only, whereas octosilicate, magadiite and kenyaite contain both Q^3 and Q^4 species. Some spectra contain more than one silicon species of the same connectedness, but it is more difficult to make further assignments: unknown structural differences are responsible for the two Q^3 lines in makatite or the three Q^4 lines in magadiite, for example. Tentative proposals have been made in both these cases: Nesbitt[1] assigned the makatite peaks on the basis of bonding to sodium while Schwieger *et al.*[2] attributed the Q^4 chemical shift variation in magadiite to differences in mean bond angles, <Si-O-Si.

The NMR technique is inherently quantitative provided suitable precautions are observed. Therefore, ^{29}Si single-pulse spectra have been used to determine ratios

of Q^3 to Q^4 silicon atoms in octosilicate, magadiite and kenyaite. However, quantitative spectra are only acquired if adequate recycle times are used and many authors have determined such ratios from saturated spectra. Their ratios are probably false, but accurate values can be determined if ^{29}Si spin-lattice relaxation times are known. This has been achieved for magadiite and octosilicate, but not for kenyaite.

Quantitative ^{29}Si SP experiments can take a large amount of spectrometer time, with recycle delays of an hour or more. In cases where quantitative work is not especially desirable, the cross-polarisation technique is particularly suitable as high-quality spectra can be obtained very rapidly. Thus, a new silicate sample can be tested by acquiring a ^{29}Si CP spectrum in an hour or less. This has been used as the primary screening method for judging the quality of samples in this work. A ^{29}Si CP spectrum gives essentially the same information as a saturated SP spectrum, though line-widths can vary and the presence of Q^4 siliceous impurities are under-represented on cross-polarisation.

This section is divided into several parts. Initially, a series of ^{29}Si SP spectra for all the layered sodium polysilicate hydrates will be displayed contiguously and discussed. Then, the spectrum of each silicate will be discussed individually. The final section contains an investigation into the effect of sample-drying on ^{29}Si NMR spectra.

5.1.2 Line-Widths and Chemical Shifts in ^{29}Si NMR Spectra

The spectra in this section will be described in terms of the width and frequency of the peaks. Several factors can be responsible for the width of a line in a ^{29}Si NMR spectrum. Broadening can be caused by poor instrumentation or experimental technique, *i.e.* inhomogeneities in B_0 or deviations from the magic-angle. Assuming that such factors can be disregarded, Engelhardt and Michel[4] list three factors which are most likely to contribute to the line width: dispersion of isotropic

chemical shifts; unaveraged dipolar interactions of the ^{29}Si nucleus with ^{1}H, ^{27}Al or other NMR-active nuclei; and the presence of paramagnetic impurities. Large chemical shift dispersions are likely in glassy or amorphous systems, where very broad lines are seen ($\Delta_{1/2} \approx$ 10-20 ppm). Perfectly ordered systems can have very narrow lines ($\Delta_{1/2} \approx$ 0.2-3 ppm). The second factor is less likely to be important in the ^{29}Si NMR spectra of layered sodium polysilicate hydrates– dipolar interactions with protons should be averaged by high-power proton decoupling and magic-angle spinning, and there should be little or no aluminium. Grimmer *et al.* illustrated the dependence of line-widths on paramagnetic impurities with a series of spectra for olivine samples, $Mg_xFe_{2-x}SiO_4$.[5] Broader lines were observed as the proportion of iron was increased.

The relationship between ^{29}Si chemical shift and connectedness, Q^s, has already been described (see section 3.1). The wide range of chemical shifts for each type of silicon atom indicate that other factors are important. Many authors have reported relationships between δ_{Si} and various structural parameters. In general, these are empirical relationships, for which there is some theoretical background.

K.A. Smith *et al.*[6] reported the dependence of δ_{Si} for many rock-forming silicates on silicon-oxygen bond-length and cation-oxygen bond-strength (*i.e.* the strength of the O-X bond in ≡Si-O-X). There was some correlation when bond-length data were plotted against chemical shift: shorter bonds corresponded to a lower frequency. However much of the data were significantly distant from a least-squares regression line. There was a better correlation between bond-strength and chemical shift: stronger bonds corresponded to a lower frequency. The data fell within ±2 % of a best-fit line and these deviations were consistent with the ±4 % errors in calculating the cation-oxygen bond strengths. Grimmer showed that a better correlation is observed between Si-O bond-length and the principal values of the ^{29}Si chemical shift tensor.[7]

J.V. Smith and Blackwell[8] looked for empirical relationships between δ_{Si} of several silica polymorphs and a number of structural parameters which could be

obtained from crystallographic data. The correlation with the secant of the mean Si-O-Si bond angle provided a better predictor of chemical shifts than mean Si-O bond-length, mean Si-Si bond-length or the mean Si-O-Si bond angle, θ. Least-squares fitting gave equation 5.1 with a correlation coefficient of 0.99811.

$$\sec\theta = -3.1571 - 0.017847\,\delta_{Si} \qquad \text{Eq. 5.1}$$

Ramdas and Klinowski[9] and Mägi *et al.*[10] also showed that the Si-O-Si bond-angle influenced the ^{29}Si chemical shift. The former included aluminium-containing silicates in their treatment while the latter also considered the distortion of the SiO_4 tetrahedron. On the basis of the general theory of NMR shielding, distorted SiO_4 tetrahedra should have a relatively high-frequency chemical shift.

Janes and Oldfield related the net charge of the silicon atom to ^{29}Si chemical shift.[11] This can be estimated by considering the electronegativities, EN, of the four groups bonded to each silicon atom. Equation 5.2 is an empirical relationship. Electronegativities for the ONa, OH, OAl and OLi groups were listed as 3.4395, 3.5882, 3.7339 and 3.4385, respectively. Using equation 5.3 to determine the electronegativity for the OSi group allows for the Si-O-Si bond angle, θ.

$$\delta_{Si} = -24.336\,\Sigma EN + 279.27 \qquad \text{Eq. 5.2}$$

$$EN(OSi) = 2.9235 + \theta/136.79^\circ \qquad \text{Eq. 5.3}$$

More elaborate methods of predicting silicate ^{29}Si chemical shifts have been reported. Sherriff and Grundy[12] successfully related δ_{Si} to a parameter, χ'', which is based on the magnetic anisotropy and the valence of the bond between the oxygen and the second-neighbour cation to the silicon atom. Prabakar *et al.*[13] defined a parameter, P, which takes into account the electronegativity and the structural description of silicate units as well as the ionic potential of any cations. This satisfactorily accounted for the chemical shift distribution in a wide range of silicates.

5.1.3 Layered Sodium Polysilicate Hydrate ^{29}Si SP Spectra

Though spectra of individual silicates will be discussed later, a general consideration of ^{29}Si NMR spectra of all the layered sodium polysilicate hydrates is worthwhile– there are certain group trends which should be emphasised.

Representative single-pulse magic-angle spinning ^{29}Si spectra for each of the layered sodium polysilicate hydrates are displayed in figure 5.1. It is likely that the makatite, kanemite, magadiite and kenyaite samples have been previously analysed by Nesbitt.[1] All the spectra were obtained using the CXP200 spectrometer with a spinning rate of around 2.5 kHz. Further experimental details may be found in table 5.1. Chemical shifts and line-widths are listed in table 5.2. The peaks have been assigned to silicon atoms of type Q^3 and Q^4 on the basis of the well-established relationship between δ_{Si} and connectedness, Q^s. It should be noted that the spectra were acquired by an inexperienced analyst with an ageing spectrometer. Spectra of comparable quality can certainly be obtained in fewer transients with a correctly-optimised, newer spectrometer (such as the CMX200).

Silicate	Sample	Recycle Delay / s	Number of Transients
Makatite	mka	30	4106
Kanemite	kna	30	2336
Octosilicate	oca	100	641
Magadiite	mga	60	1223
Kenyaite	kya	100	862

Table 5.1 Experimental details for the ^{29}Si SP spectra of the layered sodium polysilicate hydrates in figure 5.1.

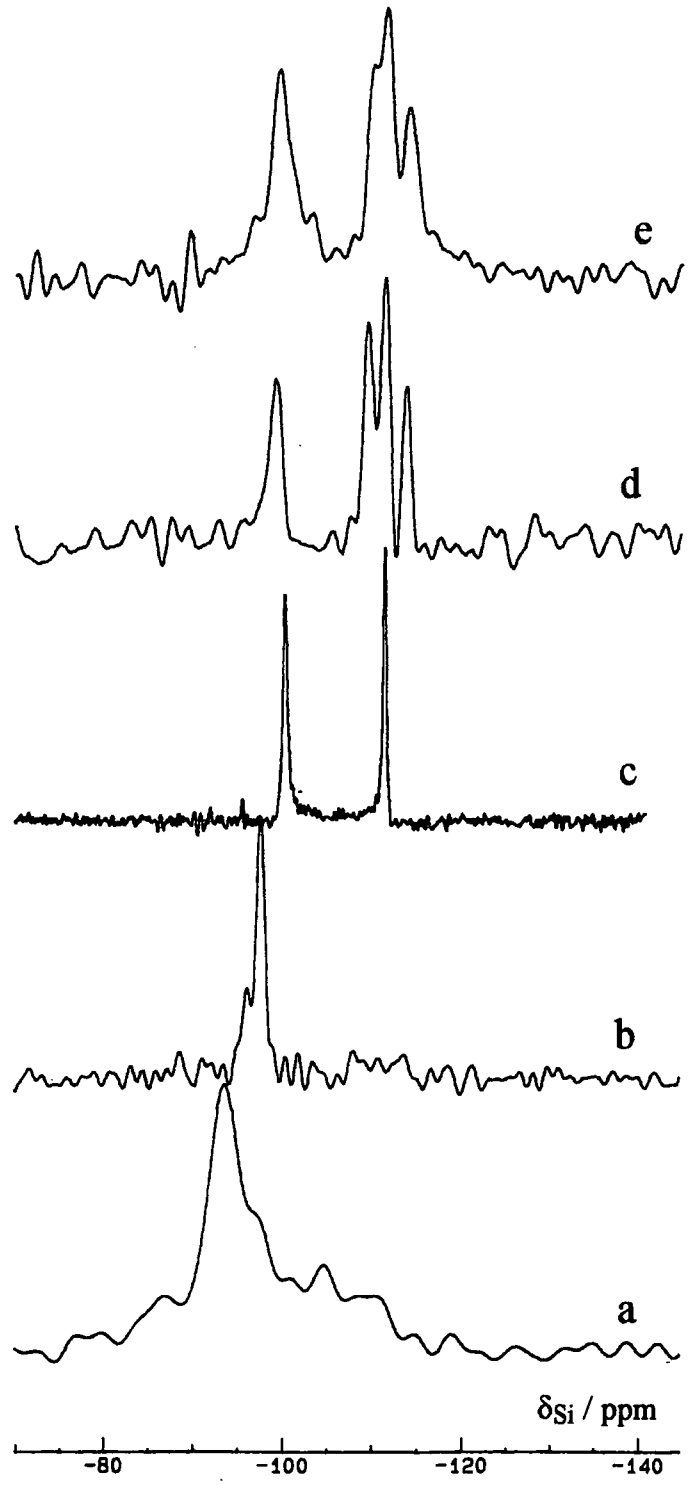

Figure 5.1 Single-pulse ^{29}Si spectra of five representative layered sodium polysilicate hydrate samples: a) makatite (mka); b) kanemite (kna); c) octosilicate (oca); d) magadiite (mga); and e) kenyaite (kya). Experimental details, chemical shifts and line-widths can be found in tables 5.1 and 5.2. Partial saturation is likely in all of these spectra.

Silicate	Sample	Q^3		Q^4	
		δ_{Si} / ppm	$\Delta_{1/2}$ / Hz	δ_{Si} / ppm	$\Delta_{1/2}$ / Hz
Makatite	mka	-93.5	200		
Kanemite	kna	-96.3	63		
		-97.6	45		
Octosilicate	oca	-100.2	16	-111.4	18
Magadiite	mga	-99.3	74	-109.5	~50
				-111.5	~60
				-113.7	~50
Kenyaite	kya	-99.4	59	-109.7	~45
				-111.5	~40
				-114.1	~40

Table 5.2 Chemical shifts and full peak-widths at half height for the ^{29}Si SP/MAS spectra of the layered sodium polysilicate hydrates, spectra displayed in figure 5.1. Line-widths can only be estimated for the overlapping (Q^4) signals in magadiite and kenyaite.

Before these spectra are considered further, a few comments should be made regarding the purity of the samples and also how typical they are of other samples studied in this work. This is the only available makatite sample and its spectrum exhibits signs of amorphous contamination with a broad absorption centred around δ_{Si} -105. The kanemite spectrum has a low-frequency shoulder, which is unique to this sample. Three octosilicate samples have been studied giving virtually the same ^{29}Si SP/MAS spectrum. The six magadiite samples are also fairly consistent, but this is certainly the best. Finally, the kenyaite spectrum is different to that of a better sample that has been used in this work.

Even though the spectra in figure 5.1 are not always those of pure representative samples, several observations can still be made. The group behaviour of the layered sodium polysilicate hydrates can be discussed with respect to the relative peak areas, multiplicities, chemical shifts and line-widths of these ^{29}Si SP/MAS spectra, *i.e.* peak size, number, frequency and sharpness.

The layered sodium polysilicate hydrates can be represented as a series: makatite, kanemite, octosilicate, magadiite, kenyaite. Formulae for all the series members may be written as $Na_2O:xSiO_2:yH_2O$, with the proportion of silica to soda, x, increasing from 4 in makatite to 22 in kenyaite. This corresponds to an increase in the condensation of the silicates, *i.e.* the proportion of Si-O-Si linkages to Si-OH or Si-ONa groups. The ^{29}Si SP/MAS spectra illustrate this well-documented trend. Makatite and kanemite both contain silicon atoms of type Q^3 only while octosilicate, magadiite and kenyaite also contain Q^4 silicon atoms in increasing proportions. As the silica to soda ratio, x, increases, the silicates should become more complex– the size of any unit cells might be expected to vary with x. More complex structures should have more distinct silicon sites resulting in ^{29}Si SP/MAS spectra with more signals. This is the observed trend in these spectra– the makatite spectrum has a single line but four may be resolved in the spectrum of magadiite.

The chemical shifts in these spectra provide ample scope for a consideration of structural similarities and dissimilarities between the layered sodium polysilicate hydrates. Nesbitt[1] proposed a very close structural relationship between makatite and octosilicate, magadiite and kenyaite, whereby multiple sheets of the former could be used to build plausible models of the rest. These octosilicate, magadiite and kenyaite spectra are characteristic of very similar structures– all contain Q^3 signals at about δ_{Si} -100 and there is also a common Q^4 absorption at δ_{Si} -111. In going from octosilicate to kenyaite, extra Q^4 peaks might evolve as the layer becomes thicker. Using this logic, a contrary conclusion can be made concerning makatite and kanemite– large δ_{Si} variations indicate structural dissimilarities. This need not necessarily be the case as several factors can affect δ_{Si}, such as average Si-O-Si bond angles and distortion of the SiO_4 tetrahedra, for example (see section 5.1.2). Nesbitt attributed the change to differences in the puckering of the silicate sheets. Makatite and kanemite are puckered single-sheet silicates with small average bond-angles and high-frequency ^{29}Si chemical shifts, whereas the multi-sheet layers may be less puckered, with larger

average bond angles and lower-frequency Q^3 signals. Less-distorted SiO_4 tetrahedra might also be expected for the more condensed silicates.

In addition to variation in chemical shift, these spectra also exhibit some variation in line-width. Octosilicate has the sharpest signals, while the (probably impure) makatite signal is broader by a factor of ten. Line-widths are very important in determining the feasibility of more-elaborate experiments or the amount of information that can be obtained from a single spectrum. For example, a zeolite ZSM-12 sample with narrow lines ($\Delta_{1/2}$ = 8 Hz) has been used for natural-abundance 2-dimensional $^{29}Si,^{29}Si$ COSY and INADEQUATE experiments by Fyfe *et al.*,[14] whereas Chuang *et al.* reported a silica gel spectrum where the lines were so broad that Q^2, Q^3 and Q^4 peaks were poorly resolved.[15] The line-widths for the layered sodium polysilicate hydrates are between these two extremes: a 2-D $^{29}Si,^{29}Si$ COSY experiment would be impractical, but multiple Q^3 or Q^4 silicon sites can be resolved. The sharpness of the octosilicate signal could be caused by the sample being exceptionally crystalline, with each peak corresponding to a narrow range of shielding environments. The broadness of the makatite peak can at least partially be attributed to overlap with the absorption of an amorphous impurity.

5.1.4 Makatite

Figure 5.2 shows a ^{29}Si CP spectrum for makatite (sample mka). This was acquired with the CMX200 spectrometer, equipped with a Doty MAS probe and 7 mm zirconia rotors. A standard cross-polarisation pulse-sequence was used, cpflip, and 512 transients were acquired with a recycle delay of 3 s, a contact time of 3.5 ms and a spinning rate of 2 kHz.

The single-pulse makatite spectrum in figure 5.1 contains a single sharp line. There is also a less intense lower-frequency shoulder and some evidence of contamination with a broad absorption around δ_{Si} -105. Cross-polarisation has a significant cosmetic effect as the sample absorptions are enhanced relative to those of the impurities. The makatite peaks are sharper, so it is clearer that there are two Q^3 signals and chemical shifts (δ_{Si} -93.1 and -94.0) can be determined precisely in spite of the significant degree of overlap.

Cross-polarisation might be expected to boost the relative intensities of the makatite signals as the efficiency of the process depends on the proximity of suitable protons. The decrease in line-width is more surprising and less easy to explain. It is possible that the broad single-pulse line-width corresponds to a range of makatite sites that are being selectively excited on cross-polarisation. A more likely explanation would be to attribute much of the observed single-pulse line-width to overlap with the contaminant signal. Cross-polarisation selectively excites the sharper makatite signals.

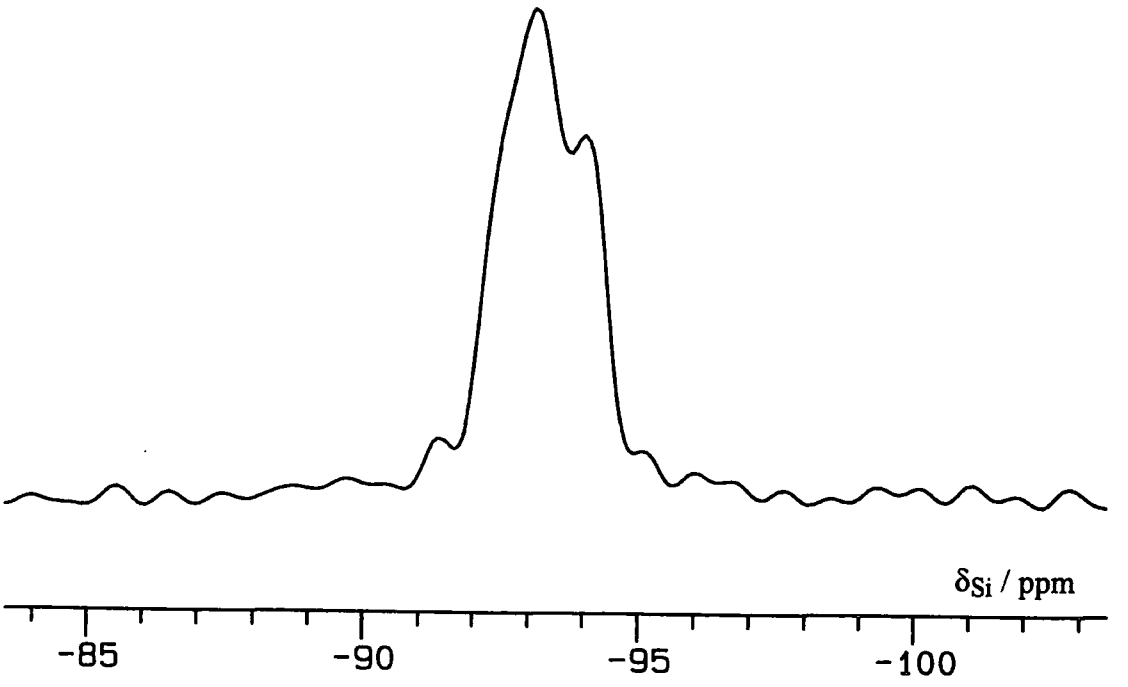

Figure 5.2 A ^{29}Si CP spectrum of makatite (sample mka).

The two Q^3 signals which are observed in the ^{29}Si NMR spectra of makatite (sample mka) may have several causes. They could correspond to two distinct makatite silicon species or to a single makatite line and a signal from an impurity.

The chemical shifts of the two signals indicates unequivocally that these are silicon sites of type Q^3. This means that there are three next-nearest neighbour silicon atoms only. The silicon atoms are tetrahedral, so there is a spare co-ordination site. It is probable that this will be filled by either a hydroxyl group or an oxide ion, with a sodium ion to balance the charges. Makatite is hydrated and this water is likely to be in a co-ordination sphere around the sodium ion. Thus, there are two plausible types of Q^3 silicon atom, $(SiO)_3\underline{Si}$-OH or $(SiO)_3\underline{Si}$-O$^-$ $[Na(H_2O)_n]^+$, and these can be named silanol and siloxide, respectively. If the formula of makatite is assumed to be $Na_2O{:}4SiO_2{:}5H_2O$, only half of the silicon atoms can be associated with sodium, *i.e.* siloxide atoms. Therefore, the other half must be silanol groups, and the formula can be rewritten, $(O_{½})_3$Si-OH.$(O_{½})_3$Si-O$Na(H_2O)_2$. Figure 5.3 is an explanatory

picture. From a consideration of stoichiometry, makatite might be expected to contain silanol and siloxide silicon atoms in a 1:1 ratio.

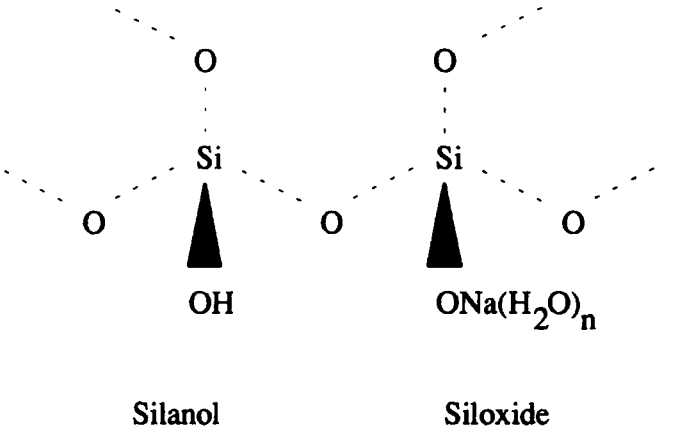

Figure 5.3 Part of a hypothetical makatite layer, to illustrate silanol and siloxide Q^3 silicon atoms.

The above paragraph is principally speculation. The ideas can be taken further with a consideration of the unit cell of makatite.[16] This was determined by single crystal X-ray diffraction, so the positions of Si, Na and O atoms are known and proton positions may be inferred. The silicon atoms can be divided into silanol and siloxide types with a consideration of the proximity of the nuclei to sodium. This was noted by Nesbitt,[1] who concluded that in each asymmetric unit, three of the silicon atoms were close to sodium, while the fourth would be bonded, *via* oxygen to a proton. The 3:1 ratio corresponded well with the ratio observed in his ^{29}Si SP spectrum. The smaller, silanol peak would be expected to be at a lower frequency than the larger siloxide signal, which also corresponded with the observed spectrum. This is an excellent, plausible theory, but a 3:1 ratio of siloxide to silanol Q^3 silicon atoms would result in a charged unit cell; the previous paragraph shows that a 1:1 ratio would be necessary for charge balance. To make the theory work an extra proton must be added to one of the silicon atoms which are bonded to sodium, *via* oxygen. Exchange is possible over the NMR time-scale, and this proton might spend its time equally over the three silicon

atoms. To represent this, the formula for makatite might be written as $(O_{½})_3Si\text{-}OH.(O_{½})_9(Si\text{-}O)_3H[Na(H_2O)_n]_2$. Figure 5.4 provides an explanatory diagram.

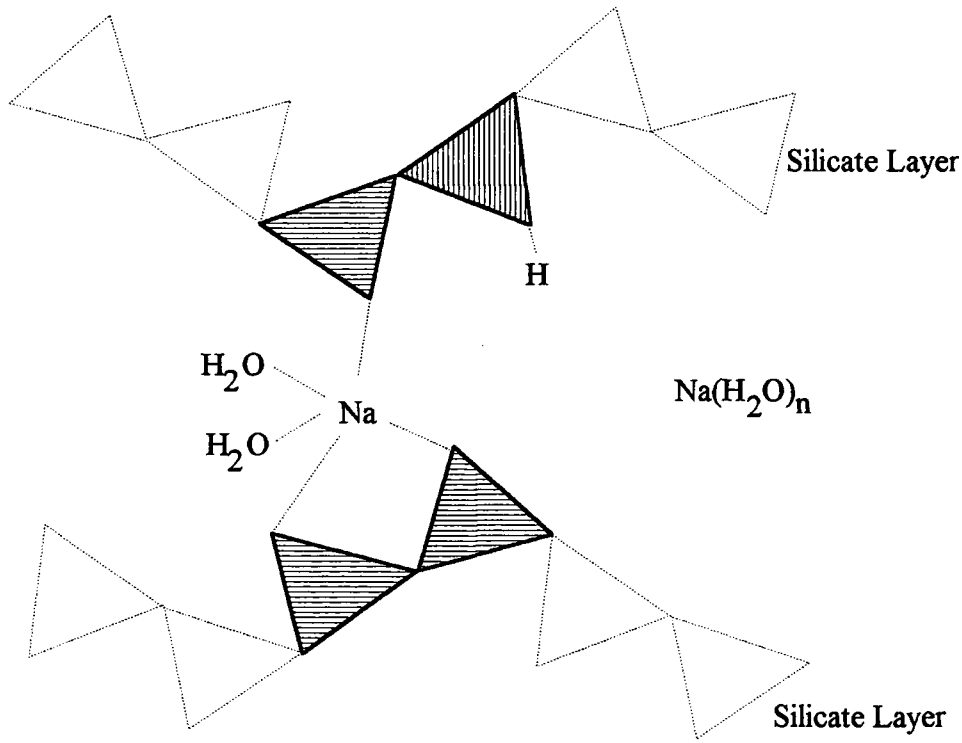

Figure 5.4 A schematic diagram of the known structure of makatite. Triangles represent SiO_4 polyhedra. Out of four silicon atoms, three will be associated with sodium ions, while one is capped by a hydroxyl group. As it stands, the structure is negatively charged and an extra proton must be added somewhere.

The makatite ^{29}Si CP spectrum in figure 5.2 was obtained with a transmitter frequency of 39.76 MHz and an acquisition time of 30 ms. Under these conditions, there are only two resolvable lines. However, four lines are seen if a longer acquisition time or a higher magnetic field is used. Figure 5.5 shows a 59.58 MHz ^{29}Si CP spectrum of makatite (sample mka), obtained using the Varian Unity Plus 300 spectrometer, equipped with a Doty MAS probe and 7 mm zirconia rotors. Forty-eight transients were used to acquire this spectrum with a recycle time of 10 s, a contact time of 3 ms and a spinning rate of 3.5 kHz; the acquisition time was 100.2 ms.

The spectrum contains four signals at δ_{Si} -92.1, -92.6, -92.9 and -93.7. These can be assigned to the four silicon atoms in the asymmetric unit of makatite. This is good evidence that the earlier assignments of Nesbitt were correct. In a less well-resolved spectrum, the three high-frequency lines give a single signal.

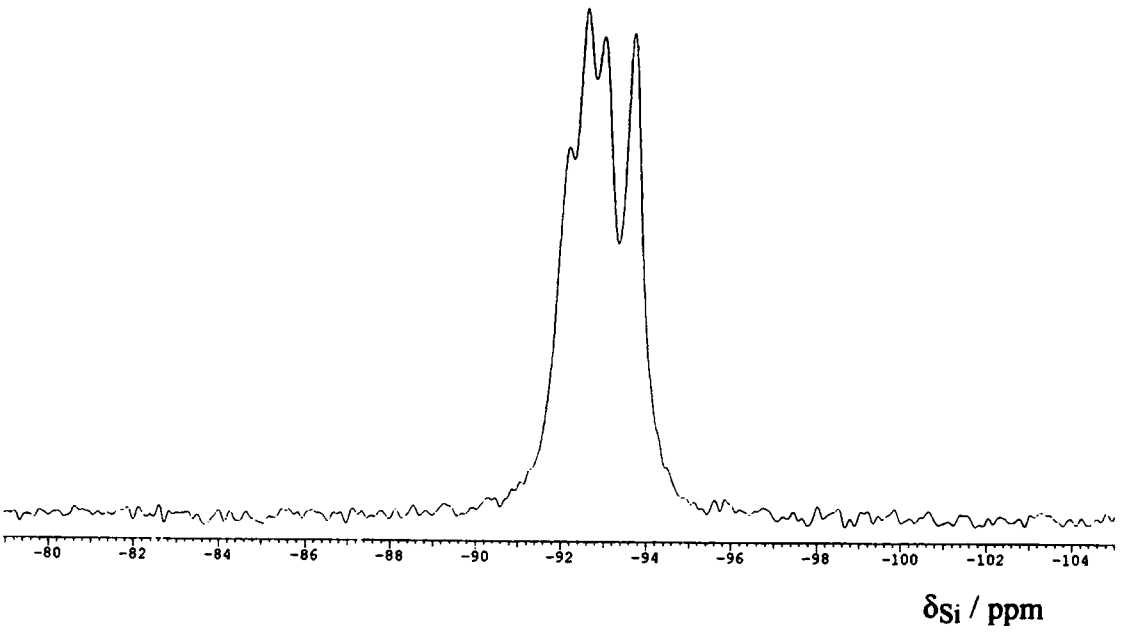

Figure 5.5 A 59.58 MHz ^{29}Si CP spectrum of makatite (sample mka).

Schwieger *et al.* studied the ion-exchange properties of makatite.[3] Since, their makatite SP and CP spectra contained a single Q^3 line, it is possible that the makatite spectrum observed here also contains a single makatite peak. The other sharp peaks could all come from impurities. This is not unlikely, since this sample is certainly contaminated. The resolution of the Schwieger *et al.* spectrum would be expected to be lower as it was acquired with a spectrometer frequency of 12 MHz; the line-width was *ca.* 50 Hz (≡ 4 ppm). Additionally, the quality of the sample must be doubted as the ^{29}Si SP spectrum includes an intense peak at δ_{Si} -107, from contaminating Q^4 silicon atoms. It should be emphasised that these are the only known ^{29}Si NMR spectra of makatite and both samples are impure.

In conclusion, a high-quality makatite ^{29}Si CP spectrum has been acquired with four distinct lines. This is better resolution than has been achieved by previous authors. The four lines can be assigned to the four silicon sites in the crystallographic asymmetric unit. However, this is the only reported makatite ^{29}Si NMR spectrum with multiple Q^3 lines. The sample was impure and contamination could be responsible for the presence of some of the signals. A ^{29}Si CP variable contact time experiment provides further information, see section 7.3.2.

5.1.5 Kanemite

Three samples of kanemite were available for study in this work, and ^{29}Si NMR spectra have been obtained for all of them. Figure 5.6 shows ^{29}Si CP spectra for samples kna and knc. The spectra were obtained with the CXP200 and CMX200 spectrometers, using standard cross-polarisation pulse-sequences, DURHCPMA and cpflip, respectively. The former was used for sample kna and it was equipped with a Doty MAS probe and 7 mm zirconia rotors. The spectrum was acquired with 2000 transients, a recycle delay of 3 s, a contact time of 1.5 ms and a spinning rate of 2.5 kHz. The latter was used for sample knc with the same probe and rotors. The spectrum was acquired with 512 transients, a recycle delay of 3 s, a contact time of 2 ms and the spinning rate was 2 kHz. Table 5.3 lists chemical shifts and line-width details for the two spectra in figure 5.6, together with values from a spectrum of sample knb (not shown), which was very similar to the spectrum of sample knc.

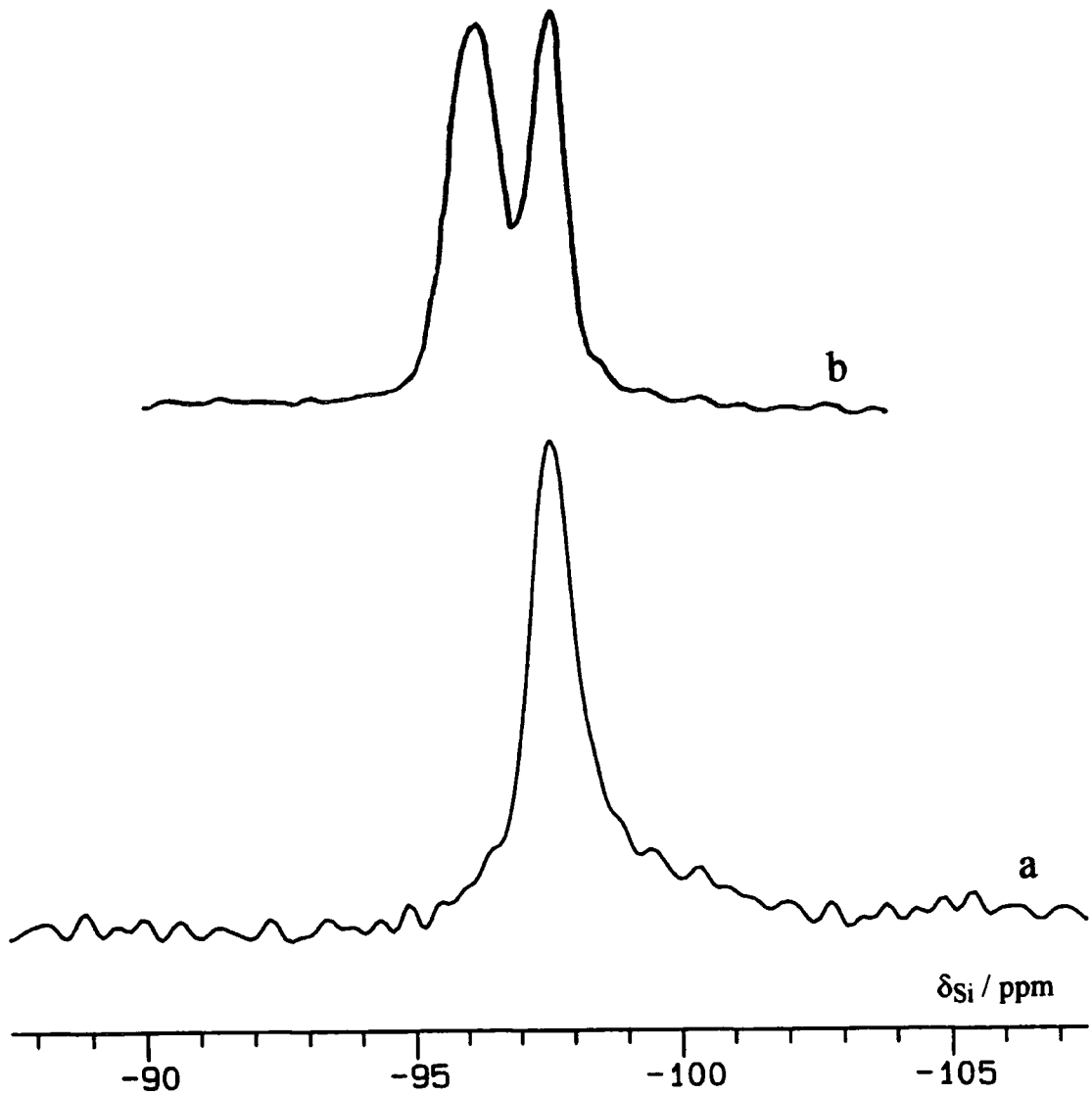

Figure 5.6 Representative ^{29}Si CP spectra for two kanemite samples: a) sample knb and b) sample kna. The spectra were acquired with different spectrometer software, but an attempt has been made to make the scale of the top spectrum correspond to the plotted scale. This has been successful to within ± 2 %.

Silicate	Sample	Peak 1		Peak 2	
		δ_{Si} / ppm	$\Delta_{1/2}$ / Hz	δ_{Si} / ppm	$\Delta_{1/2}$ / Hz
Kanemite	kna	-96.0	50	-97.6	40
Kanemite	knb			-97.7	40
Kanemite	knc			-97.6	40

Table 5.3 Chemical shifts and full peak-widths at half height for ^{29}Si CP spectra of three kanemite samples.

The spectrum of sample kna contains two lines and it is similar to the SP spectrum in figure 5.1. The spectra of samples knb and knc contain single lines, with the same chemical shift and line-width as the low-frequency signal in the spectrum of sample kna. Therefore, it can be assumed that the silicon species responsible for the low-frequency signal in the spectrum of sample kna is responsible for the single signal in the other spectra. The extra line in the former spectrum must respond to a different silicon species. The presence of two lines can not be due to slower exchange or better spectral resolution, which would result in a broader single line with an average chemical shift.

It appears that the ^{29}Si NMR spectrum with two Q^3 signals is atypical of kanemite. This becomes more obvious when other reported kanemite spectra are considered. Yanagisawa *et al.*[17] and Pinnavaia *et al.*[18] have reported spectra with lone signals at δ_{Si} -97.2 and -101, respectively; the apparently erroneous chemical shift is typical of this Pinnavaia *et al.* reference. A kanemite spectrum has also been reported by Nesbitt.[1] This does contain two signals, but it is almost certainly the same sample that has been analysed in this work.

Identifying the species responsible for the extra peak would be worthwhile. Nesbitt extrapolated his conclusions for makatite to kanemite. However the makatite and kanemite spectra obtained in this work differ in the relative intensities of the two signals. In kanemite, the low-frequency signal is more intense than the high-

frequency signals, whereas the opposite is true for makatite (at 39.76 MHz, with a short acquisition time). If the theory of Nesbitt is rejected on these grounds, alternative theories must be considered. Split Q^3 signals have been observed in a few other silicate samples, arousing some interest. Rocha and Klinowski reviewed previous literature assignments for the two equally intense lines in pure (low Iron(III) content) kaolinite ^{29}Si NMR spectra.[19] The splitting could be caused by the presence of two crystallographically distinct sites,[20] hydrogen-bonding effects,[21,22] Si-Al interactions between adjacent layers or ^{29}Si-^{27}Al scalar coupling, as with albite.[23] The latter two reasons are unlikely in kanemite, but the presence of aluminium as a contaminant should not be dismissed– Borbély *et al.* observed a shoulder in an octosilicate Q^3 peak and assumed that this was due to aluminium replacement around Q^4 silicon atoms, $(SiO)_3Si\text{-}OAl$.[24] Thomson showed that interlayer hydrogen-bonding might give two-equally intense lines if the bond is asymmetric.[21]

In summary, the ^{29}Si NMR spectrum of kanemite has a single line. However, an extra signal is seen in a single kanemite sample and finding a plausible reason would be worthwhile. Some enlightenment has been provided by ^1H MAS NMR and some ^{29}Si CP experiments, (see sections 5.2.3 and 7.3)

5.1.6 Octosilicate

Three octosilicate samples were available for study in this work. A representative spectrum is shown in figure 5.7. Octosilicate (sample occ) was analysed using the CMX200 spectrometer equipped with a Chemagnetics HX probe and 7.5 mm zirconia Pencil rotors. The spectrum was acquired with 800 transients, a recycle time of 2 s, a contact time of 2 ms and a spinning-rate of 2 kHz. Chemical shifts and line-widths for this spectrum and very similar spectra of the two other available samples (not shown) are listed in table 5.4.

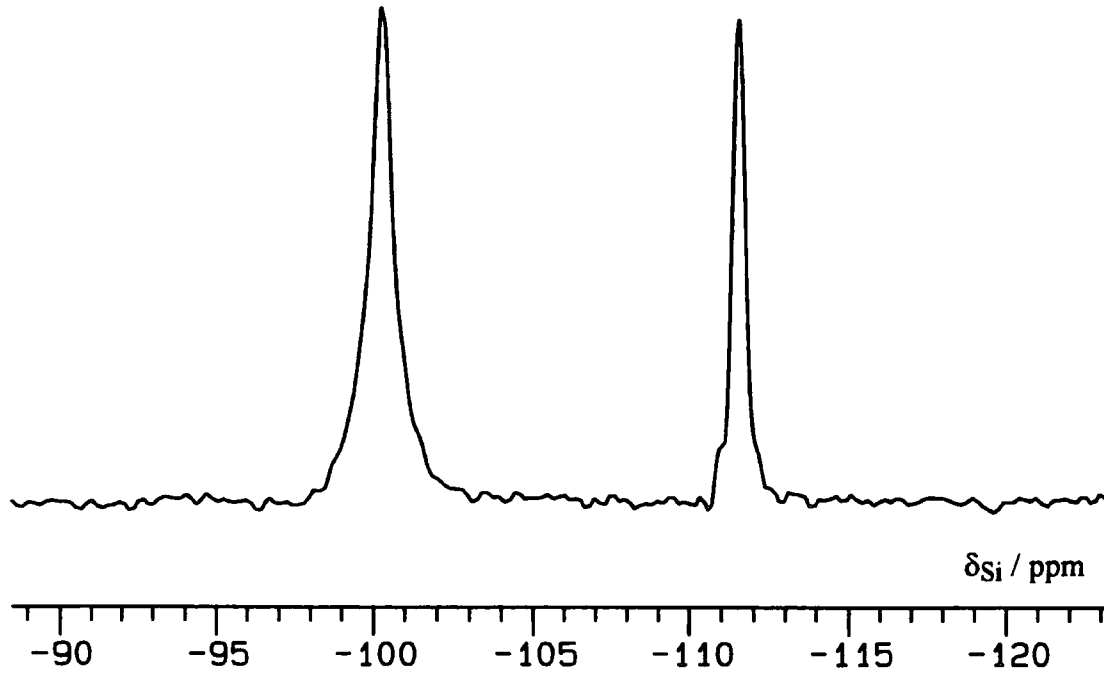

Figure 5.7 A ^{29}Si CP spectrum of octosilicate (sample occ).

Sample	Q^3		Q^4	
	δ_{Si} / ppm	$\Delta_{1/2}$ / Hz	δ_{Si} / ppm	$\Delta_{1/2}$ / Hz
oca	-100.2	37	-111.6	39
ocb	-100.2	26	-111.5	19
occ	-100.3	31	-111.5	18

Table 5.4 Chemical shifts and full peak-widths at half-height for three octosilicate samples. The spectrum for sample occ is displayed in figure 5.7.

Table 5.4 shows that the spectrum of octosilicate (sample occ) is truly representative of the other two samples available for study in this work. All the spectra consist of two signals, which can be confidently assigned to silicon atoms of types Q^3 and Q^4. The Q^3 signals tend to be broader and have a larger peak area. Both these observations can be explained with respect to the strength of the heteronuclear dipolar interaction between ^{29}Si and ^1H. Silicon atoms of type Q^3 will have closer protons: they will either be two bonds away from a silanol proton, ≡Si-OH, or near hydrated water protons, ≡Si-ONa$(H_2O)_n$. The strength of any $^{29}Si,^1H$ interactions decrease greatly with distance. Therefore, cross-polarisation will be more efficient for the Q^3 silicon atoms, but dipolar line-broadening will be more severe.

The sharpness of the lines in all the octosilicate spectra studied in this work should be emphasised. The line-widths are much smaller than those of the other layered sodium polysilicate hydrates. Some variation is observed from sample to sample and between CP and SP spectra and this can probably be attributed to variations in decoupling efficiency or possibly FID-truncation.

Several other authors have reported ^{29}Si NMR spectra for octosilicate. The CP spectrum of Borbély *et al.*[24] contained a low-frequency shoulder to the Q^3 line, which was attributed to the presence of aluminium impurities. No such shoulders have been found for the three samples in this work.

In summary, three octosilicate samples were available for this work. They all give ^{29}Si spectra with two sharp lines that can be assigned to Q^3 and Q^4 silicon sites.

5.1.7 Magadiite

Six magadiite samples were available for study in this work. A representative spectrum is shown in figure 5.8. Magadiite (sample mgf) was analysed using the CXP200 spectrometer equipped with a Doty MAS probe and 7 mm zirconia rotors. The spectrum was acquired with 9000 transients, a recycle time of 2s, a contact time of 2 ms and the spinning-rate was 4 kHz. Chemical shifts and line-widths for this spectrum and for ^{29}Si CP spectra of the other five samples (not shown) are listed in table 5.5.

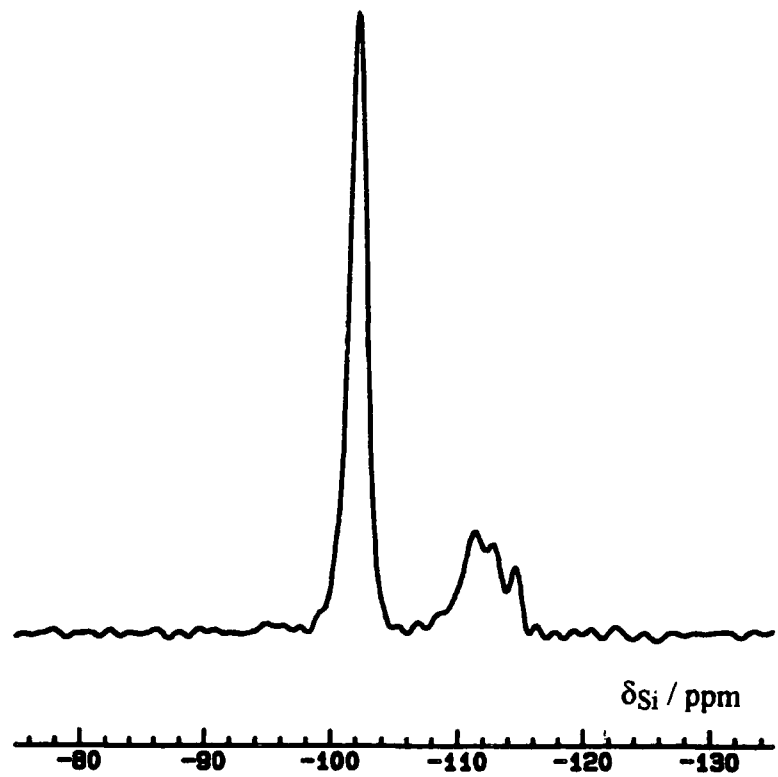

Figure 5.8 A ^{29}Si CP spectrum of magadiite (sample mgf).

Sample	Q^3		Q^4	
	δ_{Si} / ppm	$\Delta_{1/2}$ / Hz	δ_{Si} / ppm	$\Delta_{1/2}$ / Hz
mga	-99.4	59	-109.7	44
			-111.5	37
			-114.1	39
mgb	-99.5	71	-110.0	‡
			-111.5	
			-114.2	
mgc	-99.6	63	-109.9	~60
			‡	
			-113.8	~80
mgd	-99.3	75	-110.1	‡
			-111.5	
			‡	
mge	-99.6	64	‡	‡
			-111.1	
			-114.2	
mgf	-99.7	60	-110.6	‡
			-111.5	
			-114.2	

Table 5.5 Chemical shifts and full peak-widths at half-height for six magadiite samples. The spectrum for sample mgf is displayed in figure 5.8. ‡Resolving the Q^4 regions in some of these spectra was difficult. Therefore, selective chemical shifts and peak-widths are listed.

The Q^3 chemical shifts listed in table 5.5 tend to be fairly consistent. Any variation is certainly less than that observed among the many reported magadiite ^{29}Si spectra (table 3.1). Therefore, this variation can be attributed to the different referencing methods that various workers have used rather than real sample variation. The data in table 5.5 have been obtained from CP experiments at contact times which favour the Q^3 signals. Correspondingly, there is some uncertainty in the values for the Q^4 chemical shifts.

Magadiite peaks tend to be broader than those in octosilicate. The line-widths are fairly important in determining the resolution that can be seen in the Q^4 region of the spectrum. The spectrum of sample mgf, figure 5.8. is fairly representative, but the resolution observed in sample mga was quite exceptional– better than anything previously reported in the literature. Figure 5.9 is a 59.58 MHz spectrum of this sample, acquired with the VXR300 spectrometer.

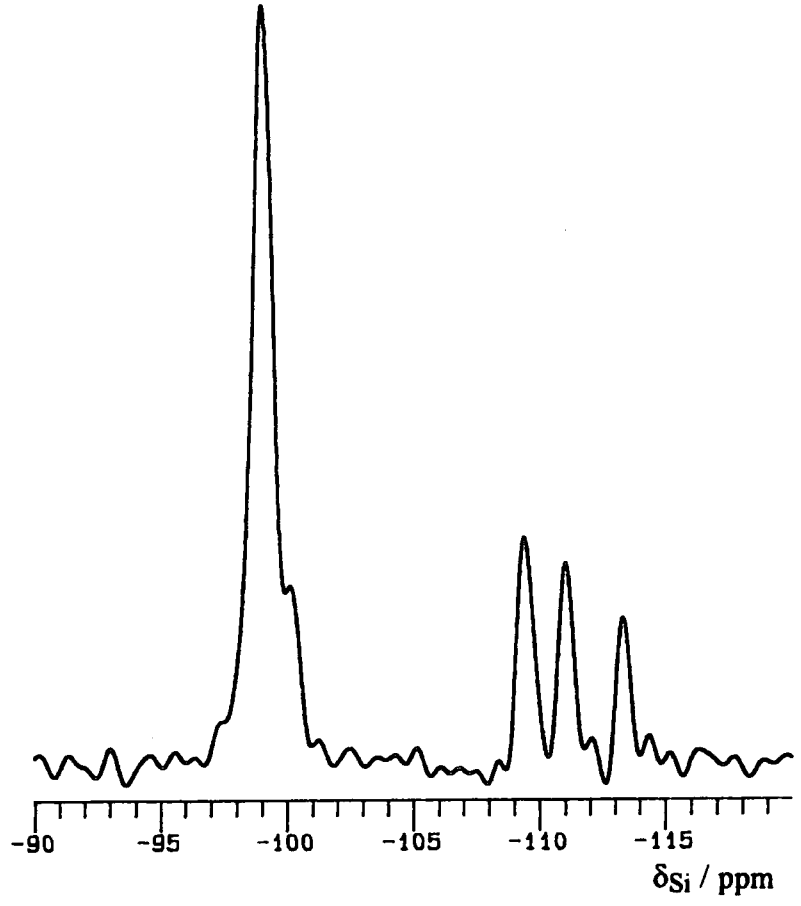

Figure 5.9 A very high-resolution magadiite ^{29}Si CP spectrum. Sample mga acquired using the VXR300 spectrometer. The spectrum was acquired with 100 transients, a recycle time of 0.5 s and a contact time of 8 ms, with a spinning rate of 4.96 kHz.

All the ^{29}Si NMR magadiite spectra in this work have contained a single Q^3 signal. Nesbitt[1] reported a second Q^3 site, which became visible in the ^{29}Si CP spectrum at high contact times– the main peak was assigned to ≡Si-OH, while the shoulder was assigned to ≡Si-O-Na$(H_2O)_x$. Attempts to repeat this result were unsuccessful in this work.

In summary, six magadiite samples have been studied in this work. Their spectra are all fairly similar. Though there is some variation in the measured chemical shifts, the values are more consistent than those reported in the literature. The Q^4 resolution observed for sample mga is quite exceptional; it is this sample which will be used for the more elaborate ^{29}Si cross-polarisation experiments which are described in chapter 7.

5.1.8 Kenyaite

A ^{29}Si single-pulse study of kenyaite was worthwhile since the Q^3:Q^4 ratio for this sample is unknown. Two kenyaite samples were available for this work. Sample kya was not particularly useful– it gave broad ^{29}Si SP lines (figure 5.1), a poor ^{29}Si CP spectrum and was visibly contaminated, *i.e.* green. Cross-polarisation was also unsuccessful for the "kenyaite-like structure", prepared by Schwieger *et al.*[2] However, sample kyb gave sharper ^{29}Si SP lines, successful ^{29}Si CP and was a white powder.

Figure 5.10 shows ^{29}Si SP and CP spectra for kenyaite (sample kyb). Both were acquired with the CMX200 spectrometer, equipped with a Chemagnetics HX probe and 7.5 mm zirconia Pencil rotors. Standard pulse programs were used to acquire the decoupled single-pulse and cross-polarisation spectra: 1pda and cpflip, respectively. The former spectrum was acquired with 880 transients, a recycle time of 60 s and a spinning-rate of 2.01 kHz. The latter was acquired with 632 transients, a recycle time of 2 s, a contact time of 3 ms and a spinning rate of 2.01 kHz. Chemical shift and line-width details for these spectra are listed in table 5.6.

Experiment	Q^3		Q^4	
	δ_{Si} / ppm	$\Delta_{½}$ / Hz	δ_{Si} / ppm	$\Delta_{½}$ / Hz
Single-Pulse	-99.4	66	-107.7	47
			~110	sh‡
			-111.1	~60
			-113.2	63
			-118.5	~60
Cross-Polarisation	-99.4	75	-107.7	75
			-109.6	~60
			-111.2	~60
			-113.4	~60

Table 5.6 Chemical shifts and full peak-width at half height for ^{29}Si SP and CP spectra of kenyaite (sample kyb). ‡ shoulder.

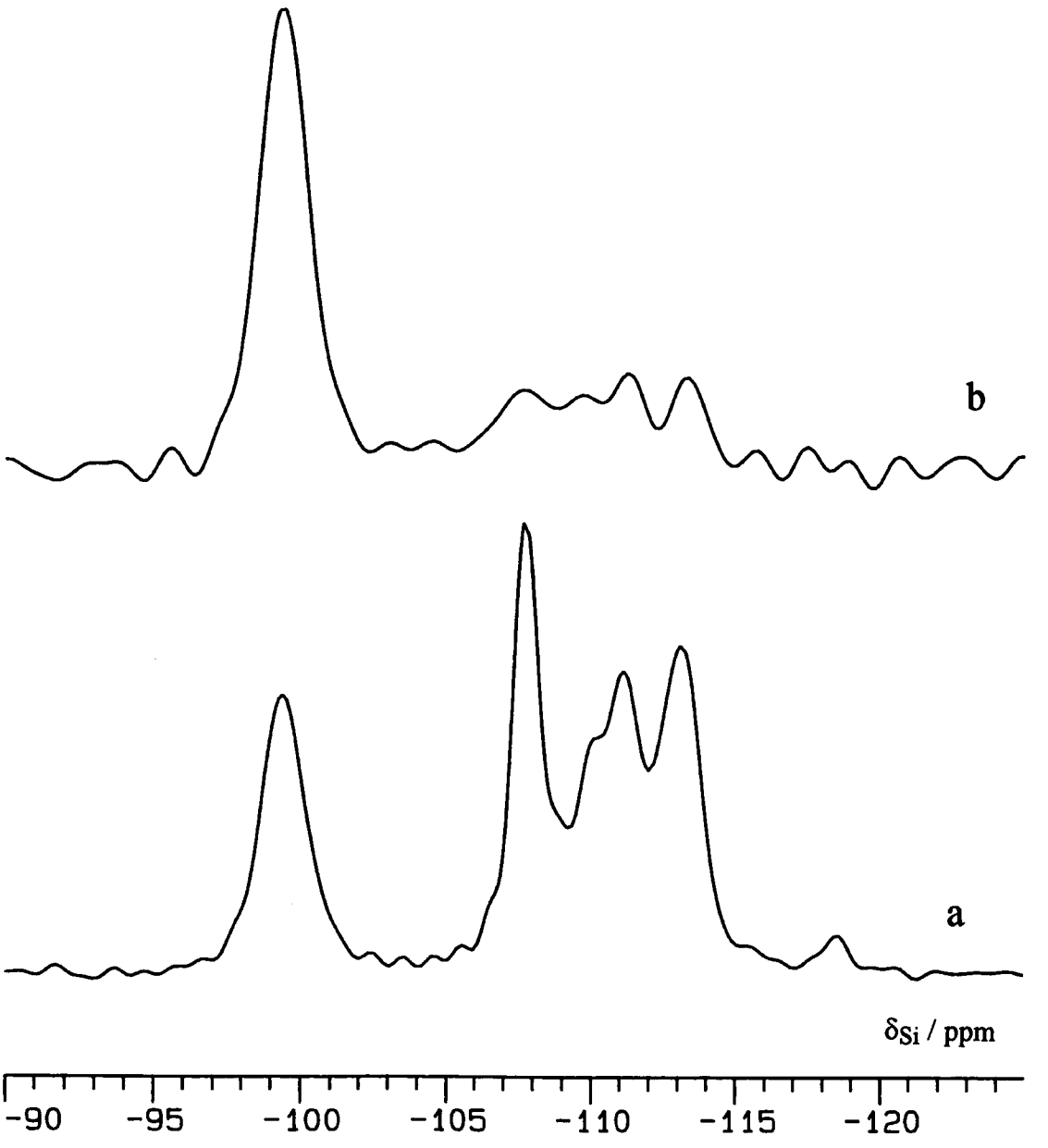

Figure 5.10 Kenyaite ^{29}Si MAS spectra (sample kyb): a) single-pulse; and b) cross-polarisation.

These results can be compared with those of Nesbitt,[1] who analysed three kenyaite samples, one of which gave high-quality ^{29}Si NMR spectra. An interesting result from his work was that the high-frequency Q^4 line, δ_{Si} -108.2, gave no signal on cross-polarisation with a contact time of 2 ms; this signal was assigned to a silicon site within the silicate layer with no neighbouring protons for cross-polarisation. Sample kyb has a similar spread of Q^4 chemical shifts as the Nesbitt sample, but the low-frequency line, δ_{Si} -107.7, gives a cross-polarisation signal. In this work it is the small, high-frequency, δ_{Si} -118.5, line which gives no signal on ^{29}Si CP.

Sample kyb was chosen for an attempt to estimate the Q^3:Q^4 ratio in kenyaite. Dailey and Pinnavaia[25] and Heidemann[26] have determined the Q^3:Q^4 ratio for magadiite. In both cases, the authors determined ^{29}Si spin-lattice relaxation times using inversion-recovery experiments before obtaining an unsaturated ^{29}Si SP spectrum with a recycle delay of five times the largest T_1-value. Such an experiment is a formidable undertaking in terms of spectrometer time (Heidemann took one month). Faster methods of determining T_1-values are available: the cross-polarisation method of Torchia, for example.[27] However, an approximate Q^3:Q^4 ratio can be determined by measuring the apparent value at different settings of the recycle delay. As the delay is increased, the spectra will become progressively less saturated and the measured value will get more accurate.

Single-pulse spectra for sample kyb were obtained using the CMX200 spectrometer with four values for the pulse delay. For each FID, 64 transients were acquired and the spinning rate was *ca.* 2 kHz. The spectra were given the same fourier-transformation, phasing and baseline-correction and the areas of the Q^3 and Q^4 absorptions were determined with the interactive integration routine of the CMXW spectrometer software. These areas are listed in table 5.7 and the results provide reasonable evidence that the ratio of Q^4 sites to Q^3 sites in kenyaite is as much as 5.

Recycle Time / s	Q^3 Area	Q^4 Area	Ratio
5	5.80	16.37	2.82
45	15.18	48.73	3.21
120	17.10	64.84	3.79
750	20.98	100.00	4.77

Table 5.7 Integrated areas from 4 kenyaite (sample kyb) spectra with varying recycle delays.

In summary, a single high-quality kenyaite sample was available for this work. The SP and CP spectra both contained a single Q^3 line and several of type Q^4. Some selectivity was observed on cross-polarisation, but not that reported by Nesbitt. The site-ratio has been determined approximately. It appears the ratio of Q^4 sites to Q^3 sites is 5:1.

5.1.9 The Effect of Drying Kanemite, Magadiite and Octosilicate

In this research, sample-dehydration has been used as a technique to obtain better-resolved ^{1}H MAS spectra and selective cross-polarisation mechanism results (see section 6.2 and chapter 7). Dried sample spectra have been obtained by storing and packing samples in a dry-box before immediate acquisition. The dry-box contained oxygen-free nitrogen circulating through P_2O_5 and Molecular Sieve 3A columns; relative humidity was <5 %. Because dehydration could have been a destructive process, it has generally been used where large quantities of sample were available. This was not the case for makatite or kenyaite.

The effect of this treatment can be investigated by comparing the ^{29}Si NMR spectra of samples before and after drying. Such spectra of representative kanemite, magadiite and octosilicate samples are shown in figure 5.11.

The spectra were acquired with the CXP200 spectrometer, equipped with a Doty MAS probe and 7 mm zirconia rotors. Spectra were acquired at the natural state of sample-hydration and after drying. A constant spinning-rate of 2.5 kHz was used for all these determinations; other experimental parameters are listed in table 5.8. The spectra are shown in figure 5.11. Chemical shift and line-width information may be found in table 5.9.

Silicate	Sample	Hydration	Number of Transients	Recycle Time / s	Contact Time / ms
Kanemite	knc	Undried	200	2	1
		Dried	1864	5	2
Octosilicate	occ	Undried	10653	5	0.75
		Dried	200	6	2
Magadiite	mgc	Undried	7000	1	0.8
		Dried	450	8	4.5

Table 5.8 Experimental Parameters for ^{29}Si CP spectra of representative kanemite, octosilicate and magadiite samples, before and after drying.

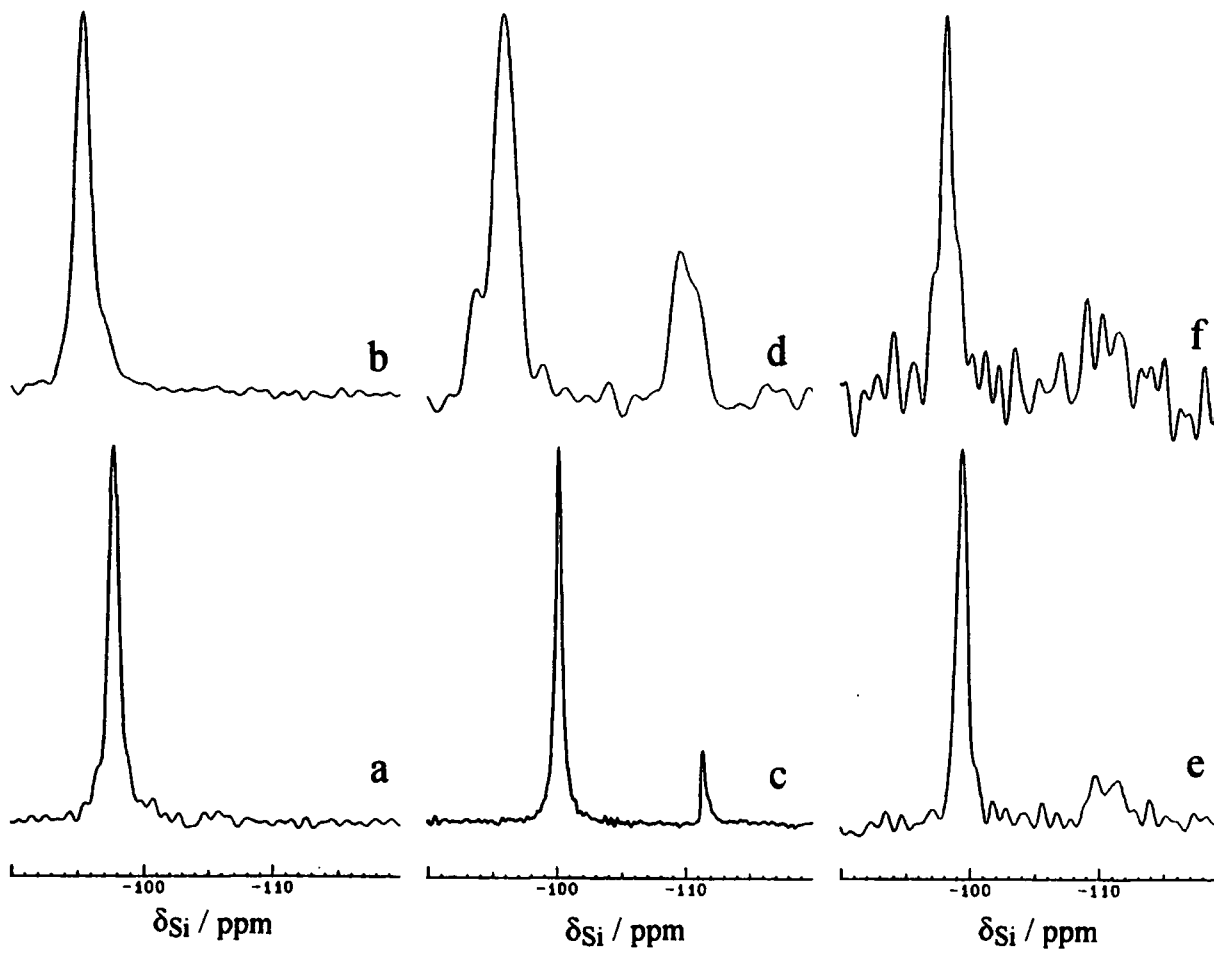

Figure 5.11 Silicon-29 CP spectra of three layered sodium polysilicate hydrates before and after drying: a) kanemite (kna); b) dried kanemite (kna); c) octosilicate (ocb); d) dried octosilicate (ocb); e) magadiite (mgc); and f) dried magadiite (mgc).

Silicate (sample)	Hydration	Q^3		Q^4	
		δ_{Si} / ppm	$\Delta_{½}$ / Hz	δ_{Si} / ppm	$\Delta_{½}$ / Hz
Kanemite (knc)	Undried	-97.6	40		
	Dried	-95.3	59		
Octosilicate (ocb)	Undried	-100.2	26	-111.5	19
	Dried	-96.0	90	-109.5	110
Magadiite (mgb)	Undried	-99.6	63	-109.9	~60
				-113.8	~80
	Dried	-98.4	43	-109.4	~50
				-111.1	~50
				-114.0	~80

Table 5.9 Chemical shifts and full peak-widths at half height for ^{29}Si CP spectra of kanemite, octosilicate and magadiite samples, before and after drying. The Q^4 signals for magadiite were small, so the line-widths were difficult to measure.

The first point that should be emphasised regarding these results is that the spectra do change as samples are dehydrated. For kanemite and octosilicate this involved a considerable shift to higher frequencies and broadening of the lines. With magadiite the changes are less dramatic.

At their natural state of hydration, the structures of these silicates will be stable and regularly arranged. Removing water will distort the silicate layers: bond angles and bond-lengths will change affecting the shielding around each silicon atom. Therefore, the chemical shift would be expected to change. The increase in line-widths might indicate that the distorted water-free structures are less regular– a wider range of shielding environments will broaden any lines. Structurally, magadiite is expected to have a thicker silicate layer than octosilicate or kanemite. This might distort less with changes in the interlayer species. Therefore, it is understandable that the ^{29}Si spectrum changes less on drying.

The important conclusion from these experiments is that the spectra of the dried species are similar to the those of the natural samples– the kanemite octosilicate

and magadiite spectra still contain one, two and several signals, respectively. Additionally, the changes are reversible. Therefore no gross structural changes have taken place with dehydration, and relating the results of further ^{1}H MAS or ^{29}Si CP experiments on dried samples to the layered sodium polysilicate hydrates in their natural state of hydration would be correct.

5.2 Hydrogen-1 NMR Spectra

5.2.1 Introduction

This section includes ^1H MAS spectra for the layered sodium polysilicate hydrates. In many cases, high-resolution spectra have been obtained, yielding important structural information. Such spectra have not been previously reported, though some less-informative CRAMPS and wide-line ^1H spectra were included in the work of Nesbitt[1] and Rojo *et al.*,[28] respectively. The proton species in the layered sodium polysilicate hydrates are of considerable importance. Many potential uses, such as catalysis or ion-exchange activity, depend on their nature. The aim of the work in this section is to obtain as much information as possible using ^1H NMR.

In general, mineral proton species can have many different forms.[29] Stoichiometric hydroxyl groups, water molecules and hydroxonium ions can form part of a crystal structure, while adsorbed water can also be present on the surface, in crystal faults or in macroscopic fluid inclusions. Additionally, Brönsted acid sites are important in aluminium-containing zeolites.

Makatite is known to contain molecular water and hydroxyl protons only.[16] Though single-crystal X-ray diffraction provides no proton information, the presence of these species can be inferred from the positions of oxygen atoms. Aqueous protons must be bonded to the water oxygens, $\underline{H}_2O$, while silanol protons cap some of the terminal oxygens, $\equiv Si\text{-}O\underline{H}$. A consideration of stoichiometry indicates that silanol and water protons are also likely to be present in the other layered sodium polysilicate hydrates. In each case, their soda:silica:water formulas can be re-written in the form of a sodium hydrogen silicate hydrate. For example, in magadiite, $Na_2O{:}14SiO_2{:}10H_2O$ is equivalent to $Na_2H'_2Si_{14}O_{29}.9H''_2O$, where protons H' and H'' represent silanol and water species, respectively.

Static ^1H NMR spectra of the layered sodium polysilicate hydrates tend to be broad, giving little information. However, as with many minerals, magic angle-

spinning can give well-resolved spectra to yield structurally significant information. The work in this section includes ^1H MAS NMR spectra for the layered sodium polysilicate hydrates. In some cases the resolution is further improved by careful sample-drying. Chemical shifts can be related to the types of species present, while the extent and shape of any spinning side-band manifolds can provide further information regarding the mobility and isolation of the proton species, together with a confirmation of the peak assignments.

Though NMR spectroscopy has proved an excellent method for investigating the layered sodium polysilicate hydrates, some supporting analysis is necessary. The water-content of a sample can be estimated by thermogravimetric analysis (TGA). Thus, the efficiency of the drying procedure can be measured.

5.2.2 Assignment of Proton Species in ^1H NMR Spectra

Engelhardt and Michel tabulated chemical shift ranges for zeolites.[4] The list assigns small chemical shift ranges to different proton types and implies that δ_H might be as instantaneously informative as δ_{Si} in the solid-state NMR of silicates and zeolites. The table includes species of no relevance to this work, such as ammonium ions and bridging hydroxo-groups, $N\underline{H}_4^+$ and Si-O<u>H</u>-Al, respectively, but it does limit the chemical shift range of terminal (silanol) protons, Si-O<u>H</u>, to between δ_H 0.5 and 2. Yesinowski *et al.* showed that this is not necessarily the case with a high-resolution ^1H MAS NMR study of several minerals, principally silicates.[29] In their work there was considerable overlap between the ranges of -Si-O<u>H</u> and $\underline{H}_2O$ absorption. Hydroxyl groups gave spectra with isotropic chemical shifts of between δ_H 0.7 and 4.3, while the silicate analcite, $NaAlSi_2O_6.H_2O$, contains stoichiometric water and had a chemical shift of δ_H 3.1.

Though the ^1H chemical shift is not an absolute indicator of proton type, spinning side-band patterns and other factors can aid assignment. Side-bands tend to be more extensive for water protons, when relatively immobile, with a characteristic

dip in signal intensity at the isotropic chemical shift (the manifold can have the appearance of a "Pake-doublet"). Eckart *et al.*[30] deconvoluted the ^1H MAS spectra of silicate glasses by fitting the side-band intensities as the sum of the patterns for two model compounds: tremolite, $Ca_2Mg_5Si_8O_{22}(OH)_2$, and analcite, $NaAlSi_2O_6.H_2O$. Kohn *et al.* used ^1H MAS NMR to study proton species in several hydrous silicate glasses.[31] Some of the spectra were very complex, but the authors managed to assign the signals to aqueous and hydroxyl proton species by consideration of chemical shifts, line-widths and spinning side-band spread. The 3.3 ppm chemical shift of suprasil, which contains protons solely as SiOH, was used as evidence for assigning low-frequency signals to silanol protons. With an additional consideration of line-widths, this evidence was used to assign hydrous silicate glass spectra with water peaks at δ_H 4.2, 4.5 and 4.7 and silanol peaks at δ_H 3.1, 3.2 and 4.3. The assignments seemed reasonable when compared with ^{29}Si NMR results. In the same study, spectra were acquired for various hydrous alkali and alkaline earth disilicate glasses. These contained two isotropic signals: lines at *ca.* δ_H 4 with extensive spinning side-bands were assigned to water protons, while the other signals at δ_H 11 to 17 were assigned to strongly hydrogen-bonded protons.

Proton chemical shifts are a good measure of the strength of hydrogen-bonding for an oxygen-bound proton. Experimental[32] and theoretical[33] studies have shown that there is a linear relationship between δ_H and the oxygen-oxygen bond distance, d(O-H···O). A short distance equates to strong hydrogen-bonding and a high isotropic chemical shift. Equation 5.4 was derived by Eckart *et al.*[30] from what they considered to be all the known trustworthy data; this covered a chemical shift range of δ_H 0-20 and a bond distance range of 240-310 pm.

$$\delta_H = 79.05 - 0.255.d(O\text{-}H\cdots O)/pm \qquad \text{Eq. 5.4}$$

Many silicates with strongly hydrogen-bonded protons have been reported. Rosenberger, Grimmer and co-workers studied the acid and basic hydroxyl groups in a

series of alkaline earth metal silicates using multiple-pulse ^1H NMR techniques (WAHUHA and WAHUHA with magic-angle spinning).[34,35,36] The acid species in $CaNaHSiO_4$ and BaH_2SiO_4 exhibited chemical shifts of δ_H 12.7 and 12.3, respectively. The O-H···O distances of these strongly H-bonded species are 2.53 to 2.55 Å– much shorter than the distances of the basic hydroxyl species they studied (d(O-H···O) > 3 Å, δ_H 2 to 4.1). Pectolite, $NaCa_2Si_3O_8(OH)$, was one of the minerals studied by Yesinowski *et al.*[29] The isotropic chemical shift, δ_H 15.8, corresponds to a strongly hydrogen-bonded proton with a short oxygen-oxygen distance– equation 5.4 predicts a value of 248 pm, which is very close to that determined by diffraction methods. The puckered layered silicate, $KHSi_2O_5$ is related to kanemite.[37] Two authors have published ^1H MAS NMR spectra of this silicate: Deng *et al.*[38] obtained a spectrum including a signal at δ_H 15.58 while Millar and Garces[39] reported a signal at δ_H 16.2. The protons in $KHSi_2O_5$ lie between silicate layer oxygen atoms separated by 2.489 Å,[40] and substituting this value into equation 5.4 gives the exact chemical shift that was reported by Deng *et al.* Kümmerlen *et al.* studied ^{29}Si CP characteristics of three sodium silicate glass samples.[41] These were found to contain strongly H-bonded protons– ^1H CRAMPS spectra contained signals at δ_H 12.0. Kohn *et al.* reported peaks at δ_H 12 and 17 for the alkali or alkaline earth disilicate glasses, $Na_2Si_2O_5.H_2O$(7.8 wt%) and $Sr_2Si_2O_5.H_2O$(4.7 wt%), respectively; a similar signal was found in $Ba_2Si_2O_5.H_2O$(3.2 wt%). Finally, Engelhardt and co-workers have reported high-frequency ^1H chemical shifts in the hydrosodalite, $Na_8[SiAlO_4]_6(OH)_2.2H_2O$, which contains an $H_3O_2^-$ ion.[42,43] The ion, [HO...H...OH]$^-$, has terminal and central protons which gave signals at δ_H -0.1 and δ_H 16.3, respectively.

5.2.3 Makatite and Kanemite

A single makatite sample was available for this work. The spectrum of this sample can be compared with those of two kanemite samples. The work has been carried out at two spectrometer frequencies and the spectrum of a carefully-dried kanemite sample has also been acquired.

Proton MAS spectra of the makatite and kanemite samples were acquired using the VXR300 spectrometer, equipped with a Doty MAS probe and 7 mm zirconia rotors. The spectrometer was tuned to give a 90° pulse-duration of 4 μs. Adequate pulse-durations, recycle delays and acquisition times were used to avoid truncation of the FID's or saturation of the spectra. All spectra were acquired with a standard single-pulse sequence; table 5.10 lists further experimental details. These spinning rates will give side-bands at *ca.* 17 ppm from the centre-bands. Figure 5.12 displays the spectra, while chemical shifts and line-widths are listed in table 5.10. Baseline-correction has been used to improve the appearance of the spectra.

Sample	Label	Number of Transients	Pulse-Duration / °	Acquisition Time / ms	Spinning Rate / kHz
Makatite	mka	1000	90	9.9	4.9
Kanemite	kna	1000	90	19.8	4.9
Kanemite	knb	500	68	9.9	4.85

Table 5.10 Experimental details for the spectra in figure 5.12.

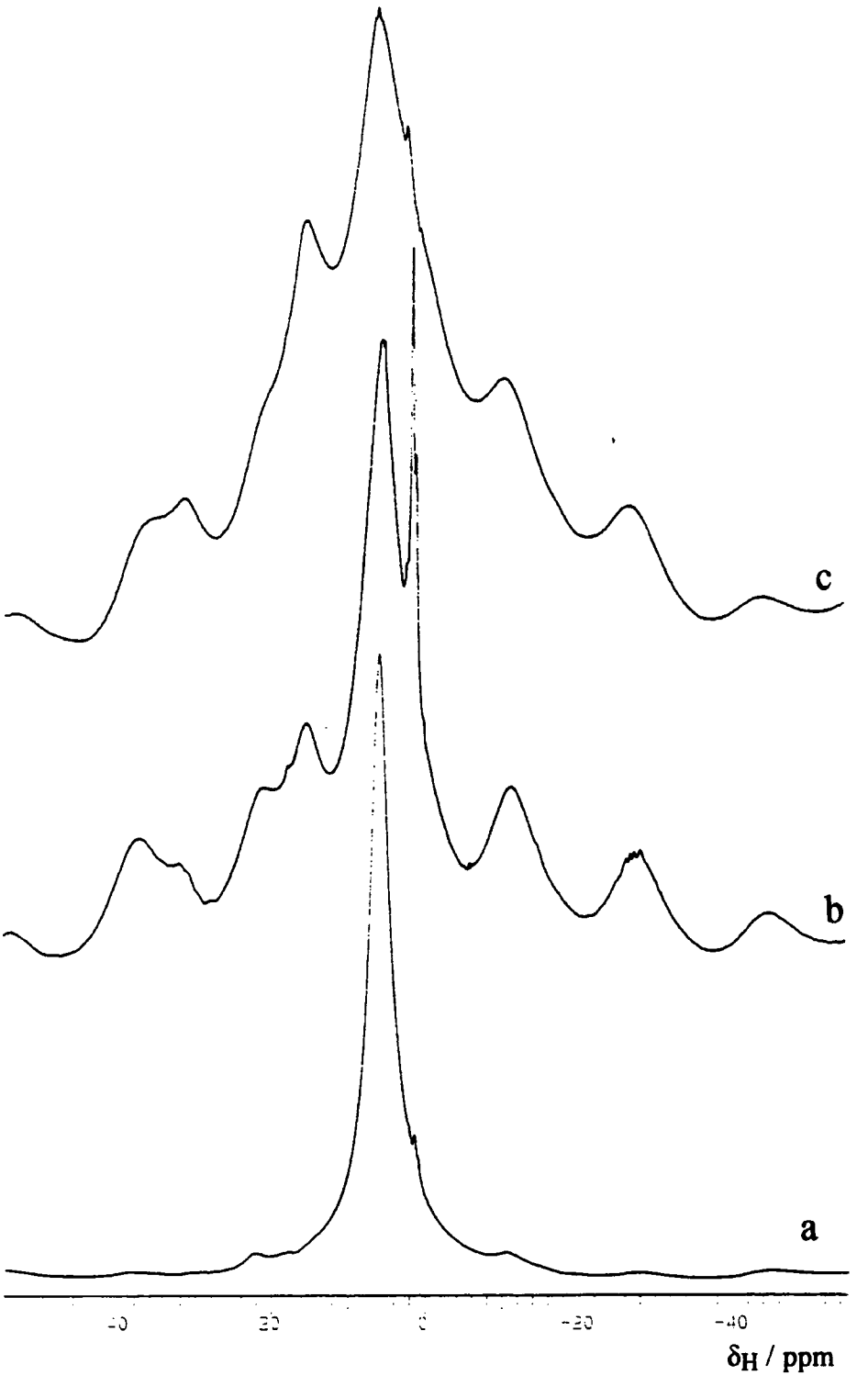

Figure 5.12 Three 300 MHz ^1H MAS NMR at a spinning rate of *ca.* 5 kHz: a) Makatite (mka); b) Kanemite (kna); c) Kanemite (knb).

Similar experiments were attempted using a spectrometer frequency of 200 MHz. The resulting spectra were broad, featureless and indistinguishable from the background absorption, even at spinning rates of 4-5 kHz. However, the spectrum of carefully-dried kanemite (sample knc) is interesting. It was acquired using the CXP200 spectrometer, equipped with a Doty MAS probe. The sample was packed in a 7 mm zirconia rotor with a close-fitting kel-F end-cap. Sixty-four transients were acquired with a recycle time of 1 s; the spinning rate was 4 kHz. The spectrum is shown in figure 5.13.

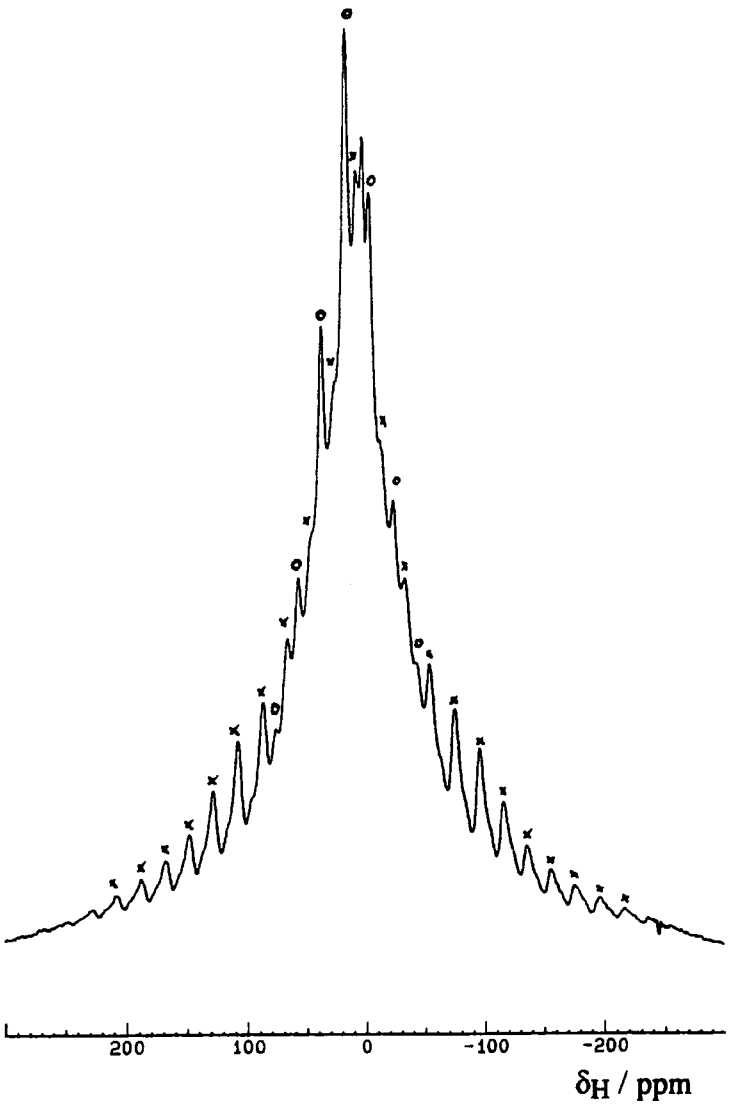

Figure 5.13 A 200 MHz ^{1}H MAS spectrum of dried kanemite (sample knc). Spinning side-bands are identified by circles (δ_{iso} = 15.5 ppm) and crosses (δ_{iso} = 6.7 ppm).

Silicate	Sample	δ_H / ppm	$\Delta_{1/2}$ / Hz
Makatite	mka	5.8	1000
Kanemite	kna	14.8	2000
		5.1	2000
		1.2	50
Kanemite	knb	14.4	2000
		4.8	3000

Table 5.11 Proton chemical shifts and line-widths (full-widths at half height) for makatite and two kanemite samples (Transmitter frequency = 300 MHz). Weak, sharp peaks have been ignored.

Assigning the makatite spectrum is straightforward as there is only one significant signal. This corresponds to silanol and aqueous proton species that are exchanging rapidly over the time-scale of the NMR experiment. This exchange must be less significant with the two kanemite samples as more than one peak is observed, in each case, at 300 MHz. Both samples contain a peak around δ_H 15, attributable to strongly hydrogen bonded protons. There is a much larger signal at δ_H 5, which can be assigned to water protons. The relative intensities of the peaks are consistent with the known formula of kanemite, $NaH_{sil}.Si_2O_5.3(H_{aq.})_2O$, where there are six water protons per silanol. The water protons have a more extensive manifold of spinning side-bands than the silanol protons– the theoretically-predicted and experimentally-observed trend described by Yesinowski *et al.*[29] Therefore, it is likely that the peak assignments are correct. There is an additional signal in the spectrum of kanemite (sample kna), with a chemical shift that is typical of non-H-bonded silanol protons. This line is appreciably sharper than the others in the spectrum; the relevant proton species must experience weaker line-broadening interactions than the other species. This kanemite sample has a ^{29}Si NMR spectrum with two signals whereas the spectrum of the other sample (knb) has only one. Chapter 7 includes ^1H,^{29}Si

correlation experiments, which provide further information regarding the differences in the ^{1}H spectra of these samples.

The spectrum of dried kanemite (sample knc) contains isotropic signals at δ_H 15.5 and 6.7, corresponding to hydrogen-bonded and water protons, respectively. Since these are weak signals, there is a significant background contribution which is responsible for the curved base-line and a sharp line at δ_H 1.2. The H-bonded proton signal has three pairs of spinning side-bands, which get weaker with their separation from the centre-band. Approximately ten pairs of spinning side-bands are visible for the water proton, covering about 80 kHz. Since the most intense lines are observed at 20 KHz from the centre-band, the spinning side-band manifold would have the shape of a Pake doublet. The reason for such a shape will be further discussed with respect to the ^{1}H MAS spectra of octosilicate (see section 5.2.4).

A strong magnetic field, corresponding to a spectrometer frequency of 300 MHz, was necessary for the acquisition of resolved spectra. It can be assumed that the peaks at 200 MHz were too broad for detection, indicating that the line-widths decrease as the magnetic field increases. Yesinowski *et al.*[29] observed that such behaviour could occur for protons with strong dipolar coupling to nuclei experiencing second order quadrupolar interactions (^{27}Al was cited as an example; in this case the nuclei would be ^{23}Na, where second-order effects are observed with these samples). Since ^{23}Na CP signals are observed for both makatite and kanemite, there must be some ^{1}H,^{23}Na dipolar coupling.

In summary, at a spectrometer frequency of 300 MHz, only one ^{1}H MAS signal is observed with makatite, corresponding to rapidly exchanging silanol and water protons. More signals are observed in kanemite ^{1}H MAS spectra, including a high-frequency resonance that is typical of strongly hydrogen-bonded protons and a signal that can be assigned to water. An extra peak is visible at *ca.* δ_H 1 in a single kanemite sample. Apart from a dried kanemite sample, 200 MHz spectra were broad and featureless.

5.2.4 Octosilicate

During the course of this work many octosilicate ^1H MAS spectra have been acquired under conditions of ambient temperature, a readily achievable spinning rate and normal sample-hydration. In this section, a representative spectrum of this sort will be compared with spectra acquired at a lower temperature, with faster sample-rotation and after careful drying. The results will be used to characterise and quantify the proton species in octosilicate.

Figure 5.14 shows four octosilicate ^1H MAS spectra. These were acquired with four probes, three spectrometers and two samples: the VXR300 spectrometer had a variable-temperature facility; spinning rates of up to 18 kHz were possible with a Chemagnetics HF probe; and the 7 mm zirconia rotors for a Doty MAS probe had close-fitting end-caps which were ideal for testing dried samples. Experimental details are listed in table 5.12. Chemical shift, line-width, and peak integration information is listed in table 5.13.

Spectrum	Sample	Spectro-meter	Probe Rotor	Freq. / MHz	Number of Transients	Recycle Delay / s	Spinning Rate / kHz
Standard	occ	CMX200	HX 7.5 mm	200.13	32	2	4.00
High-Speed	occ	CMX200	HF 4 mm	200.13	8	2	16
-60 °C	ocb	VXR300	Doty 5 mm	299.949	256	0.5	8.43
Dried Sample	ocb	CXP200	Doty 7 mm	200.13	16	3	4

Table 5.12 Hardware details and acquisition parameters for octosilicate ^1H MAS spectra.

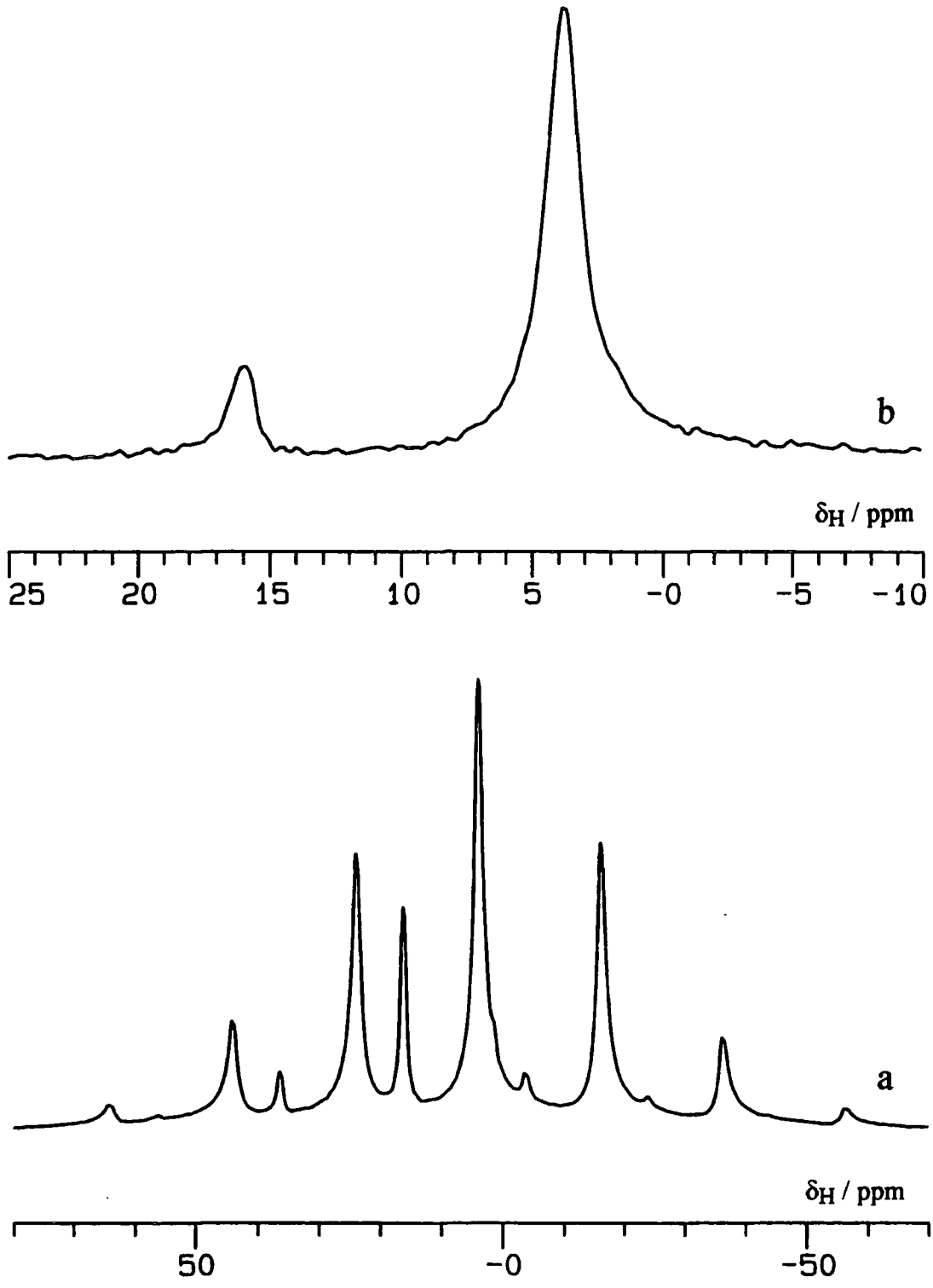

Figure 5.14 Four octosilicate ^{1}H MAS spectra: a) undried sample occ, ambient probe temperature, 4 kHz spinning rate; b) undried sample occ, ambient probe temperature, 16 kHz spinning rate. It should be noted that the spectra are plotted with different chemical shift ranges.

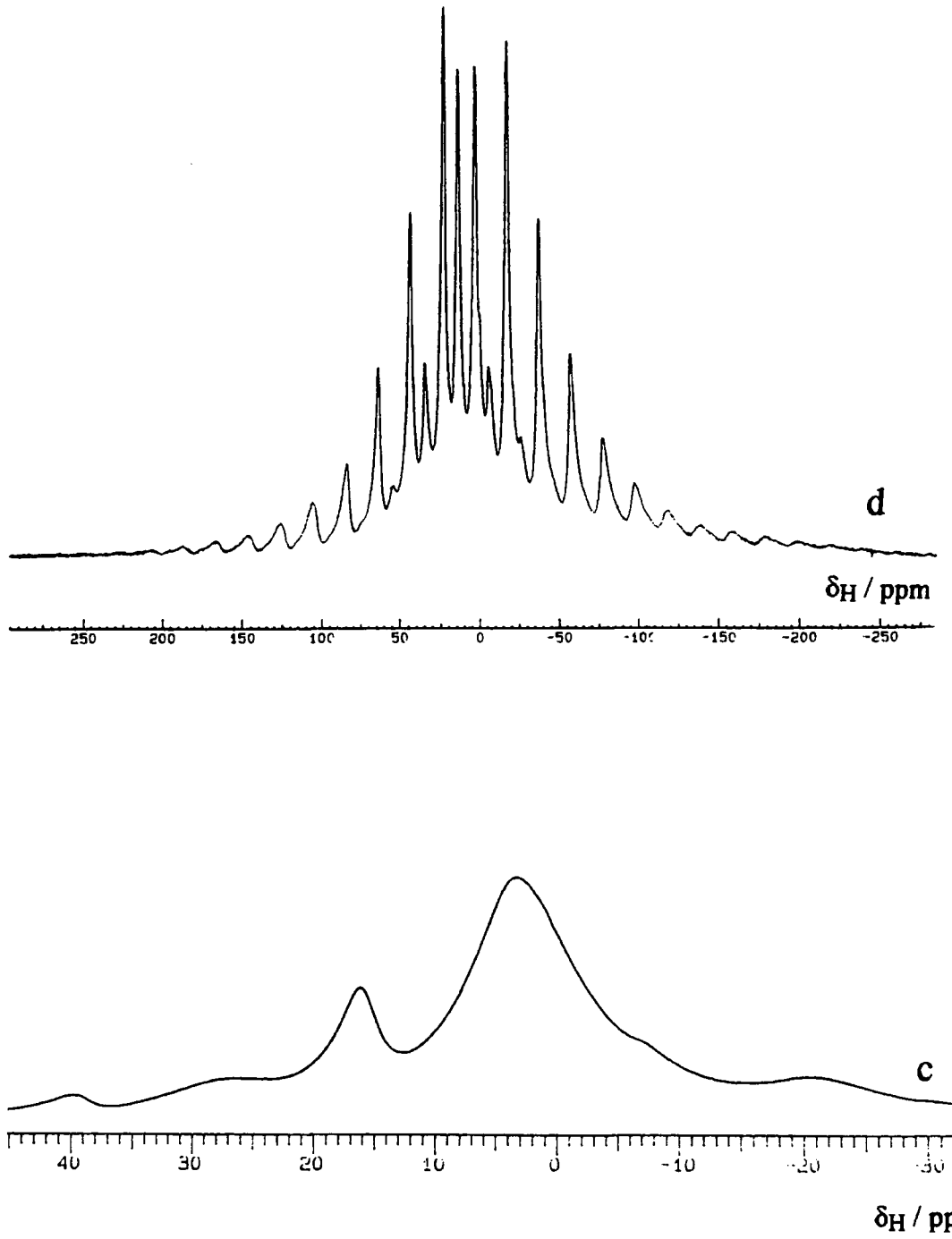

Figure 5.14 Four octosilicate ^1H MAS spectra (continued): c) undried sample ocb, -60 °C, 8.43 kHz spinning rate; d) dried sample ocb, ambient probe temperature, 4 kHz spinning rate. It should be noted that the spectra are plotted with different chemical shift ranges.

Experiment	Sample	δ_H / ppm	$\Delta_{1/2}$ / Hz	Integration	Number of visible Side-Bands
Standard	occ	16.0 3.6	260 390		4 8
High-Speed	occ	16.0† 3.8†	220 300	100.00 12.86	0 0
-60 °C	ocb	16.3 3.4	1500 3000		2 2
Dried Sample	ocb	14.7 3.2	120 140		6 20

Table 5.13 Results of four octosilicate ^1H MAS experiments. The table lists proton chemical shifts, peak-widths at half height, peak integrals for the side-band free spectrum only and the number of visible spinning side-bands. †These peaks were referenced by setting the high-frequency signal to 16 ppm; all other signals were referenced to TMS using secondary references, if necessary.

The ambient temperature spectrum of an undried sample with a spinning rate of 4 kHz (figure 5.14a) is typical of octosilicate; it has been repeated many times for three samples with similar results. The spectrum contains two signals at δ_H 16.0 and 3.6. The high-frequency signal corresponds to strongly hydrogen-bonded protons. A short oxygen-oxygen distance of 247 pm can be predicted using the linear relationship of Eckart *et al.*,[30] equation 5.4. The integrated ratio of the two signals from the high spinning rate spectrum (figure 5.14b) can be used to further assign the strongly and weakly H-bonded peaks to hydroxyl and aqueous protons. The structural formula of octosilicate can be written as $Na_2H_2Si_8O_{20}.8H_2O$ with a silanol:water proton ratio of 1:8; this is very close to the observed ratio of 1:7.78.

Several spinning side-bands are observed with a spinning rate of 4 kHz for octosilicate at ambient probe temperature. In general, side-bands are observed when magic-angle spinning partially averages inhomogeneous interactions. In octosilicate, such interactions will arise from heteronuclear dipolar coupling to silicon, oxygen and

sodium nuclei, while chemical shift anisotropy and the presence of paramagnetic impurities might also be significant. Though it generally causes homogenous interactions, homonuclear dipolar coupling can also lead to spinning side-bands in certain cases.[44]

The isotropic line is less intense than the first order side-bands for the water signal spinning side-band manifold in the dried octosilicate ^{1}H MAS spectrum. This follows the recognisable shape of a Pake doublet, which is typical of samples with isolated water molecules– the two protons behave as a two-spin system where the dominant interaction is homonuclear dipolar coupling. Such behaviour has also been reported for gypsum, $CaSO_4.2H_2O$, and analcite, $NaAlSi_2O_6.H_2O$.[29] The side-band manifold for an undried octosilicate sample is less extensive and more regularly shaped– the isotropic line is most intense. The water molecules are less isolated in this wetter sample and interactions or exchange with protons in other molecules must also be significant.

The spinning side-bands for the octosilicate silanol protons are less extensive than for the water protons. The homonuclear dipolar interaction will be weaker because the species do not have such close neighbouring proton species. Other interactions could be important, such as heteronuclear coupling to sodium or silicon and chemical shift anisotropy. In octosilicate, the former is likely– dipolar coupling between ^{29}Si or ^{23}Na nuclei and H-bonding protons has been observed by several cross-polarisation experiments (see chapter 7). The spinning side-band manifolds of the H-bonding protons in octosilicate are typical of species containing protons in hydroxyl groups, such as datolite and pyrophillite.[29]

Magic-angle spinning is ineffective in narrowing the broad lines observed in the -60 °C octosilicate spectrum. The broadening can be attributed to homogeneous interactions from homonuclear dipolar coupling which can not be averaged by MAS at available spinning-rates. Homonuclear dipolar coupling between two water molecule protons is only inhomogeneous if the two spins have equal chemical shift tensors.[44] Though this is not the case for rigid molecules, it is known that water molecules can

exchange in gypsum and other crystal hydrates at room temperature.[45] This is rapid with respect to the NMR time-scale and results in an averaging and equalisation of the two spin tensors. This or similar motion must be present at room-temperature for octosilicate where MAS is effective, but not at -60 °C. It had been predicted that cooling of gypsum would freeze out the motion to give broad lines even under MAS;[29] this behaviour has now been observed with octosilicate.

In summary, the ^1H MAS NMR spectrum of octosilicate contains two signals at δ_H 16 and δ_H 3.5 which can be confidently assigned to strongly hydrogen-bonded protons and water, respectively. The assignment can be confirmed by considering the spinning side-band manifolds and the integrated ratios of the two lines as well as their chemical shifts. If a large spinning speed is used, the spinning side-bands disappear and the peaks can be integrated accurately to give a ratio that is close to that predicted from the formula of octosilicate. The side-band manifolds of the water and silanol peaks are typical of spectra obtained from minerals containing solely water species or hydroxyl species, respectively. This is particularly true for the water signal in a dried sample.

Two pieces of structural information have been obtained from this study. Firstly, a chemical shift of 16 ppm indicates that the oxygen-oxygen distance of the atoms surrounding the H-bonding proton must be close to 247 pm. Secondly, the water molecules are unlikely to be rigid at room temperature because the relevant signal is broken up into spinning side-bands.

5.2.5 Magadiite

In the work described in this section, several ^1H MAS spectra of magadiite have been acquired. As with octosilicate, the techniques of high-speed MAS and sample drying can be used to provide better spectral resolution.

Five magadiite samples, 2 spectrometers and three probes have been used in this work. Spectra have been acquired for sample mga at spinning rates of 4 kHz and 15.5 kHz, using the CMX200 spectrometer with Chemagnetics HX and HF probes, respectively. Both probes use zirconia Pencil rotors with outside diameters of 7.5 mm (HX) and 4 mm (HF). Four samples (mgb, mgc, mge and mgf) have been analysed before and after storage in a dry-box. The CXP200 spectrometer was used for this work, equipped with a Doty MAS probe and 7 mm zirconia rotors with close-fitting kel-F end caps. Experimental details are listed in table 5.14 and the spectra are shown in figures 5.15 and 5.16. Chemical shifts are listed in table 5.15.

	Sample	Hydration State	Spinning -rate / kHz	Number of transients	Recycle time / s	Spectrometer /Probe
1	mga	not dried	4	16	2	CMX200/HX
2	mga	not dried	15.5	32	2	CMX200/HF
3	mgb	not dried	4	16	1	CXP200/Doty
4	mgb	dried	4	32	1	CXP200/Doty
5	mgc	not dried	4	4	1	CXP200/Doty
6	mgc	dried	4	16	1	CXP200/Doty
7	mge	not dried	4	16	1	CXP200/Doty
8	mge	dried	4	16	5	CXP200/Doty
9	mgf	not dried	4	16	1	CXP200/Doty
10	mgf	dried	4	16	1	CXP200/Doty

Table 5.14 Experimental details for ten magadiite ^1H MAS spectra: sample mga has been analysed at two spinning-rates, while the other four samples have been analysed before and after storage in a dry-box.

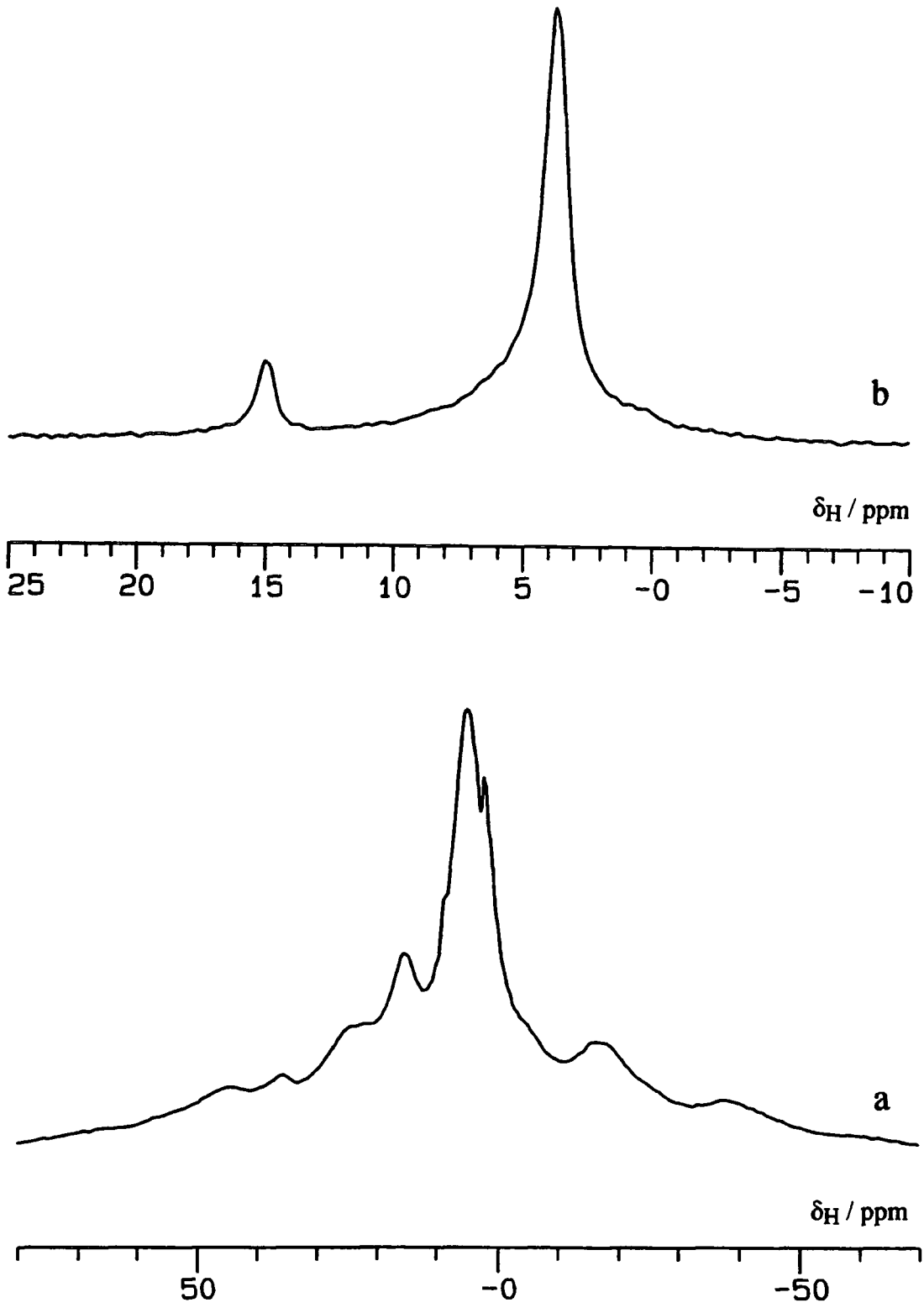

Figure 5.15 Two ^{1}H MAS spectra of magadiite (sample mga) at different spinning rates: a) 4 kHz; and b) 15.5 kHz. It should be noted that the spectra are plotted with different chemical shift ranges.

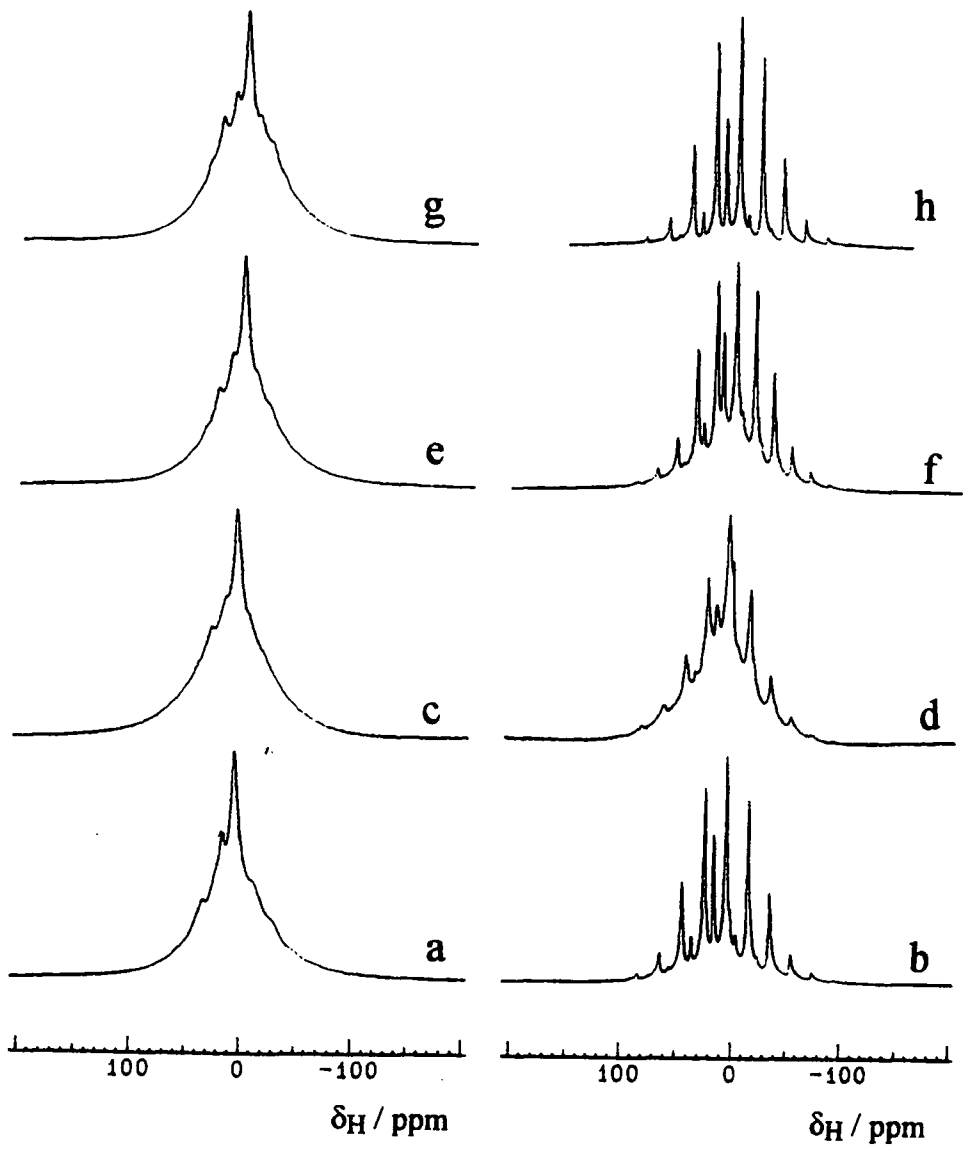

Figure 5.16 Eight magadiite ^{1}H MAS spectra of four different samples, before (left) and after (right) drying: a) undried sample mgb; b) dried sample mgb; c) undried sample mgc; d) dried sample mgc; e) undried sample mge; f) dried sample mge; g) undried sample mgf; h) dried sample mgf.

	Sample	Hydration	Spinning -Rate / kHz	δ_H / ppm	
1	mga	undried	4	15.0	5.0
2		undried	15.5	15†	3.8†
3	mgb	undried	4	15.1	5.2
4		dried	4	15.2	3.7
5	mgc	undried	4	14.0	5.3
6		dried	4	14.7	3.8
7	mge	undried	4	14.7	5.1
8		dried	4	15.2	3.7
9	mgf	undried	4	15.1	5.1
10		dried	4	15.2	3.7

Table 5.15 Chemical shift information for the ten magadiite ^1H MAS spectra shown in figures 5.15 and 5.16. † All other chemical shifts were referenced to an external standard (TMS at δ_H 0); these chemical shifts were obtained by setting the H-bonding signal to δ_H 15.

The spectra in figures 5.15 and 5.16 for undried magadiite samples at readily-achievable spinning rates contain a broad background signal from the probe (see figure 7.25a). The drying and fast-spinning techniques give spectra with a less significant background contribution.

Though the spectra are poorly resolved, two isotropic lines are evident: a strong signal at δ_H 5 and a shoulder at δ_H 15. When the samples are dried, the spectra look very similar to ^1H MAS spectra of undried octosilicate. With octosilicate, chemical shifts, spinning side-band manifolds and relative peak intensities were used to assign the signals. Similar reasoning can be used for magadiite: the more intense signals at δ_H 5, with more extensive spinning side-bands, are from water protons; and the less intense signals at δ_H 15, with fewer spinning side-bands, are from strongly H-bonded silanol protons.

The H-bonding chemical shifts are less positive than in octosilicate, corresponding to longer oxygen-oxygen distances: values of 251-252 pm can be predicted using equation 5.4. This bond-distance had to be estimated from the chemical shifts of the dried sample spectra, as the resolution of the undried sample spectra was too poor for accurate determination of the high-frequency chemical shifts.

Fast spinning provided a spectrum with two sharp lines; these could be integrated, indicating that the ratio of water protons to H-bonded protons is 9.5:1. This is close to the expected value of 9:1 (for $Na_2O{:}14SiO_2{:}10H_2O$ or $Na_2H_2Si_{14}O_{29}.9H_2O$). The resolution is better in this spectrum as the lines are slightly sharper. There is also less background contribution as all the peak intensity is concentrated at the isotropic chemical shift, rather than being spread out among several orders of spinning side-bands.

Drying magadiite sharpens the peaks in the ^1H MAS spectra. The line-widths vary from *ca.* 400 Hz (sample mgf) to *ca.* 800 Hz (sample mgc). It is feasible that this is due to different degrees of hydration. However, the line-width of the dried sample does correlate with the line-widths of the undried sample. Therefore, it is more likely that the variation can be attributed to the quality of the original sample, in terms of crystallinity or paramagnetic contamination, for example. The background absorption is relatively less intense in spectra with sharper lines.

Dried magadiite ^1H MAS spectra can be very similar to those of undried octosilicate. Since the major effect of storage in a dry-box should be a removal of water molecules, the difference between the spectra of undried magadiite and octosilicate can be attributed to extra water molecules in the interlayer space.

In summary, two proton species have been identified in magadiite: water and strongly hydrogen-bonded protons. These can be quantified with a spectrum acquired with a high spinning rate and occur in approximately the ratio that is predicted by the formula of magadiite. Drying magadiite produces a spectrum which is fairly similar to that of undried octosilicate.

5.2.6 The Thermal Behaviour of Magadiite

The thermal behaviour of magadiite was investigated with a single magadiite sample which was heated with increasing severity, in terms of temperature and time. After each step, ^1H MAS spectra were acquired. These can be compared with spectra of the same sample before the heating. The reversibility of the changes was investigated by analysing the heated sample after it had been stored at ambient temperature for two months.

Proton NMR was chosen for this investigation for two reasons. Firstly, spectra could be acquired quickly– about 10 minutes after the sample was removed from the oven. This minimised the possibility of changes in the sample over the course of the analysis. Secondly, the heating process is expected to remove water and ^1H is the logical nucleus for monitoring such changes.

Several ^1H MAS spectra of magadiite (sample mgb) were acquired using the CXP200 spectrometer, equipped with a Doty MAS probe and 7 mm zirconia rotors with close-fitting kel-F end-caps. Spectra were acquired after three heating stages: 100 °C, for ten minutes; 100 °C, overnight; and 200 °C, overnight. The sample was heated by placing an open vessel, containing *ca.* 1 g of magadiite, in an oven. A rotor was packed on removal of the sample from the oven and a spectrum was acquired immediately. In each case, 16 transients were acquired, with a recycle time of 1 s. A further spectrum was acquired after the sample had been stored at ambient temperature for two months: 32 transients were acquired with a recycle time of 1 s. The spectra are shown in figures 5.17 and 5.18. Chemical shifts and line-widths are listed in table 5.16.

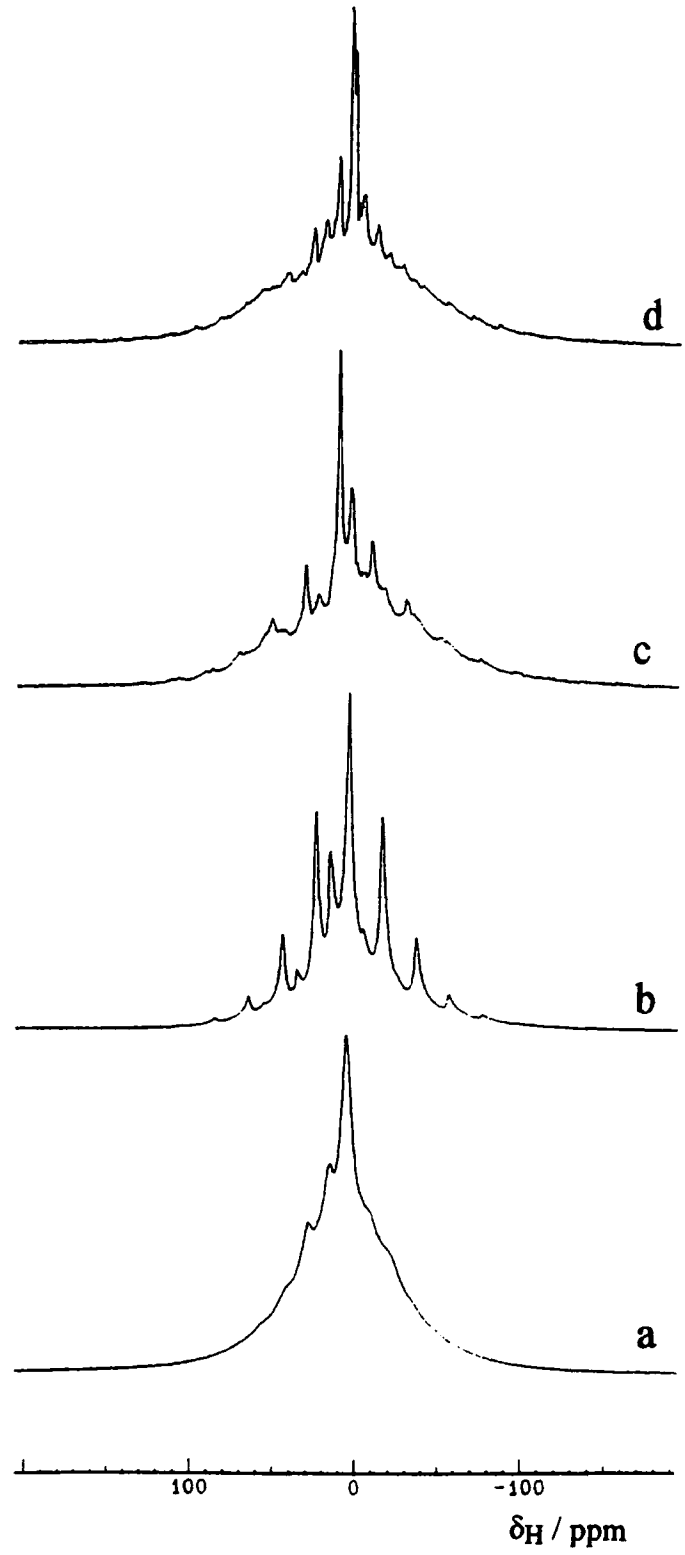

Figure 5.17 The variation in ^{1}H MAS spectra on heating magadiite (sample mgb): a) before heat-treatment; b) after being heated for 10 minutes in a oven at 100 °C; c) after being heated overnight at 100 °C; and d) after being heated overnight at 200 °C.

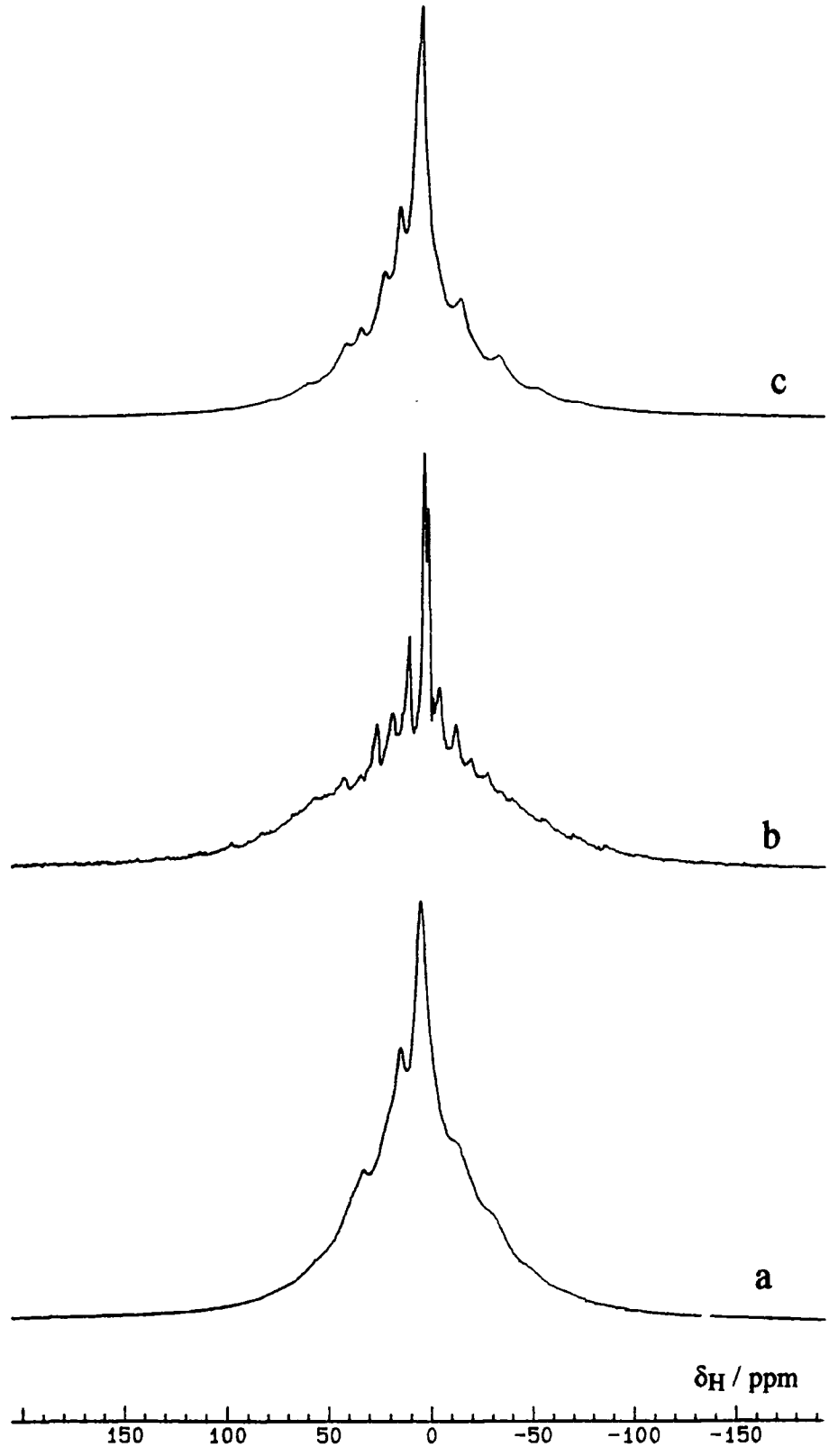

Figure 5.18 The reversibility of heating magadiite. Three ^{1}H MAS spectra of magadiite (sample mgb): a) before heat treatment; b) after being heated overnight at 200 °C; and c) after further storage at ambient temperature for 2 months.

Heating Stage	Chemical Shift, δ_H / ppm	Line-Width†, $\Delta_{1/2}$ / Hz
Before Heating	15.1 5.2	2000
10 minutes at 100 °C	14.9 3.6	1200
Overnight at 100 °C	10.6 2.8	800
Overnight at 200 °C	10.6 3.0	600
After 2 months	14.7 3.5	2000

Table 5.16 Chemical shift and line-width information for a ^1H MAS investigation into the thermal behaviour of magadiite (sample mgb). † Full-widths at half peak height; in general, these were difficult to measure for the high-frequency signal.

The spectrum before any heating (figure 5.17a) is typical of magadiite. It contains two lines from water and strongly hydrogen-bonded magadiite protons and a strong, broad signal from the probe background (see figure 7.25a). A sharp component of the proton background is visible as a shoulder on the isotropic water proton line. Placing the sample in a hot oven for just ten minutes has a large effect. The lines sharpen in exactly the same way as they do when magadiite is stored in a dry-box. Larger changes occur with more extensive heating: overnight heating at 100 °C results in a shift in the frequency of the H-bonding proton signal, corresponding to an increase in the oxygen-oxygen distance of the hydrogen-bond (a change from 250 pm to 268 pm can be estimated using equation 5.4). Overnight heating at 200 °C gives a spectrum with a very weak signal, where the sharp proton background signal is clearly visible.

The reversibility of these heat treatments can be seen from figure 5.18. Heating overnight at 200 °C changes the ^1H MAS spectrum of magadiite

considerably, but the spectrum reverts to that of a typical magadiite sample after storage at ambient temperature. These spectra imply that changes with heating up to 200 °C are reversible.

Heating magadiite could result in two reactions: loss of water and condensation of silanol protons. Two factors imply that storing magadiite at 200 °C resulted in a loss of water molecules only. Firstly, the changes in the ^{1}H MAS spectrum were reversible, which would be expected if heating only varied the structural water content in magadiite. It is less likely that condensed silanol groups would reform. Secondly, hydrogen-bonding signals are visible in all the spectra. Thermogravimetric analysis shows that this is a reasonable conclusion (see section 5.2.8, where layered sodium polysilicate hydrate thermal behaviour will be discussed in more detail).

5.2.7 Kenyaite

Only two kenyaite samples were available for analysis and one of these was of doubtful quality. Straightforward ^1H MAS spectra of each sample were obtained, but neither sample-drying nor high-speed MAS were attempted.

Proton MAS spectra for kenyaite (sample kya) were acquired at two magnetic fields (corresponding to transmitter frequencies of 200 MHz and 300 MHz). In both cases the spectrum contained two lines, at *ca.* 15 ppm and *ca.* 5 ppm. However, the lines were broad and there were extensive spinning side-bands. Since the sample was green, it was assumed that the spectrum was heavily-influenced by the presence of paramagnetic contaminants and will not be considered further.

Kenyaite (sample kyb) was analysed using the CMX200 spectrometer, equipped with a Chemagnetics HX probe and 7.5 mm zirconia Pencil rotors. A ^1H MAS spectrum was acquired with 16 transients and a recycle time of 1 s; the spinning rate was 4.98 kHz. It should be noted that in this experiment more effort was made to eliminate the presence of broad background signals (by varying acquisition parameters such as the spinning-rate, dwell-time and dead-time) than was the case with the magadiite spectra shown in figures 5.15, 5.16, 5.17 & 5.18. The spectrum is shown in figure 5.19 with two lines at δ_H 15.1 and 4.8.

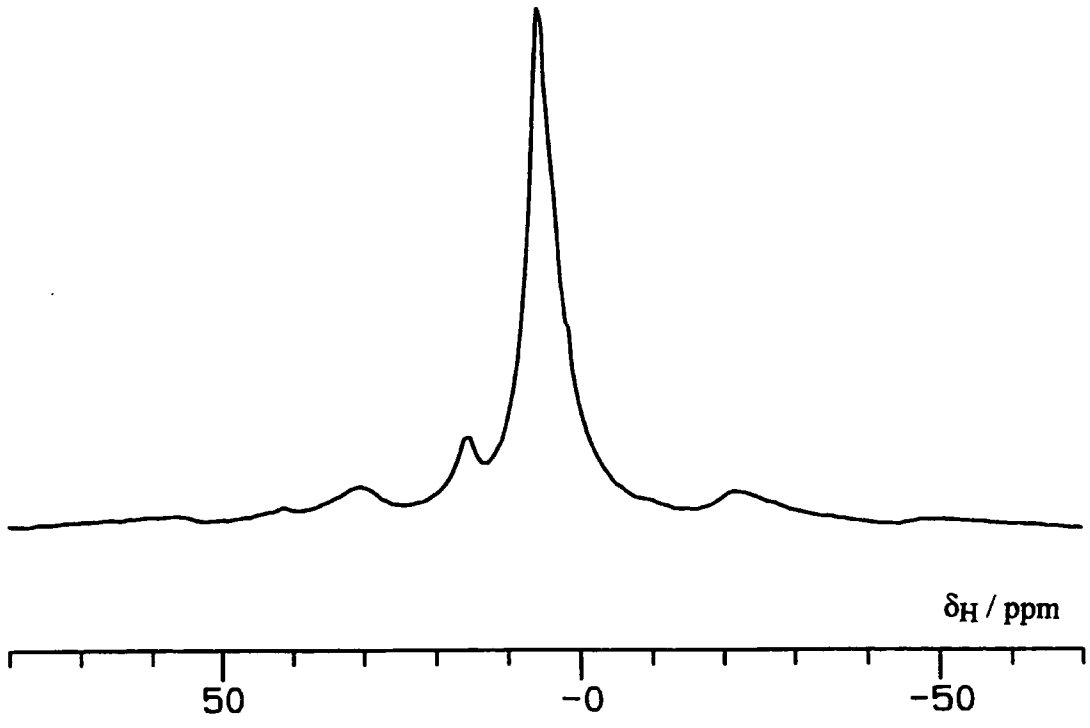

Figure 5.19 A ^{1}H MAS spectrum of kenyaite (sample kyb).

The ^{1}H MAS spectrum is fairly similar to magadiite. It consists of an intense water absorption, at δ_H 4.8, and a signal at δ_H 15.1 which can be attributed to strongly hydrogen-bonded protons. The peaks have been assigned in the same way as those for magadiite. There are spinning side-bands surrounding both signals; these are more extensive for the water proton. The chemical shift of the H-bonded protons can be related to an -O-H-O- bond-distance of 252 pm, using equation 5.4.

5.2.9 Thermogravimetric Analysis

Thermogravimetric analysis (TGA) is a useful analytical technique to support conclusions from ^1H NMR because it can quantify the amount of hydrous species in a sample. If a layered sodium polysilicate hydrate is heated it can lose all its protons as water molecules, while the associated change in mass is monitored. TGA can also distinguish between proton species by the different temperatures at which they are removed.

The experiment results in a plot of weight versus temperature. A differential plot (rate of weight-loss against temperature) can be useful, where events will be seen as peaks, with a maximum at the transition temperature. The exact value of this temperature is of limited use as it can vary greatly, depending on the atmosphere surrounding the sample or its mass; both cases affect the rate at which water is emitted or re-adsorbed. Useful information can be obtained from the overall weight-loss. Providing the sample is heated slowly enough to an adequate temperature, this value can be related to the total amount of water in the sample. TGA has also been used to estimate the efficiency of the standard drying procedure that has been used in this work.

A single sample of each of the layered sodium polysilicate hydrates underwent thermogravimetric analysis, using a Perkin-Elmer TGA7 machine. In each case, a weighed amount (1.5 to 10.5 mg) was heated up to 800 °C, at a scanning rate of 10 K/minute, in an atmosphere of oxygen-free nitrogen. To estimate the effect of the standard drying regime used in this work, a dried sample of magadiite was also analysed. This had been stored in an open sample-bottle in a dry-box for several days, before being sealed and eventually analysed. Some re-adsorption of moisture might have occurred between storage and analysis.

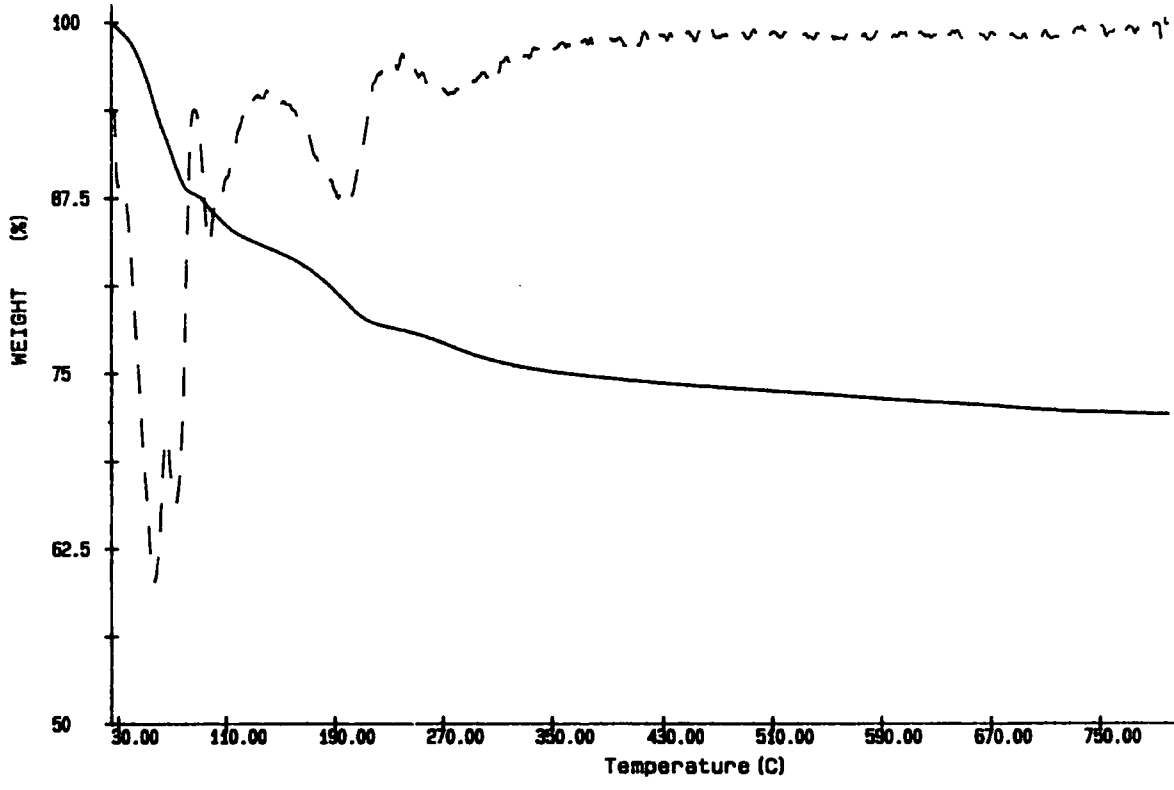

Figure 5.20 Thermogravimetric analysis results for kanemite (sample kna). Weight-loss and differential weight-loss curves are shown as unbroken and dashed lines, respectively. The abscissa scale refers to the weight-loss plot only. The shapes of the plots are typical of all the layered sodium polysilicate hydrates: several features are visible below 300 °C, while there is a more gradual weight loss above this temperature.

Weight *vs.* temperature and weight-loss rate *vs.* temperature plots were obtained for all the samples. All the graphs had the same form: several distinct events could be discriminated between room-temperature and 300 °C; while above this temperature, there was a more gradual, but significant decline in mass. Table 5.17 lists the results of the analyses– temperatures and weight-loss values of any events and a value for the overall weight-loss. As an example, figure 5.20 shows traces for kanemite.

Silicate	Sample	Features: Temperature (Weight-loss)	Total weight-loss / %
Makatite	mka	90 °C (12 %) 190 °C (5 %)	26
Kanemite	kna	60 °C (12 %) 100 °C (4 %) 200 °C (5 %) 270 °C (3 %)	27
Octosilicate	oca	90 °C (12 %) 130 °C (8 %)	23
Magadiite	mga	70 °C (7 %) 80 °C (3 %) 110 °C (2 %) 270 °C (2 %)	18
Kenyaite	kyb	90 °C (6 %) 136 °C (2 %)	10
Dried Magadiite	mga	90 °C (2 %) 120 °C (3 %) 160 °C (2 %)	10

Table 5.17 Thermogravimetric analysis results for five undried layered sodium polysilicate hydrate samples, together with similar results for magadiite, after careful drying. The features can be observed as peaks in plots of the rate of weight loss with time.

These analyses provide several bits of information of varying significance. A few general points can be made. Firstly, all the undried samples start losing mass at the beginning of the analysis. Since this starts at 30 °C, it is not unlikely that hydration and rehydration processes occur at room-temperature. Therefore, the hydration of a sample is likely to be variable– the water content of a magadiite sample is not necessarily the same as that of a different magadiite sample or even of the same sample some months later. Secondly, TGA results have frequently been reported, but there can be great variation in the temperatures, multiplicities and weight-losses of features for different samples of the same silicate.[46] Therefore, this work will concentrate on the behaviour over large temperature ranges rather than specific events. Finally, dry-box treatment clearly removes some but not all of the moisture in a sample. The water content of a magadiite sample dropped from 18 % to *ca.* 10 % on being stored in a dry-box. The final figure can only be an approximation as it was impossible to analyse the sample immediately on its removal from the dry-box and some re-adsorption of moisture could have occurred before analysis.

The reaction observed by thermogravimetric analysis is simply a loss of water with heating; for the layered sodium polysilicate hydrates, this can be represented by equation 5.5. The overall weight-loss can therefore be related to the fraction of water in each silicate. Table 5.18 shows a comparison between experimental values for the water content and those that have been calculated from formulae with a good correlation between the two figures.

$$Na_2O{:}xSiO_2{:}yH_2O \rightarrow Na_2O{:}xSiO_2 + yH_2O \qquad \text{Eq. 5.5}$$

Silicate	Formula	Total Water-content (theoretical) / %	Total Water-content (experimental) / %
Makatite	$Na_2O:4SiO_2:5H_2O$	23	26
Kanemite	$Na_2O:4SiO_2:7H_2O$	29	27
Octosilicate	$Na_2O:8SiO_2:9H_2O$	23	23
Magadiite	$Na_2O:14SiO_2:10H_2O$	17	18
Kenyaite	$Na_2O:22SiO_2:10H_2O$	12	10

Table 5.18 Comparison of theoretical water contents for the layered sodium polysilicate hydrates with those measured by thermogravimetric analysis. The theoretical total water content figures would include silanol and water protons.

The ^1H NMR data showed that there were two distinct proton species in the layered sodium polysilicate hydrates: those in water molecules and silanol protons, which can be strongly hydrogen-bonded. Thermogravimetric analysis also indicates that there are two types of proton species: those corresponding to discernible weight-loss events below 300 °C and those which correspond to a slower weight-loss at a higher temperature. Equation 5.5 can be re-written as equation 5.6, where silanol and water protons are considered separately. The water protons will be lost before the silanol protons as the involved reaction for the condensation of strongly H-bonded or silanol protons would require more energy.

$$Na_2H_2Si_xO_y.zH_2O \xrightarrow{-zH_2O} Na_2H_2Si_xO_y \xrightarrow{-H_2O} Na_2Si_xO_{y-1} \qquad \text{Eq. 5.6}$$

Theoretical weight-losses for the removal of water and silanol protons can be calculated and compared with the experimental data. The experimentally-observed weight-loss data can be divided into that which accompanied discernible low-temperature events and that which occurred more gradually at higher temperatures;

these values have been compared with values calculated from typical formulae in table 5.19. There is a reasonable correlation between the experimental and theoretical data. Therefore, it is a reasonable conclusion that water protons are lost faster and at lower temperatures than silanol protons. Additionally, thermogravimetric analysis provides some supporting evidence for the presence of distinct silanol and water proton species in the layered sodium polysilicate hydrates. To assign the several discernible low-temperature events to specific water species would be unwise: such events would not necessarily occur consistently with different samples of the same silicate.

Silicate	Experimental Weight-Loss / %		Formula	Theoretical Fraction / % (as H_2O)	
	Rapid	Slow		Water	Silanol
Makatite	18	8	$Na_2H_2Si_4O_9.3H_2O$	17.2	5.7
Kanemite	24	3	$Na_2H_2Si_4O_9.6H_2O$	24.5	4.9
Octosilicate	20	3	$Na_2H_2Si_8O_{17}.8H_2O$	20.1	2.9
Magadiite	14	4	$Na_2H_2Si_{14}O_{29}.9H_2O$	14.8	1.9
Kenyaite	8	2	$Na_2H_2Si_{22}O_9.9H_2O$	10.2	1.3

Table 5.19 A comparison of the theoretical fractions of layered sodium polysilicate hydrate water and silanol protons with the observed weight-loss from thermogravimetric analysis. The total experimental weight-loss has been divided into that which comes from discernible low-temperature events and that which occurs more slowly at higher temperatures.

In conclusion, inconsistent previously-reported data for the layered sodium polysilicate hydrates have indicated that thermogravimetric analysis data should be treated with some caution. However, this work has provided a measure of the total water content for a representative sample of each silicate which is close to that which can be predicted from typical formulae. Additionally, the total weight-loss can be attributed to two processes: rapid loss of water molecules followed by a slower loss of silanol protons. This supports the conclusion from the ^1H MAS NMR data that there are two types of proton species.

5.3 Proton Spin-Lattice Relaxation Times

5.3.1 Introduction

During the course of this work, several ^1H MAS inversion-recovery experiments have been carried out for the determination of spin-lattice relaxation times. The results have been essential for optimising experimental parameters and fitting the data from an exchange rate determination. It is the *proton* T_1-value which determines the rate of repetitive acquisition in cross-polarisation experiments (see section 2.7.4). For this reason alone, the measurements in this chapter are worthwhile, but additional information could be obtained.

The significance of the magnitude of any measured T_1-values must be doubted because many factors can influence the rate of longitudinal relaxation. These include the extent of paramagnetic contamination which can vary between samples of the same silicate. However, relative values could be interesting. Coincident relaxation times for two species within the same sample can be an indication of significant exchange processes over the time-scale of the relaxation.

Spin-lattice relaxation times have been measured for octosilicate and magadiite samples under various conditions of sample-hydration, temperature and spinning rate. Such experiments were not feasible for makatite and kanemite as the ^1H MAS spectra were not suitable and only limited work was possible with kenyaite.

Since little crucial information was gained from these experiments, the results will be reviewed briefly. A more detailed account of the experiment for octosilicate (sample occ, 16 kHz spinning rate) can be found in section 5.4.

5.3.2 Experimental Details and Results

Proton spin-lattice relaxation times have been determined for several layered sodium polysilicate hydrate samples using either the CMX200 or CXP200 spectrometers and Doty MAS, Chemagnetics HX or Chemagnetics HF probes. Standard inversion-recovery pulse sequences, t1ir and DURHSPT1, were used with CMX200 and CXP200, respectively. The former used a compensated π-pulse for inversion (*i.e.* a series of four 90° pulses which can provide accurate inversion for off-resonance signals even if slightly incorrect pulse-durations are used)[47] while the latter used a simple π-pulse. In both cases, spectra were acquired with several values of the recovery-time, τ. Values for T_1 were obtained by fitting spectral intensities to equation 2.12 using non-linear regression (SPSS for Windows) or the T1 routine of the CXP200 spectrometer. The former gives a value for T_1, 95 % confidence limits and a correlation coefficient, r^2 (not listed here). In a few cases, data obtained with the CXP200 spectrometer were analysed using both methods and similar relaxation times were obtained.

The ^1H MAS spectra of all the samples had two signals which could be assigned to strongly hydrogen-bonded and water protons. In most cases, separate spin-lattice relaxation times could be determined for both signals. However, the resolution in a few magadiite spectra was so poor that values could only be determined for the water proton signal. In all these cases, the small H-bonding signal appeared to share the same relaxation behaviour as the larger water signal.

Table 5.20 contains some experimental details together with proton spin-lattice relaxation times for several octosilicate, magadiite and kenyaite samples under different conditions of sample hydration. spinning-rate and probe temperature. Figure 5.21 shows a stacked plot of the results for octosilicate (sample occ) with a spinning rate of 4 kHz.

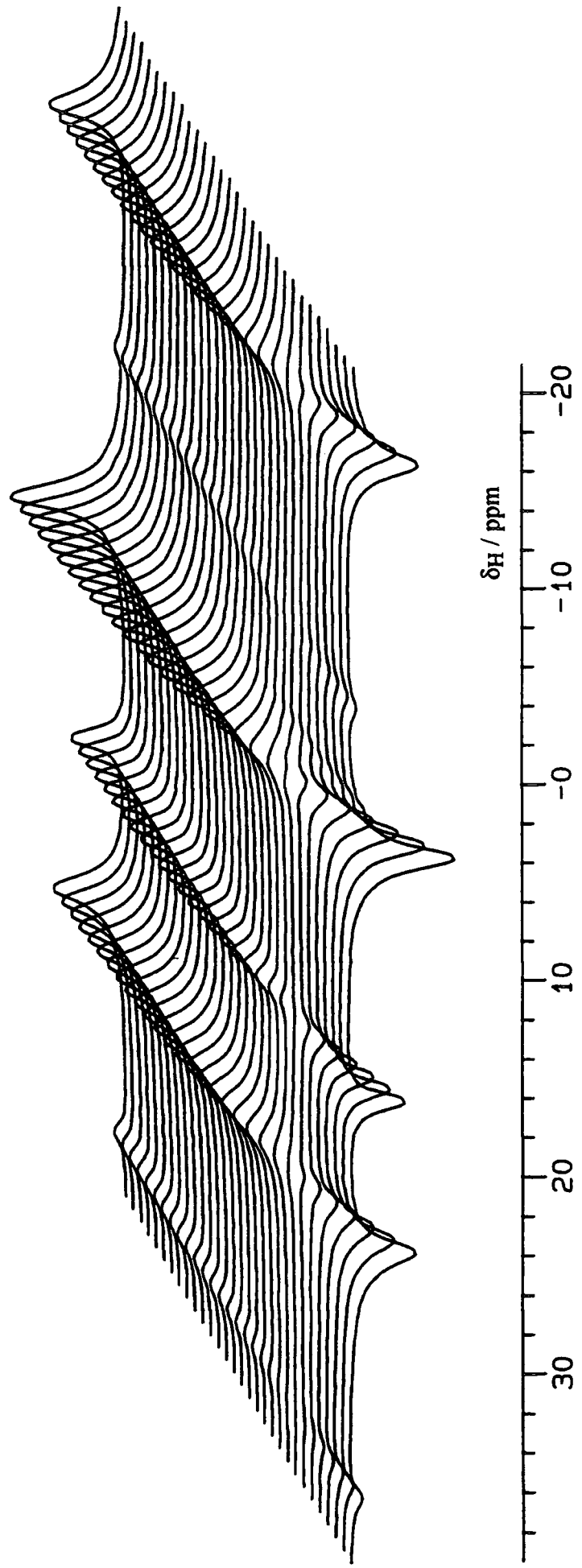

Figure 5.21 A stacked plot of the spectra from a ^1H MAS inversion-recovery experiment for octosilicate (sample occ). The sample had not been dried and a spinning rate of *ca.* 4 kHz was used. Thirty spectra are plotted here with recovery times evenly spaced between 5 ms and 150 ms.

Silicate (Sample)	Experimental Parameters				T_1 / ms†	
	NE[a]	NT[b]	RD[c]	SR[d]	H-Bonding	Water
Octosilicate (occ)	30	8	2	4	53.2 ± 1.7	53.0 ± 0.4
Octosilicate (occ)	25	16	2	16	31.8 ± 4.1	22.8 ± 0.5
Octosilicate (ocb)	25	8	2	4	50.3	50.7
Dried Octosilicate (ocb)	17	8	5	4	107 ± 5	119 ± 7
Magadiite (mga)	18	8	3	4	560 ± 50	390 ± 60
Magadiite (mgb)	20	16	1	4	‡	34
Dried Magadiite (mgb)	10	16	1	4	75	81
Magadiite (mgc)	20	8	1	4	‡	117
Dried Magadiite (mgc)	25	16	1	4	117	136
Magadiite (mge)	10	8	1	4	‡	89
Dried Magadiite (mge)	17	16	3	4	131	140
Magadiite (mgf)	10	8	1	4	‡	62 ± 14
Dried Magadiite (mgf)	20	16	1	4	96 ± 5	105 ± 5
Kenyaite (kyb)	14	8	1	5	65 ± 6	78 ± 6

Table 5.20 Experimental details and results for several layered sodium polysilicate hydrate ^{1}H MAS inversion-recovery experiments. †Error limits are not quoted for data analysed with the T1 routine of the CXP200 spectrometer. ‡In some cases, H-bonding signals could not be adequately resolved from water signals. [a]Number of experiments. [b]Number of transients. [c]Recycle time / ms. [d]Spinning-rate / kHz.

5.3.3 Discussion

Octosilicate ^1H MAS spectra contain sharp, well-resolved lines with little contribution from the probe background under the conditions used for these experiments. Therefore, equation 2.10 models the experimental data well and table 5.20 should contain accurate octosilicate T_1-values; any 95 % confidence limits should be a good measure of uncertainty. With magadiite and kenyaite, the ^1H MAS spectra have less well resolved lines and there is a larger contribution from the probe background. The T_1-values were determined by fitting the peak intensities at the chemical shift of the relevant signal. Since these can include a contribution from overlapping species, equation 2.10 might not model the experimental data correctly. Therefore, the results could be inaccurate and any quoted 95 % confidence limits will under-estimate the uncertainty. Nevertheless, many conclusions can be drawn from table 5.20.

The main conclusion from this work is that the ^1H spin-lattice relaxation times are small. The values tend to be around 100 ms, which means that short recycle time of 0.5 s to 1 s can be used in further ^1H NMR and cross-polarisation experiments. Since the ^{29}Si spin-lattice relaxation time for layered sodium polysilicate hydrates can be 100 s or more, CP can provide a rapid method of obtaining ^{29}Si spectra. Though there is some variation in all the magadiite samples, the long relaxation time for sample mga is anomalous. Of the several magadiite samples that have been studied, this is the only natural one and it gave the best-resolved ^{29}Si spectra (see section 5.1). It is possible that all these observations might be related: a different method of formation has produced a purer sample and less paramagnetic contamination would result in larger values of T_1 and sharper spectral lines.

The value of T_1 is clearly influenced by the hydration of the sample. The drying procedure tends to increase the spin-lattice relaxation time. This was noticed by Clarke[48] in zeolites and it can be related to mobility– the protons in the dried samples are more rigid and relax more slowly. Moreover, average proton-proton

distances will increase with drying. A more surprising observation is that the spinning rate appears to affect octosilicate T_1-values. It is difficult to explain why relaxation should be so much faster at a high spinning-rate, but it should be remembered that spinning a sample at 16 kHz in a small rotor is quite a violent process.

For each sample, hydrogen-bonded and water proton spin-lattice relaxation times tend to be similar. This might be caused by complete or significant mixing between the proton species over the time-scale of the longitudinal relaxation. If this were the case, any difference in intrinsic relaxation times would be averaged by chemical-exchange or spin-diffusion and a single T_1-value would be measured. Sample-drying reduces the extent of mixing, but there is still little difference between T_1 for the hydrogen-bonding and water protons. Though the rate of mixing might be less, T_1 is larger so there is a longer time for the mixing to occur.

5.3.4 Conclusion

Proton spin-lattice relaxation times have been measured for many samples of octosilicate, magadiite and kenyaite. The values tend to be small enough for short recycle times to be feasible in further cross-polarisation or ^1H NMR experiments, though one magadiite sample is anomalous. The longitudinal relaxation rate of water and H-bonded protons in the same sample are similar. This might be caused by mixing between the species by spin-diffusion or chemical-exchange. Such mixing will be further investigated in section 5.4.

5.4 Spin-Diffusion and Chemical Exchange Between Protons

5.4.1 Introduction

A study of spin-diffusion or chemical exchange between proton species in layered sodium polysilicate hydrates was essential for the explanation and confirmation of several ^{29}Si and ^{23}Na cross-polarisation experiments, which are included in chapter 7 of this work. They can also provide further information about the proton species themselves. For reasons of sample-availability and the suitability of ^{1}H MAS spectra, this study is restricted to octosilicate and magadiite.

The term chemical exchange will be used to describe the reaction where a water proton and a hydrogen-bonding proton swap positions; this is represented by equation 5.6 where the different proton species are indicated by subscripts, A and B. The chemical shift of an individual proton will change over the course of this reaction. Spin-diffusion describes the process whereby magnetisation is exchanged between species; this is represented by equation 5.7, where the superscripts α and β represent the $\pm$½ energy levels. In this case, there is no change in chemical shift for an individual proton. Distinguishing between the two processes is difficult and the term "mixing" will be used to mean either spin-diffusion or chemical exchange.

$$\text{-O-H}_A\text{-O} + \text{H}_B\text{-O-H} \xrightarrow{\text{Chemical Exchange}} \text{-O-H}_B\text{-O} + \text{H}_A\text{-O-} \qquad \text{Eq. 5.6}$$

$$\text{-O-H}\alpha\text{-O} + \text{H}\beta\text{-O-H} \xrightarrow{\text{Spin -Diffusion}} \text{-O-H}\beta\text{-O} + \text{H}\alpha\text{-O-H} \qquad \text{Eq. 5.7}$$

Chemical exchange is easy to visualise but spin-diffusion merits further explanation. The concept of spin-diffusion was first postulated by Bloembergen to account for the rapid spin-lattice relaxation that occurs in samples with paramagnetic impurities.[49] It has been described as the process whereby dipolar interactions between nuclear spins cause the propagation of dipolar and Zeeman order throughout

a crystal lattice.[50] The term describes two processes. In spatial spin-diffusion,[51] the interaction occurs through space by a diffusion of spin-temperature. However, in octosilicate or magadiite, spectral spin-diffusion is more likely as the proton species are quite distinct– their chemical shifts are separated by *ca.* 10 ppm. Here the magnetisation is transferred across frequency space.[51] In general, the process is most efficient when the exchange is energy-neutral. Since the energy required is equivalent to the difference in Zeeman energy-level separations, the efficiency of spectral spin-diffusion depends on the overlap between the NMR signals of the two exchanging species. For spectrally-resolved species, the extent of this overlap will depend on line-widths. Thus, the process occurs where dipolar interactions can "bridge the gap" in the Zeeman energy levels.[52] The rate of any spin-diffusion depends on the strength of these interactions, which are weak in dilute or mobile systems. In a dilute system, the interacting species are well-separated, while mobility can lead to an averaging of the interaction with time.

Spin-diffusion and chemical exchange are relevant to this work because they have an averaging effect on relaxation behaviour. Proton relaxation times can be detected *via* cross-polarisation in several useful experiments (see chapter 7). Though hydrogen-bonding and water protons might have intrinsically different relaxation properties, mixing over the lifetime of the relevant relaxation process can average the differences so that a single non-selective result is seen. Thus, coincident T_1- or $T_{1\rho}$-values could be caused by complete spin-diffusion or chemical exchange over the time-scale of the relevant relaxation process. Mixing can also preclude any selectivity which might be observed in 2-dimensional experiments to determine cross-polarisation mechanisms.

The technique of sample drying has been extensively used in this work to reduce the extent of spin-diffusion or chemical exchange. With the former, the decrease in rate can be attributed to a sharpening of the ^1H NMR peaks and a reduction in overlap; with the latter, the rate of exchange will decrease according to the law of mass-action. Thus, the two mixing processes are quite difficult to tell apart.

Two-dimensional exchange spectroscopy may be used to detect the presence of spin-diffusion or chemical exchange. The pulse-sequence consists of three $\pi/2$ pulses and is shown in figure 5.22. Such sequences have been reported by Jeener *et al.*,[53] for solution-state work and by Szeverenyi *et al.*,[54] for CP/MAS in the solid-state.

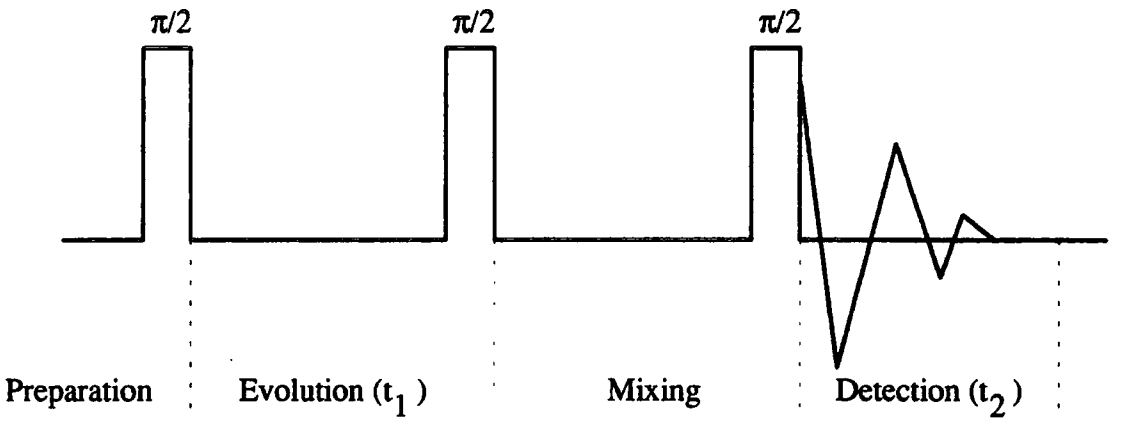

Figure 5.22 Pulse-sequence for 2-dimensional exchange spectroscopy.

The sequence can be divided into four parts. The preparation period places the proton magnetisation into the xy-plane of the rotating frame of reference. During the evolution period, the magnetisation relaxes under identical conditions to those for detection in a conventional ^{1}H MAS experiment. During the mixing time the magnetisation is positioned along the z axis before a third $\pi/2$ pulse places it back in the xy-plane for detection. A 2-dimensional spectrum is obtained by acquiring several spectra with incrementally increasing values of the evolution time, t_1, followed by 2-dimensional Fourier-transformation over t_1 and t_2. If there is no exchange, the individual proton species, A and B, say, will trace out similar FID's during both t_1 and t_2 and the 2-D spectrum will have signals along the diagonal at positions corresponding to their chemical shifts, (δ_A,δ_A) and (δ_B,δ_B). Exchanging species will be coded for one chemical shift during t_1 and another during t_2; this will lead to cross-peaks in the spectrum, (δ_A,δ_B) and (δ_B,δ_A). For chemical exchange, the species do actually swap chemical shifts with the exchange process. With spin-diffusion, cross-

peaks are seen because the exchange of magnetisation during the mixing time also involves an exchange of the frequency-coding that occurred during t_1.

5.4.2 Octosilicate $^1H,^1H$ 2-Dimensional Exchange Spectroscopy

The aim of the experiments was to investigate spin-diffusion or chemical exchange between the proton species in octosilicate, using $^1H,^1H$ 2-dimensional exchange spectroscopy. Five spectra were acquired: three were needed to test the method and then two spectra showed whether the rate of mixing was affected by sample-hydration.

Initially, the $^1H,^1H$ 2-dimensional exchange spectroscopy pulse sequence (figure 5.22) was used to acquire a spectrum with a mixing time of 8 ms. This had been the contact time in several cross-polarisation experiments in which spin-diffusion or chemical exchange appeared to influence the results (see chapter 7). Mixing is detected in the form of cross-peaks in the 2-dimensional spectra, but such signals might also arise from artefacts. Since these experiments involved techniques that were new to the spectrometer system (*i.e.* 2-D NMR), an additional spectrum was acquired to confirm the origin of any cross-peaks. With a delay of 1 ms, mixing will be less extensive: real cross-peaks should be smaller but artefacts would probably not change. Spinning side-bands were visible in the first two spectra. Therefore, a third spectrum was acquired to test the importance of rotor-synchronisation, where the mixing time is equal to an integral number of rotor periods. Two further spectra were acquired to compare the rate of spin-diffusion or chemical exchange in dried and undried octosilicate samples.

Two-dimensional $^1H,^1H$ exchange spectra for octosilicate were acquired with the CMX200 spectrometer, equipped with a Chemagnetics HX probe and 7.5 mm zirconia Pencil rotors. The experiments used a specially-written pulse program (based on figure 5.22) and a macro for automation. Five spectra were acquired. Each 2-D

data set consisted of 256 FID's of 256 data points. For each spectrum, the dwell time in both dimensions was 10 μs, corresponding to an acquisition time of 2.561 ms and a spectral width of 100 kHz. Zero-filling to 1 k and line-broadening were applied before fourier-transformation. The transmitter was offset to the low-frequency side of the 1-dimensional spectrum as the 2-D spectra were symmetrised about one axis. (Later attempts at acquiring hyper-complex data to produce phasable, non-symmetrised spectra were only partially successful.) Selective, absolute-value mode portions of the full spectra for each experiment are shown in figures 5.23, 5.24, 5.25, 5.26 and 5.27 together with slices through the chemical shift of the H-bonding proton. Further experimental details are listed in table 5.21.

Spectrum	Hydration	Mixing Time / ms	Spinning Rate / kHz	Number of Rotor Periods	Number of Transients	Recycle Time / s
Figure 5.23	Undried	8	3.96	31.7	4	1.5
Figure 5.24	Undried	1	3.96	3.96	4	1.5
Figure 5.25	Undried	8.08	3.96	32	4	1.5
Figure 5.26	Undried	7.8	4.10	32	4	1
Figure 5.27	Dried	7.8	4.10	32	16	1

Table 5.21 Further experimental parameters for the octosilicate 2-dimensional $^1H,^1H$ exchange spectra shown in figures 5.23-7.

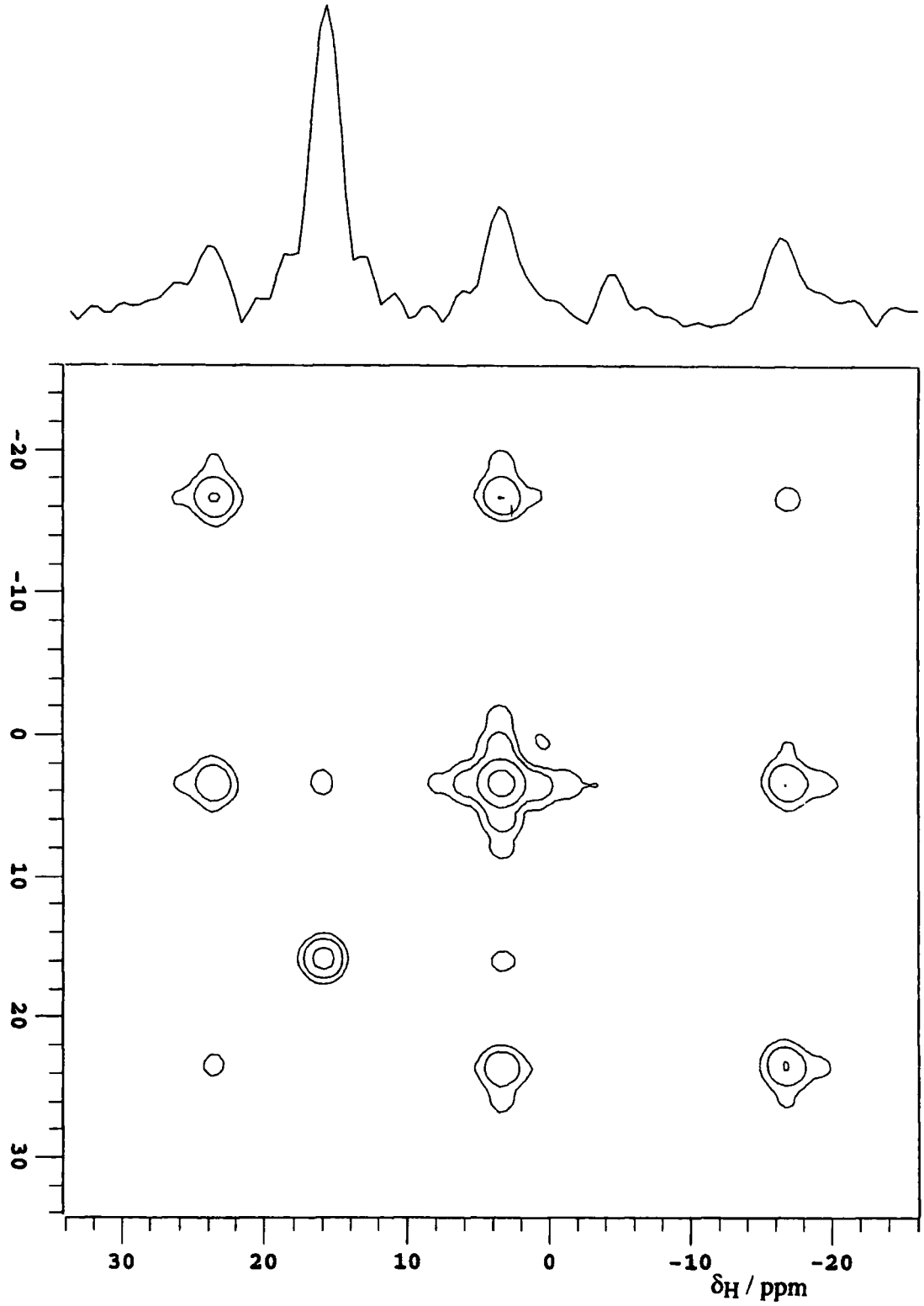

Figure 5.23 A 2-dimensional $^1H,^1H$ exchange spectrum of octosilicate (sample occ) with a mixing time of 8 ms and a spinning rate of 3.96 kHz. A slice through $\delta_H = 16$ is shown above the 2-D contour plot.

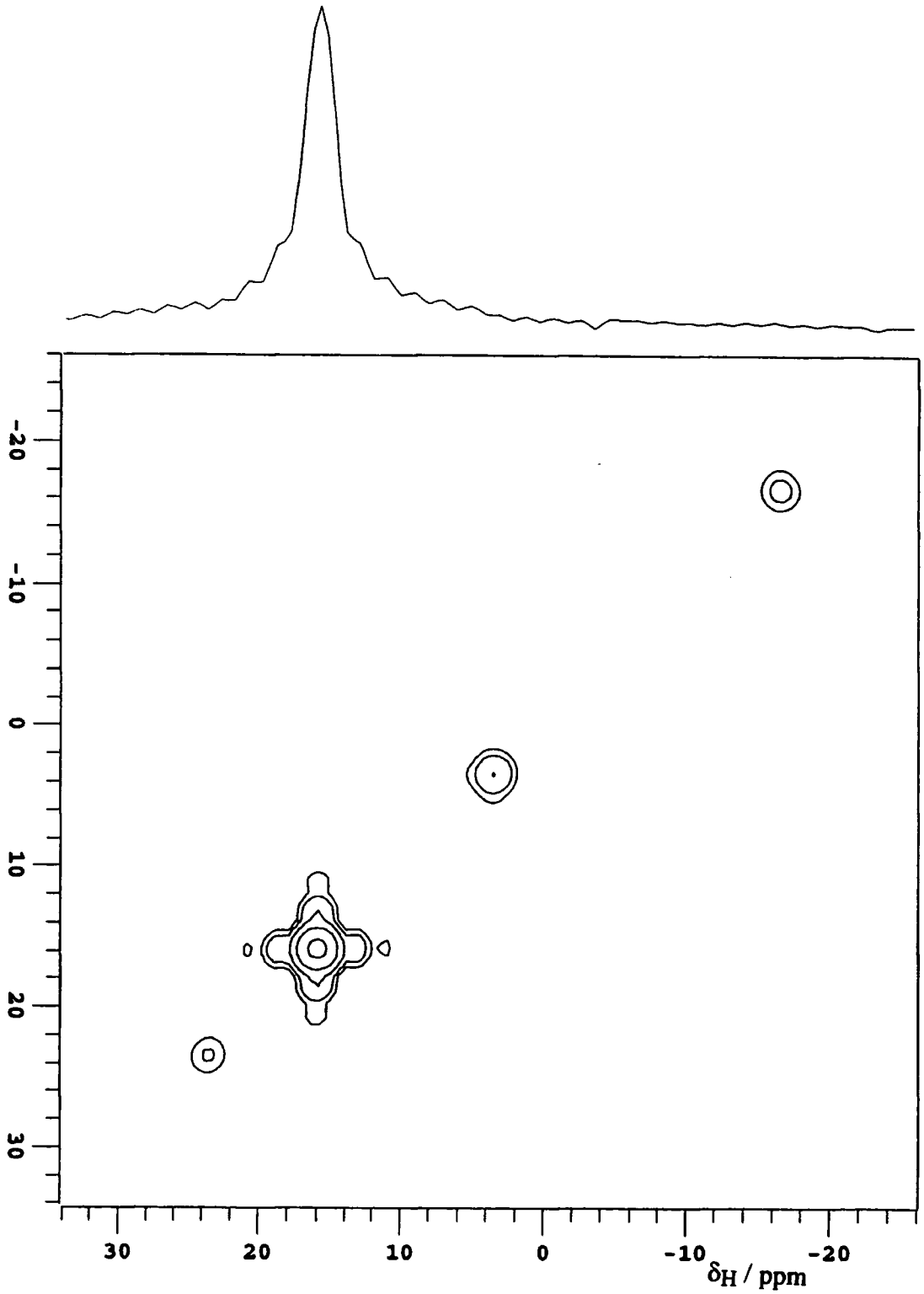

Figure 5.24 A 2-dimensional $^1H,^1H$ exchange spectrum of octosilicate (sample occ) with a mixing time of 1 ms and a spinning rate of 3.96 kHz. A slice through $\delta_H = 16$ is shown above the 2-D contour plot.

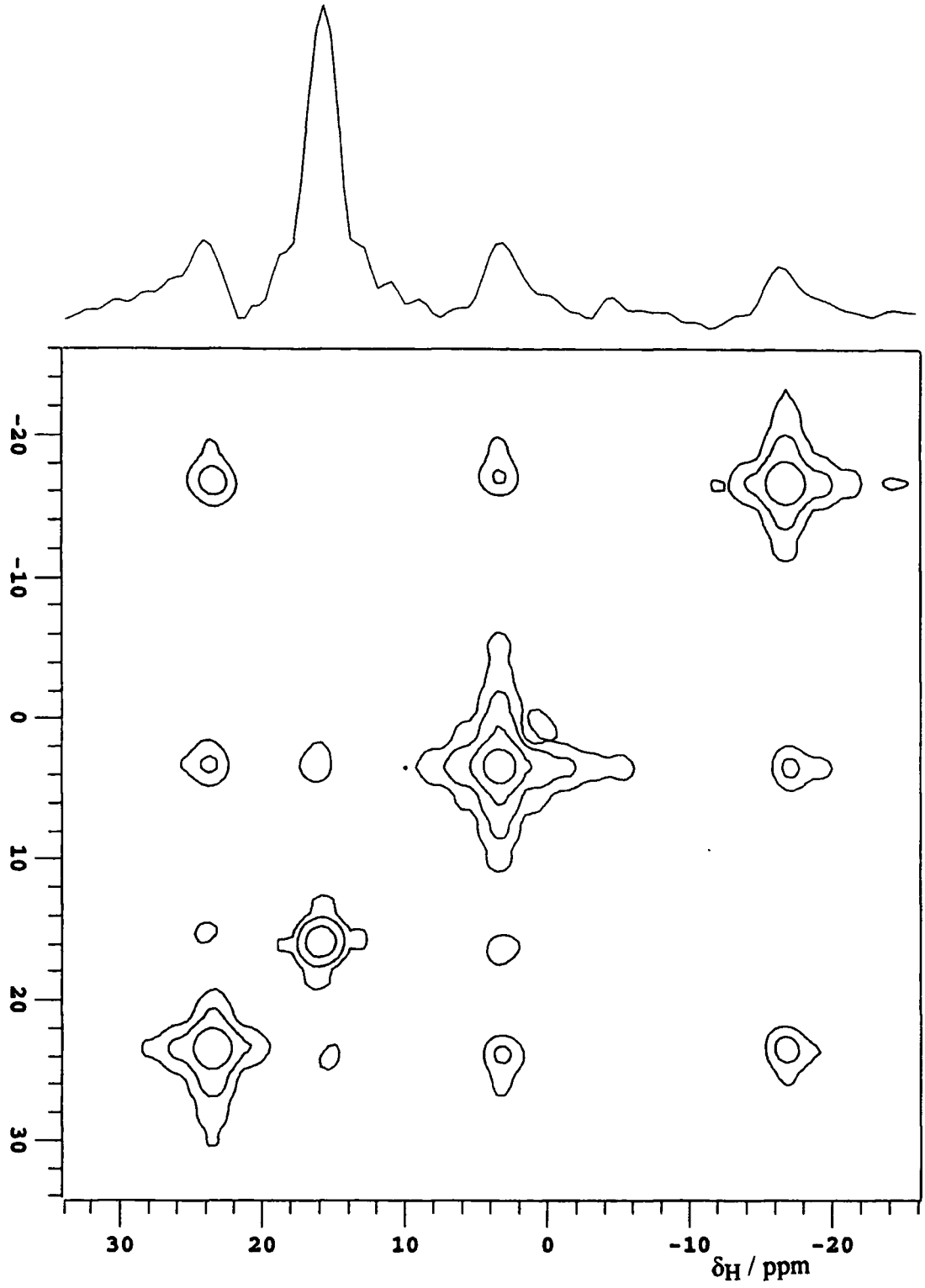

Figure 5.25 A 2-dimensional $^1H,^1H$ exchange spectrum of octosilicate (sample occ) with a mixing time of 8.08 ms and a spinning rate of 3.96 kHz. A slice through $\delta_H = 16$ is shown above the 2-D contour plot.

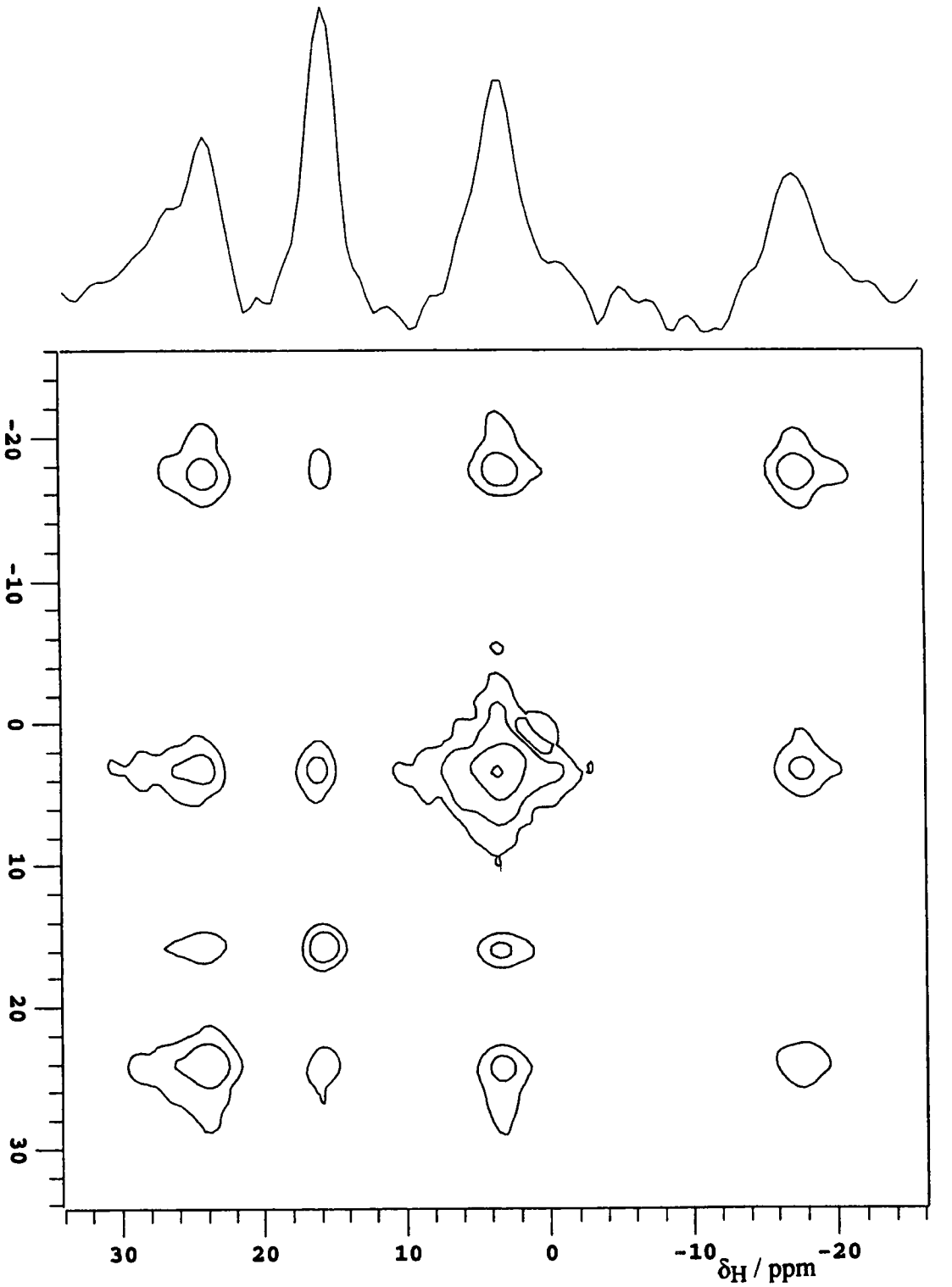

Figure 5.26 A 2-dimensional $^1H,^1H$ exchange spectrum of undried octosilicate (sample occ) with a mixing time of 7.8 ms and a spinning rate of 4.10 kHz. A slice through $\delta_H = 16$ is shown above the 2-D contour plot.

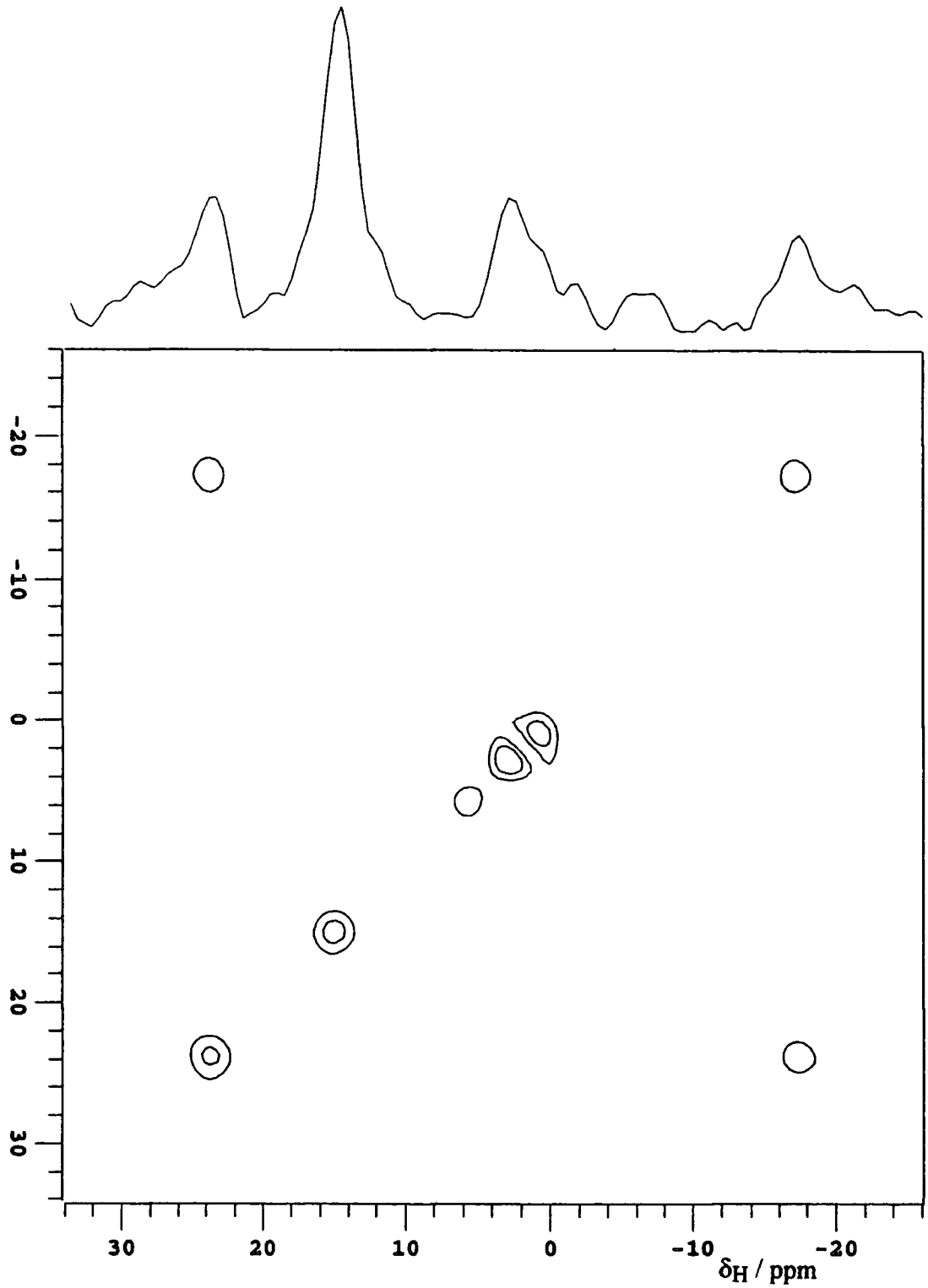

Figure 5.27 A 2-dimensional $^1H,^1H$ exchange spectrum of dried octosilicate (sample occ) with a mixing time of 7.8 ms and a spinning rate of 4.1 kHz. A slice through δ_H = 14.6 is shown above the 2-D contour plot.

Figure 5.23 shows a 2-dimensional $^1H,^1H$ exchange spectrum for octosilicate with a mixing time of 8 ms. The spectrum contains 13 peaks, 5 along the diagonal and 8 cross-peaks. The diagonal peaks at δ_H 16 and 4 can be assigned to hydrogen-bonding and water protons respectively, while the peak at 1 ppm comes from the probe background; water proton first-order spinning side-bands are also visible. The star shape of some signals is typical of peaks in magnitude-mode 2-D spectra. The cross-peaks between the isotropic hydrogen-bonding and water protons are evidence of spin-diffusion or chemical exchange. It is difficult to quantify the extent of this mixing from a contour plot as the height of the observed peaks can be artificially varied by changing the floor of the plot– the level below which contours are not plotted. By taking a slice through the chemical shift of the H-bonding proton signal, the heights of the diagonal signal and cross-peaks can be judged relative to a constant base-line. In this case, there is a strong isotropic water signal and two spinning side-bands which are indicative of extensive spin-diffusion or chemical exchange over the mixing time of this experiment.

The experiment was repeated with a shorter mixing time to check that the observed cross-peaks are real and not artefacts (figure 5.24). No cross-peaks are visible in the 1 ms spectrum and the slice through 16 ppm contains only the isotropic H-bonding proton signal. Since the extent of the cross-peaks does vary with the mixing time it is likely that they are a true indication of mixing processes, rather than an artefact.

The first experiment used a spinning speed of 3.96 kHz, so the 8 ms mixing time was not an integral number of rotor periods (8 x 3.96 = 31.7). Rotor-synchronisation is necessary in exchange experiments where there are spinning side-bands. Over a mixing time with a non-integral number of rotor periods, magnetisation that is coded for one side-band (or the centre-band) at the end of t_1 can be coded for another at the beginning of t_2. This will decrease the intensity of the diagonal signals in favour of cross-peaks between the same species. This theory was tested by running a rotor-synchronised experiment with a mixing time of 8.08 ms or 32 rotor periods

(figure 5.25). Though the mixing time was varied by only a small amount, the spectrum looks quite different, with more intense diagonal peaks. Rotor-synchronisation is clearly worthwhile.

Figures 5.26 and 5.27 show the effect of drying octosilicate on the rate of spin-diffusion or chemical exchange. In the spectrum of the undried sample there are considerable cross-peaks which are not present when the same experiment is repeated with the dried material. The slices show that the effect is not as striking as the contour plots indicate. However, the relative intensities of the water proton signals (*i.e.* cross-peaks) are less with the dried sample. Drying the sample clearly reduces the rate of mixing.

In summary, these experiments have detected spin-diffusion or chemical exchange between water and proton species in octosilicate over a mixing time of *ca.* 8 ms. This has been identified in the form of cross-peaks in 2-dimensional spectra. It is unlikely that the cross-peaks are artefacts as their intensity has been shown to be dependent on the duration of the mixing time. The intensity of the diagonal peaks can be increased with rotor-synchronisation– using a mixing time that is an integral number of rotor-periods. The extent of mixing has been shown to depend on the hydration of octosilicate. With a mixing time of 8 ms, spin-diffusion and chemical exchange are less evident after a sample has been dried.

5.4.3 Magadiite 2-Dimensional $^1H,^1H$ Exchange Spectroscopy

Two 2-D $^1H,^1H$ exchange spectra were acquired with a mixing time of *ca.* 8 ms. The aim of the experiments was to investigate the effect of drying magadiite on the extent of mixing between proton species. As with octosilicate, the work was necessary for the confirmation of some $^{29}Si,^1H$ CP correlation experiments (see chapter 7). With a contact time of 8 ms in these experiments, a selective result was only obtained with a dried sample.

Two $^1H,^1H$ exchange spectra were acquired for magadiite (sample mgf) using the CMX200 spectrometer, equipped with a Chemagnetics HX probe and 7.5 mm zirconia Pencil rotors. One portion of the sample was analysed after storage under ambient conditions of humidity, while a second portion was analysed after careful drying. Drying was achieved by packing the sample in a Kel-F insert and storing it overnight in a dry-box (relative humidity <5 ppm H_2O). A spinning rate of 4.10 kHz was used in each case; the mixing time was 32 rotor periods, 7.80 ms. All other parameters are listed in table 5.22. Selected portions of the spectra are shown in figures 5.28 and 5.29 together with slices through the chemical shift of the hydrogen-bonding proton.

Spectrum	Hydration	Number of FIDS	Number of Transients	Recycle Time / s	Dwell Time / μs
Figure 5.28	Undried	128	8	1	10
Figure 5.29	Dried	256	4	1	10

Table 5.22 Experimental details for magadiite 2-dimensional $^1H,^1H$ 2-dimensional exchange spectra.

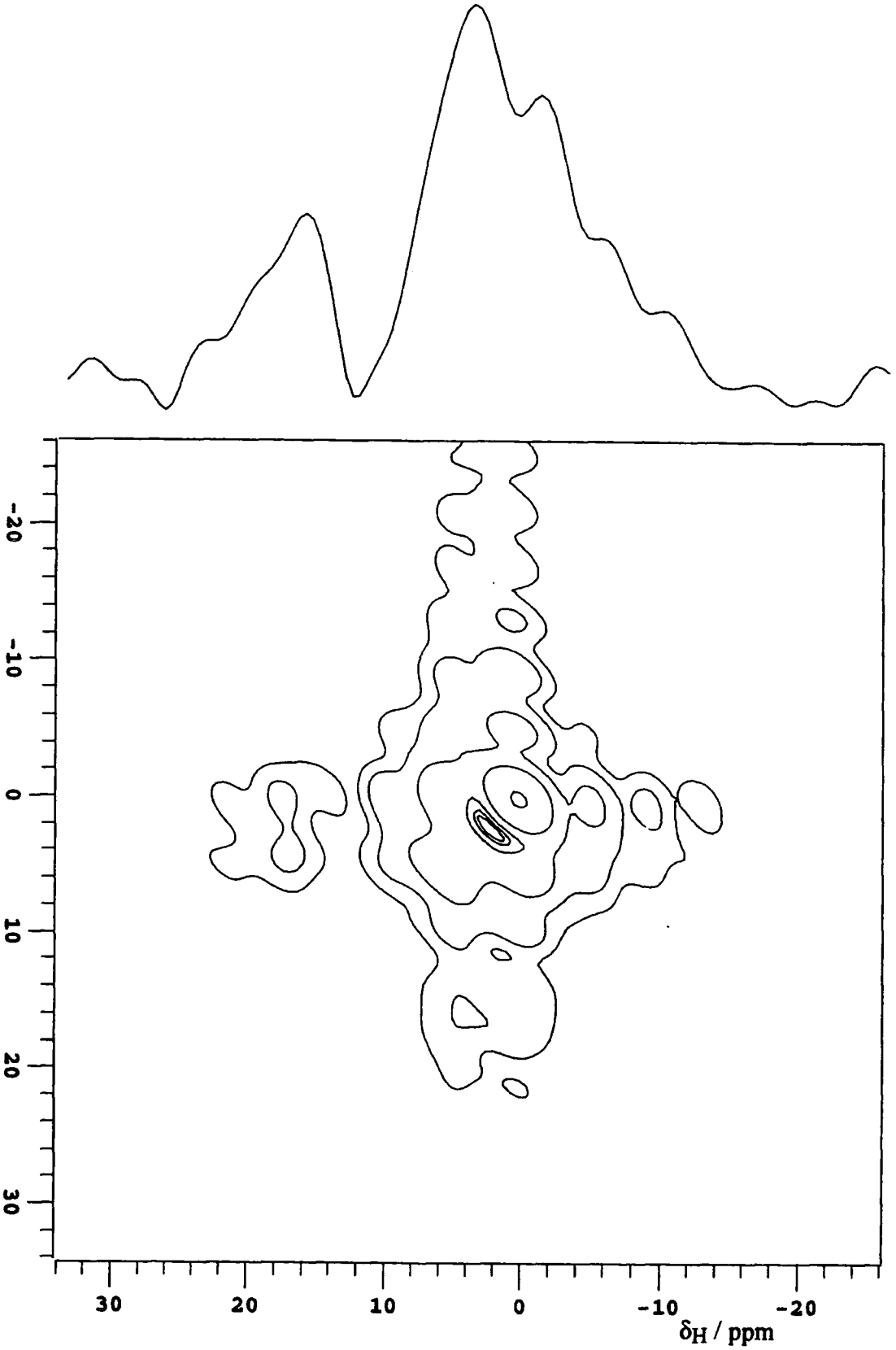

Figure 5.28 A 2-dimensional $^1H,^1H$ exchange spectrum of undried magadiite (sample mgf) with a mixing time of 7.8 ms and a spinning rate of 4.10 kHz. A slice through δ_H 15 is shown above the 2-D contour plot.

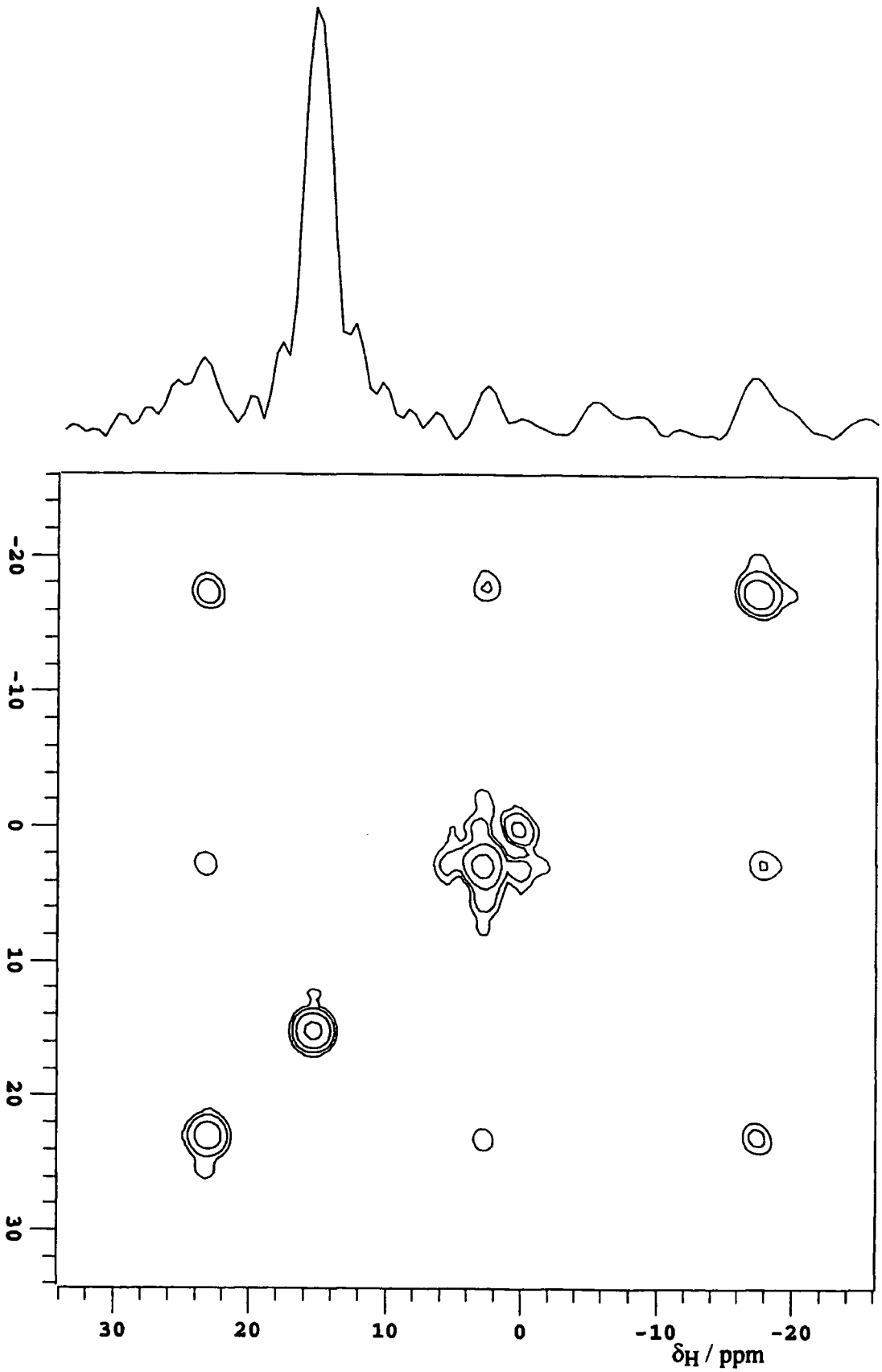

Figure 5.29 A 2-dimensional $^1H,^1H$ exchange spectrum of dried magadiite (sample mgf) with a mixing time of 7.8 ms and a spinning rate of 3.96 kHz. A slice through δ_H 14.6 is shown above the 2-D contour plot.

The quality of the undried sample spectrum is particularly poor. This is typical of magadiite ^1H MAS experiments where the two peaks are broad and poorly resolved. However, the spectrum does contains a diagonal water proton signal and cross-peaks with the H-bonding signal. The cross-peaks indicate that there is significant spin-diffusion or chemical exchange between the proton species over the mixing time of 8 ms. The spectrum of the dried sample is of a higher quality, with sharper, better-resolved peaks. Cross-peaks are still visible in this spectrum, indicating that there is some mixing between the protons species. The significance of this mixing in the two cases, can be compared by considering the slices in figures 5.28 and 5.29. The intensity of the water proton signals is less in the slice of the dried sample, indicating less-significant mixing.

In summary, spin-diffusion or chemical exchange between proton species has been detected in magadiite with 2-dimensional ^1H,^1H exchange spectroscopy. This method can not distinguish between the two processes. The rate of mixing between proton species in magadiite decreases when the sample is carefully dried. As with octosilicate, this decrease can be related to less rapid spin-diffusion, due to sharper ^1H MAS spectral lines giving less overlap, or less rapid chemical exchange, where fewer species exchange more slowly due to the law of mass-action.

5.4.4 A Time-Scale for the Exchange

This section contains the results of an experiment to determine the rate of the exchange between water and H-bonding protons in octosilicate. There were two parts to the successful octosilicate experiment: selective inversion of one of the ^1H MAS signals followed by a variable delay to monitor the extent of any relaxation.

The aim of the inversion step is to selectively invert one signal so that it is 180° out of phase with the other one. There are several possible ways of doing this including DANTE and sequences involving soft pulses, for example. The DANTE sequence includes a series of n π/n or $\pi/2n$ pulses which is only equivalent to a full π or $\pi/2$ pulse for nuclei which are on-resonance; other nuclei will unaffected. A conventional pulse excites nuclei over a wide range of frequencies to include all the possible species in a sample, but a longer, lower-power, or soft, pulse can selectively excite nuclei over a narrow range of frequencies. In this work selective excitation has been achieved with a method which relies on the fact that the rate of precession of xy-plane rotating-frame magnetisation is dependent on the offset of the Larmor frequencies from the transmitter frequency. The method has been reported by Connor *et al.*[55] and Zvezerenyi *et al.*[56]

The method works because the precession of a nucleus in the rotating-frame xy-plane depends on the difference between the transmitter frequency and the relevant Larmor frequency. On resonance, there is no precession and xy-plane magnetisation will decay back to equilibrium exponentially with time; this can be detected by conventional acquisition. If the transmitter is off-resonance by a frequency Δf, the magnetisation will nutate about the z-axis with an angular velocity, $2\pi\Delta f$. If transverse relaxation is ignored, a delay to allow for this precession can have the same effect as a conventional pulse: $\tau = \frac{1}{2}\Delta f^{-1}$, for a π pulse; and $\tau = \frac{1}{4}\Delta f^{-1}$, for a $\pi/2$ pulse. If a system contains two distinct nuclei, A and B, and the transmitter is offset with $\Delta f_A = 2\Delta f_B$, the delay, τ, can be chosen to place the magnetisation vectors 90° or 180° out of phase. To summarise, selective inversion can be achieved with a 90° pulse and

a carefully chosen delay, τ; a further 90° pulse places the magnetisation vectors back into the z-plane (figure 5.30).

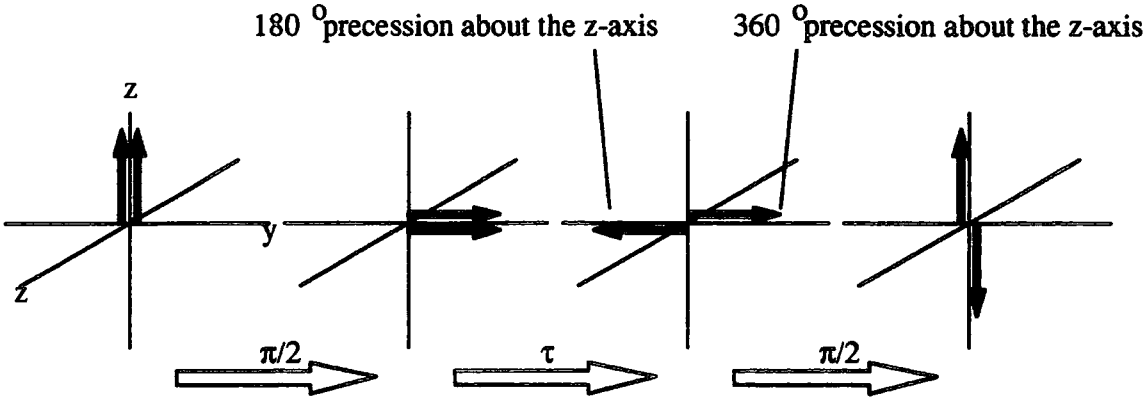

Figure 5.30 Selective inversion by allowing the magnetisation of the two distinct proton species to precess about the z-axis by 360° and 180°.

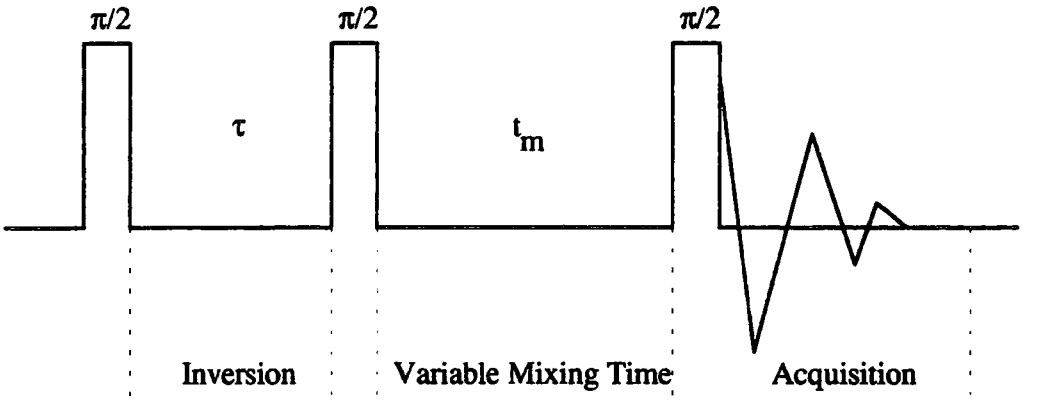

Figure 5.31 A pulse-sequence to measure the extent of mixing after selective inversion.

This inversion method has been used in a three-pulse sequence where a delay, t_m, is varied to monitor the extent of mixing (figure 5.31). The initial pulse places the magnetisation of both nuclei into the xy-plane of the rotating frame of reference. With the transmitter frequency set correctly, the inversion delay, τ, is equivalent to 180° and 360° pulses for the two species. The second pulse places the magnetisation along the z-axis. During the mixing time, t_m, the species can interact, *via* spin-diffusion or chemical exchange, while they return to equilibrium through longitudinal relaxation.

The extent of the mixing and relaxation is measured by a third 90° pulse, which places the magnetisation back into the xy-plane for detection.

Two processes occur as t_m is increased. Firstly, the magnetisation of each nucleus, M^A and M^B, decays back to equilibrium by spin-lattice relaxation. The rate of this decay is proportional to the deviation, ΔM, of the magnetisation vectors from their equilibrium values, M_∞ (equations 5.8 and 5.9). The second process is mixing between the species; the rate of this process is proportional to the difference in the relative deviation from equilibrium, $\Delta M/M_\infty$, for each line (equations 5.10 and 5.11, where k_A and k_B are exchange rate constants). The equations can be combined to give equations 5.12 and 5.13.

$$\frac{dM^A}{dt} = \frac{M_\infty^A - M_t^A}{-T_1^A} \qquad \text{Eq. 5.8}$$

$$\frac{dM^B}{dt} = \frac{M_\infty^B - M_t^B}{-T_1^B} \qquad \text{Eq. 5.9}$$

$$\frac{d}{dt}\left(\frac{M^A}{M_\infty^A}\right) = k_A\left(\frac{\left(M_\infty^B - M_t^B\right)}{M_\infty^B} - \frac{\left(M_\infty^A - M_t^A\right)}{M_\infty^A}\right) \qquad \text{Eq. 5.10}$$

$$\frac{d}{dt}\left(\frac{M^B}{M_\infty^B}\right) = k_B\left(\frac{\left(M_\infty^A - M_t^A\right)}{M_\infty^A} - \frac{\left(M_\infty^B - M_t^B\right)}{M_\infty^B}\right) \qquad \text{Eq. 5.11}$$

$$\frac{d}{dt}\left(\frac{M^A}{M_\infty^A}\right) = \frac{\left(M_\infty^A - M_t^A\right)}{-M_\infty^A T_1^A} + k_A\left(\frac{\left(M_\infty^B - M_t^B\right)}{M_\infty^B} - \frac{\left(M_\infty^A - M_t^A\right)}{M_\infty^A}\right) \qquad \text{Eq. 5.12}$$

$$\frac{d}{dt}\left(\frac{M^B}{M_\infty^B}\right) = \frac{\left(M_\infty^B - M_t^B\right)}{-M_\infty^B T_1^B} + k_B\left(\frac{\left(M_\infty^A - M_t^A\right)}{M_\infty^A} - \frac{\left(M_\infty^B - M_t^B\right)}{M_\infty^B}\right) \qquad \text{Eq. 5.13}$$

The final equations are considerably simpler if the two species are equally populous. This was the case in the work of Field *et al.* who studied the chemical exchange process between the two hydride ions in an octahedral iron complex, $FeH_2[P(CH_2CH_2CH_2PMe_2)_3]$.[57]

A selective-inversion experiment was carried out for octosilicate (sample occ) using the CMX200 spectrometer with a Chemagnetics HF probe. Several spectra were acquired with different values of the mixing time using a specially-written pulse program and a macro for automation. A spinning rate of *ca.* 16 kHz was used in this experiment; under these conditions, the spectrum consists of two lines, at δ_H 16 and 3.5, with minimal spinning side-bands. The water proton signal (3.5 ppm) is broader and more intense than the hydrogen-bonding signal (16 ppm). The peaks are separated by 2.441 kHz: the transmitter was offset by this value to the high-frequency side of the H-bonding signal. Setting τ to 200 μs gave selective inversion of the water proton signal. Forty FID's were acquired with non-incrementally increasing values of the mixing time, t_m. Each FID consisted of 16 transients with a recycle time of 2 s. Intensities of the resultant spectra are plotted in figure 5.32(a) and figure 5.32(b) is a stacked plot. Spin-lattice relaxation times for both signals were obtained in a separate experiment (see section 5.3.3 for experimental details). The spectral intensities are plotted in figure 5.33(a), together with curves that have been simulated from the results of non-linear regression analysis. A stacked plot of the data is shown in figure 5.33(b). The results of the regression analysis are listed in table 5.23.

Signal	δ_H / ppm	T_1 / ms	r^2
H-Bonding	16.0	31.8 ± 4.1	0.99691
Water	3.9	22.8 ± 0.5	0.99983

Table 5.23 Regression results for a ^1H MAS inversion-recovery experiment for octosilicate (sample occ).

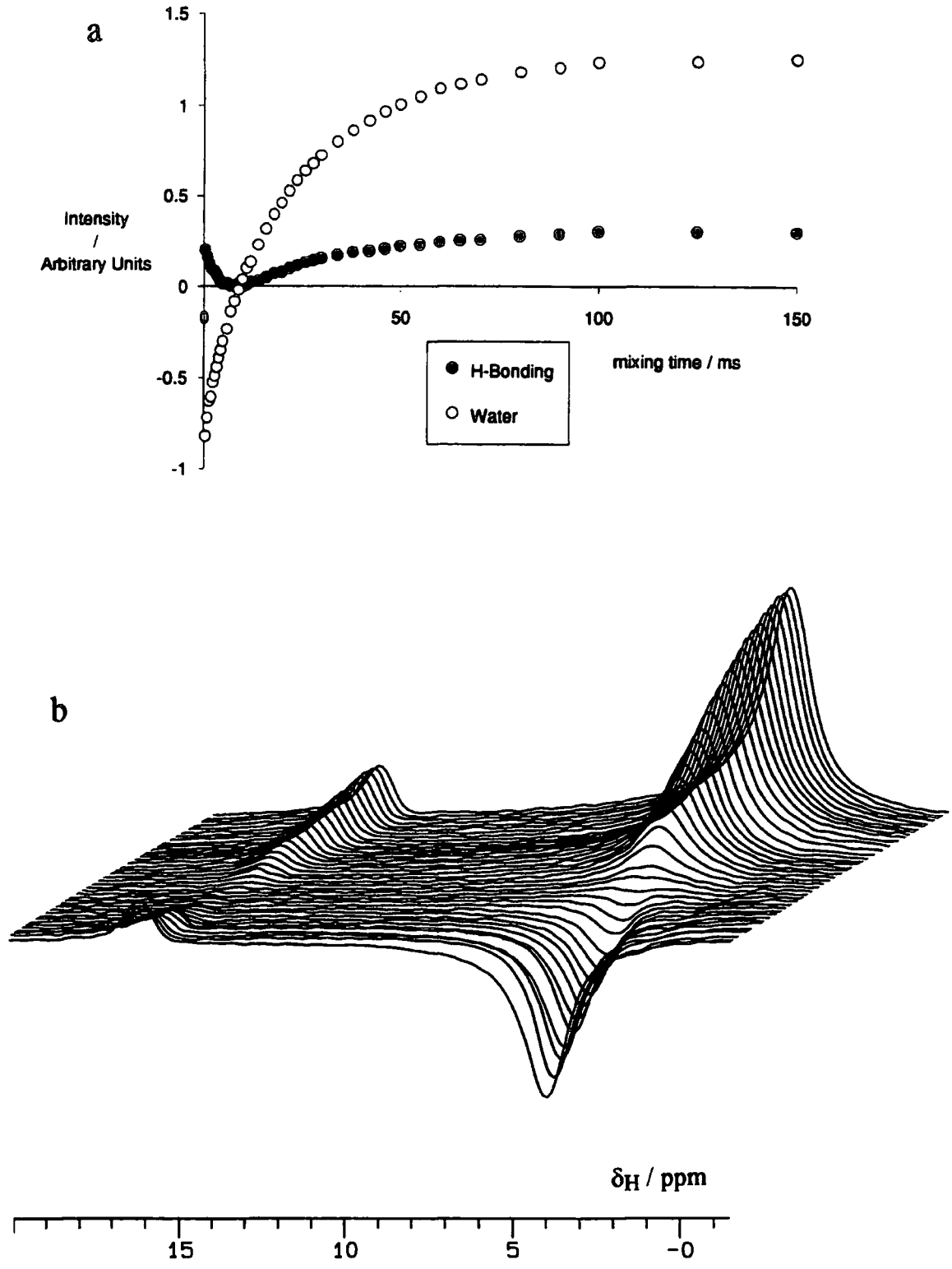

Figure 5.32 The results of a selective-inversion experiment for octosilicate (sample occ): a) a graph; and b) a stacked plot. Variation in the mixing time, t_m, is not incremental.

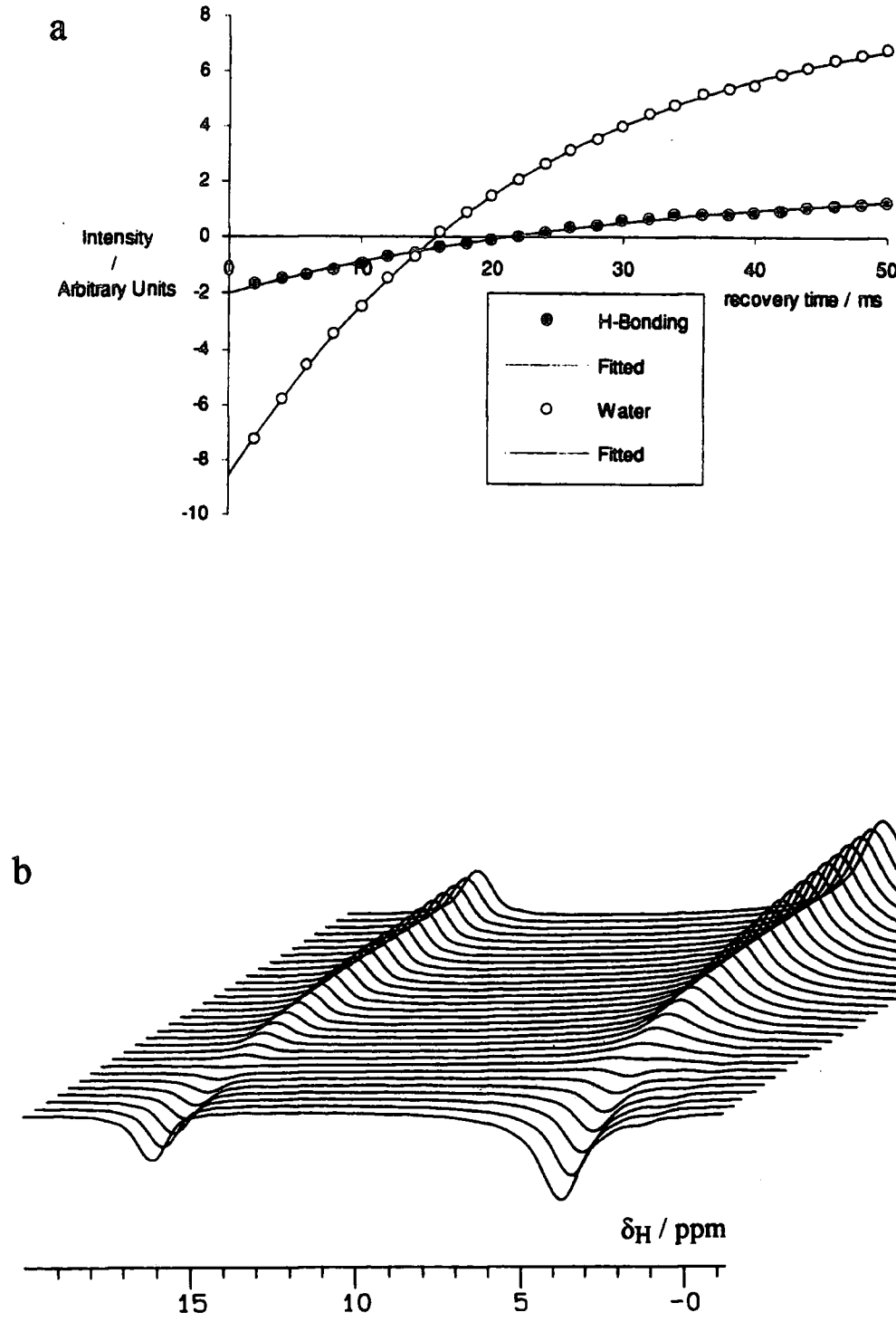

Figure 5.33 The results of an inversion-recovery experiment for octosilicate (sample occ): a) a graph; and b) a stacked plot. Variation in the recovery time is incremental.

Regression methods are unsuitable for analysing the data from the selctive-inversion experiment. Field *et al.* modelled their previously-mentioned selective-inversion data using an iterative least-squares fitting procedure which used a Runge-Kutta algorithm to integrate twin differential equations.[57] A less rigorous approach has been used in this case. Curves were simulated from several parameters and compared with the experimental data by eye, until the best fit was obtained.

The first step in simulating the curves was to divide the experimental mixing-time range of 150 ms into 1500 increments. A value for the relative signal intensity at zero-time could be read off the graph in figure 5.32a. Further values for the relative signal intensity were approximated by estimating the change in magnetisation, δM, over a small time interval, δt, using equation 5.14. The change in magnetisation can be added to a previously calculated value, M_i, to create a new value, M_{i+1} (equation 5.15). Equation 5.16 can be obtained by combining equations 5.14 and 5.15, and dividing by M_∞. This is a reasonable approximation, provided the time interval is small. Any deviations will come from using the derivative at t_i, rather than an average value for the time interval, t_i to t_{i+1}. Since the simulated curves were similar whether increments of 0.01 ms or 0.1 ms were used, equation 5.14 is a valid approximation.

$$\delta M = \delta t . \frac{dM}{dt} \qquad \text{Eq. 5.14}$$

$$M_{i+1} = M_i + \delta M \qquad \text{Eq. 5.15}$$

$$\left(\frac{M_t}{M_\infty}\right)_{i+1} = \left(\frac{M_t}{M_\infty}\right)_i + (t_{i+1} - t_i)\left(\frac{d}{dt}\left(\frac{M_t}{M_\infty}\right)\right)_i \qquad \text{Eq. 5.16}$$

The relaxation behaviour of the water protons must be known for the derivative in equation 5.16 to be calculable. Fortunately, the behaviour can be closely modelled by simple spin-lattice relaxation. The effect of any exchange can be ignored because the water signal is large with respect to the H-bonding proton signal. Figure

5.34 shows that this is the case. The experimental data are plotted with two fitted curves: the first uses values from the regression of these data; the second uses the previously determined value for T_1 (table 5.23) and equilibrium and zero intensity values which were chosen to fit the data. Both fitted curves model the experimental behaviour well so either can be used to model the H-bonding signal intensity with a fairly accurate description of the water signal behaviour.

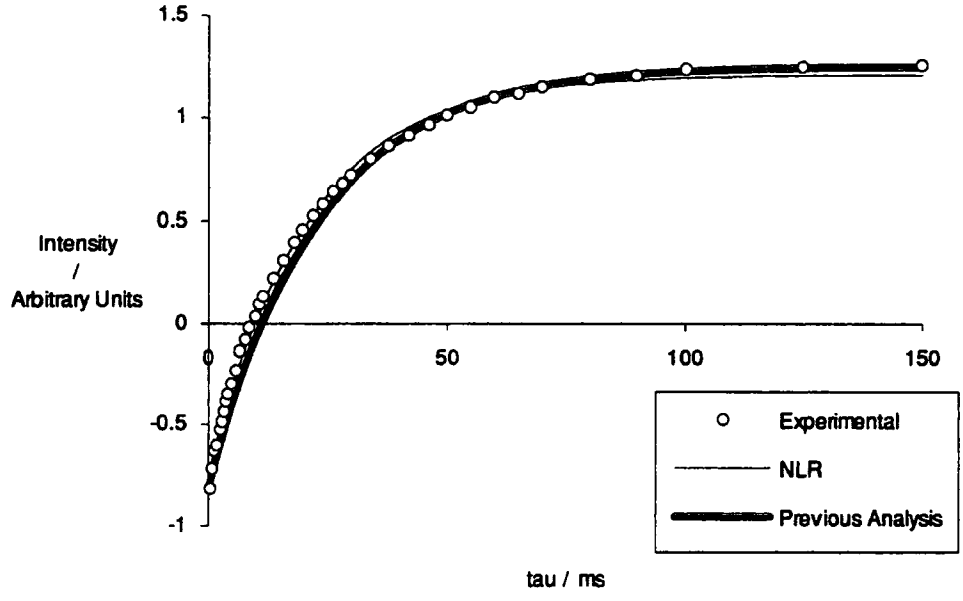

Figure 5.34 Modelling the water signal intensity data for a selective inversion experiment for octosilicate (sample occ). Two curves are included: the first is simulated with values obtained by non-linear regression (NLR) of these data, $M_\infty = 1.21$, $M_0 = -0.76$ and $T_1 = 20.6$ ms; the second is simulated from a previously-determined value of T_1, and the extrapolated extremities of this plot, $M_\infty = 1.25$, $M_0 = -0.82$ and $T_1 = 22.8$ ms.

The H-bonding signal data were modelled using equation 5.17. There are five unknowns in this equation: the initial H-bonding and water proton signal intensities, M_0^{HB} and M_0^{W}; ^1H spin-lattice relaxation times for the hydrogen-bonding and water protons, T_1^{HB} and T_1^{W}; and the exchange rate constant, k. Since the T_1-values were independently determined, and the initial intensity values could be extrapolated from figure 5.32a, a best fit for the data was obtained by varying k. This is displayed in figure 5.35 and used the values listed in table 5.24.

An interesting conclusion from the results of this experiment is that the inversion-recovery experiment gives a good measure for the intrinsic spin-lattice relaxation time of the water protons only. The value determined for the H-bonded protons is in fact an average of the values for both species. Therefore, the value of T_1^{HB} that has been used to model the data is probably too small. However, varying this parameter between 30 ms and 40 ms had little effect on the fit of the simulated curve to the experimental data.

$$\left(\frac{M_t^{HB}}{M_\infty^{HB}}\right)_{i+1} = \left(\frac{M_t^{HB}}{M_\infty^{HB}}\right)_i - (t_{i+1} - t_i)\left(\frac{1 - \left(\frac{M_t^{HB}}{M_\infty^{HB}}\right)_i}{-T_1^{HB}} + k\left(\left(1 - \frac{M_0^W}{M_\infty^W}\right)\exp\left(-t_i / T_1^W\right) - \left(1 - \frac{M_t^{HB}}{M_\infty^{HB}}\right)\right)\right)$$

Eq. 5.17

Parameter	Symbol	Value
Initial H-bonding proton signal intensity	M_0^{HB}	$0.66M_\infty^{HB}$
H-Bonding proton spin-lattice relaxation time	T_1^{HB}	32 ms
Initial Water proton signal intensity	M_0^{W}	$0.66M_\infty^{W}$
Water proton spin-lattice relaxation time	T_1^{W}	22.8 ms
H-bonding proton exchange rate constant	k	0.18 ms^{-1}

Table 5.24 Parameters for the best-fit to selective inversion data of the octosilicate hydrogen-bonding proton signal.

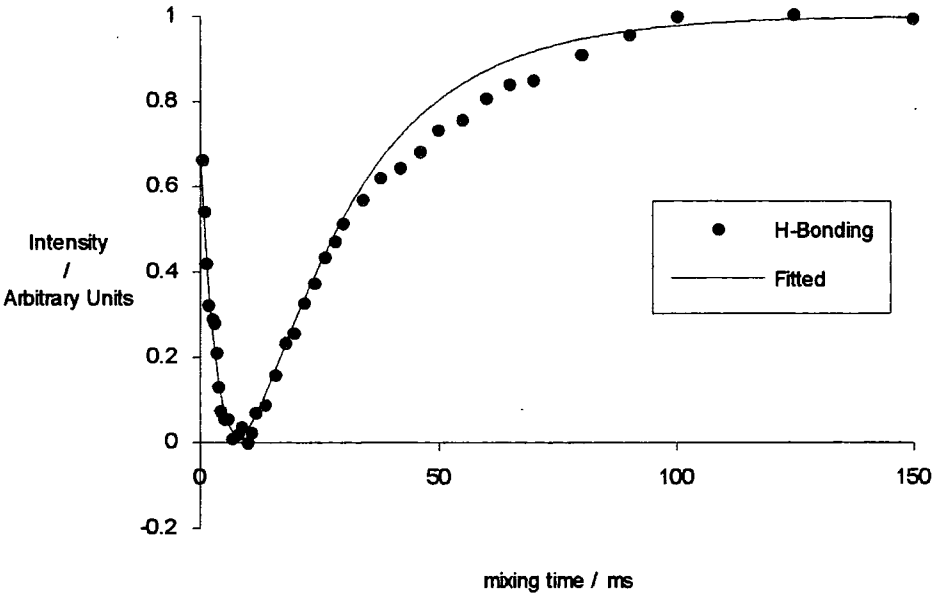

Figure 5.35 Experimental data and a simulation for a selective-inversion ^1H MAS experiment on octosilicate (sample occ). This is the behaviour of the H-bonding protons, only.

Simulation gave a reasonable fit to the experimental data, particularly around the minimum of the curve. The observed deviations between 30 ms and 80 ms could not be accounted for using this model, but they could be due to spinning-rate fluctuations or heating effects. The precision of the exchange rate value can be estimated at ±0.02 ms; varying k by this amount in either direction gave a noticeably poorer fit. The value of 0.18 ms^{-1} has been measured with respect to the H-bonding proton. There are eight times as many water protons in octosilicate, so the exchange rate with respect to these protons would be much slower, *ca.* 0.023 ms^{-1}.

The exchange rates can be compared with the spin-lattice relaxation times measured under the same conditions. The T_1-values of 20 ms and 30 ms correspond to relaxation rates of 0.05 ms^{-1} and 0.03 ms^{-1} for the water and H-bonding protons, respectively. With the hydrogen-bonded protons, the exchange is faster than spin-lattice relaxation. Therefore, the rate of any longitudinal relaxation will be influenced by mixing with the water protons. It is likely that the T_1-value that has been measured

by inversion-recovery is an average of the intrinsic values for the water and H-bonding protons. With the water protons, the exchange rate is slow with respect to the longitudinal relaxation: this fits with the experimental behaviour shown by figure 5.34, where there appeared to be little contribution from exchange in the recovery of the inverted signal. If the rate of longitudinal relaxation for the water protons was slower, a common, averaged value of T_1 would be observed for both signals. This is the case at a spinning-rate of 4 kHz, where, both water and H-bonding protons have spin-lattice relaxation times of *ca.* 50 ms (see section 5.3.3).

The relevance of the measured exchange rates should be considered. This experiment was carried out with fast spinning, but most of the experiments in this work were carried out at spinning-rates of 5 kHz, or less. A change in spinning-rate could affect the rate of mixing: broader ^{1}H MAS spectral lines would cause more rapid spin-diffusion while different temperatures and pressures might affect the rate of chemical exchange. However, the measured exchange rate can explain why coincident spin-lattice relaxation times are measured at 4 kHz, but not at 16 kHz. Therefore, it is likely to be a reasonable estimate.

In summary, approximate exchange rates of 0.18 ms^{-1} and 0.023 ms^{-1} have been calculated for the interaction between octosilicate H-bonding and water protons, respectively. The time-scale of this exchange is particularly relevant to cross-polarisation experiments where contact time of up to 15 ms have been used. Significant mixing might be expected if long contact times are used, while results that can distinguish between H-bonding and water protons might be possible at short contact times. Alternatively, similarly-selective results might be seen in cases where the rate of exchange is reduced– in dried samples, for example. The exchange rates were measured with a spinning-rate of 16 kHz, extreme conditions where the proton relaxation behaviour of octosilicate might be quite different to more readily-achievable spinning-rates. However, the reasonable accuracy of the results can be confirmed by comparing them with ^{1}H MAS spin-lattice relaxation times.

5.5 Sodium-23 NMR

5.5.1 Introduction

Few ^{23}Na NMR studies of the layered sodium polysilicate hydrates have been reported. Nesbitt obtained broad, uninformative spectra of makatite and kanemite.[1] However, structurally significant results have been obtained for magadiite and kenyaite. Rojo *et al.* assigned the two peaks in a magadiite ^{23}Na SP spectrum to different interlayer locations for sodium ions (see figure 3.4).[28] Nesbitt showed that only one of the signals observed in some magadiite and kenyaite spectra was present in a cross-polarisation spectrum.[1,58] This was assigned to hydrated interlayer sodium ions, while the other sodium site was assumed to be isolated within the silicate layer.

In this work ^{23}Na SP spectra have been obtained for all the layered sodium polysilicate hydrates at two magnetic fields. Where relevant, cross-polarisation spectra have been acquired in an attempt to repeat the result of Nesbitt, and some ^{23}Na spin-lattice relaxation times have been determined. Powder X-ray diffraction has been used as a supporting analytical technique.

5.5.2 Theory

The relevant isotope for sodium NMR, ^{23}Na, is 100 % abundant with a spin quantum number, I, of 3/2. The quadrupolar nature of the nucleus ($I \neq ½$) has an important effect on the frequencies of transitions leading to NMR spectra. When a sodium nucleus is placed in a magnetic field, Zeeman splitting will produce 2I+1 non-degenerate energy levels. In the absence of other interactions, these are equally spaced and resonance will occur at a single frequency, ν_L, the Larmor frequency. The quadrupolar interaction perturbs the energy levels so that they are no longer equally-spaced. By convention, there are two different effects depending on the strength of the quadrupolar interaction: first-order quadrupolar effects come from small

perturbations on the Zeeman energy levels, while larger perturbations can cause second-order quadrupolar effects.

Equation 5.18 gives transition frequencies, $\Delta\nu$, for a nucleus which experiences Zeeman and weak quadrupolar interactions leading to first-order effects. The quadrupolar coupling constant, χ, is defined in equation 5.19. The value of χ depends on the particular nucleus (^{23}Na or ^{17}O, for example) through the quadrupole moment, eQ, a measure of charge distribution. The geometry of the particular nuclear site also influences χ through eq_{zz}, a component of the electric field gradient tensor. The angle between q_{zz} and the magnetic field is θ. Transition frequencies can easily be calculated with respect to ν_L, θ and χ: these are shown in figure 5.36.

$$\Delta\nu = \nu_L - \frac{3}{8}\chi\frac{2m_I - 1}{I(2I-1)}(3\cos^2\theta - 1) \qquad \text{Eq. 5.18}$$

$$\chi = \frac{e^2Qq_{zz}}{h} \qquad \text{Eq. 5.19}$$

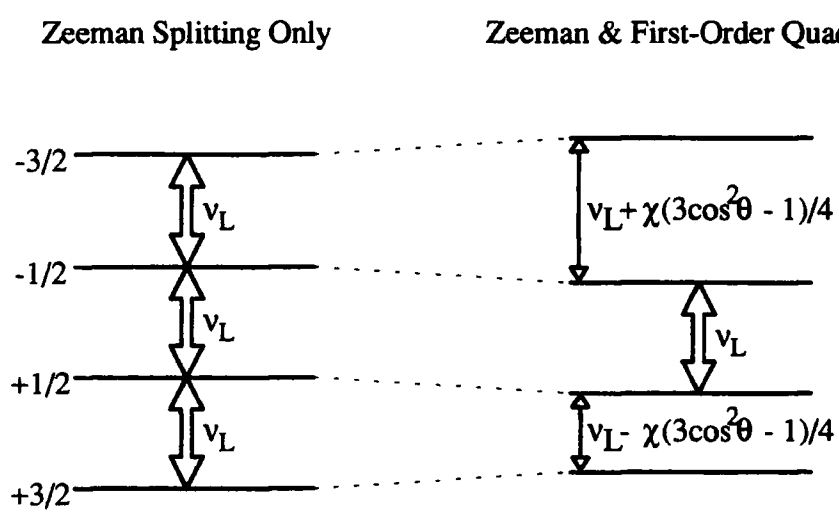

Figure 5.36 Energy levels and transitions frequencies for a ^{23}Na nucleus (I = 3/2) in a magnetic field. In the absence of a quadrupolar interaction, resonance occurs at the Larmor frequency, ν_L, only. This is also the case for the central transition even when there are first-order quadrupolar interactions, but the frequencies of the other transitions include angular and χ terms.

Figure 5.36 shows that the central transition, $m_I=+½ \rightarrow m_I=-½$, is unaffected by first-order quadrupolar effects and independent of θ. A typical spectrum of a powder containing all orientations of θ would have a strong line at the Larmor frequency, while the other transitions might give broader, less easily-detectable lines.

Stronger quadrupolar interactions lead to second-order effects. In this case the central transition, $m_I=+½ \rightarrow m_I=-½$, is affected and line-shapes, chemical shifts and line-widths can be distorted. The influence of the quadrupolar interaction can move the centre of gravity of observed signals away from the isotropic chemical shift. Fyfe shows that this can be represented by equation 5.20, for magic-angle spinning.[59] Because of this potential deviation, it is not usually possible to record isotropic chemical shifts, δ_{Na}, from ^{23}Na NMR spectra. In this work, apparent chemical shifts will be represented by the symbol, δ_{Na}*.

$$\nu_{CG} - \nu_0 = \frac{\nu_Q^2}{30\,\nu_0}\left(I(I+1) - \frac{3}{4}\right)\left(1 + \frac{\eta^2}{3}\right) \qquad \text{Eq. 5.20}$$

In equation 5.20, ν_{CG} is the centre of gravity of the signal, while ν_0 and ν_Q are proportional to the applied field and the quadrupolar coupling constant, respectively; η is an asymmetry parameter. It should be noted that second-order quadrupolar effects are inversely-proportional to the applied magnetic field. Therefore, any distortions can be minimised by working at as high a magnetic field as possible.

Magic-angle spinning is important in the NMR of quadrupolar nuclei. It can average broadening from heteronuclear dipolar, shielding anisotropy and first-order quadrupolar interactions. However, second-order quadrupolar interactions are not completely averaged with this technique as the angular dependence is more complex than a $3\cos^2\theta$-1 term. Special techniques can be used to achieve line-narrowing, for example: double rotation (DOR),[60] using a special rotor in which the sample spins around two axes simultaneously; dynamic-angle spinning (DAS),[61] where a spinning rotor can flip between two angles; variable-angle spinning (VAS),[62] using an angle

which is more effective than 54.7 °; and sonically-induced NMR,[63] where ultrasound is applied to a suspension of the sample.

With second-order effects, the outer transitions can be so broad that they are not excited by a conventional pulse, thus the central transition is selectively excited. This is important with respect to quantification since the intensity of such a signal will be 40 % of that observed in the non-selective case. Additionally, the optimum pulse-duration for a selective pulse can be shorter than that for a non-selective pulse, by a factor, I+½, the Rabi factor, depending on the value of the quadrupolar coupling constant.[64]

5.5.3 Makatite and Kanemite ^{23}Na Single-Pulse Spectra

Nesbitt acquired ^{23}Na SP spectra for makatite and kanemite using a 200 MHz spectrometer.[1] The spectra were broad and difficult to assign. Similar spectra have been acquired in this work together with sharper spectra acquired with a 300 MHz spectrometer.

Makatite and kanemite ^{23}Na SP spectra were acquired with two spectrometers at two magnetic fields. The VXR300 spectrometer (frequency = 79.346 MHz) was equipped with a Doty MAS probe and 7 mm zirconia rotors. The CMX200 spectrometer (frequency = 52.938 MHz) was equipped with a Chemagnetics HX probe and 7.5 mm zirconia Pencil rotors. Pulse-durations were approximately half the optimum value for the sodium chloride solution reference. Further experimental details may be found in table 5.25. The spectra are shown in figures 5.37 and 5.38. Apparent chemical shifts, δ_{Na}*, and a measure of the width of the total signal are listed in table 5.26.

Silicate	Sample	Spectro-meter	Numbers of Transients	Recycle Delay / s	Spinning Rate / kHz
Makatite	mka	VXR300	200	2	5.20
Kanemite	kna	VXR300	500	2	5.07
Makatite	mka	CMX200	788	1	1.96
Kanemite	knb	CMX200	1024	1	4.08

Table 5.25 Acquisition parameters for 79.346 MHz (VXR300) and 52.938128 MHz (CMX200) ^{23}Na SP spectra of makatite and kanemite.

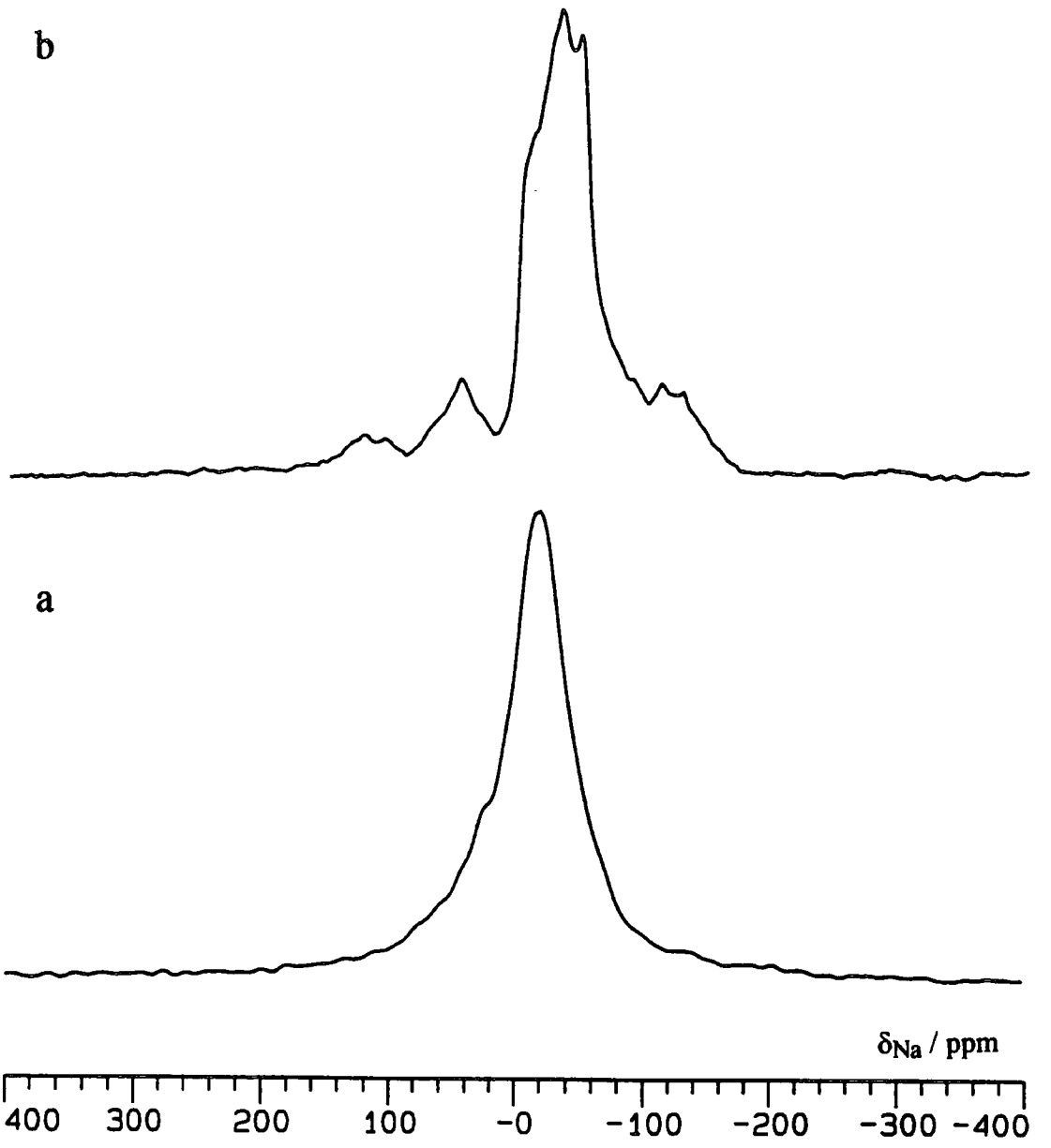

Figure 5.37 Sodium-23 SP spectra with a spectrometer frequency of 79.346 MHz: a) makatite (sample mka); and b) kanemite (sample kna).

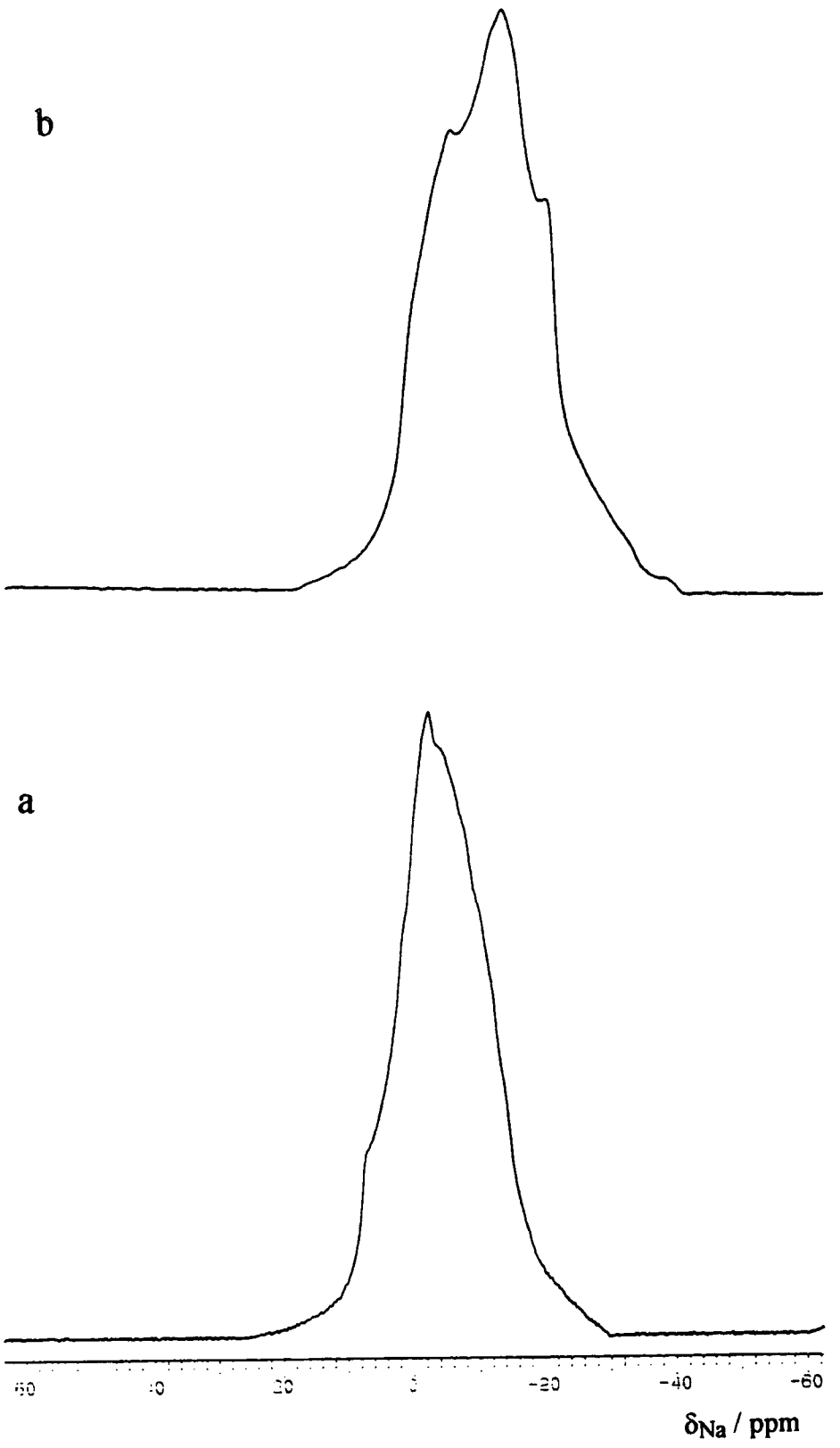

Figure 5.38 Sodium-23 SP spectra with a spectrometer frequency of 52.938128 MHz: a) makatite (sample mka); and b) kanemite (sample kna).

Silicate	Sample	Spectrometer Frequency / MHz	Apparent Chemical Shift, δ_{Na}* / ppm	Total Width, $\Delta_{1/2}$ / Hz
Makatite	mka	79.346	-2.7	1300
Kanemite	kna	79.346	-12.1	2200
Makatite	mka	52.938128	-17.2	2800
Kanemite	knb	52.938128	-33.2	2900

Table 5.26 Chemical shift and line-width information for ^{23}Na SP spectra of makatite and kanemite. The apparent chemical shift relates to the frequency of the signal maximum, while the width is the full-width at half-height of the whole absorption.

The known unit cell of makatite contains two distinct sodium ions in a 1:1 ratio.[16] Assigning these makatite spectra with respect to this unit cell is not possible as they are too distorted. Similarly, little information can be obtained from the kanemite spectra. The distortions can be attributed to second order quadrupolar effects as the chemical shift appears to depend heavily on the spectrometer frequency. Since there are second-order effects it is probable that only the central transitions are being excited.

The ^{23}Na SP spectra obtained by Nesbitt for these samples were similarly uninformative.[1] However, better spectra might be acquired with a higher spectrometer frequency: the absorptions would be narrower and distinct sodium species might be resolvable. Alternatively, interesting spectra might be obtained with any of the special techniques for quadrupolar nuclei, such as DAS, DOR, VAS or sonically-induced NMR. Mueller *et al.* obtained a successful ^{23}Na DAS spectrum for a $Na_2C_2O_4$ sample which had a similar ^{23}Na SP/MAS spectrum to the 52.8 MHz spectrum of kanemite in this work (figure 5.38b).[61]

5.5.4 Octosilicate, Magadiite and Kenyaite ^{23}Na Single-Pulse Spectra

Nesbitt acquired ^{23}Na SP spectra for several magadiite and kenyaite samples. Some had two peaks while others had one signal. The extra peak was assumed to be structurally important as it gave no signal on cross-polarisation and could be assigned to isolated sodium ions.[1,58] In this work several new octosilicate, magadiite and kenyaite samples were available for study, together with some that had probably previously been analysed by Nesbitt. Examples of each silicate have been found with one and two ^{23}Na SP signals. As with makatite and kanemite, ^{23}Na SP spectra for these samples have been obtained at two spectrometer frequencies.

Single-pulse ^{23}Na spectra have been acquired using the CMX200, CXP200, VXR300 and Varian Unity Plus 300 spectrometers. These have been equipped with Chemagnetics HX and Doty MAS probes. The former used 7.5 mm zirconia Pencil rotors, while the latter used 7 mm zirconia or sapphire rotors. With all the spectrometers, standard single-pulse sequences were used. Further experimental details may be found in table 5.27. Spectra are shown in figures 5.39, 5.40, 5.41 and 5.42; contiguous plotting was not always possible as different spectrometers were used. Apparent chemical shift and line-width details are listed in table 5.28.

Silicate (Sample)	Spectro-meter Frequency	Spectro-meter	Numbers of Transients	Recycle Time / s	Spinning-Rate / kHz
Octosilicate	52.938	CMX200	16	2	2.06
(oca)	79.342	Unity Plus	200	2	4.0
Magadiite	52.938	CMX200	100	1	2
(mgf)	79.342	Unity Plus	300	2	4.3
Kenyaite	52.938	CMX200	260	1	2.04
(kyb)	79.346	VXR300	20	30	3.92
Octosilicate	52.938	CMX200	12	60	4.1
(occ)	79.342	Unity Plus	28	30	4.1
Magadiite	52.938	CMX200	156	100	4
(mga)	79.346	VXR300	40	30	3.90
Kenyaite	52.938	CXP200	244	10	3.9
(kya)	79.342	Unity Plus	32	30	2.5

Table 5.27 Experimental details for the acquisition of ^{23}Na SP spectra of two samples each of octosilicate, magadiite and kenyaite.

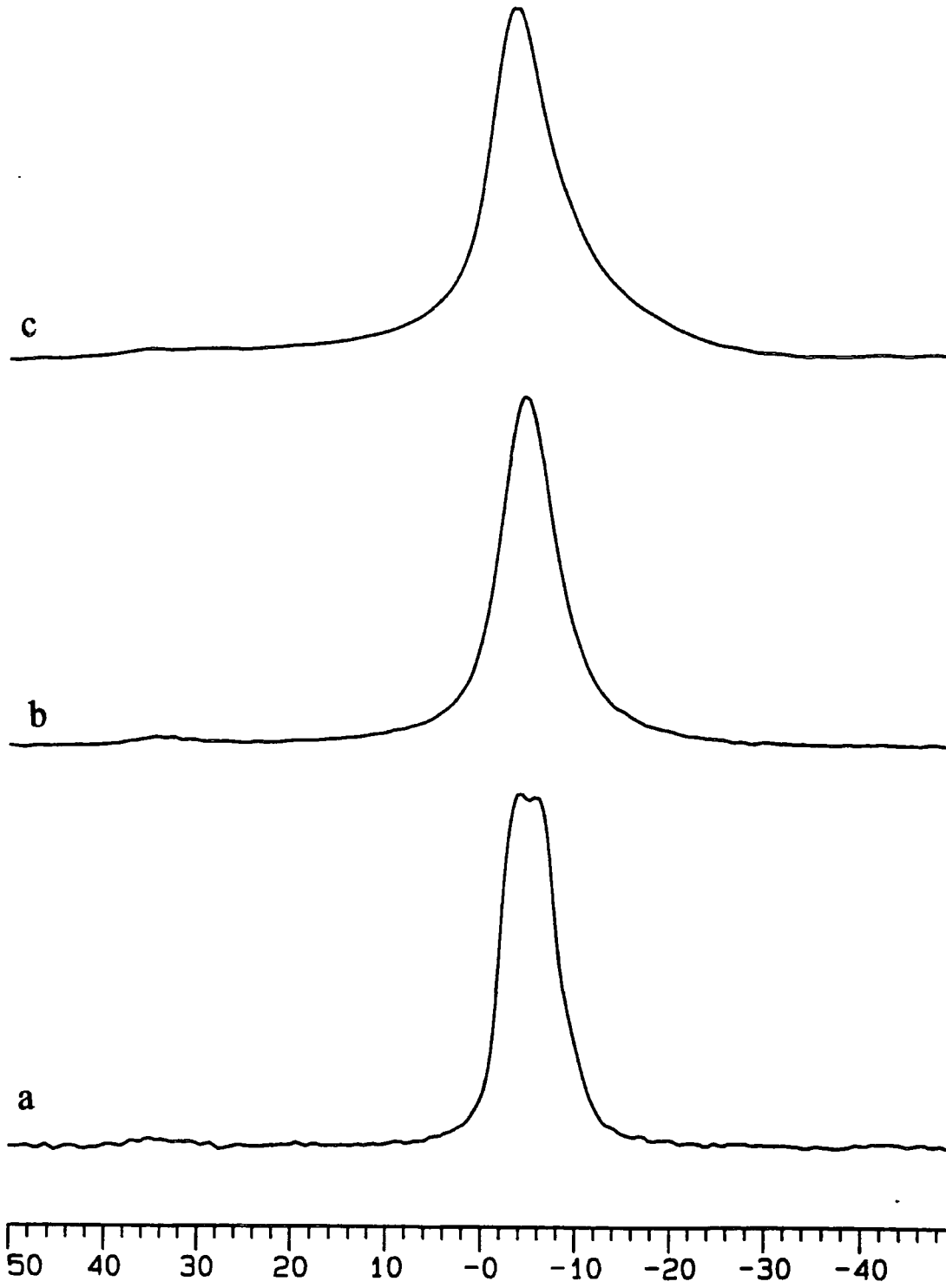

Figure 5.39 Single-pulse ^{23}Na spectra (spectrometer frequency = 52.938 MHz) for three layered sodium polysilicate hydrate samples: a) octosilicate (sample oca); b) magadiite (sample mgf); and c) kenyaite (sample kyb).

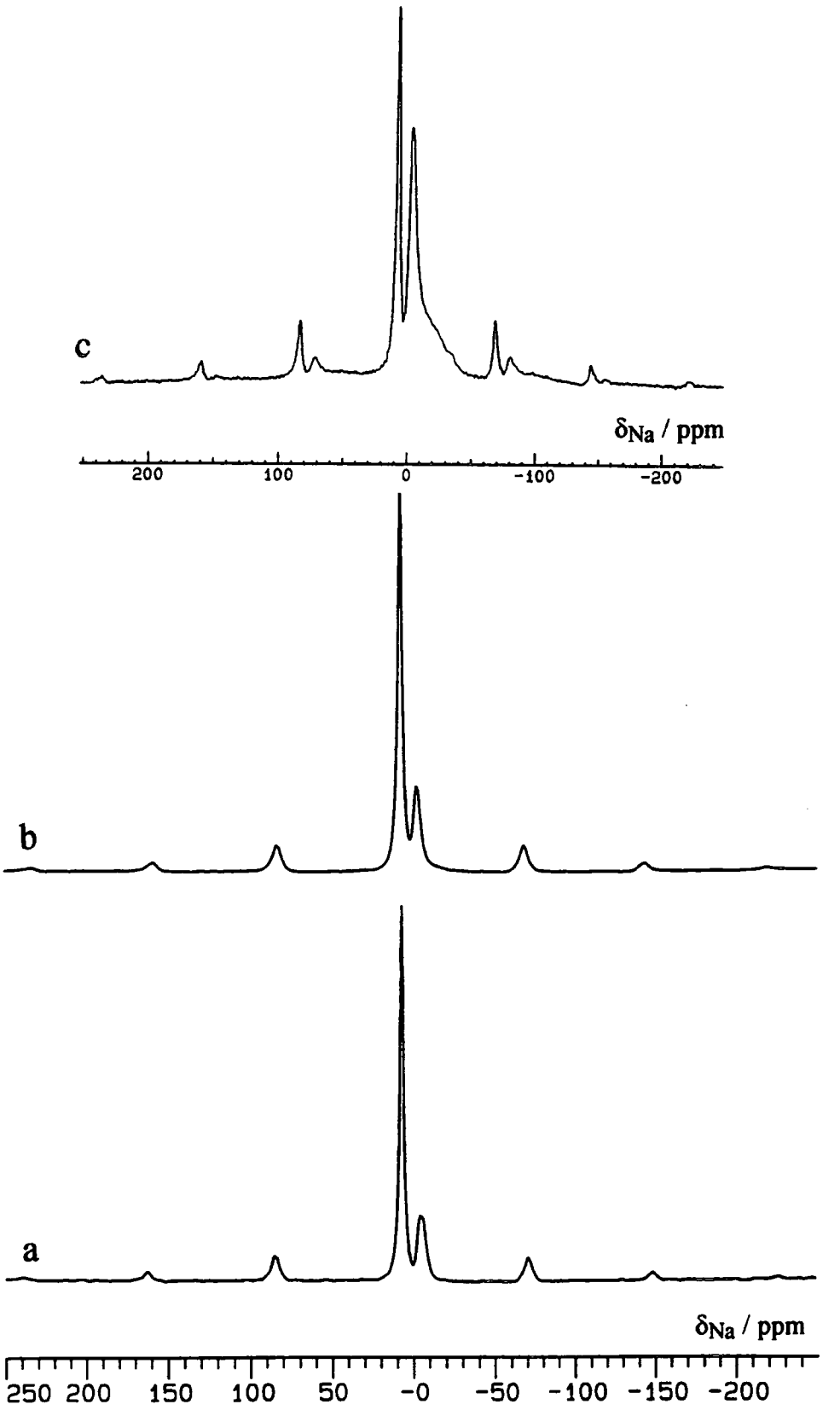

Figure 5.40 Single-pulse ^{23}Na spectra (spectrometer frequency = 52.938 MHz) for three layered sodium polysilicate hydrate samples: a) octosilicate (sample occ); b) magadiite (sample mga); and c) kenyaite (sample kya).

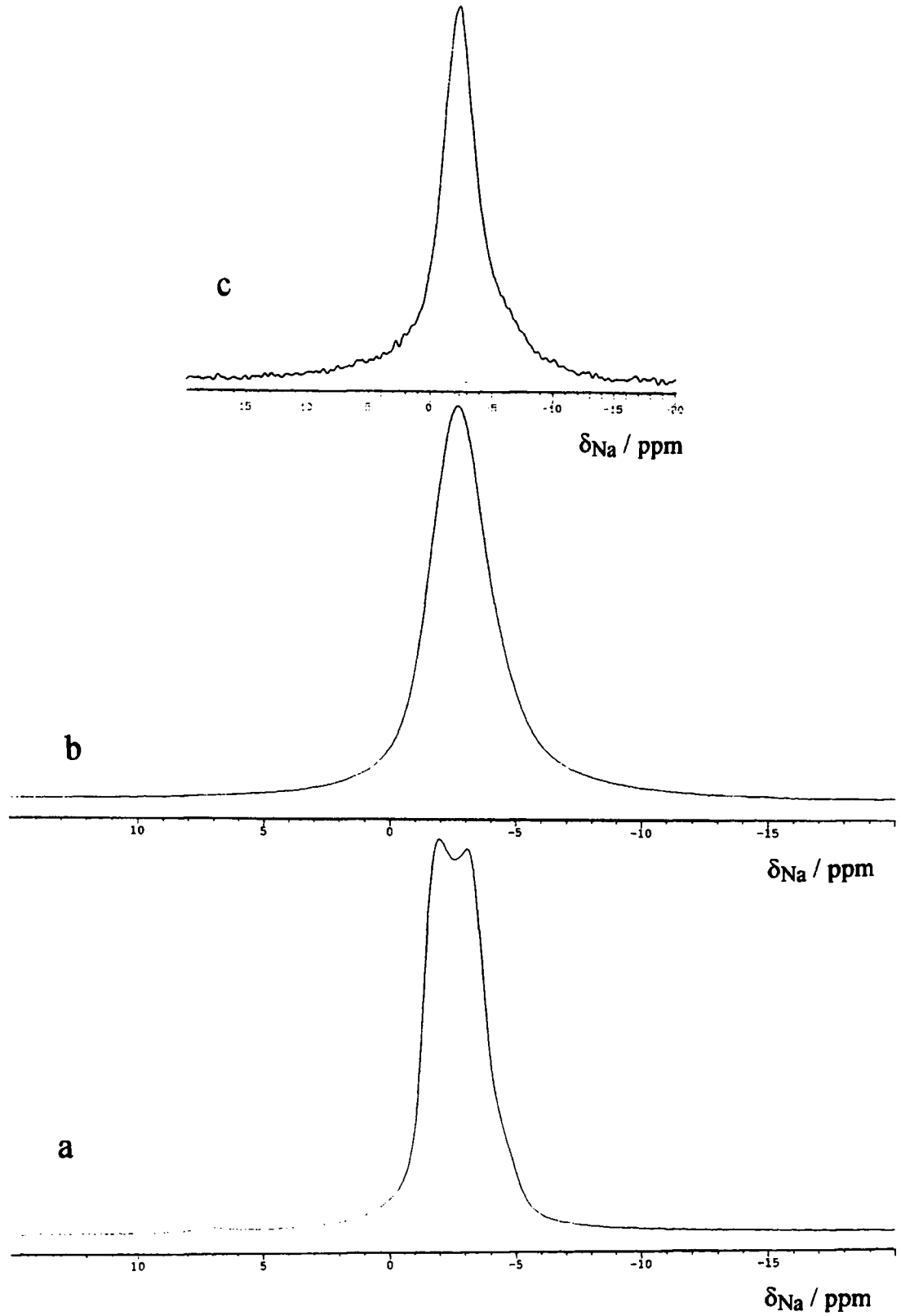

Figure 5.41 Single-pulse ^{23}Na spectra (spectrometer frequency = 79.3 MHz) for three layered sodium polysilicate hydrate samples: a) octosilicate (sample oca); b) magadiite (sample mgf); and c) kenyaite (sample kyb).

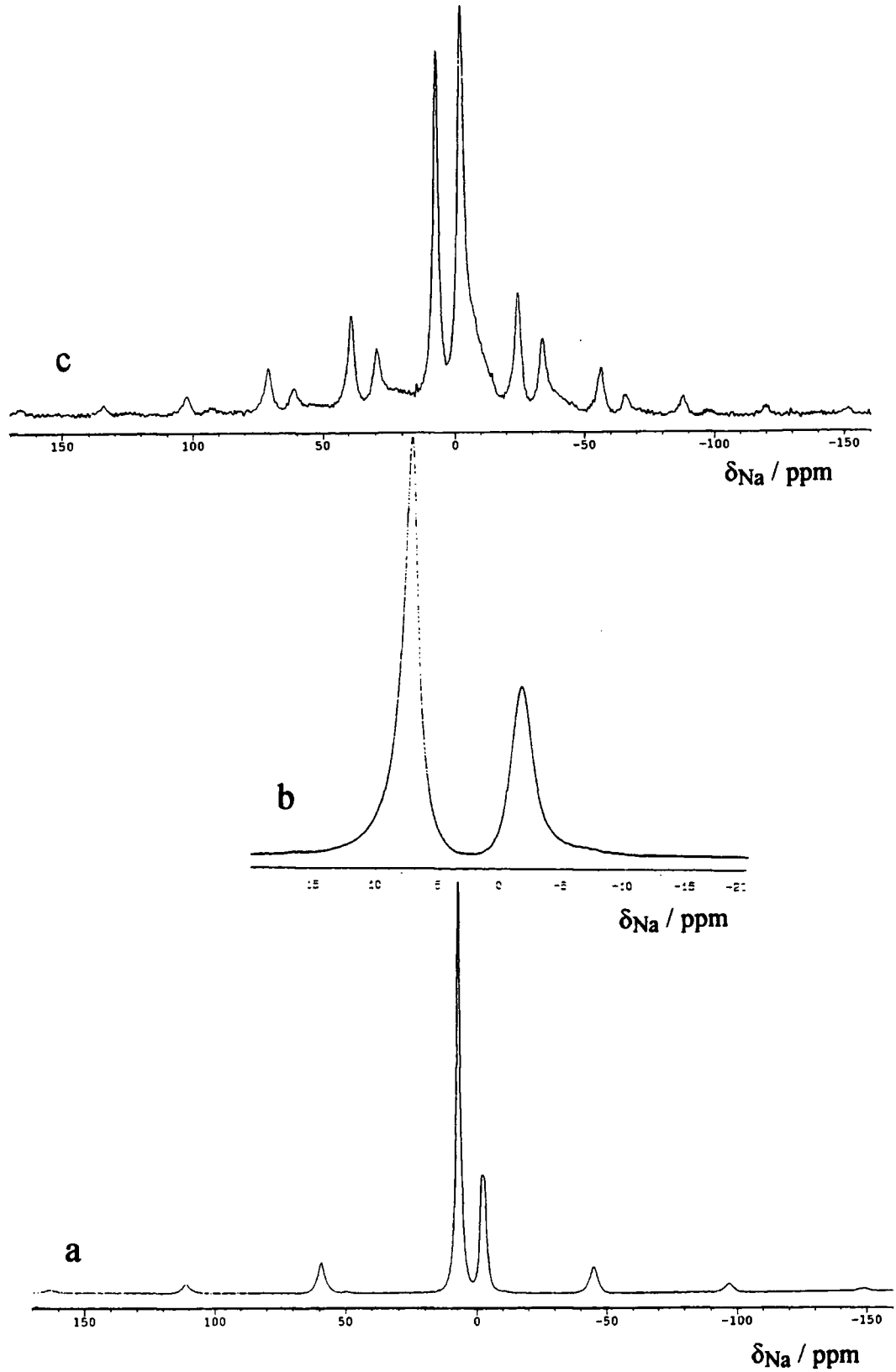

Figure 5.42 Single-pulse ^{23}Na spectra (spectrometer frequency = 79.3 MHz) for three layered sodium polysilicate hydrate samples: a) octosilicate (sample occ); b) magadiite (sample mga); and c) kenyaite (sample kya).

Silicate (sample)	52.938 MHz Spectrometer Frequency				79.3 MHz Spectrometer Frequency			
	δ_{Na}* / ppm	$\Delta\frac{1}{2}$ / Hz	δ_{Na}* / ppm	$\Delta\frac{1}{2}$ / Hz	δ_{Na}* / ppm	$\Delta\frac{1}{2}$ / Hz	δ_{Na}* / ppm	$\Delta\frac{1}{2}$ / Hz
Octosilicate (oca)			-4.0 -5.6†	330‡			-2.1 -3.1†	210‡
Magadiite (mgf)			-4.6	350			-2.6	225
Kenyaite (kyb)			-4.3	400			-1.9	200
Octosilicate (occ)	7.0	150	-4.8	430	7.1	125	-2.4	200
Magadiite (mga)	7.1	210	-3.1	320	7.3	140	-1.7	200
Kenyaite (kya)	7.5	250	-4.0	400	7.1	200	-2.3	225

Table 5.28 Apparent chemical shifts, δ_{Na}*, and full-widths at half peak, $\Delta\frac{1}{2}$, heights for the ^{23}Na SP spectra of two samples each of octosilicate, magadiite and kenyaite. Chemical shifts are measured relative to aqueous sodium chloride (1 mol dm^{-3}). As there is some variation in the spectrometer frequencies and standard solutions that have been used, they are reproducible to ±0.5 ppm, only. †Unresolved doublet. ‡The total width of the doublet.

Two types of octosilicate, magadiite and kenyaite sample have been identified. Some samples have a single ^{23}Na SP peak while two are observed in others. These were the only two kenyaite studies available for this work, but all the other magadiite and octosilicate samples that were tested gave ^{23}Na SP spectra with a single signal around δ_{Na}* -3, at 52.938 MHz. The samples with two signals seem to be rarer and literature examples of such samples have all been natural.[1,28] However, there is no simple correlation between sample-origin and the number of signals– natural samples have given only one signal in the work of Nesbitt,[1] while the octosilicate sample in this work is, of course, synthetic.

The chemical shift and line-width details in table 5.28 show that the single peak observed in most samples is similar to the low-frequency line in any spectra with two peaks. It is likely that the species responsible for these signals is the same and present in all samples of octosilicate, magadiite or kenyaite. Thus, the second signal in some samples corresponds to sodium ions of a type which are not found in the other samples.

The chemical shifts of the rarer, high-frequency signals are approximately the same in all three samples at both magnetic fields– the observed range of the values, 0.5 ppm, is the same order as the reproducibility of the measurements. There is much more variation in the lower frequency signal chemical shifts. These vary from sample to sample and also vary significantly with magnetic field. It can be concluded that second-order effects are being observed with the lower-frequency signals only.

Both spectra of octosilicate (sample oca) consist of a convoluted absorption at a negative chemical shift. The shape of the lines could be caused by overlapping distinct species or quadrupolar interactions distorting a single signal. The low-frequency signal of octosilicate (sample occ) is distorted at the higher magnetic field, only. Since second-order quadrupolar effects decrease with increasing magnetic field, it is likely that slightly different sodium species are being resolved in these spectra. Spectra obtained at a still higher magnetic field might confirm such a conclusion.

5.5.5 Identification of the Species Responsible for Extra ^{23}Na Single-Pulse Signals

Two types of octosilicate, magadiite and kenyaite sample have been identified by ^{23}Na NMR. For octosilicate, particularly, ^{1}H MAS and ^{29}Si NMR spectra are very similar for the two types of sample (see sections 5.1.6 and 5.2.4). Powder X-ray diffraction patterns were measured for both types of octosilicate sample to investigate any structural differences which might be responsible for the extra sodium species.

Figure 5.43 shows powder X-ray diffraction patterns for two octosilicate samples. Sample ocb has a single ^{23}Na SP signal, while sample occ has two signals. These were acquired with a Phillips PW1050 powder diffractometer. The results were analysed using Sietrononics trace processing software for spike removal, Cu Kα2 subtraction and d-spacing calculation. In both cases, the patterns are similar to those previously reported for octosilicate[24] and the strong peak at 8.20° 2θ corresponds to a basal-spacing, d_{001}, of 11.1 Å. There are extra, intense lines in the pattern for sample occ at 31.68° 2θ and 45.42° 2θ. These and some smaller signals are clearly shown in figure 5.43(c) which is the difference of the two patterns– the negative peaks are an octosilicate powder pattern and the positive peaks correspond closely to a sodium chloride pattern figure 5.43(d). Therefore, it seems likely that the extra signal observed in some samples of octosilicate, magadiite and kenyaite is due to contamination with sodium chloride.

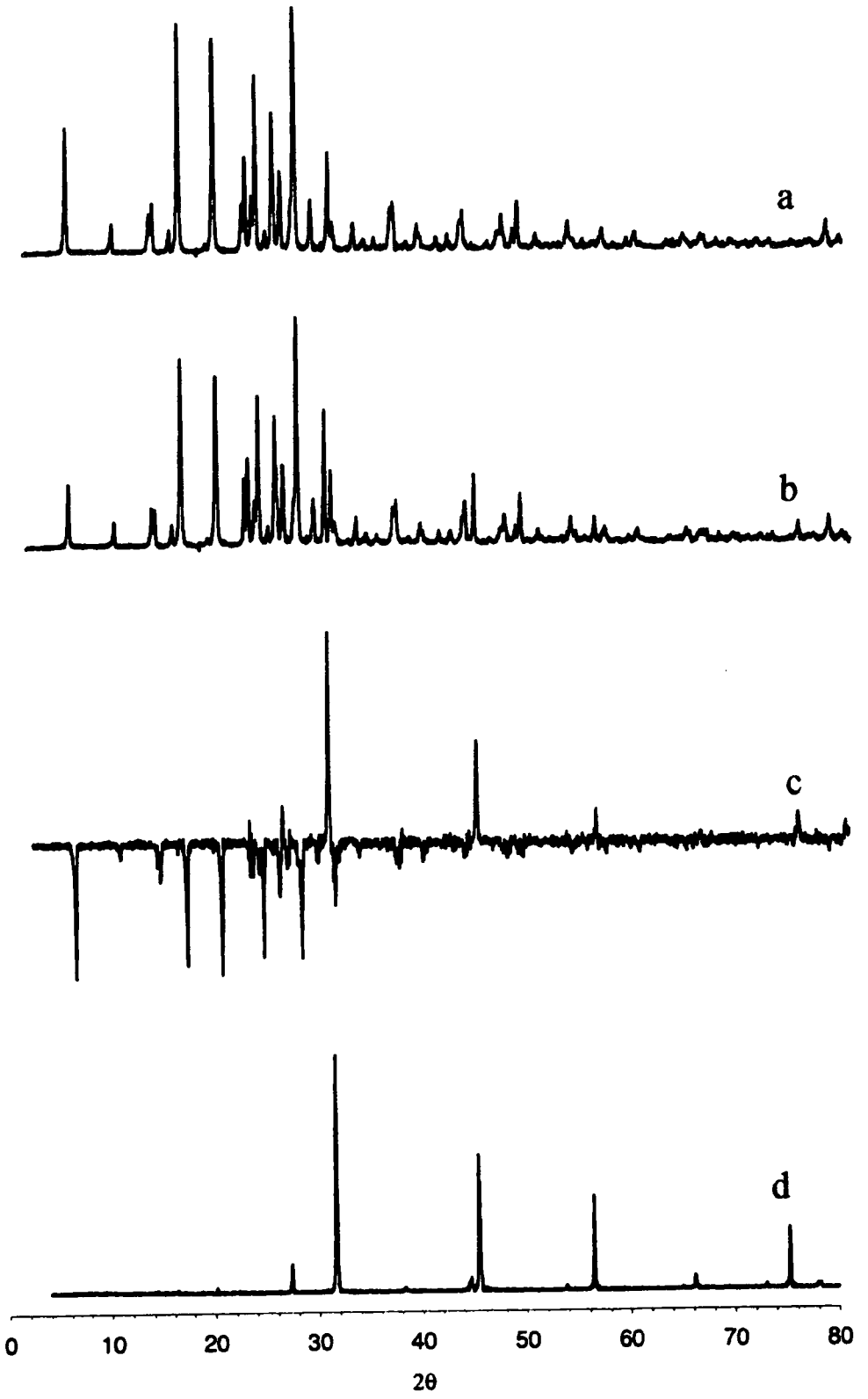

Figure 5.43 Powder X-ray diffraction patterns: a) octosilicate (sample ocb); b) octosilicate (sample occ); c) the difference between (b) and (a); and d) sodium chloride.

To test the hypothesis, a ^{23}Na single-pulse spectrum of an octosilicate (sample occ, 0.1009 g) and sodium chloride (0.0510 g) mixture was acquired using the CMX200 spectrometer, equipped with 7.5 mm zirconia Pencil rotors (figure 5.44). The acquisition parameters were 16 transients, a recycle-delay of 75 s and a spinning-rate of 3 kHz.

The spectrum consists of two isotropic lines at δ_{Na}* 7.0 and δ_{Na}* -5 together with several spinning side-bands. The peaks can be integrated to give a value of 16 for the ratio of δ_{Na}* 7.0 signals (and spinning side-bands) to the lower-frequency signal. The spectrum can be compared with figure 5.40(a), the ^{23}Na SP spectrum of octosilicate (sample occ). The only effect of adding salt to octosilicate is an increase in the relative intensity of the δ_{Na}* 7 signal. Therefore, it is very likely that sodium chloride is responsible for this signal and the similar signals in magadiite (sample mga) and kenyaite (sample kya).

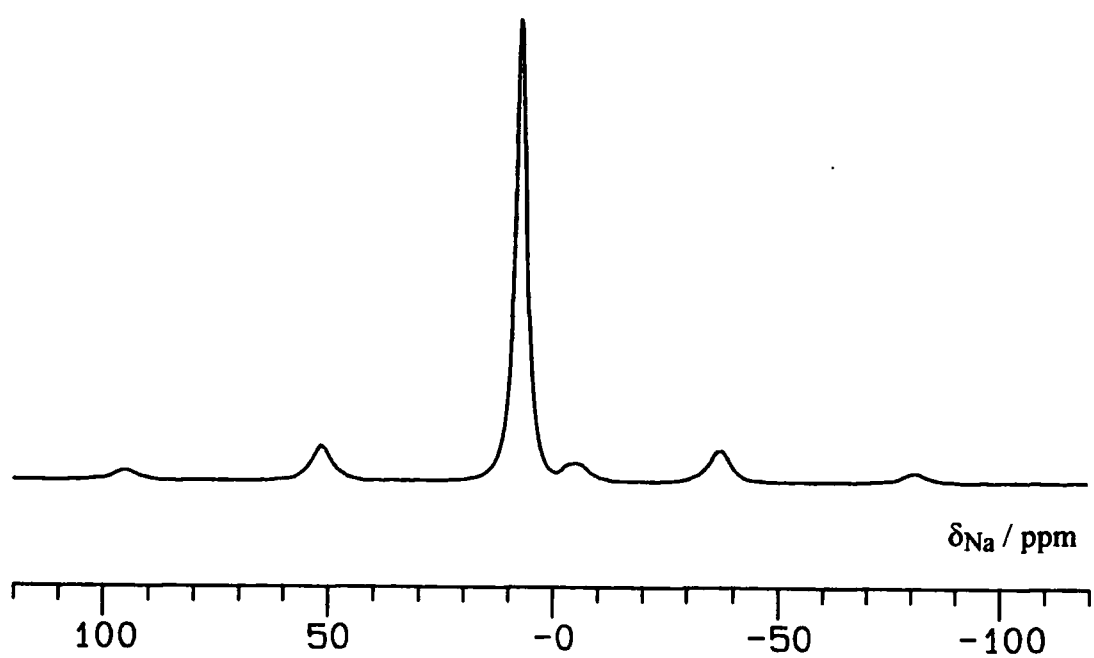

Figure 5.44 Sodium-23 SP spectrum of an octosilicate and sodium chloride mixture.

5.5.6 Reassessment of the ^{23}Na NMR Data

The powder X-ray diffraction patterns in figure 5.43 clearly show that the extra ^{23}Na SP signal for some octosilicate, magadiite and kenyaite samples is due to contamination with sodium chloride. Thus, the interesting conclusion of Nesbitt, concerning the intralayer siting of the relevant sodium species has been disproved. Prior to obtaining the p-XRD result, comparison of the two types of ^{23}Na NMR signal and the two types of sample had appeared an essential area for research in this work. Therefore, many NMR results have been attained which are now of limited importance. These results and the results from the preceding section are summarised in table 5.29.

Experiment	Sodium Chloride Signal	Layered Sodium Polysilicate Hydrate Signal	Further Information
Apparent Chemical Shift, δ_{Na}* / ppm	*ca.* 7	-2 to -5	A general result– all samples at both magnetic fields
Effect of Increasing the Spectrometer Frequency	Little significant change.	Sharper lines are obtained at less-negative apparent chemical shifts.	A general result– all samples at both magnetic fields
Cross-Polarisation Behaviour	No signal	Signal	A general result– all samples at 52.9 MHz
Spin-Lattice Relaxation Time T_1 / s	13.1 ± 0.3^a 12.3 ± 3.3^b	0.0039 ± 0.0003^a 0.0084 ± 0.0010^b	52.9 MHz Octosilicate (occ)[a] Magadiite (mga)[b]

Table 5.29 Comparison of the NMR results for the two ^{23}Na SP signals observed in some samples of octosilicate, magadiite and kenyaite.

The environment of the sodium nucleus in sodium chloride is cubic. Since this is a symmetrical environment, there should be no electric field gradient at the nucleus and a zero value for the quadrupolar coupling constant might be expected (equation 5.19). Therefore, the invariance of the chemical shift of the ^{23}Na SP signal with spectrometer frequency is understandable. There are no protons in NaCl, so a cross-polarisation signal would not be expected. The long spin-lattice relaxation is consistent with the lack of protons and zero value of χ.

The chemical shift and line-widths of the layered sodium polysilicate hydrate ^{23}Na SP signals vary considerably with spectrometer frequency in line with second order effects from strong quadrupolar interactions. The silicates are hydrous, so a CP signal is understandable, and the short spin-lattice relaxation times are more typical of quadrupolar nuclei.

Gaining quantitative information regarding the extent of the NaCl contamination in these samples is difficult. Firstly, the selectivity of the spectrum must be considered: the central transition comprises 40 % of the total signal intensity. Additionally, the optimum pulse-durations of the NaCl and layered sodium polysilicate hydrate signals in these samples are not necessarily the same, since the value for a selectively excited signal will be smaller than that for a case with weak quadrupolar interactions.[64] For an approximation, the integrated intensities of the octosilicate (sample occ) and magadiite (sample mga) spectra in figure 5.40 will be used; these are 3.3:1 and 4:1, respectively for the ratio of sodium chloride signals to layered sodium polysilicate hydrate signals. If it is assumed that all NaCl transitions are observed while only the central transition for the silicate is seen, then these values over-estimate the ratio of moles of sodium in NaCl to moles of sodium in octosilicate or magadiite by a factor of 5/2. The formula mass of sodium chloride is 58.5 g mol^{-1}, while the formulae masses of octosilicate and magadiite ($Na_2O{:}8SiO_2{:}9H_2O$ and $Na_2O{:}14SiO_2{:}10H_2O$) are 704 g mol^{-1} and 1082 g mol^{-1}, respectively. If the silicate values are halved they represent the mass per mole of sodium. Equation 5.21 shows how these ratio and formula mass values can be related to the fraction of NaCl (by

weight) in each sample. The extent of sodium chloride contamination can be estimate at 18 % and 15 % by mass for octosilicate (sample occ) and magadiite (sample mga), respectively.

$$\text{fraction by mass of NaCl} = \left(\frac{58.5 \times \text{ratio}}{58.5 \times \text{ratio} + 2.5 \times \frac{\text{formula mass}}{2}} \times 100 \right)\% \qquad \text{Eq. 5.21}$$

$$\text{in octosilicate (sample occ):} \quad \left(\frac{58.5 \times 3.3}{58.5 \times 3.3 + 2.5 \times \frac{704}{2}} \times 100 \right)\% = 18\ \%$$

$$\text{in magadiite (sample mga):} \quad \left(\frac{58.5 \times 4}{58.5 \times 4 + 2.5 \times \frac{1082}{2}} \times 100 \right)\% = 15\ \%$$

Though the accuracy of these values must be doubted, it is clear that sodium chloride contamination at a significant level is responsible for the extra ^{23}Na SP signals in some samples of octosilicate, magadiite and kenyaite. Such contamination is understandable: natural samples of these silicates come from soda-rich lakes, while sodium chloride is used as a starting material in the preparation of octosilicate.

Addenda

Though the ^{23}Na SP/MAS spectra in this chapter do certainly exhibit second-order quadrupolar effects, more information can be obtained from the chemical shifts and line-widths.

Since the width of the kanemite absorption behaves regularly with spectrometer frequency (*i.e.* $\Delta_{½} \propto 1/\nu_L$), it is likely that the spectra contain a single signal. The isotropic chemical shift, δ_{iso} and ν_Q, the quadrupole interaction constant (e^2qQ/h) can be calculated using the following equation.[64]

$$\delta = \delta_{iso} - \frac{6000}{\nu_L^2}\left(1+\frac{\eta^2}{3}\right)\nu_Q^2$$

Two simultaneous equations can be formed. With the reasonable simplification $(1+\eta^2/3)=1$, these have solutions of $\delta_{iso} = 4.8$ ppm and $\nu_Q = 4.2$ MHz.

The octosilicate, magadiite and kenyaite spectra have signals around δ_{Na}* -2 and -4 for the two spectrometer frequencies. Using the same equation, these chemical shifts give $\delta_{iso} = -1$ ppm and $\nu_Q = 1.3$ MHz.

The isotropic chemical shifts can be related to the co-ordination around the sodium ion. If 0 ppm corresponds to co-ordination of 6, then the value for kanemite is smaller: possibly 5, which is observed in makatite. The calculated ν_Q values are typical of those listed by Freude and Haase for several sodium compounds.*

* D. Freude and J. Haase in *NMR: Basic Principles and Progress 29*, P. Diehl *et al.* (eds.), Springer-Verlag, Berlin, 1993.

References

1 G.J. Nesbitt, Ph.D. Thesis, University of Durham, 1986.

2 W. Schwieger, D. Heidemann and K.-H. Bergk, *Rev. Chim. Minérale*, 1985, **22**, 639-650.

3 W. Schwieger, K.-H. Bergk, D. Heidemann, G. Lagaly and K. Beneke, *Zeitschrift für Kristallographie*, 1991, **197**, 1-12.

4 G. Engelhardt and D. Michel, *High-Resolution Solid-State NMR of Silicates and Zeolites*, J. Wiley and Sons, Chichester, 1987.

5 A.-R. Grimmer, F. v. Lampe, M. Mägi and E. Lippmaa, *Z. Chem.*, 1983, **23**, 342.

6 K.A. Smith, R.J. Kirkpatrick, E. Oldfield and D.M. Henderson, *Am. Mineral.*, 1983, **68**, 1206-1215.

7 A.-R. Grimmer, *Chem. Phys. Lett.*, 1985, **119**, 416-420.

8 J.V. Smith and C.S. Blackwell, *Nature*, 1983, **303**, 223-225.

9 S. Ramdas and J. Klinowski, *Nature*, 1984, **308**, 521-523.

10 M. Mägi, E. Lippmaa, A. Samoson, G. Engelhardt and A.-R. Grimmer, *J. Phys. Chem.*, 1984, **88**, 1518-1522.

11 N. Janes and E. Oldfield, *J. Am. Chem. Soc.*, 1985, **107**, 6769.

12 B.L. Sherriff and H.D. Grundy, *Nature*, 1988, **332**, 819-822.

13 S. Prabakar, K.J. Rao and C.N.R Rao, *Chem. Phys. Lett.*, 1991, **183**, 176-182.

14 C.A. Fyfe, Y. Feng, H. Gies, H. Grondey and T.T. Kokotailo, *J. Am. Chem. Soc.*, 1990, **112**, 3264-3270.

15 I.S. Chuang, D.R. Kinney, C.E. Bronnimann, R.C. Ziegler and G.E. Maciel, *J. Phys. Chem.*, 1992, **96**, 4027-4034.

16 H. Annehed, L. Fälth and F.J. Lincoln, *Zeitschrift für Kristallographie*, 1982, **159**, 203-210.

17 T. Yanagisawa, K. Schimizu, K. Kuroda and C. Kato, *Bull. Chem. Soc. Japan*, 1990, **63**, 988-992.

18 T.J. Pinnavaia, I.D. Johnson and M. Lipsicas, *J. Solid State Chem.*, 1986, **63**, 118-121.

19 J. Rocha and J. Klinowski, *J. Magn. Reson.*, 1990, **90**, 567-568.

20 P.F. Barron, *Nature*, 1983, **303**, 49-50.

21 J.G. Thompson and P.F. Barron, *Clays and Clay Minerals*, 1987, **35**, 38-42.

22 J.G. Thompson, *Clays and Clay Minerals*, 1984, **32**, 223.

23 D.E. Woessner and J.C. Trewella, *J. Magn. Reson.*, 1984, **59**, 352.

24 G. Borbély, H.K. Beyer and H.G. Karge, *Clays and Clay Minerals*, 1991, **39**, 490-497.

25 J.S. Dailey and T.J. Pinnavaia, *Journal of Inclusion Phenomena and Molecular Recognition in Chemistry*, 1992, **13**, 47-61.

26 D. Heidemann, Poster, Eleventh International Meeting on NMR Spectroscopy, 1993.

27 D.A. Torchia, *J. Magn. Reson.*, 1978, **30**, 613-616.

28 J.M. Rojo, E. Ruiz-Hitzky and J. Sanz, *Inorg. Chem.*, 1988, **27**, 2785-2790.

29 J.P. Yesinowski, H. Eckert and G.R. Rossman, *J. Am. Chem. Soc.*, 1988, **110**, 1367-1375.

30 H. Eckert, J. Yesinowski, L.A. Silver and E.M. Stolper, *J. Phys. Chem.*, 1988, **92**, 2055-2064.

31 S.C. Kohn, R. Dupree and M.E. Smith, *Nature*, 1989, **337**, 539-541.

32 B. Berglund and R.W. Vaughan, *J. Chem. Phys.*, 1980, **73**, 2037.

33 C.M. Rohlfing, L.C. Allen and R. Ditchfield, *J. Chem. Phys.*, 1983, **79**, 4958.

34 H. Rosenberger, R. Zeiss and A.-R. Grimmer, *Z. Chem.*, 1975, **15**, 162-163.

35 A.-R. Grimmer and H. Rosenberger, *Z. Chem.*, 1978, **18**, 378.

36 H. Rosenberger and A.-R. Grimmer, *Z. anorg. allg. Chem.*, 1979, **448**, 11-22.

37 A. Kalt and R. Wey, *Bull. Groupe fr. Argiles*, 1968, **20**, 205.

38 Z.Q. Deng, J.F. Lambert and J.J. Fripiat, *Chemistry of Materials*, 1989, **1**, 375-380.

39 D.M. Millar and J.M. Garces in M.L. Occelli and H.E. Robson, eds., *Synthesis of Microporous Minerals Vol. II*, 1992, Van Nostrand Rheinhold, New York, 1992, 187-206.

40 M.T. Le Bihan, A. Kalt and R. Wey, *Bull. Soc. Fr. Minéral. Cristallogr.*, 1971, **94**, 15.

41 J. Kümmerlen, L.H. Merwin, A. Sebald and H. Kepler, *J. Phys. Chem.*, 1992, **96**, 6405-6410.

42 G. Engelhardt, J. Felsche and P.Sieger, *J. Am. Chem. Soc.*, 1992, **114**, 1173-1182.

43 G. Engelhardt, P.Sieger and J. Felsche, *Angew. Chem. Int. Ed. Engl.*, 1992, **31**, 1210-1212.

44 M.M. Maricq and J.S. Waugh, *J. Chem. Phys.*, 1979, **70**, 3300.

45 C.L. McKnett, C.R. Dybowski and R.W Vaughan, *J. Chem. Phys.*, 1975, **63**, 4578.

46 D.N. Smith, Ph.D. Thesis, University of Aberdeen, 1981.

47 (a) S.W. Homans, *A Dictionary of Concepts in NMR*, Clarendon Press, Oxford, 1989, 49-51. (b) M.K. Levitt, *J. Magn. Reson.*, 1982, **48**, 234.

48 P. Clarke, Ph.D. Thesis, University of Durham, 1991.

49 N. Bloembergen, *Physica*, 1949, 15, 186.

50 R.R. Ernst, G. Bodenhausen and A. Wokaun, *Principles of Nuclear Magnetic Resonance in One and Two Dimensions*, Clarendon Press, Oxford, 1987.

51 D. Suter and R.R. Ernst, *Phys. Rev. B*, 1982, **25**, 6038.

52 N. Bloembergen, S. Shapiro, P.S. Pershau and J.O. Artman, *Phys. Rev.*, 1959, **114**, 445-459.

53 J. Jeener, B.H. Meier, P. Bachmann and R.R. Ernst, *J. Chem. Phys.*, 1979, **71**, 4546.

54 N.M. Svezerenyi, M.J. Sullivan and G.E. Maciel, *J. Magn. Reson.*, 1982, **47**, 462-475.

55 C. Connor, A. Naito, K. Takegoshi and C.A. McDowell, *Chem. Phys. Lett.*, 1985, **113**, 123-128.

56 N.M. Svezerenyi, A. Bax and G.E Maciel, *J. Am. Chem. Soc.*, 1983, **105**, 2579-2582.

57 L.D. Field, N. Bampos and B.A. Messerle, *Magn. Res. in Chem.*, 1991, **29**, 36-39.

58 R.K. Harris and G.J. Nesbitt, *J. Magn. Reson.*, 1988. **78**, 245.

59 C.A. Fyfe in P. Granger and R.K. Harris, eds., *Multinuclear Magnetic Resonance in Liquids and Solids– Chemical Applications*, Kluwer Academic Publishers, Dordrecht, 1990, 311-337.

60 A. Samoson and E. Lippmaa, *J. Magn. Reson.*, 1989, **84**, 410-416.

61 K.T. Mueller, B.Q. Sun, G.C. Chingas, J.W. Zwanziger, T. Terad and A. Pines, *J. Magn. Reson.*, 1990, **86**, 470-487.

62 S. Ganapathy, S. Schramm and E. Oldfield, *J. Chem. Phys.*, 1982, **77**, 4360-4365.

63 J. Homer, Lecture, Eleventh International Meeting on NMR Spectroscopy, University College, Swansea, 1993.

64 R. Challoner, Ph.D. Thesis, University of Durham, 1989.

Chapter Six Acidification and Ion-Exchange

6.1 Introduction

The capacity for ion-exchange is an important property of the layered sodium polysilicate hydrates. New silicate phases can be prepared with simple reactions where sodium ions are replaced by protons or metal cations. In this work, five different silicic acids of kanemite, octosilicate and magadiite have been prepared from suspensions of the parent sodium silicate in dilute hydrochloric acid. The products have been characterised by a variety of analytical techniques: ^{29}Si CP NMR, thermogravimetric analysis, powder X-ray diffraction and ^{1}H MAS NMR.

The treatment of minerals with acid solutions tends to give amorphous products.[1] However, crystalline phases have been reported from some silicates: meta-, di- and trisilicates (Schwarz and Menner, 1924);[2] gillespite, (Pabst, 1958)[3] apophyllite, carletonite and gillespite (Lagaly and Matouschek, 1980);[4] and $KHSi_2O_5$ (Wey and Kalt, 1967).[5] The layered sodium polysilicate hydrates also produce crystalline phases.

There are several possible ways of naming silicate acidification products and the general term silicic acid will be used in this work. They have also been called "crystalline phyllosilicic acids", "crystalline silica hydrates" and the term "leached" can be used (leached kenyaite, for example). No systematic nomenclature exists for naming individual silicic acids; an H- prefix will be used to name those derived from minerals (H-magadiite, H-apophyllite, *etc.*).[1] Mineral names (magadiite, for example) will be used solely to refer to sodium forms, though a prefix, Na-, might sometimes be added for emphasis.

Many authors have investigated the exchange of sodium for protons over the last thirty years and the work of Beneke, Lagaly and co-workers has been particularly extensive.[1,6-10] The resultant silicic acids have been characterised by several techniques, including powder X-ray diffraction, thermogravimetric analysis and, more

recently, ^{29}Si NMR. The analyses reveal that the products are still hydrated layered materials, though they have smaller basal spacings and less structural water. H-Makatite has been studied Schwieger *et al.*[11] They reported a 7 ppm change in the makatite Q^3 chemical shift on acidification. No NMR studies of kanemite acidification products have been reported, though work by Beneke and Lagaly[6] and Kalt and Wey[12] indicated that the products are disilicic acids. Several stable forms of $H_2Si_2O_5$ have been reported, along with many NMR, p-XRD and TGA analyses.[13,14] Borbély *et al.* prepared two H-octosilicate samples. Mild heating created one form from the other and caused a large change in ^{29}Si Q^3 chemical shift.[15] Heidemann *et al.* reported ^{29}Si NMR spectra for what was probably the high-temperature form.[16] Previously, Iler had shown that drying an H-octosilicate sample at 30 °C gave a product with a smaller basal spacing.[17] Many examples of H-Magadiite exist in the literature, with some variation in reported basal-spacings. In 1969, Brindley made the first silicic acid with a basal-spacing of 11.2 Å.[18] A similar value for H-magadiite has been reported by two authors,[19-20] but values of *ca.* 13 Å have also been reported.[8,16,21-23] The work of Lagaly *et al.* indicated that one phase changed into the other at 250 °C.[8] Beneke and Lagaly showed that leaching kenyaite could result in many different phases, with a variety of basal spacings.[1] Heidemann *et al.*[16] and Yanagisawa *et al.*[20] reported ^{29}Si NMR spectra for single H-kenyaite samples.

6.2 Synthesis

Several different ways have been reported for the preparation of silicic acids from layered sodium polysilicate hydrates. Many authors (Pinnavaia *et al.*[22] and Sprung *et al.*,[23] for example) have used the method of Lagaly *et al.*[8] for preparing H-magadiite: an aqueous suspension of the silicate (10-20 g per 100 ml of H_2O) is acidified by HCl (0.1 N) to pH 2 within 24 hours. The pH is kept stable for another 24 hours then the product is washed with water and air-dried.

Dailey and Pinnavaia[21] acidified an aqueous suspension of magadiite (18.5 g in 460 ml) with dilute aqueous HCl (0.1 N) to pH 1.9 over 12 hours. This was then centrifuged to obtain a solid product which was washed with water until chloride-free and dried in air at 40 °C. Schwieger *et al.*[11] made H-makatite by a room-temperature reaction of makatite with HCl (1 N) in a solid-to-liquid ratio of 1:100. Heidemann *et al.*[16] prepared H-octosilicate, H-magadiite and H-kenyaite by stirring the parent Na-forms with a threefold excess of HCl (0.1 N) for 24 hours at 20 °C. Brindley[18] treated natural magadiite with HCl (N/10) and washed the H-magadiite product until it was chloride-free. Borbély *et al.*[15] ion-exchanged sodium octosilicate with hydrochloric acid (1 mol dm^{-3}, 100 ml g^{-1}). The product was washed until the effluent was acid-free and then dried at room temperature. Beneke and Lagaly[1] reported that if kenyaite was stored in an excess of dilute mineral acid (for instance, HCl (0.1 mol dm^{-3})), then all interlayer sodium ions are replaced by protons. Leached silicates can also be prepared by careful titration or by treatment with aqueous aluminium salt solutions.

The method that has been used in this work is based on that of Schwieger *et al.* for makatite.[11] Thus, suspensions of the layered silicate (1 g) in an aqueous acid solution (100 cm^3) were stirred for between 30 minutes and 24 hours. The product was then filtered (fluted filter-paper, ambient pressure) and allowed to dry in air. Several silicic acids were made using this general method; more specific details are listed in table 6.1. A single sample of Al^{3+}-washed octosilicate was produced at Unilever Port Sunlight Research Laboratories.

Parent Na-Silicate	Acid Solution	Reaction Time / hours	Product
Kanemite (knc)	HCl (1 mol dm^{-3})	0.5	H-Kanemite (hka)
Kanemite (knc)	HCl (1 mol dm^{-3})	24	H-Kanemite (hkb)
Octosilicate (occ)	HCl (1 mol dm^{-3})	1	H-Octosilicate (hoa)
Octosilicate (ocb)	†	†	H-Octosilicate (hob)
Octosilicate (ocb)	HCl (1 mol dm^{-3})	5	H-Octosilicate (hoc)
Magadiite (mgb)	Al^{3+} (0.1 mol dm^{-3})	5	H-Magadiite (hma)
Magadiite (mgc)	HCl (1 mol dm^{-3})	0.75	H-Magadiite (hmb)

Table 6.1 Experimental details for the preparation of seven silicic acids from kanemite, octosilicate and magadiite. †Prepared by Dr. P. Graham at Unilever Port Sunlight Laboratories.

All the products were initially analysed by ^{29}Si NMR. The spectra showed that two types of H-octosilicate and H-magadiite were prepared. Thus, the seven silicic acids listed in table 6.1 correspond to five distinct phases. The two H-kanemite samples and two of the H-octosilicate samples (hob and hoc) were very similar.

6.3 Silicon-29 NMR

This section contains ^{29}Si CP spectra for the five different types of silicic acid sample that have been prepared from kanemite, octosilicate and magadiite. The cross-polarisation technique was chosen because high quality spectra could be acquired more quickly than with the single-pulse method.

The spectra were obtained using the CMX200 spectrometer, equipped with either a Doty MAS probe and 7 mm zirconia rotors or a Chemagnetics HX probe and 7.5 mm zirconia Pencil rotors. Further experimental details are listed in table 6.2. Contact times were chosen on the basis of variable contact time experiments. The spectra are shown in figure 6.1 and chemical shift and line-width information is listed in table 6.3.

Silicic Acid	Sample	Spinning-Rate / kHz	Number of Transients	Recycle Time / s	Contact Time / ms	Probe
H-Kanemite	hkc	2.0	32	2	4	HX
H-Octosilicate	hoa	1.98	64	2	4	HX
H-Octosilicate	hob	2	36	3	3	Doty
H-Magadiite	hma	2	128	3	4	Doty
H-Magadiite	hmb	2.04	128	2	5	HX

Table 6.2 Experimental Details for the acquisition of ^{29}Si CP spectra for five silicic acid samples.

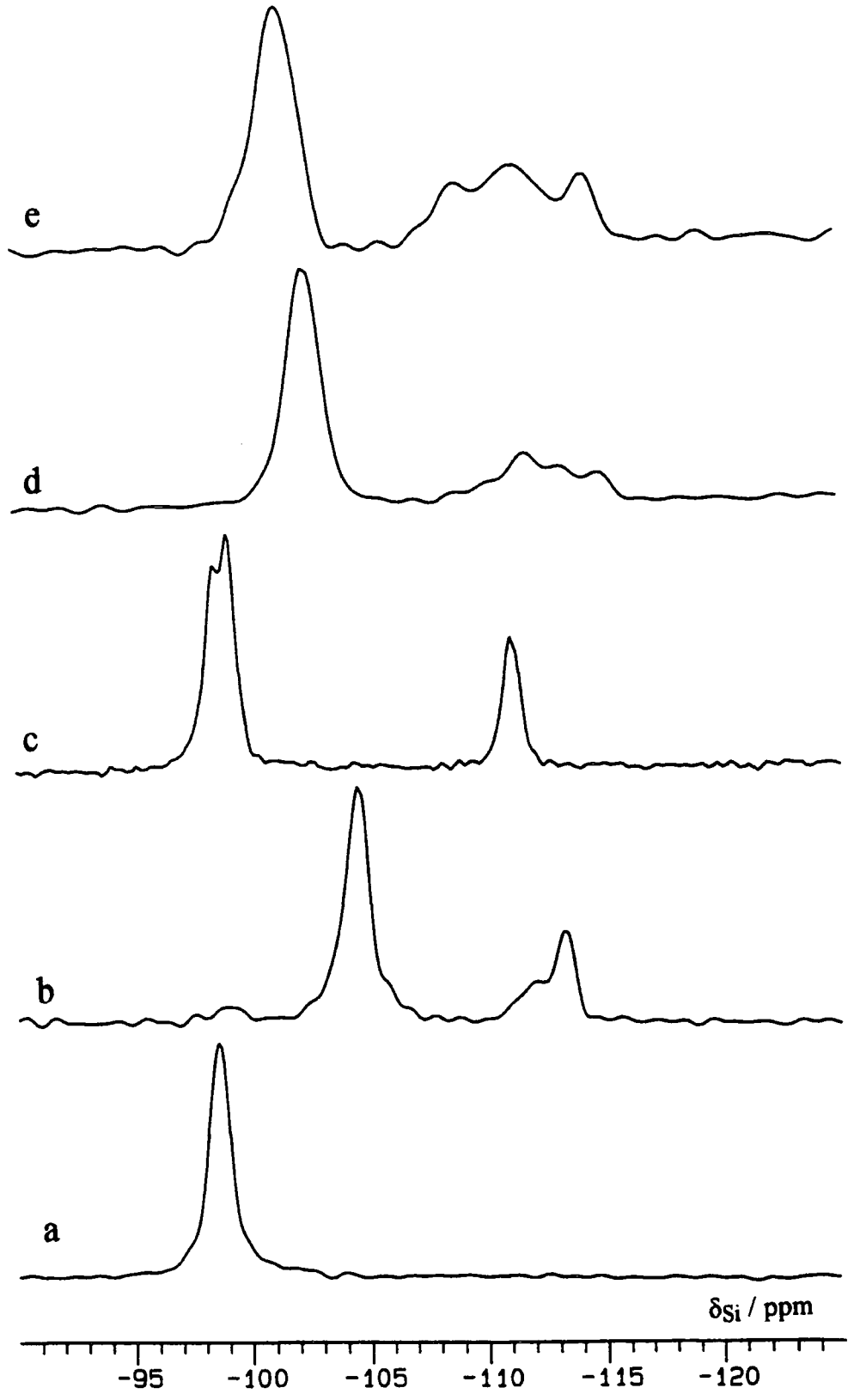

Figure 6.1 Silicic acid ^{29}Si CP spectra: a) H-kanemite (sample hkc); b) H-octosilicate (sample hoa); c) H-octosilicate (sample hob); d) H-magadiite (sample hma); and e) H-magadiite (sample hmb).

Silicate	Sample	Peak	δ_{Si} / ppm	$\Delta_{1/2}$ / Hz
H-Kanemite	hka	Q^3	-98.6	50
H-Octosilicate	hoa	Q^3	-98.9†	
			-104.4	44
		Q^4	-112.0†	
			-113.2	44
H-Octosilicate	hob	Q^3	-98.4‡	60
		Q^3	-99.0‡	
		Q^4	-111.2	34
H-Magadiite	hma	Q^3	-102.5	66
		Q^4	-111.8	60*
		Q^4	-113.1	60*
		Q^4	-114.9	60*
H-Magadiite	hmb	Q^3	-101.4	95
		Q^4	-109.1	75*
		Q^4	-112.0	150*
		Q^4	-114.6	75*

Table 6.3 Chemical shift and line width information for ^{29}Si CP spectra of five silicic acids. †Weak lines due to an impurity. ‡Two lines of approximately equal intensity and line-width (*ca.* 30 Hz). *Estimated line-widths of weak signals.

The spectra of H-kanemite (sample hka) and H-octosilicate (sample hob) are very similar to those of samples hkb and hoc, respectively (not shown). Five types of silicic acid have been prepared– there is a significant difference between the chemical shifts of the two types of H-octosilicate and H-magadiite sample. The weak signals in H-octosilicate (sample hoa) appear to come from a small amount of the other type of H-octosilicate sample.

No H-kanemite samples have been reported in the literature, but the spectrum of sample hka can be compared with the acidification products of α-$NaSi_2O_5$, $KHSi_2O_5$ and β-$NaSi_2O_5$. Beneke and Lagaly reported that these disilicic acids ($H_2Si_2O_5$-II, $H_2Si_2O_5$-III and $H_2Si_2O_5$-IV, respectively) are produced when kanemite

is washed with acid.[6] Heidemann *et al.*[24] reported ^{29}Si NMR spectra for acid-washed α- and β-$NaSi_2O_5$, while Millar and Garces[13] and Deng *et al.*[14] have acquired similar spectra for several acid-washed $KHSi_2O_5$ samples. The H-kanemite spectrum in this work is most similar to that of the Probe-B sample of Heidemann *et al*, obtained from β-$NaSi_2O_5$ (*i.e.* $H_2Si_2O_5$-IV). This contains a signal at δ_{Si} -98.4 with an extra shoulder at δ_{Si} -101.9, which is not observed with H-kanemite.

Three H-octosilicate ^{29}Si NMR spectra have been reported, previously. The silicic acid of Borbély *et al.*[15] (δ_{Si} -99 and -111) changed to a different form on heating (δ_{Si} -103 and -111), while Heidemann *et al.*[16] prepared a single sample (δ_{Si} -104.0 and -112.2). In this work, the chemical shifts of H-octosilicate (sample hob) are found to be similar to those of the low-temperature form of Borbély *et al.* and those of sample hoa are similar to the results for the single sample of Heidemann *et al.* and the high-temperature form of Borbély *et al.*

Several authors have obtained ^{29}Si NMR spectra for single H-magadiite samples, with some variation in the reported chemical shifts. No attempt will be made to relate samples hma and hmb to previously-reported silicic acids.

In general, the silicic acid spectra have the same number of signals as the parent sodium forms, but they are broader and shifted. Since the spectral multiplicities are the same, it is likely that the silicic acids retain many of the structural features of their parent sodium forms. Thus the layered nature, degree of condensation and topology of the silicate layers are not affected significantly by the acidification reaction. The line-broadening can be attributed to a wider diversity of crystallographically distinct sites, or an increase in the number of crystallographic defects, rather than any variation in natural line-widths. Variation in chemical shifts is more interesting and merits further consideration. Table 6.4 compares the Q^3 ^{29}Si chemical shifts of the silicic acids and their parent sodium silicates. A similar table was compiled by Schwieger *et al.*[11]

Parent Silicate (Sample)	Q^3 δ_{Si} / ppm	Silicic Acid (Sample)	Q^3 δ_{Si} / ppm	Difference / ppm
Na-Kanemite (knc)	-97.6	H-Kanemite (kna)	-98.6	-1.0
Na-Octosilicate (occ)	-100.3	H-Octosilicate (hoa)	-104.4	-3.1
Na-Octosilicate (ocb)	-100.2	H-Octosilicate (hob)	-99.7	+1.5
Na-Magadiite (mgb)	-99.5	H-Magadiite (hma)	-102.5	-3.0
Na-Magadiite (mgc)	-99.5	H-Magadiite (hmb)	-101.4	-1.9

Table 6.4 The effect of the acidification reaction on the ^{29}Si Q^3 chemical shifts.

Two factors might change the ^{29}Si chemical shift as layered sodium polysilicate hydrates are treated with acid. As sodium ions are replaced by protons, the silicate layers could rearrange. Losing sodium ions varies the electronegativity of the groups surrounding the silicon nuclei, while structural changes will alter bond-angles and bond-lengths. Structural changes have been shown empirically to affect δ_{Si} (see section 5.1.2). Schwieger *et al.*[11] attributed the large chemical shift difference (*ca.* 7 ppm) between makatite and H-makatite to such structural differences, while Borbély *et al.*[15] proposed that the silicate layer in octosilicate was sheared considerably in the formation of an H-octosilicate sample.

The expected δ_{Si} change on replacing sodium ions with protons can be estimated using an empirical relationship proposed by Janes and Oldfield,[25] (equation 6.1). Silicon-29 chemical shifts of silicates can be predicted by summing the group electronegativities, EN, of the four ligands surrounding the silicon atom. These values have been determined for many possible ligands, including ONa and OH, with values of 3.4395 and 3.5822, respectively. Equation 6.2 shows the expected difference in chemical shift, $\Delta\delta$, between a sodium siloxide, $(SiO)_3\underline{Si}$-ONa and a silanol, $(SiO)_3\underline{Si}$-OH (a negative value indicates a lower frequency for the silanol peak).

$$\delta_{Si} / ppm = -24.336\ \Sigma EN + 279.27 \qquad \text{Eq. 6.1}$$

$$\Delta\delta / ppm = -24.336(3.5822-3.4395) = -3.47 \qquad \text{Eq. 6.2}$$

Thus, a low-frequency shift on acidification of 3.5 ppm can be predicted. Since this is approximately the value observed for two of the silicic acids in this work, it can be speculated that the bond-angles and bond-lengths in H-octosilicate (sample hoa) and H-magadiite (sample hma) are similar to those in the parent sodium silicates. Significantly smaller values of δ_{Si} are seen for the other silicic acids. This implies that there is some distortion of the silicate layers in these samples on acidification. In considering such conclusions it must be remembered that the Na-silicate Q^3 silicon nuclei are unlikely to be sodium siloxides– ^1H NMR indicates that the layered sodium polysilicate hydrates contain hydrogen-bonded silanol groups, ≡Si-O···H-O-Si≡, where the sodium ion is less strongly-bonded (see section 5.2).

6.4 Thermogravimetric Analysis

Thermogravimetric analysis has been used previously to analyse samples of the layered sodium polysilicate hydrates (see section 5.2.9). Total water contents were estimated from the results and two types of proton species were identified. Similar information should be obtained from the analysis of the silicic acids.

Five silicic acid samples underwent thermogravimetric analysis using a Perkin-Elmer TGA7 machine. The H-octosilicate and H-magadiite samples (hoa, hob, hma and hmb) were heated up to 800 °C while analysis of the H-kanemite sample (hka) was restricted to a maximum temperature of 400 °C. In previous work, higher temperatures had induced the formation of a glassy phase which could not be removed from the crucibles. Traces for the analyses are shown in figures 6.2, 6.3 and 6.4, while details for the temperatures of discernible events and weight-loss data are listed in table 6.5.

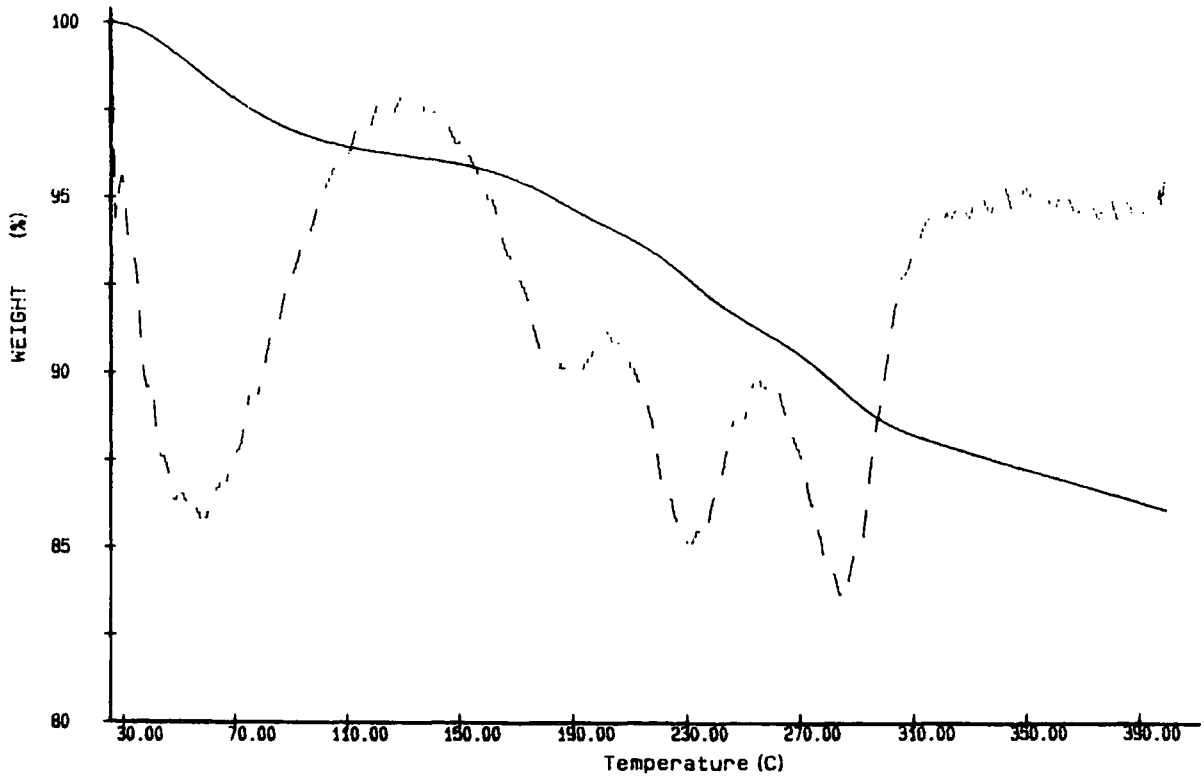

Figure 6.2 Results for the thermogravimetric analysis of H-kanemite (sample hkb): weight (unbroken line, y-axis scale, % units) and rate of weight-loss (broken line, arbitrary units with dimensions of mass/time).

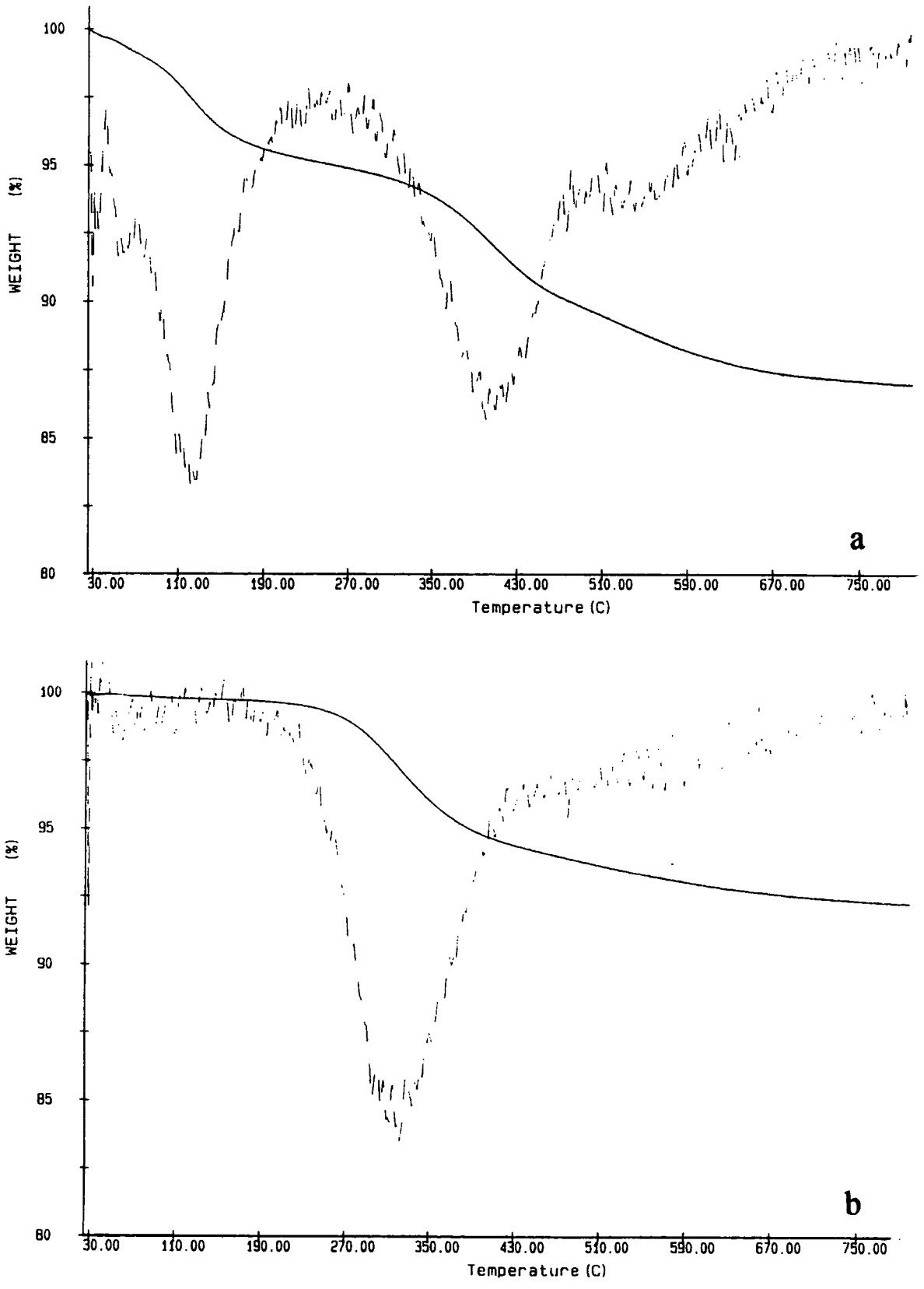

Figure 6.3 Results for the thermogravimetric analysis of h-octosilicate: a) sample hoa; and b) sample hob. In each case, the two lines represent weight (unbroken line, y-axis scale, % units) and rate of weight-loss (broken line, arbitrary units with dimensions of mass/time).

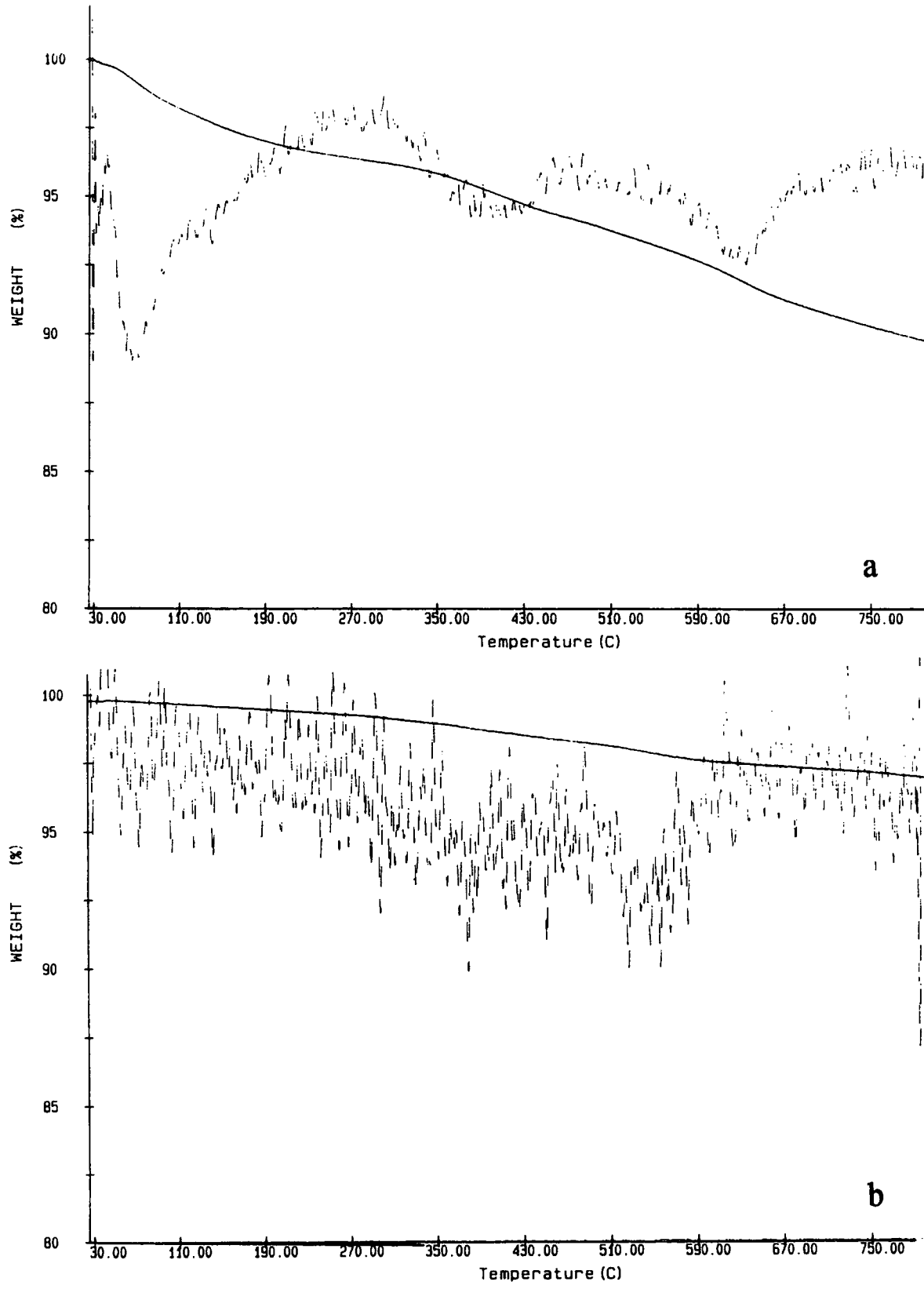

Figure 6.4 Results for the thermogravimetric analysis of h-magadiite: a) sample hma; and b) sample hmb. In each case, the two lines represent weight (unbroken line, y-axis scale, % units) and rate of weight-loss (broken line, arbitrary units with dimensions of mass/time).

Silicic Acid	Sample	Events		Overall Weight-Loss / %
		Temperature / °C	Weight-Loss / %	
H-Kanemite	hkb	60	4	14
		190	2	
		230	2.5	
		290	2.5	
H-Octosilicate	hoa	120	5	13.0
		400	5	
H-Octosilicate	hob	310	5	7.7
H-Magadiite	hma	70	4	10.2
		360	2	
		610	2	
H-Magadiite	hmb	none	n/a	2.9

Table 6.5 Thermogravimetric analysis results for five silicic acid samples.

In section 5.2.9, thermogravimetric analysis events were related to two processes by their temperatures and rates. Loss of molecular water occurs at low temperature in discernible features, *i.e.* peaks in the differential traces, while condensation of silanol groups occurs more slowly at higher temperatures. Using similar reasoning here, it might be concluded that H-kanemite, H-octosilicate (sample hoa) and H-magadiite (sample hma) contain significant amounts of molecular water, while H-octosilicate (sample hob) and H-magadiite (sample hmb) principally contain protons as silanol groups. Further calculations are possible.

The total amount of water in each silicic acid sample can be related to a formula, $SiO_2{:}xH_2O$. Using values of 60 and 18 for the formula masses of SiO_2 and H_2O, respectively, the total weight-loss, y %, can be related to x using equation 6.3. This can be rearranged to give equation 6.4.

$$y\ \% = \left(\frac{100 \times 18x}{18x + 60}\right)\ \% \qquad \text{Eq. 6.3}$$

$$x = \frac{1}{30}\left(\frac{1}{y} - \frac{1}{100}\right)^{-1} \qquad \text{Eq. 6.4}$$

Thus, a formula, $SiO_2{:}xH_2O$, can be determined from a TGA weight-loss, y %. These will be accurate if it is assumed that the proton/sodium exchange was complete and the total weight loss measured by TGA accurately reflected the water content of the sample. Such assumptions should be considered further.

The extent of the exchange of sodium ions for protons has been quantified by Iler, for H-octosilicate[17] and Pinnavaia *et al.* and Rojo *et al*, for H-magadiite.[19,22] The level of sodium in these silicic acid products was low: 0.008 %, <0.001 % and 0.3 %, respectively. Other authors have quoted elemental analysis data which implies that their silicic acid products contain no sodium.[1,6,8,16,19] Therefore, it can be assumed that the silicic acids prepared in this work contain no sodium. For some samples, this has been verified by ^{23}Na NMR, where insignificant signals are seen.

Thermogravimetric analysis might under-estimate the overall water content as the duration and maximum temperature of the analysis might be insufficient to drive off all the water in the sample. Lagaly *et al.* showed that this was plausible– an H-magadiite sample ($14SiO_2.6.4H_2O$) still contained some protons even after heating to 1200 °C ($14SiO_2.1.5H_2O$).[8] In this work, some samples appear to be still losing weight at the maximum analysis temperatures. Therefore, the total water content of these samples might be larger than that indicated by TGA.

Overall, equation 6.4 should provide reasonably accurate formulae, $SiO_2{:}xH_2O$, though the value of x might be under-estimated. These are listed in table 6.6.

Silicic Acid	Sample	y / %	x	Formula
H-Kanemite	hkb	14	0.54	SiO_2:0.54H_2O
H-Octosilicate	hoa	13.0	0.50	SiO_2:0.50H_2O
H-Octosilicate	hob	7.7	0.28	SiO_2:0.28H_2O
H-Magadiite	hma	10.2	0.38	SiO_2:0.38H_2O
H-Magadiite	hmb	2.9	0.10	SiO_2:0.10H_2O

Table 6.6 Experimentally-derived formulae for five silicic acid samples.

As predicted by Beneke and Lagaly, the formula for the H-kanemite sample corresponds very closely to that of a disilicic acid, $H_2Si_2O_5$ or SiO_2:0.5H_2O. This would be expected to contain protons as silanol groups only. Since the thermogravimetric analysis trace for this sample contained several low-temperature events, silanol groups do not always condense slowly at high temperatures. Millar and Garces reported similar traces for acidified $KHSi_2O_5$ samples.[14]

The H-octosilicate and H-magadiite total weight losses can be compared with theoretical values for silicic acids which contain protons solely as silanol groups. Equation 6.5 shows that the formula of a layered sodium polysilicate hydrate, Na_2O:αSiO_2:βH_2O, can be represented as that of a hydrated sodium hydrogen silicate. If acidification exchanges all the sodium ions for protons, the product will have a formula, αSiO_2:2H_2O if it contains no molecular water (equation 6.6). A theoretical water content, z %, can be calculated for such a silicic acid with equation 6.7. Table 6.7 compares theoretical and experimental water contents for H-octosilicate and H-magadiite.

Parent Silicate: $Na_2O{:}\alpha SiO_2{:}\beta H_2O \equiv Na_2H_2Si_\alpha O_{2\alpha+2}.(\beta\text{-}1)H_2O$ Eq. 6.5

Silicic Acid: $H_4Si_\alpha O_{2\alpha+2} \equiv \alpha SiO_2{:}2H_2O$ Eq. 6.6

Water Content : $$z = \frac{2\times18\times100}{60\alpha+2\times18} = \frac{300}{5\alpha+3}$$ Eq. 6.7

Silicic Acid	Sample	Experimental Water Content y / %	Parent Silicate	α	Theoretical Water Content z / %
H-Octosilicate	hoa	13.0	Octosilicate	8	7.0
H-Octosilicate	hob	7.7	Octosilicate	8	7.0
H-Magadiite	hma	10.2	Magadiite	14	4.1
H-Magadiite	hmb	2.9	Magadiite	14	4.1

Table 6.7 Theoretical and experimental silicic acid water contents.

Table 6.7 shows that two types of silicic acid have been prepared from octosilicate and magadiite. The water contents of H-octosilicate (sample hob) and H-magadiite (sample hmb) are similar to those of the theoretical silicic acid samples which contain protons solely as silanol groups. The other two samples, H-octosilicate (sample hoa) and H-magadiite (sample hma) lose more weight on heating– this can be attributed to the presence of molecular water. Therefore, the two types of H-octosilicate and H-magadiite can be considered to be anhydrous and hydrated samples.

The Q^3 ^{29}Si chemical shifts of the two H-octosilicate sample are consistent with the high- and low-temperature forms reported by Borbély *et al.* However, in the work of Borbély *et al*, the sample with the low-frequency chemical shift was the low-temperature form, while in this work it is the anhydrous form. Logically, a low-temperature hydrated form would be expected.

6.5 Proton MAS NMR

This section contains ^1H MAS spectra of the five types of silicic acid samples. Such spectra have not been previously reported.

The spectra were acquired using the CMX200 spectrometer, equipped with either a Doty MAS probe and 7 mm zirconia rotors or a Chemagnetics HX probe and 7.5 mm zirconia Pencil rotors. In both cases a standard single-pulse sequence was used. Further experimental details may be found in table 6.8, while the spectra are displayed in figure 6.5. Chemical shifts and line-widths are listed in table 6.9.

Silicate	Sample	Probe	Numbers of Transients	Recycle Delay / s	Spinning-Rate / kHz
H-Kanemite	hkc	HX	16	2	4
H-Octosilicate	hoa	HX	32	2	1.96
H-Octosilicate	hoc	HX	32	3	4
H-Magadiite	hma	HX	16	2	4
H-Magadiite	hmb	Doty	16	2	4

Table 6.8 Experimental details for ^1H MAS spectra of five silicic acid samples.

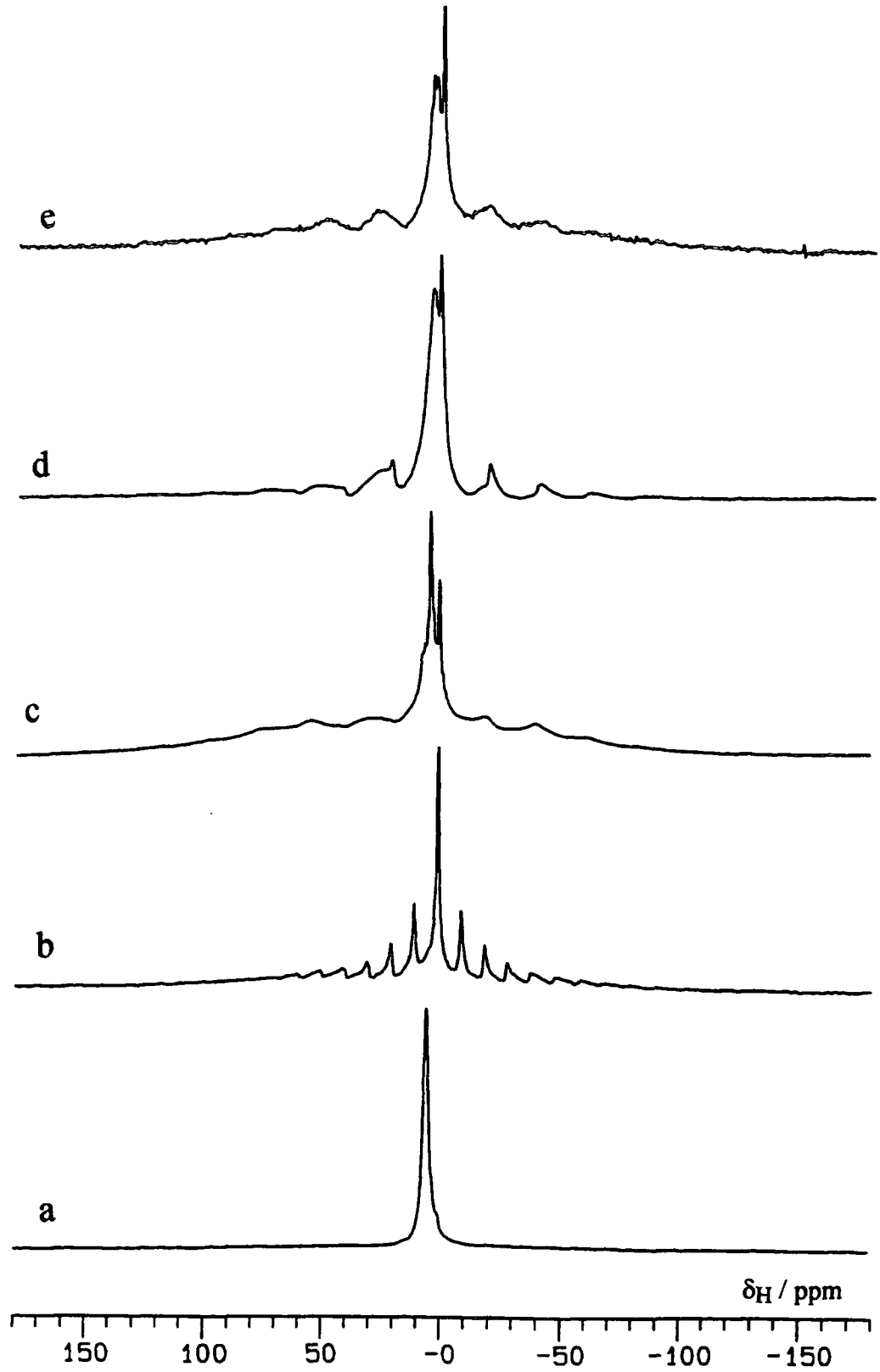

Figure 6.5 Proton MAS spectra for five silicic acid samples: a) H-kanemite (sample hkb); b) H-octosilicate (sample hoa); c) H-octosilicate (sample hoc); d) H-magadiite (sample hma); and e) H-magadiite (sample hmb).

Silicate	Sample	δ_H / ppm	$\Delta_{1/2}$ / Hz
H-Kanemite	hkc	5.7	500
H-Octosilicate	hoa	2.0	300
H-Octosilicate	hoc	1.3	500
		4.9	500
H-Magadiite	hma	2.0	500
		4.6	1500
H-Magadiite	hmb	1.8	500
		5.6	1000

Table 6.9 Chemical shift and approximate line-widths for the five silicic acid spectra in figure 6.5.

The spectrum of H-kanemite contains a single line at δ_H 6 – this is approximately the same chemical shift as that reported by Millar and Garces[14] for a disilicic acid, d-$H_2Si_2O_5$, prepared from $KHSi_2O_5$. If the H-kanemite sample is a disilicic acid, as indicated by TGA and ^{29}Si NMR, then silanol protons are being detected. In the parent Na-kanemite, the silanol protons are strongly hydrogen-bonded (δ_H 15). The strength of the H-bonding is clearly weaker in the silicic acid, corresponding to larger oxygen-oxygen distances. Deng *et al.*[13] observed similar acidification behaviour with $KHSi_2O_5$, for which the structure is known.[26] Strong interlayer H-bonds, -O-H···O-, are present in $KHSi_2O_5$. On acidification, these are protonated, and repulsion between silanol groups might force the silicate layers apart (see figure 6.6). This is a plausible model for the structural changes that occur as kanemite is washed with acid. Additionally, it is possible that the arrangement of the hydrogen bonds in $KHSi_2O_5$ and Na-kanemite are similar.

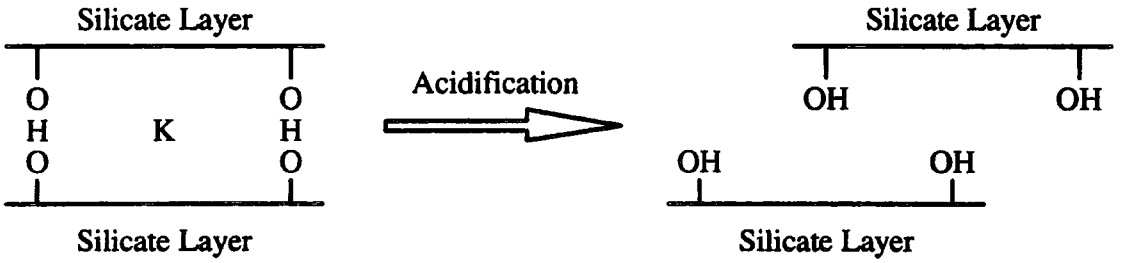

Figure 6.6 A schematic diagram to show the effect of acidification on the structure of $KHSi_2O_5$.

The spectrum of H-octosilicate (sample hoa) contains a single isotropic line at δ_H 2 with several spinning side-bands. Thermogravimetric analysis showed that there were likely to be silanol and water protons in this sample. The chemical shift of the single observed signal is typical of silanol protons, but the broad spread of spinning side-bands is more typical of water protons (see section 5.2.2). It is possible that these species are exchanging rapidly in this sample.

The spectra of the other three samples are fairly similar. They all contain two lines at δ_H 1 to 2 and δ_H 5. Under the conditions used, the probe background gives a sharp line around δ_H 1 and a broader higher-frequency line (see figure 7.25a). Therefore, these spectra should be considered with some caution. The low-frequency signal in H-magadiite (sample hma) has weak spinning side-bands, which are also observed in H-octosilicate (sample hoa). In both samples, the thermogravimetric analysis results imply that silanol and water proton species are present.

The important result from all these analyses is that no strongly hydrogen-bonded protons have been detected as high-frequency signals. This implies that sodium ions are responsible for their presence in the kanemite, octosilicate and magadiite. It is likely that the hydrogen-bonds are being formed between silanol protons, ≡Si-OH, and siloxide oxygen ions, ≡Si-O$^-$, with sodium ions, Na^+, balancing the charges. Such a conformation is known to be present in $KHSi_2O_5$ (with potassium ions). It has already been stated that the kanemite H-bonding protons might be similar, but this is also a plausible confirmation for octosilicate and magadiite.

6.6 Powder X-Ray Diffraction

Powder X-ray diffraction patterns have been measured for each of the five types of silicic acid. These should give a value for the basal spacings of these samples as well as providing information regarding their crystallinity.

Powder X-Ray diffraction patterns were measured using a Phillips PW1050 powder diffractometer. The results were analysed using Sietronics trace processing software for spike removal, Cu Kα2 subtraction and d-spacing calculation. The patterns are shown in figure 6.7 while table 6.10 lists basal spacings, d_{001}. This is the d-spacing of the lowest-angle peak and corresponds to the repeat distance of the silicate layers.

Silicate	Sample	Basal Spacing, d_{001} / Å	Parent-Silicate Basal Spacing† d_{001} / Å
H-Kanemite	hkb	6.10	10.3[a]
H-Octosilicate	hoa	9.03	11.10[b]
H-Octosilicate	hob	7.46	11.10[b]
H-Magadiite	hma	13.76	15.58[c]
H-Magadiite	hmb	12.08	15.58[c]

Table 6.10 Powder X-ray diffraction results for the five types of silicic acid sample. These are compared with values for the parent sodium silicate. [a]Literature Value.[27] [b]Section 5.5.5. [c]Literature Value.[18]

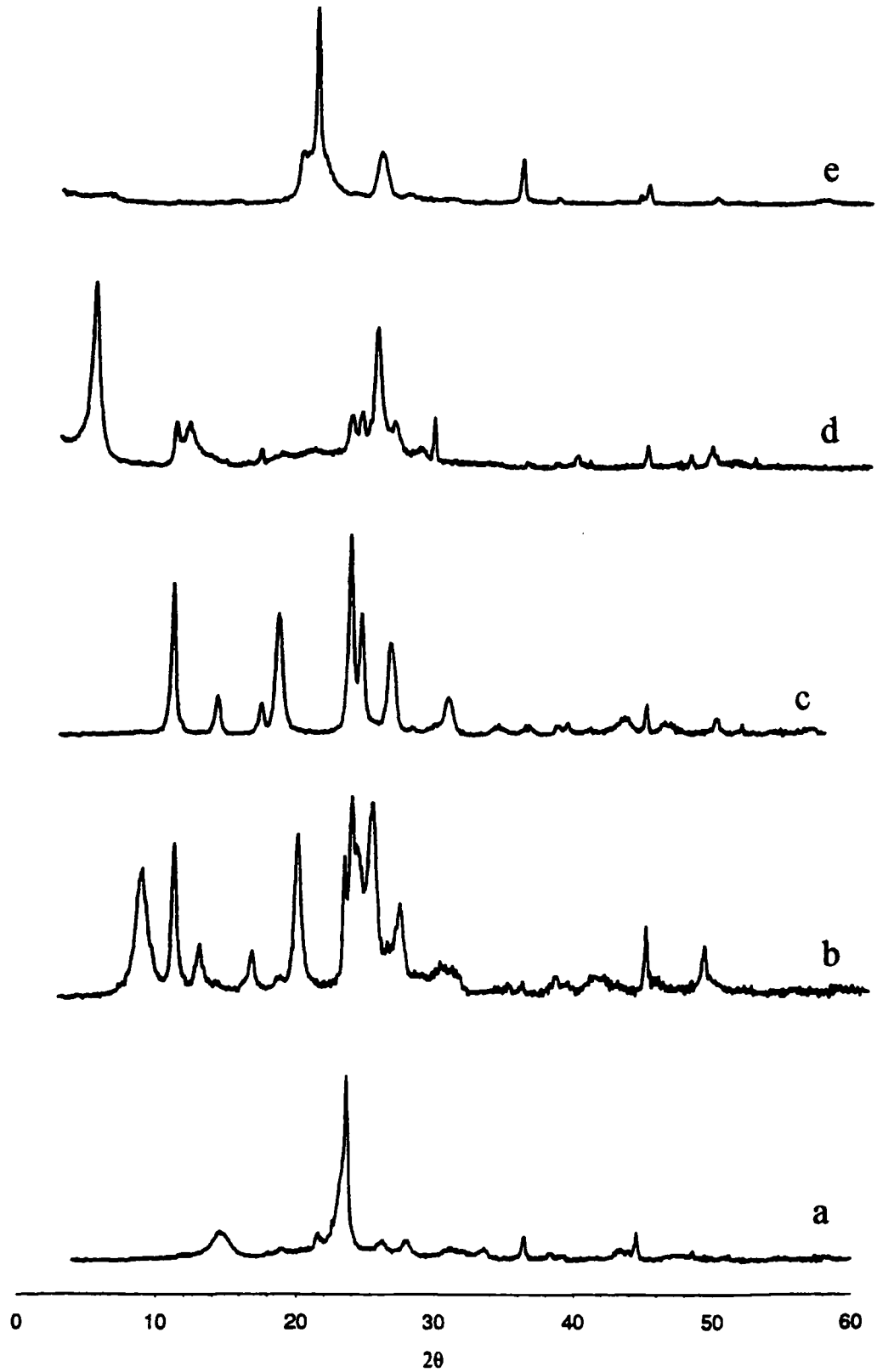

Figure 6.7 Powder X-ray patterns for five silicic acid samples: a) H-kanemite (sample hkb); b) H-octosilicate (sample hoa); c) H-octosilicate (sample hob); d) H-magadiite (sample hma); and e) H-magadiite (sample hmb).

In general, powder X-ray diffraction patterns of the layered sodium polysilicate hydrates have many sharp lines with a strong peak at a low angle, corresponding to the basal spacing. These silicic acid patterns have fewer broader lines. This is consistent with the line-broadening observed in ^{29}Si CP spectra and can be attributed to a lower level of crystallinity. The basal spacings of the silicic acids are also smaller than those of their parent sodium forms. With most of the silicic acids these can be measured precisely from a strong line, but in H-kanemite the line is broad and in H-magadiite (sample hmb) it is weak.

Millar and Garces titrated $KHSi_2O_5$ with acid.[14] Powder patterns were measured for samples corresponding to different degrees of potassium exchange. The powder pattern of this H-kanemite sample is very similar to that of $KHSi_2O_5$, where 99 % of the potassium has been exchanged for protons. Therefore, this H-kanemite sample is clearly a disilicic acid.

The basal spacings of the two H-octosilicate samples can be compared with previously-reported values: Heidemann *et al.* reported a single sample (d_{001} = 7.31 Å);[16] Iler measured a value of 9.25 Å from a wet sample which shrunk to 7.43 Å, on drying at 30 °C;[17] and the low- and high-temperature forms of Borbély *et al.* had basal spacings of 7.38 Å and 7.1 Å, respectively.[15] In this work, the hydrated sample (hoa) is probably similar to the single sample of Heidemann *et al.* and the wet sample of Iler, while the anhydrous sample is similar to that obtained by Iler on drying. For both pairs of H-octosilicate and H-magadiite samples, it is the hydrated from which has the larger basal spacing.

6.7 Summary

The single H-kanemite sample is certainly a disilicic acid. Thermogravimetric analysis predicts a formula which is very close to $H_2Si_2O_5$, while the powder X-ray diffraction pattern is very similar to an acidification product of $KHSi_2O_5$. Relating the NMR data for this sample to previously-reported $H_2Si_2O_5$ analyses is difficult– slightly different phases are prepared from α- and β-$NaSi_2O_5$, while several stable products can be made by washing $KHSi_2O_5$, so there are many different forms. The ^{29}Si NMR spectra were similar to the β-$NaSi_2O_5$ acid of Heidemann *et al.*[24] while the ^1H MAS spectrum was similar to that reported by Deng *et al.* for an acid product of $KHSi_2O_5$.[13]

Borbély *et al.* prepared two H-octosilicate samples.[15] One could be made by heating the other sample. From ^{29}Si CP spectra, it appeared that the H-octosilicate samples in the present work were similar high- and low-temperature forms. However, thermogravimetric analysis and powder X-ray diffraction showed that this was not the case. The two samples correspond to anhydrous and hydrated forms of H-octosilicate. Figure 6.8 is an explanatory diagram.

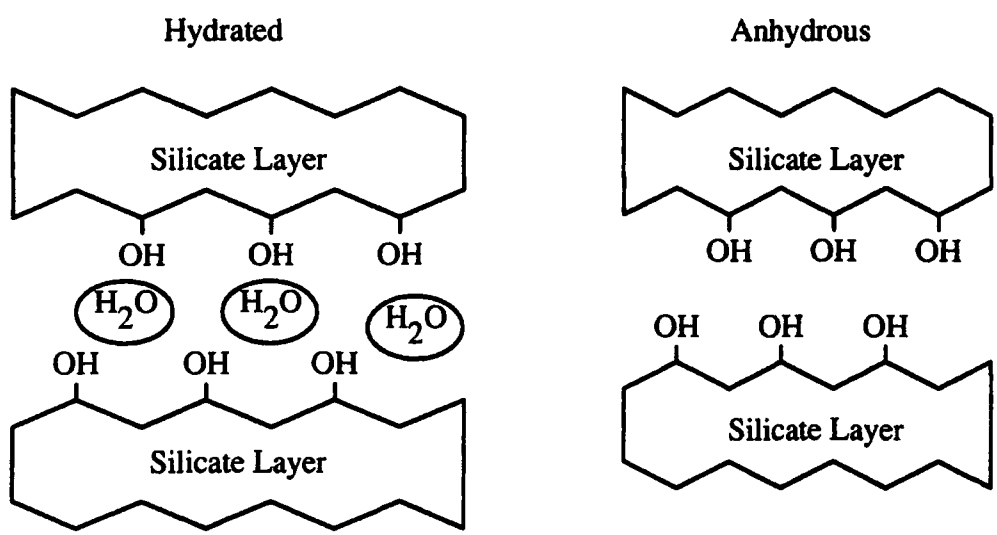

Figure 6.8 Schematic diagram of hydrated and anhydrous forms of H-octosilicate or H-magadiite.

The anhydrous samples contain silanol protons species only. They have smaller basal spacings and higher-frequency ^{29}Si Q^3 chemical shifts than the hydrated forms which also contain molecular water. Similar conclusions can be made for the two types of H-magadiite sample that have been prepared in this work. The analytical data are consistent with a larger interlayer spacing for the hydrated samples.

The ^1H MAS spectra in this section provide one important conclusion. In ^1H MAS spectra for kanemite, octosilicate and magadiite, a high-frequency peak can be assigned to strongly hydrogen-bonded protons. Such signals are not present in the spectra of the acid-exchanged forms. This implies that the hydrogen-bonds are being formed between silanol protons and siloxide oxygen ions– the formation of such bonds requires a sodium ion for charge balance. Deng *et al.* showed that there were strongly hydrogen-bonded protons in $KHSi_2O_5$,[13] which are not present after washing with acid. The structure of this disilicate is known, and the conformation of the hydrogen-bonds provides a plausible model for kanemite, octosilicate and magadiite.

References

1 K. Beneke and G. Lagaly, *Am. Mineral.*, 1983, **68**, 818-826.

2 R. Schwarz and E. Menner, *Dtsch. Chem. Ges.*, 1924, **57**, 1477-1481.

3 A. Pabst, *Am. Mineral.*, 1958, **43**, 970-980.

4 G. Lagaly and R. Matouschek, *Neues Jahrbuch für Mineralogische Abhandlugen*, 1980, **138**, 81-93.

5 R. Wey and A. Kalt, *C. R. Acad. Sci. Paris*, 1967, **265**, 1437-1440.

6 K. Beneke and G. Lagaly, *Am. Mineral.*, 1977, **62**, 763-771.

7 G. Lagaly, K. Beneke and A. Weiss, *Am. Mineral.*, 1975, **60**, 642-649.

8 G. Lagaly, K. Beneke and A. Weiss, *Am. Mineral.*, 1975, **60**, 650-658.

9 G. Lagaly, *Adv. Colloid Interface Sci.*, 1979, **11**, 105-148.

10 K. Beneke, H.H. Kruse and G. Lagaly, *Z. anorg. allg. chem.*, 1984, **518**, 65-76.

11 W. Schwieger, K.-H. Bergk, D. Heidemann, G. Lagaly and K. Beneke, *Zeitschrift für Kristallographie*, 1991, **197**, 1-12.

12 A. Kalt and R. Wey, *Bull. Groupe fr. Argiles*, 1968, **20**, 205.

13 Z.Q. Deng, J.F. Lambert and J.J. Fripiat, *Chemistry of Materials*, 1989, **1**, 375-380.

14 D.M. Millar and J.M. Garces in M.L. Occelli and H.E. Robson, eds., *Synthesis of Microporous Minerals Vol. II*, 1992, Van Nostrand Rheinhold, New York, 1992, 187-206.

15 G. Borbély, H.K. Beyer and H.G. Karge, *Clays and Clay Minerals*, 1991, **39**, 490-497.

16 D. Heidemann, W. Schwieger and K.-H. Bergk, *Z. anorg. allg. Chem.*, 1987, **555**, 129-142.

17 R.K. Iler, *J. Coll. Sci.*, 1964, **19**, 648-657.

18 G.W. Brindley, *Am. Mineral.*, 1969, **88**, 1583-1591.

19 J.M. Rojo, E. Ruiz-Hitzky and J. Sanz, *Inorg. Chem.*, 1988, **27**, 2785-2790.

20 T. Yanagisawa, M. Harayama, K.Kuroda and C. Kato, *Solid State Ionics*, 1990, **42**, 15-19.

21 J.S. Dailey and T.J. Pinnavaia, *Chem. Mater.*, 1992, **4**, 855-863.

22 T.J. Pinnavaia, I.D. Johnson and M. Lipsicas, *J. Solid State Chem.*, 1986, **63**, 118-121.

23 R. Sprung and M.E. Davies, *Ind. Eng. Chem. Res.*, 1990, **29**, 213-220.

24 D. Heidemann, A.R. Grimmer, C. Hübert, P. Starke and M. Mägi, *Z. anorg. allg. chem.*, 1985, **528**, 22-36.

25 N. Janes and E. Oldfield, *J. Am. Chem. Soc.*, 1985, **107**, 6769.

26 M.T. Le Bihan, A. Kalt and R. Wey, *Bull. Soc. Fr. Minéral. Cristallogr.*, 1971, **94**, 15.

27 Z. Johan and G.F. Maglione, *Bull. Soc. fr. Mineral. Cristallogr.*, 1972, **95**, 371.

Chapter Seven Cross-Polarisation

7.1 Introduction

Section 2.7.4 introduced the concept of cross-polarisation whereby spectra of isotopically-dilute nuclei could be obtained via a transfer of magnetisation from abundant protons within a sample. This occurs particularly efficiently at the Hartmann-Hahn matching condition, $\gamma_I B_{1I} = \gamma_S B_{1S}$, and can give spectra with substantially improved signal-to-noise relative to the single-pulse method, in favourable conditions. The spectra can also be acquired more quickly since the recycle time for repetitive acquisition is dependent on proton spin-lattice relaxation times, rather than those of the dilute nuclei, such as ^{29}Si or ^{13}C. For this reason alone, cross-polarisation is a very useful method, but, since its success depends on an interaction between the rare and abundant spins, much can be learnt about the relationship between the relevant nuclei. In this work, cross-polarisation has been extensively used in an attempt to extract information about the relative positions of silicon, sodium and hydrogen sites within the layered polycrystalline silicate hydrates.

The efficiency of the cross-polarisation process depends on the nature of the heteronuclear dipolar interaction. The strength of the interaction decreases greatly with distance and it can be averaged by motion. Thus, information is available because efficient CP is only seen for nuclei which have neighbouring protons of a suitable rigidity.

In some cases a lone CP spectrum can be informative– for instance, where it lacks a signal that was contained in the single-pulse spectrum. Such a signal corresponds to a site which has no nearby protons of suitable rigidity for cross-polarisation. Further information can be obtained by running a series of CP spectra with different values of the contact time. The results can be analysed to obtain a time constant, T_{IS}, the cross-polarisation or cross-relaxation time– a measure of CP efficiency. Fitting variable contact time data also gives a second time constant, $T_{1\rho}$,

the *proton* rotating frame spin-lattice relaxation time. It can be better to measure this constant by modifying the standard CP pulse sequence so that proton magnetisation decays under spin-locking before cross-polarisation. Proton $T_{1\rho}$ values can be measured indirectly by CP in this way, because the observed CP signal directly measures the proton magnetisation before the contact time. Comparison of these with more directly measured values can identify the proton source of the CP. A similar strategy can be used to measure proton spin-lattice relaxation times, and the idea can be extended to a method where the equivalent of a proton spectrum is acquired in the t_1 period of a 2-dimensional pulse sequence. Two-dimensional fourier-transformation yields a correlation spectrum where cross-peaks link the proton source of the CP to the relevant dilute spin site.

7.2 Theory

7.2.1 The Dynamics of Cross-Polarisation

The CP sequence starts with a ^1H 90° pulse. This places the net proton magnetisation into the xy-plane of the rotating frame of reference where it is spin-locked by a second pulse, 90° out of phase with the first. Meanwhile, the dilute-spin channel radiofrequency is switched on and transfer of magnetisation will occur with maximum efficiency at the Hartmann-Hahn matching conditions. Rotating frame spin-lattice relaxation of both proton (I) and dilute spin (S) magnetisation occurs simultaneously with this transfer. An equation for the evolution of the dilute-spin magnetisation with time can be derived from a consideration of the spin-temperature of the system.[1] The inverse spin-temperatures of the abundant and rare spins, β_I and β_S, respectively, are proportional to xy-plane magnetisation in the rotating frame. This equation will be relevant for the case of cross-polarisation to a single S-spin from either a single I-spin or several I-spins which are completely averaged by spin-diffusion or exchange.

Assuming that the exchange of magnetisation occurs with conservation of energy within the rotating frame, equation 7.1 applies.

$$\frac{d\beta_I}{d\beta_t} + \varepsilon\alpha^2 \frac{d\beta_S}{d\beta_t} = 0 \qquad \text{Eq. 7.1}$$

$$\varepsilon = \frac{N_S S(S+1)}{N_I I(I+1)} \qquad \text{Eq. 7.2}$$

$$\alpha = \frac{\gamma_S B_S}{\gamma_I B_I} \qquad \text{Eq. 7.3}$$

In equation 7.1, ε represents the relative amounts of each of the nuclei (equation 7.2) and α is a mismatch parameter to represent deviation from the Hartmann-Hahn matching conditions (equation 7.3). In the simplest picture of cross-polarisation, three processes are occurring (figure 7.1). Magnetisation (equivalent to inverse spin-temperature, β) is being transferred between the I spins and S spins; this occurs at a rate characterised by the cross-polarisation time, T_{IS}. Meanwhile, both nuclei are being spin-locked and relaxing at a rate characterised by their spin-lattice relaxation times in the rotating frame of reference, $T_{1\rho}$. Overall, the S spin temperature is decaying towards the instantaneous I spin temperature. Differential equations 7.4 and 7.5 can be deduced for the rate of change of the inverse spin temperature of the S and I spins, respectively.

$$\frac{d\beta_S}{dt} = -\frac{(\beta_S - \beta_I)}{T_{IS}} - \frac{\beta_S}{T_{1\rho}^S} \qquad \text{Eq. 7.4}$$

$$\frac{d\beta_I}{dt} = -\varepsilon\alpha^2 \frac{(\beta_I - \beta_S)}{T_{IS}} - \frac{\beta_I}{T_{1\rho}^I} \qquad \text{Eq. 7.5}$$

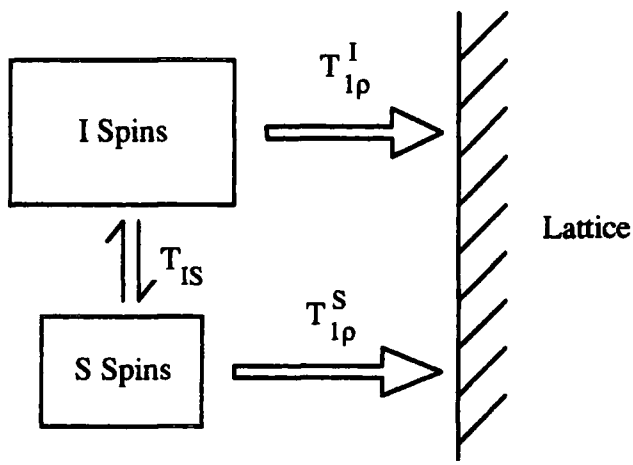

Figure 7.1 The processes that occur during the cross-polarisation contact time: transfer of magnetisation from the abundant spins to the rare spins, while the magnetisation of both nuclei is decaying with $T_{1\rho}$.

To solve these equations, initial conditions (equation 7.6) can be chosen by remembering that the xy-plane magnetisation of the dilute, S, spins is zero before the contact time. Equations 7.7 to 7.11 are the solutions.

$$\beta_S(0) = 0,\ \beta_I(0) \neq 0 \qquad \text{Eq. 7.6}$$

$$\beta_S(t) = \beta_I(0)\frac{1}{a^+ - a^-}\left(\exp\left(\frac{-a_- t}{T_{IS}}\right) - \exp\left(\frac{-a_+ t}{T_{IS}}\right)\right) \qquad \text{Eq. 7.7}$$

$$\beta_I(t) = \beta_I(0)\frac{1}{a^+ - a^-}\left\{(1-a_-)\exp\left(\frac{-a_- t}{T_{IS}}\right) - (1-a_+)\exp\left(\frac{-a_+ t}{T_{IS}}\right)\right\} \qquad \text{Eq. 7.8}$$

$$a_\pm = a_0\left(1 \pm \sqrt{1 - b/a_0^2}\right) \qquad \text{Eq. 7.9}$$

$$a_0 = \frac{1}{2}\left(1 + \varepsilon\alpha^2 + \frac{T_{IS}}{T_{1\rho}^I} + \frac{T_{IS}}{T_{1\rho}^S}\right) \qquad \text{Eq. 7.10}$$

$$b = \frac{T_{IS}}{T_{1\rho}^I}\left(1 + \frac{T_{IS}}{T_{1\rho}^S}\right) + \varepsilon\alpha^2\frac{T_{IS}}{T_{1\rho}^S} \qquad \text{Eq. 7.11}$$

The variation of the S-spin magnetisation, $M_S(t)$, during the contact time is given by equation 7.12, where $M_S(0)$ is proportional to the number of S spins.

$$M_S(t) = M_S(0)\alpha\frac{\gamma_I}{\gamma_S}\frac{\beta_S(t)}{\beta_I(0)} \qquad \text{Eq. 7.12}$$

Readily usable equations relating the observed S-spin magnetisation to the contact time can be obtained by substituting equations 7.7-11 into equation 7.12. This somewhat formidable undertaking can be made easier by considering several possible simplifications. Firstly, it is likely that the Hartmann-Hahn matching will be exact ($\alpha = 1$), the S-spins are dilute ($\varepsilon \sim 0$) and that rotational frame longitudinal relaxation

is only significant for the abundant nuclei ($1/T_{1\rho}^S = 0$). In this case, the parameters a_0, b, a_+ and a_- reduce to $(1 + \psi)/2$, ψ, 1 and ψ, respectively, where ψ is $T_{IS}/T_{1\rho}$. Substitution of these values into equations 7.7 and 7.8 gives equations 7.13 and 7.14, and the behaviour of S-magnetisation with the contact time is described by equation 7.15. A second simplification is to assume that there is no significant rotational frame longitudinal relaxation at all. In this case, equation 7.16 describes the variation in S-magnetisation with contact time.

$$\beta_S(t) = \frac{\beta_I(0)}{1 - T_{IS} / T_{I\rho}^I}\left(\exp\left(-t / T_{I\rho}^I\right) - \exp(-t / T_{IS})\right) \qquad \text{Eq. 7.13}$$

$$\beta_I(t) = \beta_I(0)\exp\left(-t / T_{I\rho}^I\right) \qquad \text{Eq. 7.14}$$

$$M_S(t) = \frac{\gamma_I}{\gamma_S}\frac{M_S(0)}{1 - T_{IS} / T_{I\rho}^I}\left(\exp\left(-t / T_{I\rho}^I\right) - \exp(-t / T_{IS})\right) \qquad \text{Eq. 7.15}$$

$$M_S(t) = \frac{\gamma_I}{\gamma_S} M_S(0)(1 - \exp(-t / T_{IS})) \qquad \text{Eq. 7.16}$$

The pre-exponential parts of equations 7.15 and 7.16 show that the ratio of the CP signal to the single pulse signal, $M_S(0)$, can be γ_I/γ_S. This is the same result that was derived in section 2.7.4. Equation 7.17 is a readily-usable form of equation 7.15 and 7.16, where M_0 is proportional to the number of S spins and λ is shown by equation 7.18. It is possible to account for the rotating frame relaxation of the S nuclei by including an extra term in the equation for λ (equation 7.19).[2]

$$M_S(t) = \frac{M_0}{\lambda}(1 - \exp(-\lambda t / T_{IS}))\exp\left(-t / T_{I\rho}^I\right) \qquad \text{Eq. 7.17}$$

$$\lambda = 1 - T_{IS} / T_{I\rho}^I \qquad \text{Eq. 7.18}$$

$$\lambda = 1 - T_{IS} / T_{1\rho}^{I} + T_{IS} / T_{1\rho}^{S} \qquad \text{Eq. 7.19}$$

Figure 7.2 is a simulated curve to show typical behaviour of the observed signal intensity, $M_S(t)$, with time. The signal increases as abundant spin magnetisation is transferred to the dilute spin nucleus and eventually decays exponentially with the $T_{1\rho}$ of the abundant nuclei.

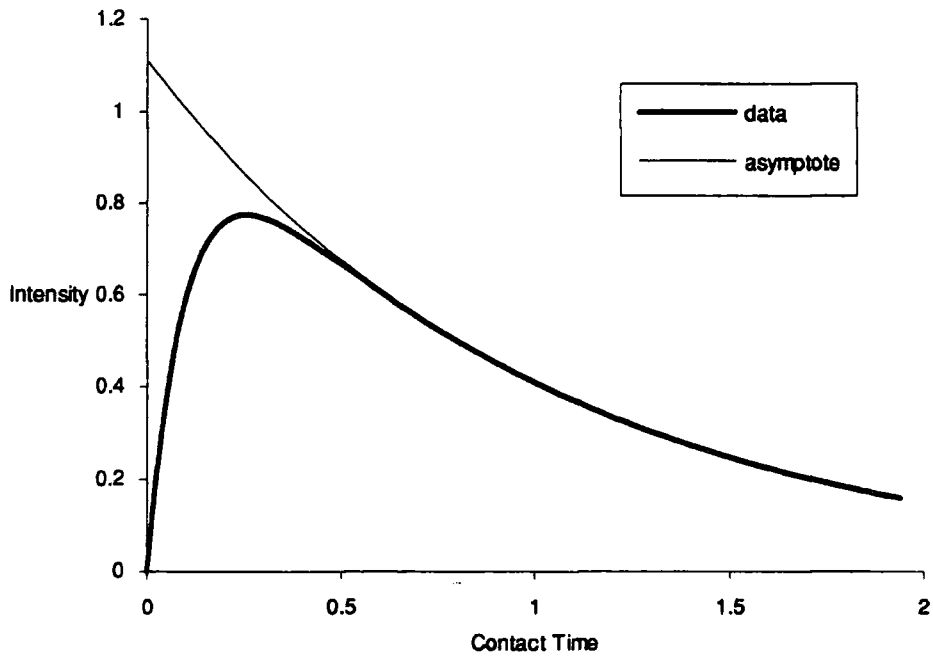

Figure 7.2 The variation of signal intensity with contact time. The contact time axis is in units of $T_{1\rho}$ while the intensity axis is in units of M_0. In this case $T_{IS} = T_{1\rho}/10$. The asymptote is obtained from the equation $M_t = M_0 \exp(-t/T_{1\rho})/\lambda$.

The dynamics of cross-polarisation are commonly investigated with a variable contact time experiment– spectra are obtained at several different values of the contact time. In many cases, fitting the results to equations 7.17 and 7.18 will give the values of three constants, M_0, T_{IS} and $T_{1\rho}$. The parameter M_0 is quantitative and

proportional to the number of active nuclei within the sample, and the $T_{1\rho}$-value can be used to identify or provide information about the proton source of the cross-polarisation. The cross-polarisation time, T_{IS}, is a measure of efficiency of the process. In general terms, efficient CP is observed between nuclei that are close and not too mobile. More exactly, T_{IS} is a function of the second moments, M_2, of the homo- and heteronuclear dipolar couplings. Consequently it varies with the reciprocal of the sixth root of the IS distance (equation 7.20).[3,4]

($M_2 = \int_{-\infty}^{\infty} (\omega - \langle\omega\rangle)^2 f(\omega) d\omega \Big/ \int_{-\infty}^{\infty} f(\omega) d\omega$, where $\langle\omega\rangle$ is the mean angular frequency)

$$(T_{IS})^{-1} \propto \frac{M_2^{IS}}{\sqrt{M_2^{II}}} \propto r_{IS}^{-6} \qquad \text{Eq. 7.20}$$

It should be noted that the minimum value of T_{IS} (*i.e.* the most efficient cross-polarisation) does not necessarily occur at the Hartmann-Hahn matching condition (α=0 in equation 7.3). In systems consisting of a dilute-spin nucleus and a proton source which is distinct from the other protons in a sample, rapid magic-angle spinning can modulate the behaviour of T_{IS} with α, so that the most efficient cross-polarisation is observed away from the Hartmann-Hahn matching condition. Such effects are observed in systems with mobile or dilute protons, where there are weak homonuclear dipolar interactions. Stejskal *et al.* reported this phenomenon for ^{13}C CP/MAS NMR of adamantane.[5]

Many assumptions have been used to obtain equation 7.17. Therefore, there are many cases where it does not adequately describe variable contact time data. The most obvious distortion from ideal behaviour is where cross-polarisation occurs from two separate proton types with distinct relaxation times for each source. Kümmerlen *et al.* reported such a phenomenon in sodium silicate glasses.[6] Their results were fitted to equation 7.21 and a reasonable correlation was obtained. The cross-polarisation behaviour from each proton source, distinguished by the superscripts (1) and (2), is simply summed to provide the behaviour of the whole sample.

$$M_t = \frac{M_0^{(1)}}{\lambda^{(1)}}\left(\exp\left(-t / T_{1\rho}^{(1)}\right) - \exp\left(-t / T_{IS}^{(1)}\right)\right) + \frac{M_0^{(2)}}{\lambda^{(2)}}\left(\exp\left(-t / T_{1\rho}^{(2)}\right) - \exp\left(-t / T_{IS}^{(2)}\right)\right)$$

Eq. 7.21

The authors note that this treatment requires the assumption that there is no spin-diffusion between the separate proton sources. The behaviour of signal intensity with contact time can be more complex, if this is not the case. Müller *et al.*[7] found that the ^{13}C CP signal from a single crystal of ferrocene oscillated with the contact time. The effect was particularly noticeable at some orientations of the sample to the magnetic field. The results were consistent with the system shown in figure 7.3.

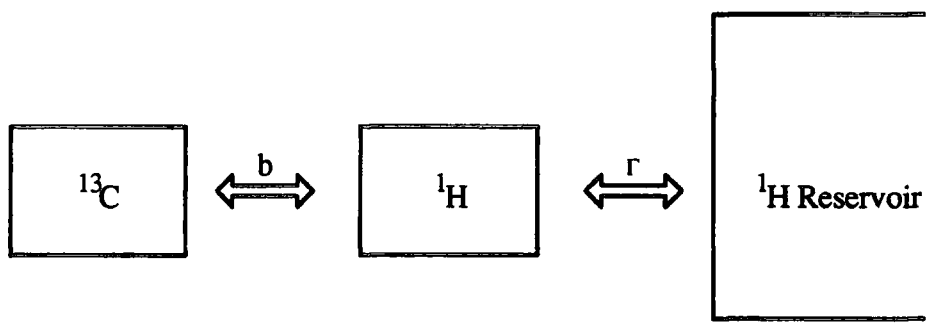

Figure 7.3 A schematic diagram of the model of Müller *et al.*[7] for ^{13}C cross-polarisation in ferrocene. The ^{13}C spin interacts with a single proton only, through dipolar coupling, b. This proton interacts with the rest of the protons in the sample by spin-diffusion at a rate, Γ.

The authors were able to derive an equation from this model which fitted the data very well (equation 7.22). R represents the rate of spin-diffusion (more commonly, T_{II}^{-1}) and b represents the dipolar coupling constant (more commonly D_{HH}). A few assumptions were necessary, including the fact that the Hartmann-Hahn matching conditions were exactly met. When this is so, the oscillatory frequency, $\omega_{osc.}$, is b/2. Otherwise it is given by equation 7.23, where d represents the mismatch. Resonance offsets further influence the rate of oscillations.

$$M_t \propto 1 - \exp(-Rt) - \tfrac{1}{2}\exp(-3Rt/2)\cos\left(\tfrac{1}{2}b/t\right) \qquad \text{Eq. 7.22}$$

$$\omega_{osc.} = \sqrt{(d^2 + b^2)/4} \qquad \text{Eq. 7.23}$$

The cross-polarisation dynamics of ferrocene are such that the rate of magnetisation transfer was dependent only on the spin-diffusion rate while rotating frame spin-lattice relaxation was very slow. Walther *et al.*[3] reported oscillatory ^{29}Si CP behaviour in porous silica gels where an additional consideration of $T_{1\rho}$ and T_{IS} was necessary for the derivation of an equation to fit the results. Equation 7.24 is effectively a combination of equations 7.17 and 7.22. The spin-diffusion rate is represented by a time constant, T_{II}, and the fraction of protons which form the main proton source is denoted by a parameter, a. A large value of a, *i.e.* close to unity, would indicate that normal behaviour is dominant, while a small value corresponds to dominant oscillatory behaviour.

$$M_t = \frac{M_0}{\lambda}\left(e^{-t/T_{1\rho}} - ae^{-t/T_{IS}} - (1-a)\left(\tfrac{1}{2}e^{-t/T_{II}} + \tfrac{1}{2}e^{-3t/2T_{II}}\cos\left(\tfrac{1}{2}bt\right)\right)\right)$$

Eq. 7.24

In summary, an equation has been derived for variable contact time behaviour. This corresponds to the case where the Hartmann-Hahn matching condition is exactly met and a single dilute S-spin is being polarised by a single proton source (*i.e.* a single type of proton or several proton species which are completely averaged by spin-diffusion). Several other cases have been reported where variable contact time behaviour is irregular. Two distinct proton types can provide the source for the polarisation transfer. Alternatively, CP can occur from proton sources that are distinct from the main proton bath in a sample. In this case, oscillations are seen at a frequency which depends on the rate of spin-diffusion between the two proton types and their relative proportions, as well as any transmitter offset and deviations from the Hartmann-Hahn matching conditions.

7.2.2 Methods of Determining CP Mechanisms

The variable contact time experiment is an indirect source of information regarding the proton species of a sample. Fitting the results to equation 7.17 gives a value of $T_{1\rho}$, a *proton* rotating frame spin-lattice relaxation time for the CP source. In a simple case, this value can be compared with directly measured values for all the proton types in a sample to deduce the mechanism for the cross-polarisation. Such a method is not universally applicable for several reasons: variable contact time curves can be oscillatory and difficult to analyse; significant spin-diffusion or chemical exchange over the time-scale of the cross-polarisation can mean that an average value of $T_{1\rho}$ is measured; many spectra are needed to fit results to equation 7.17; $T_{1\rho}$ can be difficult to measure for samples with poorly resolved ^1H MAS signals; and the distinct proton species might have similar intrinsic relaxation times. However, there are other methods of deducing CP mechanisms. This work has used both 1- and 2-dimensional methods.

There is a more general method of obtaining proton relaxation times using cross-polarisation. The pulse sequence for CP measurement is simply the conventional ^1H NMR sequence with the acquisition step replaced by a constant contact time and acquisition in the S-channel. The method is possible because the detected S-magnetisation at the end of the contact time is proportional to the proton magnetisation preceding it (see equation 7.13). Figure 7.4 shows how inversion recovery and variable spin-locked delay pulse sequences can be modified to measure T_1 and $T_{1\rho}$ of the protons indirectly.

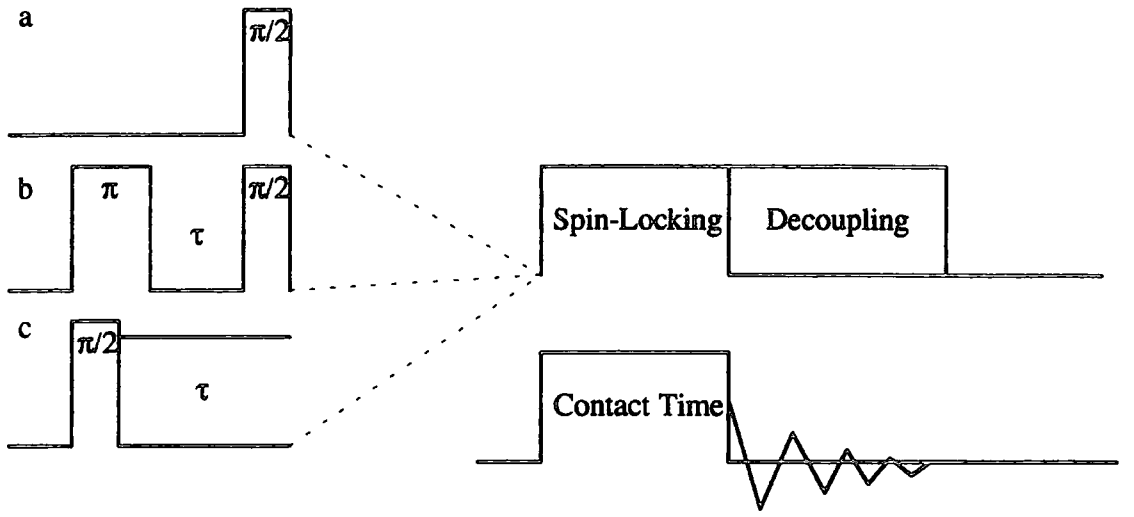

Figure 7.4 A cross-polarisation pulse sequence (a) and two modifications for the indirect measurement of T_1 and $T_{1\rho}$ by CP: b) inversion recovery followed by CP; and b) variable spin-locked delay followed by CP. In each case, several spectra are acquired with different values of the delay, τ. The resulting spectral intensities can be fitted to yield the value of the relevant relaxation time.

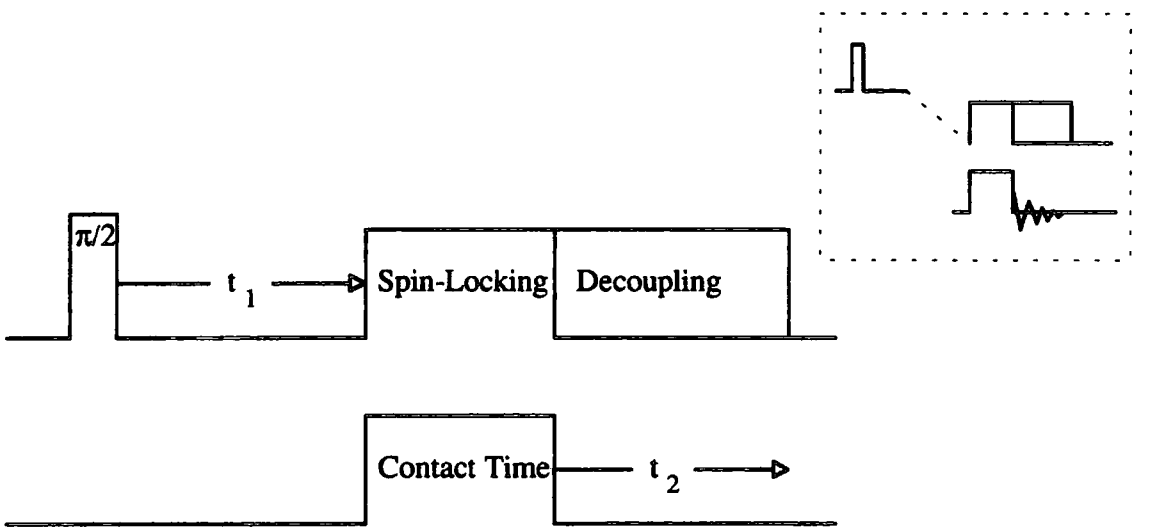

Figure 7.5 A pulse sequence for 2-dimensional correlation spectroscopy. The inset emphasises the similarity between this pulse sequence and those in figure 7.4. This effectively measures T_2^* (and δ) for the protons rather than T_1 or $T_{1\rho}$.

The 2-dimensional method uses a similar strategy to these 1-dimensional methods, in that a ^{1}H MAS FID is traced out before the contact time. This method was initially reported by Vega in 1988 for two zeolite samples, anhydrous H-rho and hydrated Ca,Na-A.[8] Similar methods have since been reported by Fyfe *et al.*, for hydrous silicate glasses[9] and Schmidt-Rohr *et al.*,[10] for correlating ^{13}C CP spectra with wide-line proton spectra; neither authors cite Vega. The pulse-sequence is shown in figure 7.5.

Several spectra are acquired with incrementally increasing values of t_1 to give a 2-dimensional data set. Fourier-transformation over t_2 will therefore give several ^{29}Si spectra corresponding to different t_1 values. The method works because the silicon signal detected in t_2 is a direct measure of the magnetisation of the proton source for CP at the end of t_1. Therefore, the behaviour of the ^{29}Si signal intensities with t_1 is essentially that of a ^{1}H FID, which will give a normal ^{1}H MAS spectrum on fourier-transformation over t_1. The resulting spectrum has axes corresponding to the ^{29}Si and ^{1}H chemical shifts. Signals are observed where δ_{Si} corresponds with δ_{H} of the proton source for the cross-polarisation.

Vega[8] recommended a $^{1}H,^{1}H$ experiment to support conclusions regarding $^{29}Si,^{1}H$ correlation. This is shown in figure 7.6a. In section 5.4 of this work, spin-diffusion or chemical exchange has been detected by a different pulse sequence (figure 7.6b). Both methods can detect proton spin-diffusion or chemical exchange: the former method detects mixing processes in the rotating frame of reference, where $T_{1\rho}$ is relevant, whereas the latter methods detects in the laboratory frame of reference, where T_1 is relevant. If mixing is significant the $^{29}Si,^{1}H$ experiment can not distinguish between proton sites.

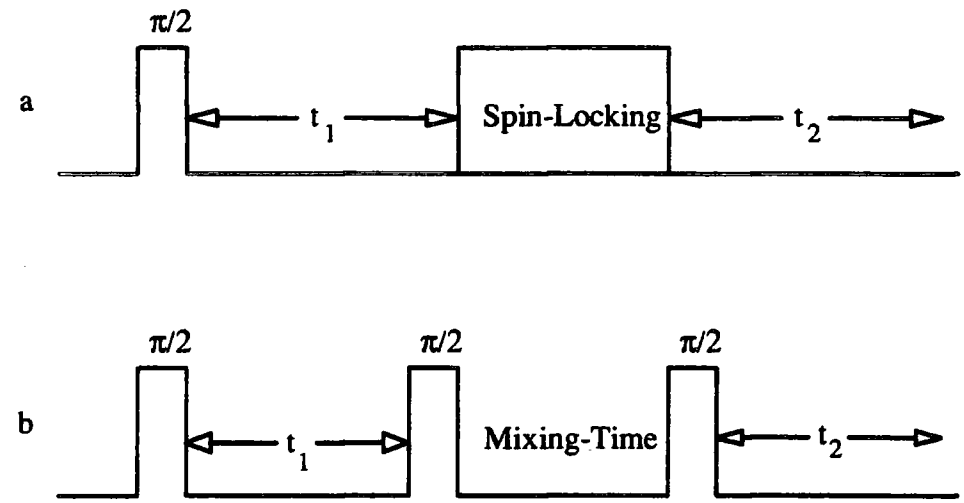

Figure 7.6 Two pulse sequences for determining the extent of proton mixing (spin-diffusion or spin-exchange) during a $^{29}Si,^{1}H$ 2-dimensional correlation spectroscopy experiment. In both cases, the protons are allowed to mix for a time equivalent to the contact time: a) this is the spin-locking time; b) this is the mixing time.

7.3 Makatite & Kanemite ^{29}Si CP Behaviour

7.3.1 Introduction

Most kanemite ^{29}Si NMR spectra have a single Q^3 signal. However, two lines are seen in the spectrum of one anomalous sample. Resolved Q^3 signals are also seen in the ^{29}Si NMR spectrum of the single available makatite sample. Therefore, there are three types of sample with which a search for similarities and differences in ^{29}Si CP behaviour can be made.

7.3.2 Cross-Polarisation Dynamics

This section consists of a determination of the dynamics of ^{29}Si CP for the kanemite sample with two signals and makatite which has several resolved signals. The aim of the work was to compare the behaviour of the two samples.

Variable contact time experiments were carried out for each sample using different spectrometers. The CXP200 spectrometer was used for the kanemite experiment, while the Varian Unity Plus 300 spectrometer was necessary for extra resolution in the makatite spectrum. In each case, several spectra were acquired with different contact times while all other parameters were kept the same. For kanemite (sample kna), 13 FID's of 2000 transients were acquired with a 3 s recycle delay and a spinning rate of 2.5 kHz. For makatite (sample mka), 15 FID's of 88 transients were acquired with a 10 s recycle delay and a spinning rate of 3.01 kHz. The resolution of the makatite spectra was enhanced with gaussian broadening before zero-filling and fourier-transformation, while no apodisation was necessary for the kanemite spectra. Peak intensities were fitted to equation 7.17 using non-linear regression. Table 7.1 lists values of M_0, T_{IS} and $T_{1\rho}$ for each signal in makatite and kanemite. Figures 7.7 and 7.8 show plots of signal intensity with contact time together with curves that were simulated from the regression values.

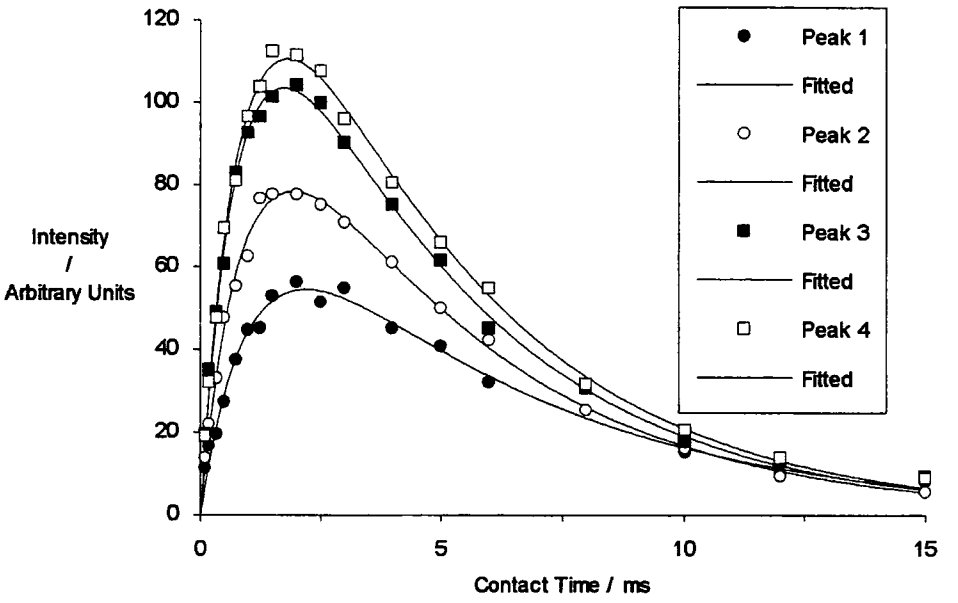

Figure 7.7 Variable contact time curves for makatite (sample mka). Filled and unfilled circles and squares represent the experimental data, while the lines are the results of a simulation using the fitted values of M_0, T_{IS} and $T_{1\rho}$.

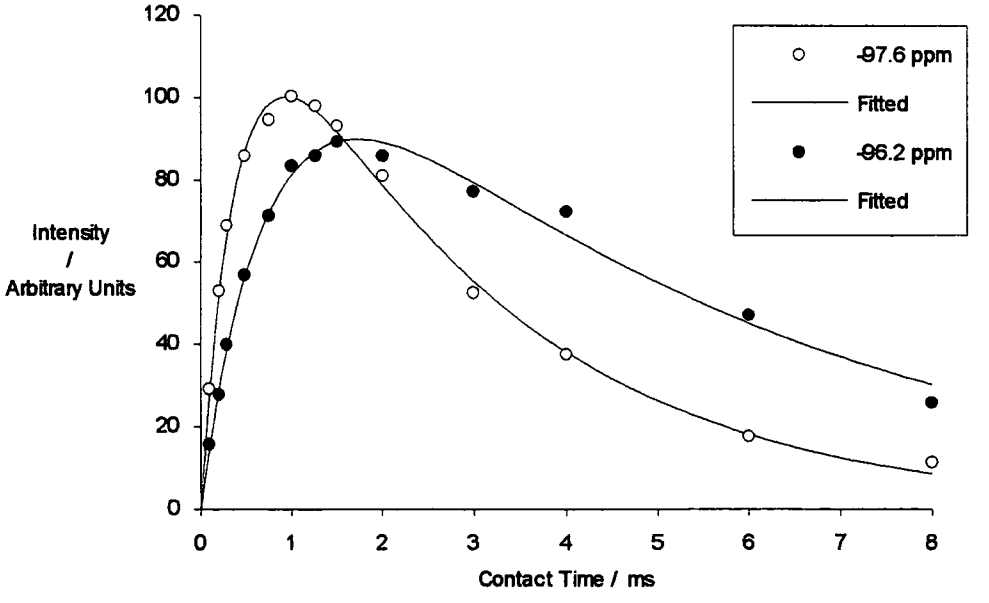

Figure 7.8 Variable contact time curves for kanemite (sample kna). Filled and unfilled circles represent the experimental data, while the lines are the results of a simulation using the fitted values of M_0, T_{IS} and $T_{1\rho}$.

Silicate (Sample)	δ_{Si} / ppm	Peak	M_0 / a.u.	$T_{1\rho}$ / ms	T_{IS} / ms	r^2
Makatite (mka)	-92.2	1	82 ± 9	5.43 ± 0.95	1.10 ± 0.21	0.98350
	-92.6	2	121 ± 9	4.48 ± 0.51	1.00 ± 0.12	0.99418
	-93.0	3	155 ± 9	4.32 ± 0.38	0.87 ± 0.08	0.99609
	-93.7	4	169 ± 10	4.28 ± 0.39	0.93 ± 0.09	0.99625
Kanemite (knb)	-97.6		142 ± 8	2.7 ± 0.3	0.43 ± 0.04	0.99590
	-96.4		127 ± 13	5.0 ± 0.9	0.78 ± 0.14	0.98968

Table 7.1 Results of fitting makatite (sample mka) and kanemite (sample kna) variable contact time results to equation 7.17. The quoted errors are 95% confidence limits obtained from the regression analysis and r^2 is a correlation coefficient.

It should be noted that in both cases, the signal intensities were obtained from overlapping lines, which would tend to average any differences in variable contact time behaviour. The overlap was greatest for makatite, but the resolution was probably adequate for the purposes of this experiment. The experiments produced satisfactory curves which fit equation 7.17 reasonably well; the results provide a good basis for drawing conclusions. The equations give the poorest fit for the low-frequency kanemite signal at δ_{Si} -96.4 and the high-frequency makatite signal at δ_{Si} -92.2; this is evident from low correlation coefficients and by inspection of figures 7.7 and 7.8. Further experiments will provide an explanation for this observation with kanemite, while the makatite signal was the least well-resolved in the ^{29}Si CP spectrum.

In this experiment, makatite and kanemite behave quite differently. The signals in makatite behave similarly with contact time, giving T_{IS} and $T_{1\rho}$ values which are nearly the same, while for kanemite the values for each site are very different.

If the poorly-resolved high-frequency signal is ignored, the rotating frame spin-lattice relaxation times for the makatite lines are insignificantly different. The silicon sites are either coupling with the same proton source or with two different

sources which mix significantly through spin-diffusion or chemical exchange over the time-scale of the experiment. A firmer conclusion can be drawn for kanemite, where the two rotating frame spin-lattice relaxation times are very different. The two silicon sites are coupling with distinct proton species with incomplete spin-diffusion or spin-exchange over the time-scale of the experiment.

With kanemite, cross-polarisation is significantly faster for the high-frequency signal. The difference is quite marked, T_{IS} for the high-frequency signal being about half the low-frequency value. The values for the makatite signals are all very similar.

7.3.3 The Mechanism for Cross-Polarisation: $^{29}Si,^{1}H$ Correlation

Deducing the mechanism of $^{1}H,^{29}Si$ CP for makatite is trivial. There are four silicon signals in the ^{29}Si CP spectrum and one signal is observed in the ^{1}H MAS spectrum (see sections 5.1.4 and 5.2.3). For all sites, ^{29}Si cross-polarisation occurs *via* magnetisation transfer from this single proton type.

The mechanism for kanemite can be determined by 2-dimensional $^{1}H,^{29}Si$ correlation spectroscopy experiments, together with a consideration of the extent of mixing between proton species by chemical exchange or spin-diffusion. This method has been used for two kanemite samples: sample kna has two ^{29}Si CP signals and three in a ^{1}H MAS spectrum, whereas sample knb has a single ^{29}Si CP signal and two peaks in a ^{1}H NMR spectrum.

For each sample, 2-dimensional $^{29}Si.^{1}H$ correlation spectra were acquired using the VXR300 spectrometer and a previously-written pulse program based on that reported by Vega (figure 7.5).[8] For sample kna, the 2D data-set was built up of 64 FID's of 256 data points. For each FID, 800 transients were acquired with a contact time of 1 ms and a recycle delay of 0.5 s. The spinning-rate was 5.02 kHz. The proton and silicon spectral widths were 50 and 5.872 kHz respectively. For sample knb, the 2D data-set was built up of 64 FID's of 256 data points. For each FID, 800 transients were acquired with a contact time of 1 ms and a recycle delay of 0.5 s. The spinning-rate was 5.14 kHz. The proton and silicon spectral widths were 50 and 5.882 kHz respectively. The 2-D spectra are shown in figures 7.9 and 7.10.

A 2-dimensional $^{1}H,^{1}H$ spectrum was acquired for sample kna using the VXR300 spectrometer, equipped with a Doty high speed MAS probe with 5 mm zirconia rotors, and a pulse program based on that of Szeverenyi (figure 7.6b). The spinning rate was 12.7 kHz and the 2-dimensional data-set was built up of 128 FID's of 576 data points. For each FID, 16 transients were acquired with a recycle delay of 0.5 s and a mixing time of 1 ms. The spectral widths in each dimension were 20 kHz. The result is displayed in figure 7.11.

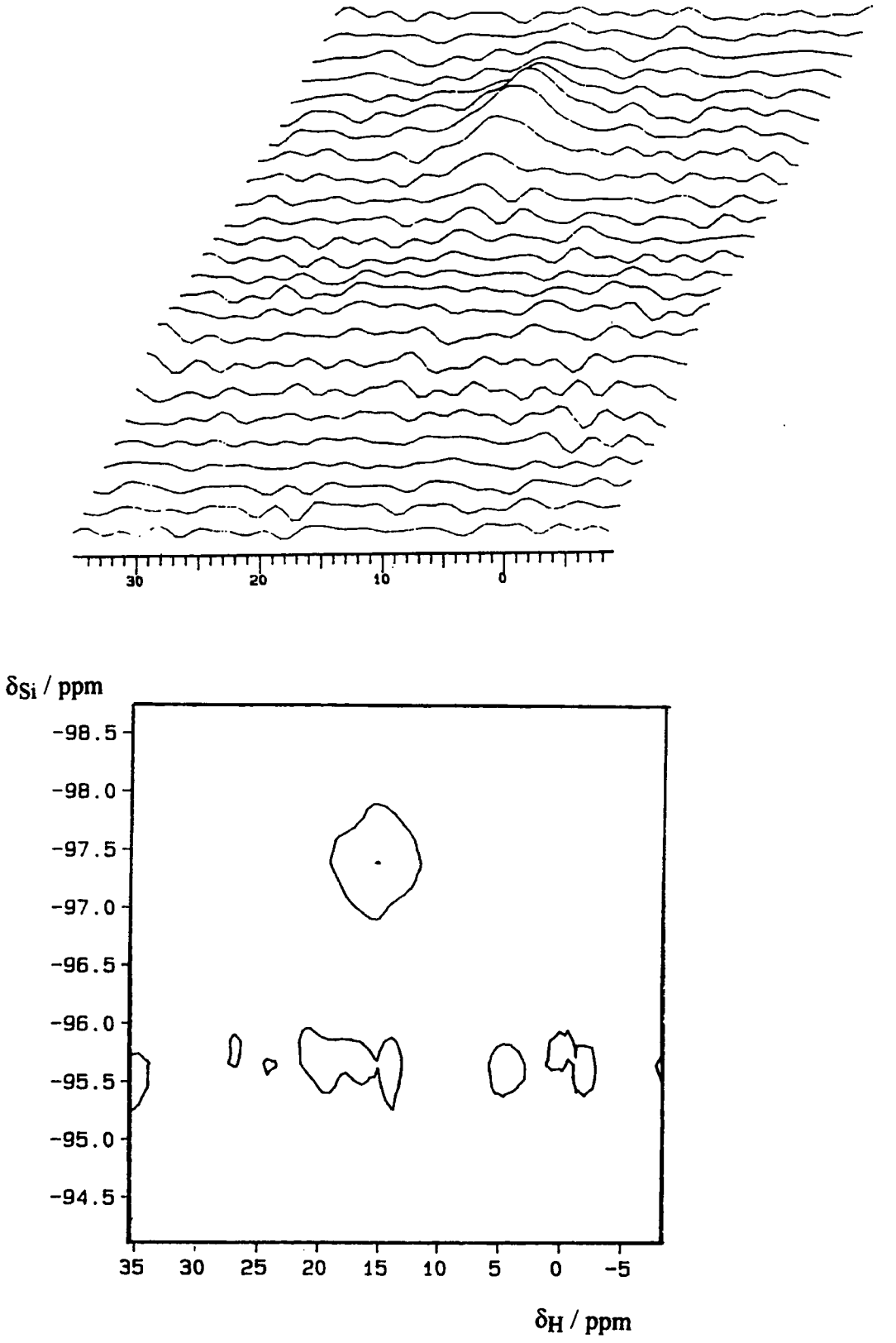

Figure 7.9 A 2-dimensional $^{1}H,^{29}Si$ correlation spectrum of kanemite (sample kna). A contour spectrum is displayed above a stacked plot.

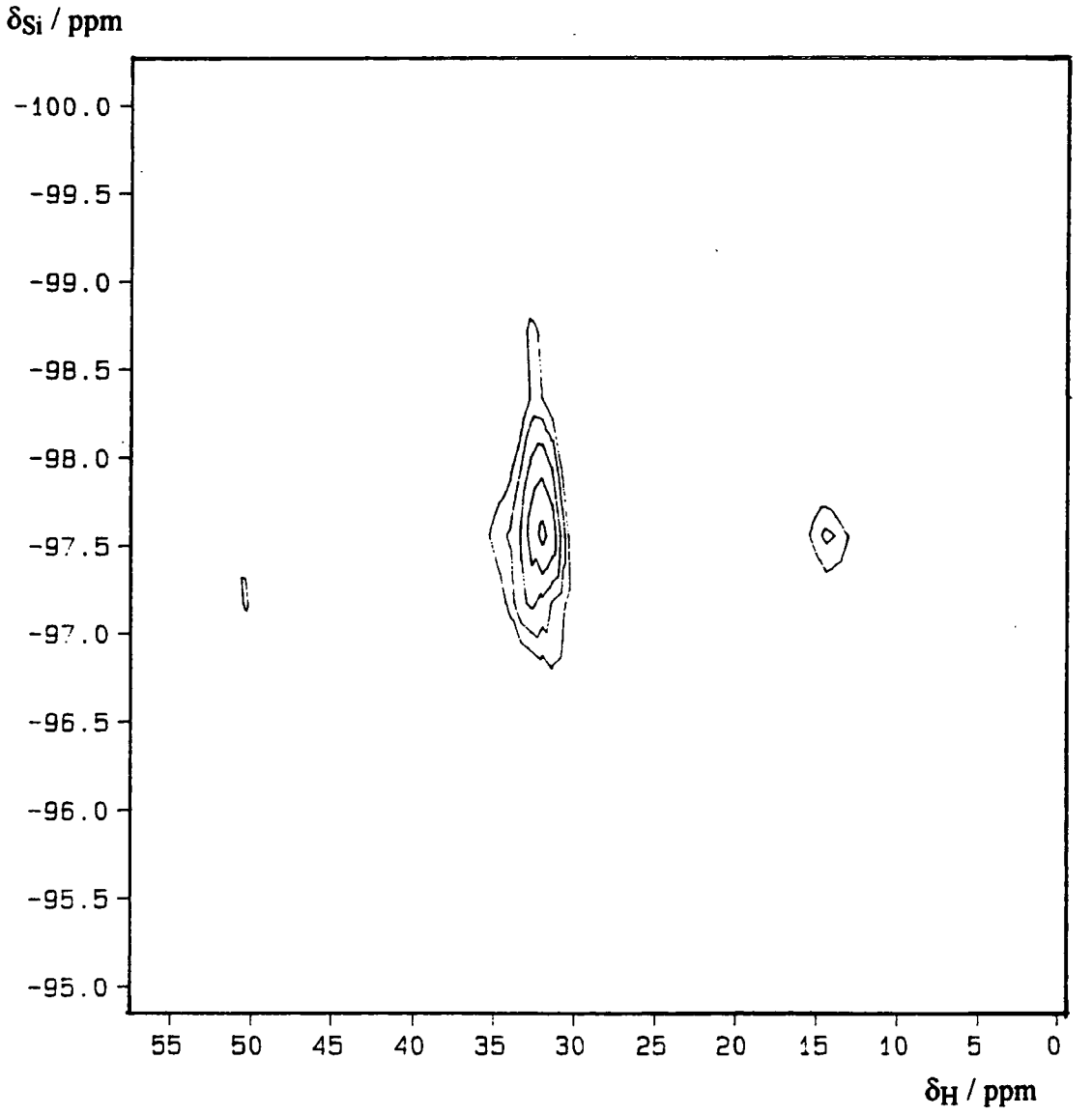

Figure 7.10 A 2-dimensional $^{1}H,^{29}Si$ correlation spectrum of kanemite (sample knb).

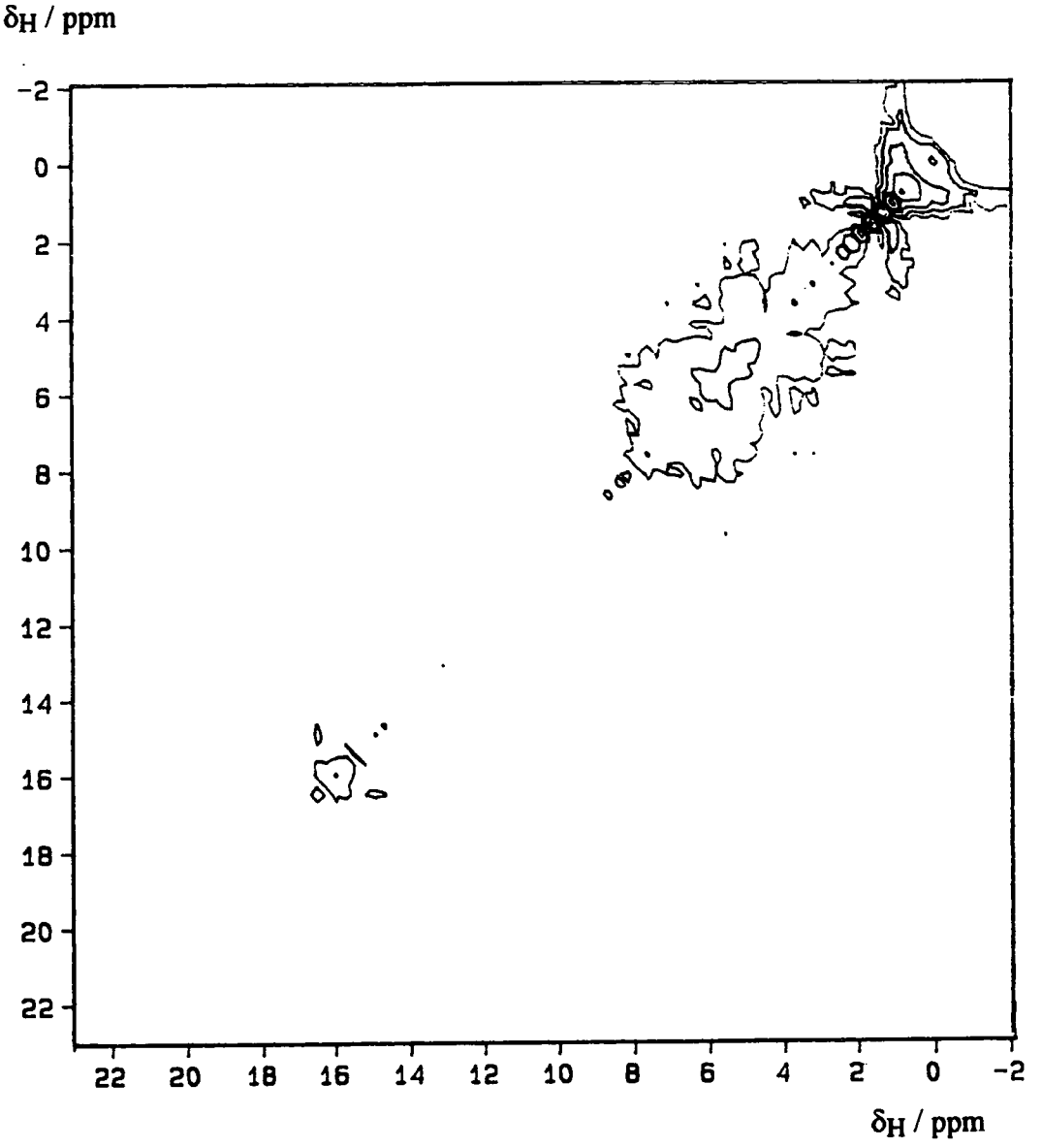

Figure 7.11 A ^1H,^1H exchange spectrum for kanemite (sample kna). The diagonal corresponds to a conventional ^1H MAS spectrum. If there were any, cross-peaks would have been evidence of spin-diffusion or chemical-exchange. The line-shapes are very difficult to explain, but there are diagonal peaks at δ_H 1, 4 and 15.

A ^{29}Si CP spectrum of kanemite (sample kna) contains two lines (figure 5.6b). A ^{1}H MAS spectrum of this sample has three centre-band signals at δ_H 15, 4 and 1, (figure 5.12b). These can be assigned to strongly hydrogen-bonded, water and silanol protons, respectively. In the $^{29}Si,^{1}H$ correlation spectrum, with a spinning speed of 5.02 kHz and a transmitter frequency of 300 MHz, spinning side-bands are expected to be visible at multiples of *ca.* 17 ppm from the central lines. There is only one signal in the ^{29}Si CP spectrum of sample knb (figure 5.6a). The proton spectrum contains two centre-band proton signals at δ_H 15 and 4 (figure 5.12c). These can be assigned to strongly hydrogen-bonded and water protons, respectively. Again, spinning side-bands are expected to be at multiples of *ca.* 17 ppm from the centre-bands in the 2-D spectrum.

A projection of the kanemite (sample kna) 2-dimensional spectrum onto the silicon axis should give a spectrum similar to figure 5.6b. In the 2-D spectrum all the intensity of the low-frequency signal seems to come from the H-bonding proton alone, so a strong peak is seen at δ_H 15. The intensity of the high-frequency signal is smeared over a larger range, so the peaks are smaller and poor signal-to-noise makes it more difficult to deduce the correlation. However, the contour plot shows peaks at δ_H 35, 20, 4 and -8 ppm due to cross-polarisation from the water proton and three spinning side-bands. Peaks around δ_H 15 and 1 are also visible, corresponding to coupling with the strongly and weakly hydrogen-bonding protons. Since correlation was observed between three proton signals and one silicon site, it is necessary to consider the extent of mixing between proton species over the time-scale of the cross-polarisation (a contact time of 1 ms). As no cross-peaks are observed in figure 7.11, the 2-D $^{1}H,^{1}H$ exchange spectrum with a mixing time of 1 ms, spin-diffusion or chemical exchange is insignificant over the time-scale of the $^{29}Si,^{1}H$ experiment. Therefore, all the peaks in this spectrum come from direct rather than indirect correlation: $^{1}H,^{29}Si$ CP, rather than $^{1}H \leftrightarrow ^{1}H,^{29}Si$ CP.

The 2-dimensional $^{29}Si,^{1}H$ correlation spectrum of kanemite (sample knb) contains peaks corresponding to the lone ^{29}Si signal. These occur at proton chemical

shifts corresponding to the H-bonding proton and two spinning side-bands, only. Therefore, they can be assigned to correlation between the silicon site and H-bonding protons. The peak intensities are surprising– the spinning side-band is much larger than the centre-band signal. This is probably due to a spike or artefact underneath the low intensity signal at δ_H *ca.* 30– not an uncommon occurrence in 2-D NMR, *viz.* figure 7.29. A $^1H,^1H$ exchange experiment was not necessary for this sample, since the $^{29}Si,^1H$ experiment gave a selective result and the ^{29}Si CP mechanism is clear. Cross-polarisation occurs via a transfer of magnetisation from the H-bonding protons only to the single silicon site.

7.3.4 Conclusions

The work in this chapter consists of two different ^{29}Si CP experiments on three layered polycrystalline silicate hydrate samples. Variable contact time experiments were used to investigate the two samples with more than one ^{29}Si signal, while $^{29}Si,^1H$ correlation spectroscopy experiments were used to investigate the two samples with more than one ^1H signal. Complementary experiments on the samples with one ^{29}Si or ^1H signal would have given trivial results.

Makatite and the kanemite sample with two Q^3 peaks have different CP dynamics. In makatite the many Q^3 signals behave similarly: cross-polarisation occurs with slightly different efficiencies to proton types with the same rotating frame spin-lattice relaxation time. Since only one signal is observed in the ^1H MAS spectrum of makatite, the mechanism for CP is clear– cross-polarisation to all silicon sites occurs via a transfer of magnetisation from a single detectable proton species. When observable, the two Q^3 sites in kanemite have quite distinct CP dynamics. The low-frequency signal cross-polarises more efficiently than the high-frequency signal to a proton with a much shorter rotating frame spin-lattice relaxation time. The CP mechanism for the high-frequency signal is a transfer of magnetisation from all three

proton species. There is no significant mixing between the three proton sources, so the shape of the variable contact time curve in figure 7.8 could be due to the summation of three individual curves; this is quite possible as the curve contains local maxima and the simple model of cross-polarisation from a single proton source provided a very poor fit to the data using non-linear regression. If this was the case, the fitted T_{IS} and $T_{1\rho}$ values would be fairly meaningless. The low-frequency signal has the same mechanism as the lone signal in other kanemite samples– ^{29}Si cross-polarisation occurs *via* a transfer of magnetisation from the hydrogen-bonded protons only. Overall, these are clear results that provide some room for speculation over the spectroscopic and structural reasons for the observed differences in ^{29}Si and ^{1}H spectral multiplicities, CP dynamics and CP mechanism.

The structure of makatite has been resolved by single-crystal x-ray diffraction, providing positions for the silicon, oxygen and sodium atoms, within a unit cell. The siting of the oxygen atoms make it likely that there are silanol and water proton species. Since just one signal is observed in a ^{1}H SP/MAS makatite spectrum, the differences between these sites must be averaged over the time-scale of the NMR experiment, either by chemical-exchange or by spin-diffusion. With kanemite, several distinct proton species are visible in proton spectra, so the extent of averaging must be much less over a similar time-scale. Because the sites are distinct, selectivity is observed in ^{29}Si cross-polarisation. The significant factor in causing makatite and kanemite to behave differently might be the spectral overlap between a hydrogen-bonding proton and the other proton species in a sample. There is no evidence for strong H-bonding in makatite, so a silanol proton signal would be expected to overlap considerably with that of a water proton– the work of Yesinowski *et al.*[11] indicated that both signals would occur around δ_H 1 to 6 (see section 5.2.2). Rapid spin-diffusion gives a single line in the proton spectrum at an average chemical shift. There is strong hydrogen-bonding in kanemite corresponding to a signal at δ_H 15. Since there will be minimal overlap between this line and aqueous proton signals, spin-diffusion is less efficient, separate ^{1}H MAS peaks are seen and some selectivity

is observed on cross-polarisation. The above speculation excludes consideration of the silanol proton in kanemite (sample kna) at δ_H 1. Since no mixing is observed between this species and water, it is possible that the location of these protons is distinct from the other protons in the sample. Further consideration will be saved for chapter 8.

Finally, the assignment of the ^{29}Si peaks should be considered. The makatite signals have been assigned to the four silicon atoms in the known asymmetric unit, though it is possible that some of the signals could come from a contaminant (see section 5.1.4). This still seems a reasonable assignment and the similar CP behaviour of all the signals probably makes the presence of an impurity resonance less likely. The low-frequency kanemite signal, which is seen in all samples, is bonded to a strongly hydrogen-bonded proton. The high-frequency signal, which is only seen in one sample, can not be classified as easily, since it couples with three types of proton.

7.4 Silicon-29 CP Dynamics of Octosilicate, Magadiite and their Silicic Acids

This section contains details of variable contact time experiments for samples of H-octosilicate and H-magadiite. The results can yield values of M_0, $T_{1\rho}$, and T_{IS}. These are useful parameters: M_0 is quantitative; $T_{1\rho}$ can be used to identify the proton source of the cross-polarisation; and T_{IS} can be related to the distance between these protons and the rare-spin nuclei which are being detected in the CP spectrum. The ^{29}Si CP spectra of these samples contain several signals. Determining cross-polarisation dynamics for these might provide useful information; particularly regarding the two Q^3 signals in anhydrous H-octosilicate and the three Q^4 signals in H-magadiite.

The variable contact time spectra were acquired using the CMX200 spectrometer, equipped with a Doty MAS probe and zirconia 7 mm rotors. A standard pulse sequence, cp was used with a macro to automatically vary the contact time, and save files. Table 7.2 lists the experimental details.

Silicate	Sample	Recycle Delay / s	Spinning Rate / kHz	Number of Transients	Number of FID's
H-Octosilicate	hob	3	2.02	100	20
H-Octosilicate	hoa	3	2.02	100	20
H-Magadiite	hma	3	2.0	64	16

Table 7.2 Experimental details for the variable contact time experiments.

For each experiment, all FID's were subjected to the same zero-filling, apodisation and fourier-transformation routine. The values of spectral intensity with contact time were initially fitted to equation 7.17 to obtain M_0, T_{IS} and $T_{1\rho}$. This was successful for the Q^3 signals, but the Q^4 behaviour could only be modelled by fitting with a fixed value of $T_{1\rho}$– that obtained from the Q^3 data. Variable spin-locked delay experiments have shown that it is reasonable to assume that proton rotating frame

spin-lattice relaxation observed through the Q^3 signals occurs at the same rate as that observed through the Q^4 signals.

Figures 7.12 and 7.13 display the results for each sample together with simulated curves using values obtained from the fitting, which are listed in table 7.3. Multiple Q^3 and Q^4 peaks have been described using labels. Reported errors relate to the asymptotic 95% confidence intervals provided by the fitting method. The r^2 parameter is $1-\{\Sigma(\text{residuals}^2)/\ \Sigma(\text{corrected values}^2)\}$ and again is provided by the fitting routine.

Silicate	Peak	δ_{Si} / ppm ($\Delta_{½}$ / Hz)	M_0 / a. u.†	T_{IS} / ms	$T_{1\rho}$ / ms	r^2
H-Octosilicate	Q^3	-104.4 (44)	4.33 ± 0.09	1.04 ± 0.04	13.8 ± 0.7	0.99846
(hoa)	Q^4	-113.2 (44)	3.93 ± 0.26	7.90 ± 0.91	Q^3-Value	0.99347
H-Octosilicate	Q^3a	-98.4 (30)	4.80 ± 0.13	1.15 ± 0.07	71 ± 18	0.99781
(hob)	Q^3b	-99.0 (30)	5.85 ± 0.15	1.20 ± 0.06	74 ± 19	0.99807
	Q^4	-111.2 (38)	7.93 ± 0.18	8.21 ± 0.33	Q^3-Value	0.99960
H-Magadiite	Q^3	-102.5 (66)	1.42 ± 0.03	1.11 ± 0.06	31.6 ± 3.7	0.99770
(hma)	Q^4a	-111.8 (60)	0.72 ± 0.06	8.96 ± 1.28	Q^3-Value	0.99644
	Q^4b	-113.1 (60)	0.89 ± 0.10	13.1 ± 2.1	Q^3-Value	0.99784
	Q^4c	-114.9(60)	0.65 ± 0.20	14.8 ± 6.2	Q^3-Value	0.98823

Table 7.3 Fitted results of variable contact time experiments. The term Q^3-value indicates that the Q^4 data were fitted using the Q^3 $T_{1\rho}$ value. Where $T_{1\rho}$ is described as infinite, the data have been fitted to equation 7.17. †The units of M_0 are arbitrary.

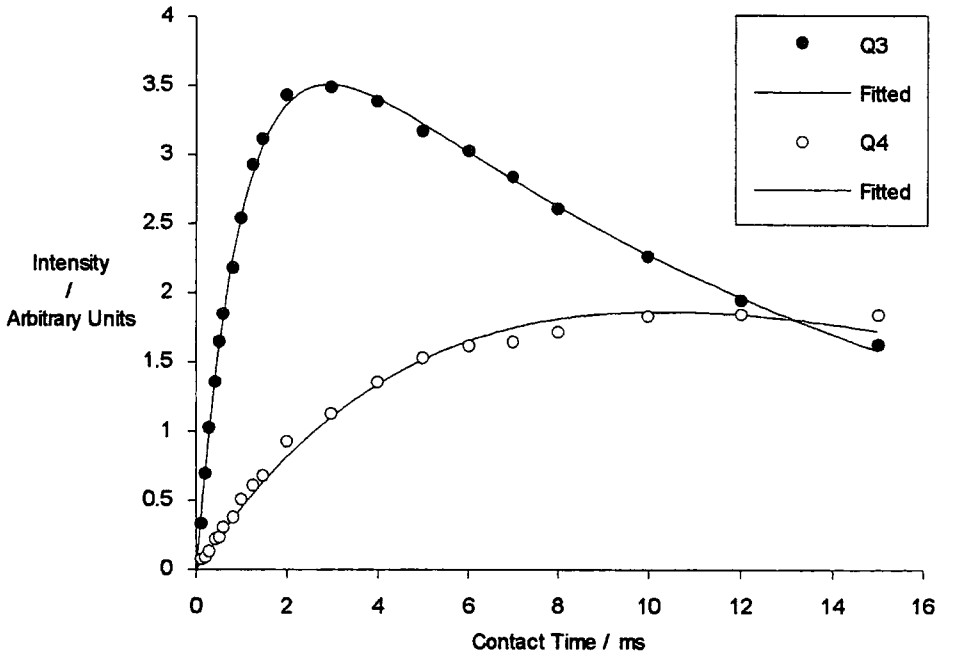

a

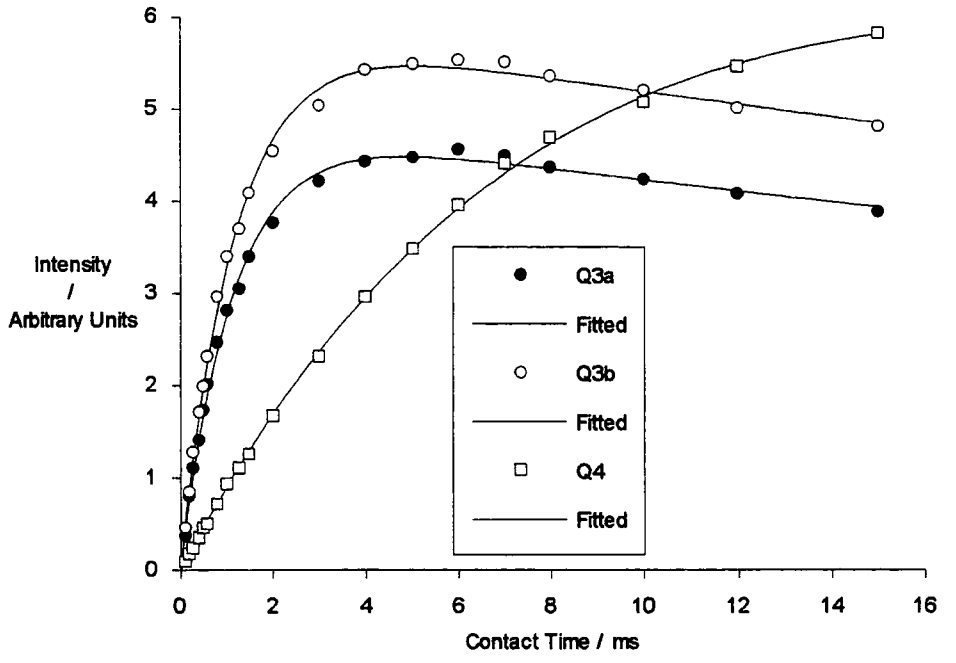

b

Figure 7.12 Variable contact time results and fitting for two H-octosilicate samples: a) hydrated sample hoa; and b) anhydrous sample hob. The experimental data are represented by circles and squares, while solid lines represent curves simulated from fitted values of M_0, T_{IS} and $T_{1\rho}$.

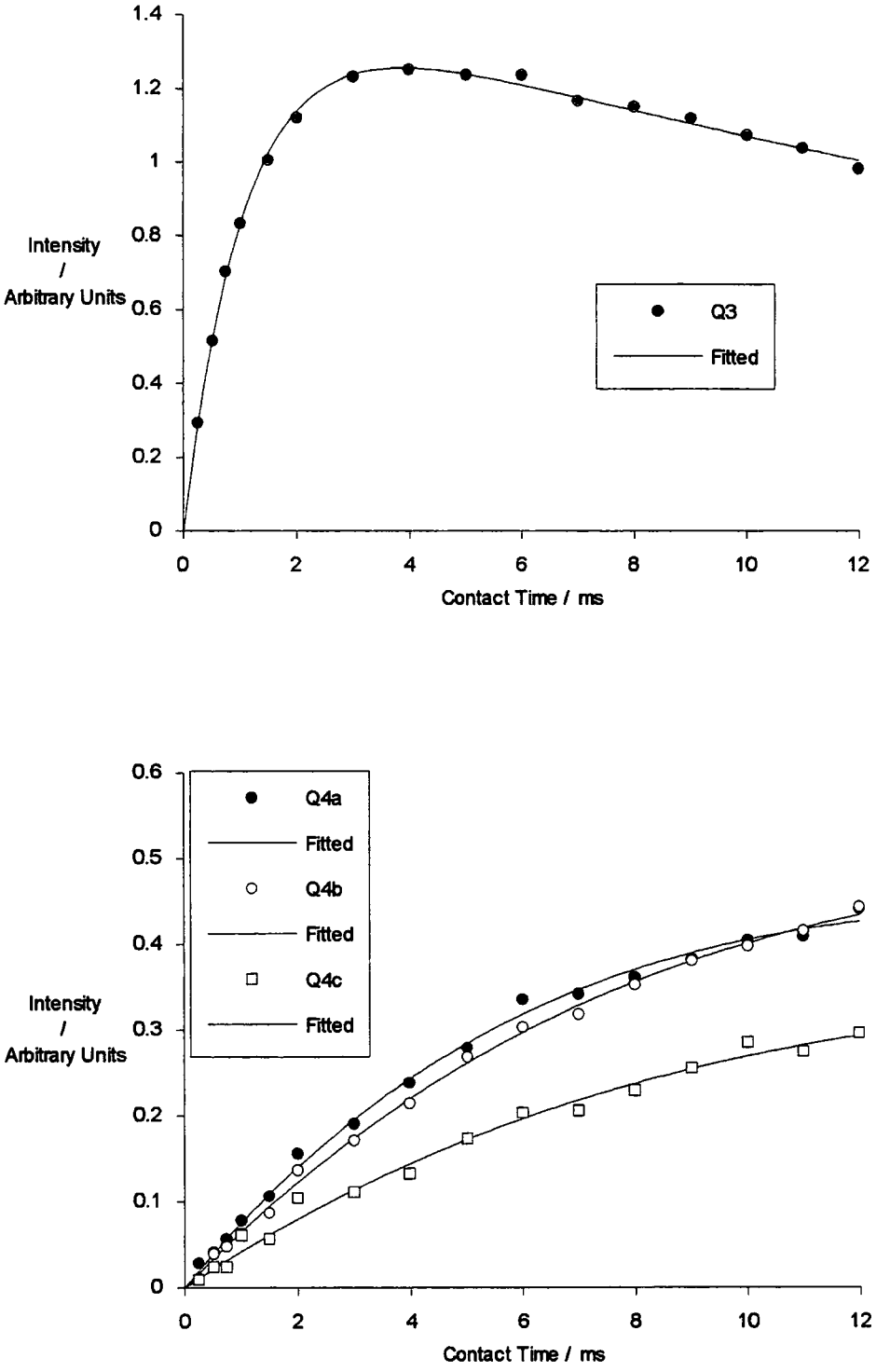

Figure 7.13 Variable contact time results and fitting for hydrated H-magadiite (hma). The Q^4 curves (below) are displayed with a different vertical scale to the Q^3 graph (above). The experimental data are represented by filled and empty circles and squares, while solid lines represent curves simulated from fitted values of M_0, T_{IS} and $T_{1\rho}$.

The M_0 parameters should be quantitative, but, since intensities rather than peak areas were measured, the width of the signals must also be considered The ratios of Q^3 sites to Q^4 sites can be compared with those which have been determined from single-pulse ^{29}Si spectra for the parent sodium silicates– 1:1 for octosilicate and 1:3 for magadiite.[12,13] The two lines in H-octosilicate (sample hoa) have similar values of M_0 and similar peak widths. Therefore, these CP results are consistent with a Q^3:Q^4 ratio of 1:1. A similar Q^3:Q^4 ratio might be deduced for H-octosilicate (sample hob), where M_0 for the two narrower Q^3 signals is smaller than the value for the single Q^4 line. The four H-magadiite lines have similar widths and the M_0 values indicate that there are two Q^3 species for each of the three Q^4 species, corresponding to a Q^3:Q^4 ratio of *ca.* 1:1.5. A value of 1:3 would be expected, so the Q^4 signals are being under-represented in the ^{29}Si cross-polarisation spectra.

The two Q^3 signals in H-octosilicate (sample hob) could represent two crystallographically distinct sites or a single signal which is being split by interactions with neighbouring nuclei. Such split Q^3 resonances were discussed in connection with the ^{29}Si spectra of kanemite (see section 5.1.5) and similar factors are relevant here. Since the variable contact time curves of the two signals are very similar, it is unlikely that gross structural differences are responsible for the splitting.

Cross-polarisation time constants, T_{IS} have been measured for 4 Q^3 and 5 Q^4 silicon sites. All the Q^3 values are *ca.* 1 ms, values for the H-octosilicate Q^4 silicon atoms and the highest-frequency Q^4 site in H-magadiite are *ca.* 8 ms, and the values for the other Q^4 sites in H-magadiite are *ca.* 14 ms. The value of T_{IS} depends on the separation and relative mobility of the silicon nuclei and the proton source of the cross-polarisation. The Q^3 silicon species are likely to be silanol groups, ≡Si-OH, with similar proton-silicon separations in both H-octosilicate samples and H-magadiite. The correspondence in T_{IS}-values indicates that the relative mobility of the silicon and proton species is similar in all three samples. Assuming this is the case, the Q^4 signals can be assigned on the basis of their silicon-proton separations.

Thus, the Q^4 signals in the two H-octosilicate samples and the high-frequency signal in H-magadiite are equally distant from protons: these might all correspond to Q^4 silicon atoms which have a neighbouring silicon atom of type Q^3. The other signals in H-magadiite are significantly further away from protons and are likely to have neighbouring silicon atoms of type Q^4 only. Figure 7.14 is an explanatory diagram. This is a tentative conclusion that has been drawn from H-magadiite ^{29}Si CP spectra end low-intensity Q^4 lines. Confirmation could be obtained from a variable contact time experiment with a larger spread of time values or alternatively with a $^{29}Si,^{29}Si$ correlation spectroscopy experiment. These experiments are generally only feasible if enriched materials are available. However, natural abundance experiments have been reported by Fyfe *et al.*,[12] for samples with very sharp lines, and Kolodziejski *et al.*[13] The latter deduced the $^{29}Si,^{29}Si$ connectivity in mordenite using J-scaled[14] correlation spectroscopy (the width and δ_{Si} range of the mordenite signals are fairly similar to those in magadiite). Since magadiite spectra can be acquired with cross-polarisation, these experiments should be possible within a reasonable amount of spectrometer time.

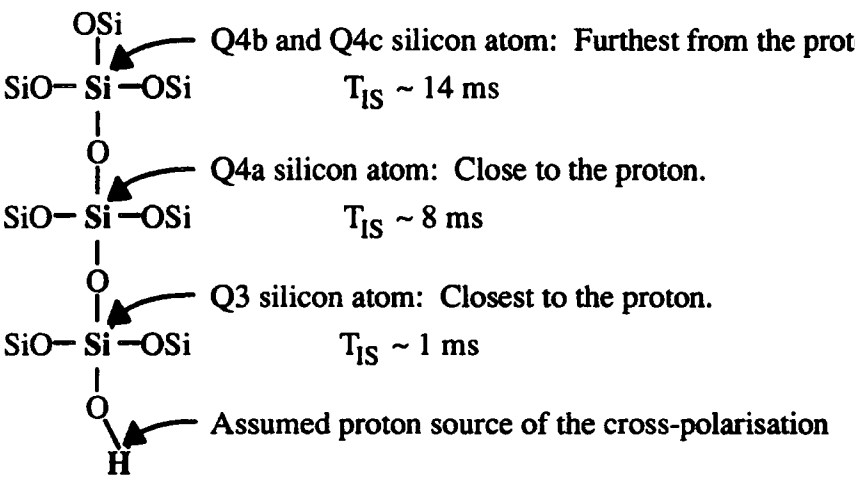

Figure 7.14 A schematic diagram to show the possible structural relationship between the silicon sites responsible for the four ^{29}Si NMR signals in H-magadiite (sample hma). Larger values of T_{IS} correspond to a larger separation from the proton source for cross-polarisation.

Several other variable contact time experiments were carried out for Na-magadiite and Na-octosilicate samples. In these experiments, the curves of signal intensity with contact time tended to be oscillatory. As an example, figure 7.15 shows the results of a variable contact time experiment for octosilicate (sample occ). Fitting the data to obtain precise values for M_0, T_{IS} or $T_{1\rho}$ was impossible. Nevertheless, the oscillations are an interesting phenomenon that can be explained with respect to the work of Müller *et al.* and Walther *et al.*[7,3] The experiments in section 5.4. showed there was significant mixing between the proton species in these samples over the time-scale of a typical cross-polarisation experiment. Spin-diffusion can introduce an oscillatory component into the transfer of magnetisation between protons and silicon nuclei.

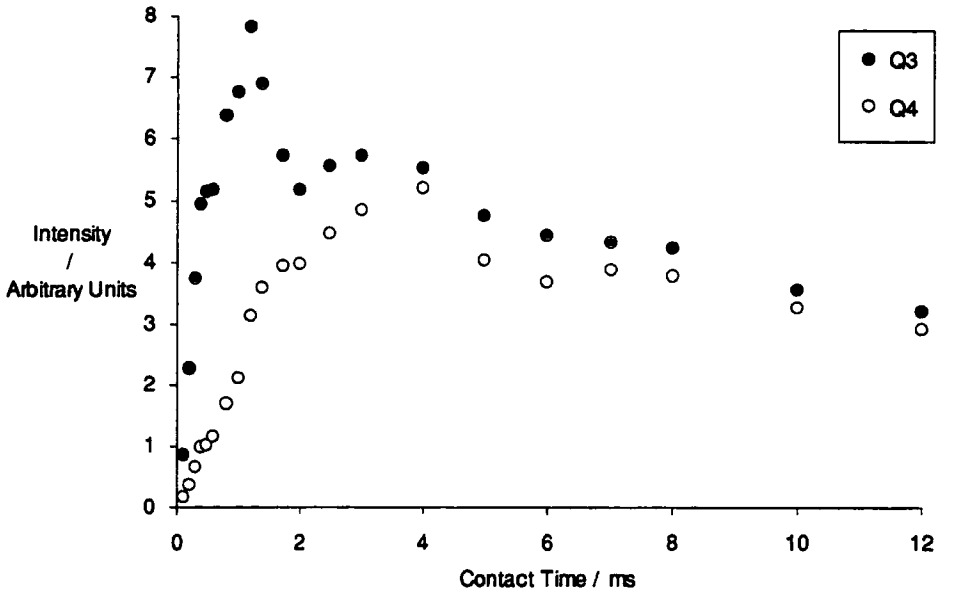

Figure 7.15 The results of a ^{29}Si CP variable contact time experiment for octosilicate (sample occ). Twenty-one spectra of 200 transients were acquired with a recycle time of 3 s and a spinning rate of 2 kHz.

In summary, quantitative information has been obtained from variable contact time experiments for three silicic acid samples. If the T_{IS} values are related to the distance between the silicon nucleus and a silanol proton, the three Q^4 signals in H-

magadiite can be assigned by the connectedness of their neighbouring silicon atoms. The low-frequency lines correspond to silicon sites with Q^3 and Q^4 neighbours, while the other silicon sites will have Q^4 neighbours, only. Qualitative information can be obtained from similar experiments with Na-octosilicate and Na-magadiite. The variable contact time curves indicate that the proton source of the cross-polarisation is distinct from the rest of the protons in the sample. Spin-diffusion between the two types of proton, which has been detected in these silicates, is responsible for oscillatory behaviour of signal intensity with contact time.

7.5 The Mechanism of $^{29}Si,^{1}H$ Cross-Polarisation in Octosilicate

7.5.1 Introduction

Section 7.2.2 showed that cross-polarisation mechanisms can be determined by 1- and 2-dimensional methods. There are two types of silicon site in octosilicate, Q^3 and Q^4, and two types of proton species– hydrogen-bonded and water. The work in this section will show which of the proton species is the source of magnetisation for cross-polarisation for each of the silicon sites.

7.5.2 One-Dimensional Methods

The viability of 1-dimensional methods for determining cross-polarisation mechanisms depends on the resolution of the proton species, in terms of their chemical shifts and their relaxation times. The two octosilicate proton signals are sharp with excellent resolution at achievable spinning rates (see section 5.2.4). However, under such conditions, they have similar spin-lattice relaxation times, T_1 (see section 5.3.2). Therefore, no attempt was made to determine the CP mechanism by comparison of directly and indirectly measured proton spin-lattice relaxation times. A null cross-polarisation experiment would have just been possible as proton inversion-recovery spectra show that zero H-bonding proton signal is observed at a slightly different recovery-time to zero water proton signal (figure 5.21). However, any CP signal observed around the null-times of the two species would have been at a low intensity, whatever the mechanism for cross-polarisation.

Experiments in section 5.4 have shown that the similar T_1-values are understandable because the two types of proton mix significantly through spin-diffusion or chemical exchange over the time-scale of the relaxation. Rotating frame spin-lattice relaxation times, $T_{1\rho}$, are smaller than T_1, and the mixing should be less extensive over the shorter time-scale. The experiments in this section are an attempt to

deduce the ^{29}Si cross-polarisation in octosilicate by measuring $T_{1\rho}$ indirectly, through ^{29}Si CP, and directly, through ^{1}H MAS NMR.

Two methods of indirect $T_{1\rho}$ measurement (*i.e. via* ^{29}Si CP) were available. Proton rotating frame spin-lattice relaxation times can be measured with variable contact time or variable spin-locked delay experiments. An example of the former for octosilicate (sample occ) has been described in section 7.4; the results are displayed in figure 7.15. The plot of signal intensity with contact time is oscillatory: irregular behaviour could be caused by spectral noise, spectrometer instability or dipolar oscillations of the sort observed in ferrocene. The former is unlikely, because the level of baseline noise is slight, equivalent to *ca.* 2 % of the most intense signal. Further speculation about whether the fluctuations are caused by spectrometer instability or dipolar oscillations is unnecessary here; it is sufficient to say that these results are not suitable for the determination of $T_{1\rho}$. A spin-locked delay experiment should provide much more useful results.

Variable spin-locked delay ^{29}Si CP and ^{1}H MAS experiments for octosilicate (sample occ) were carried out using the CMX200 spectrometer, equipped with a Doty MAS probe and 7 mm zirconia rotors. In each case, spectra were attained at several delay times, τ, while all other parameters were kept constant. Existing pulse sequences were used, t1rhoh for ^{29}Si CP and t1rho for ^{1}H MAS, while a macro was used for automation. Further experimental details are listed in table 7.4.

Method	Number of Experiments	Number of Transients	Recycle Delay / s	Spinning Rate / kHz	Contact Time / ms
^{29}Si CP	10	200	3	2	2
^{1}H MAS	32	16	3	4	n/a

Table 7.4 Experimental details for two measurements of proton $T_{1\rho}$-values for octosilicate (sample occ).

In each case the peak intensities of the resultant spectra were fitted to equation 2.13 using non-linear regression. The results of the statistical analysis are shown in tables 7.5 and 7.6. The experimental data are plotted in figures 7.16 and 7.17, together with simulations from the results of the statistical analysis.

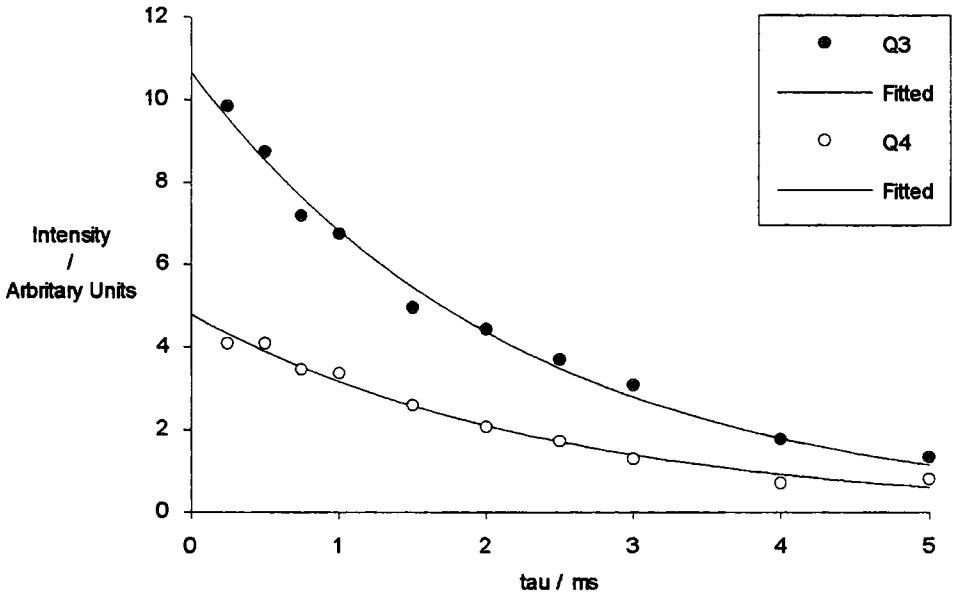

Figure 7.16 The results of a spin-locked delay ^{29}Si CP experiment for octosilicate (sample occ). Filled and unfilled circles represent the experimental data while the lines are the results of a simulation, from fitted values.

Signal	$T_{1\rho}$ / ms	r^2
Q^3	2.23 ± 0.25	0.99011
Q^4	2.41 ± 0.33	0.98418

Table 7.5 Results of fitting the ^{29}Si CP spin-locked delay experimental data for octosilicate (sample occ) to a mono-exponential equation using non-linear regression. The quoted errors are 95 % confidence limits and r^2 is a correlation coefficient.

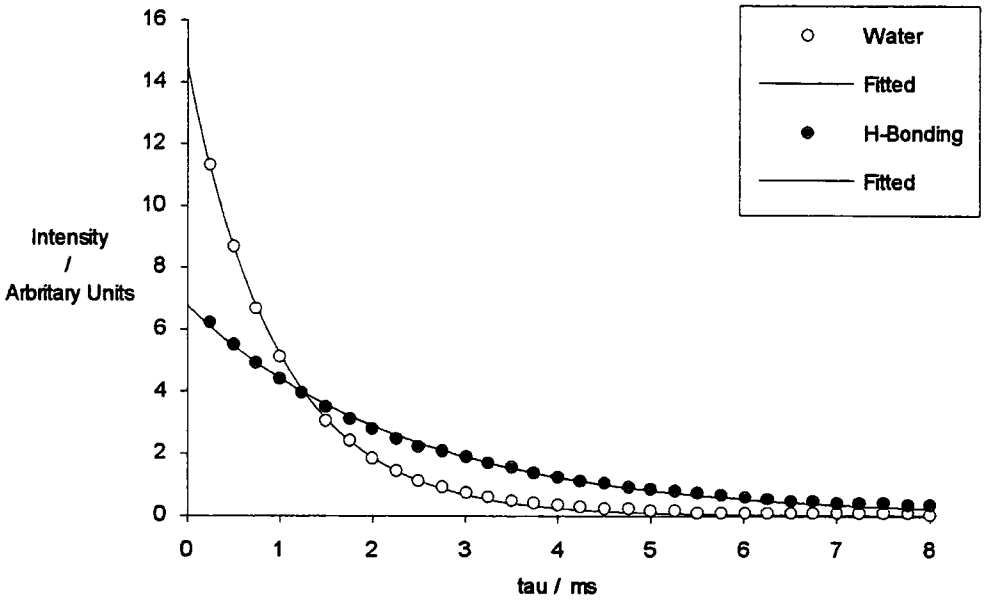

Figure 7.17 The results of a spin-locked delay ^{1}H MAS experiment for octosilicate (sample occ). Filled and unfilled circles represent the experimental data while the lines are the results of a simulation, from fitted values.

Signal	$T_{1\rho}$ / ms	r^2
H-Bonding	2.36 ± 0.06	0.99775
Water	0.98 ± 0.02	0.99932

Table 7.6 Results of fitting the ^{1}H MAS spin-locked delay experimental data for octosilicate (sample occ) to a mono-exponential equation using non-linear regression. The quoted errors are 95 % confidence limits and r^2 is a correlation coefficient.

Both experiments provided useful results. The ^{1}H MAS data fitted well to a mono-exponential equation, giving significantly different relaxation times. The correlation coefficients are close to unity and the simulated curves and experimental data are coincident. Therefore, these are fairly precise values. Though there are some deviations from the fitted lines in figure 7.16, these appear to be random and the $T_{1\rho}$-values obtained from ^{29}Si CP can be used with some confidence. Variable spin-locked delay experiments are more useful than variable contact time experiments for

determining proton rotating frame spin-lattice relaxation times for two reasons. Firstly, the behaviour of signal intensity with time is simpler and can be fitted to an equation with just two unknowns, M_0 and $T_{1\rho}$. Variable contact time data are fitted to an equation with three unknowns, M_0, T_{IS} and $T_{1\rho}$. More samples (*i.e.* spectra) are necessary for the fitting, as there is an extra variable. More transients per spectrum might also be required as the signal intensity tends to zero at short delay times as well as long delay times. Since the experiment takes longer, it is more likely that spectrometer instabilities will distort the results. The second advantage of the variable spin-locked delay experiment is that only the proton species are irradiated during the variable delay, so no dipolar oscillations should be seen.

In summary, precise values of proton rotating frame spin-lattice relaxation times have been obtained for a single octosilicate sample using direct and indirect methods– *via* ^{1}H MAS and ^{29}Si CP, respectively. The values obtained for the Q^3 and Q^4 silicon signals were (2.23 ± 0.25) ms and (2.41 ± 0.33) ms, respectively. These are insignificantly different from the value determined for the H-bonding proton signal, (2.36 ± 0.06) ms and significantly different from the value obtained for the water proton (0.98 ± 0.02) ms. Therefore, it can be concluded that the mechanism for ^{1}H,^{29}Si cross-polarisation for octosilicate is a transfer of magnetisation from the H-bonding protons to both types of silicon sites.

The success of this experiment can be attributed to three characteristics of the proton species in octosilicate; sharp lines in the ^{1}H MAS spectra; a large difference in chemical shift (10 ppm); and incomplete mixing of the water and hydrogen bonding protons, by spin-diffusion or chemical exchange, over the time-scale of the experiment. It is possible that all these points are related. Spin-diffusion will be slow for proton species which have sharp ^{1}H MAS lines with little overlap. An exchange-rate has been determined previously for mixing between water and H-bonding protons in octosilicate (*ca.* 0.2 ms^{-1}, with respect to the H-Bonding protons at a spinning-rate of 16 kHz). Though different conditions were used in these experiments, it is likely that the rate of exchange is slower than the rate of rotating frame spin-lattice

relaxation. Therefore, different $T_{1\rho}$-values were measured and a successful experiment was possible.

7.5.3 A Two-Dimensional Method

The method of Vega[8] and Fyfe *et al.*[9] can be used to obtain 2-dimensional $^{29}Si,^{1}H$ correlation spectra for octosilicate. Vega asserted that a consideration of ^{1}H spin-diffusion or chemical exchange is necessary for a complete understanding of the results of these experiments. Such experiments have been described in section 5.4 of this work.

Two-dimensional $^{29}Si,^{1}H$ correlation spectra for octosilicate (sample oca) were acquired at two contact times, 8 ms and 1 ms, using the VXR300 spectrometer equipped with a Doty MAS probe and 7 mm zirconia rotors. The pulse sequence is that of Fyfe *et al.*[8] (figure 7.5). In each case 64 FID's were accumulated with a recycle time of 0.5 s. For the longer contact time, each FID contained 704 data points of 96 transients, while the spinning rate was 5 kHz and the spectral widths were 8 kHz and 16.7 kHz in the silicon and proton dimensions, respectively. For the shorter contact time, each FID contained 512 data points of 1000 transients, while the spinning rate was 4.46 kHz and the spectral widths were 5.5617 kHz and 16.7 kHz in the silicon and proton dimensions, respectively. The spectra are shown as contour plots and stacked plots in figures 7.18 and 7.19.

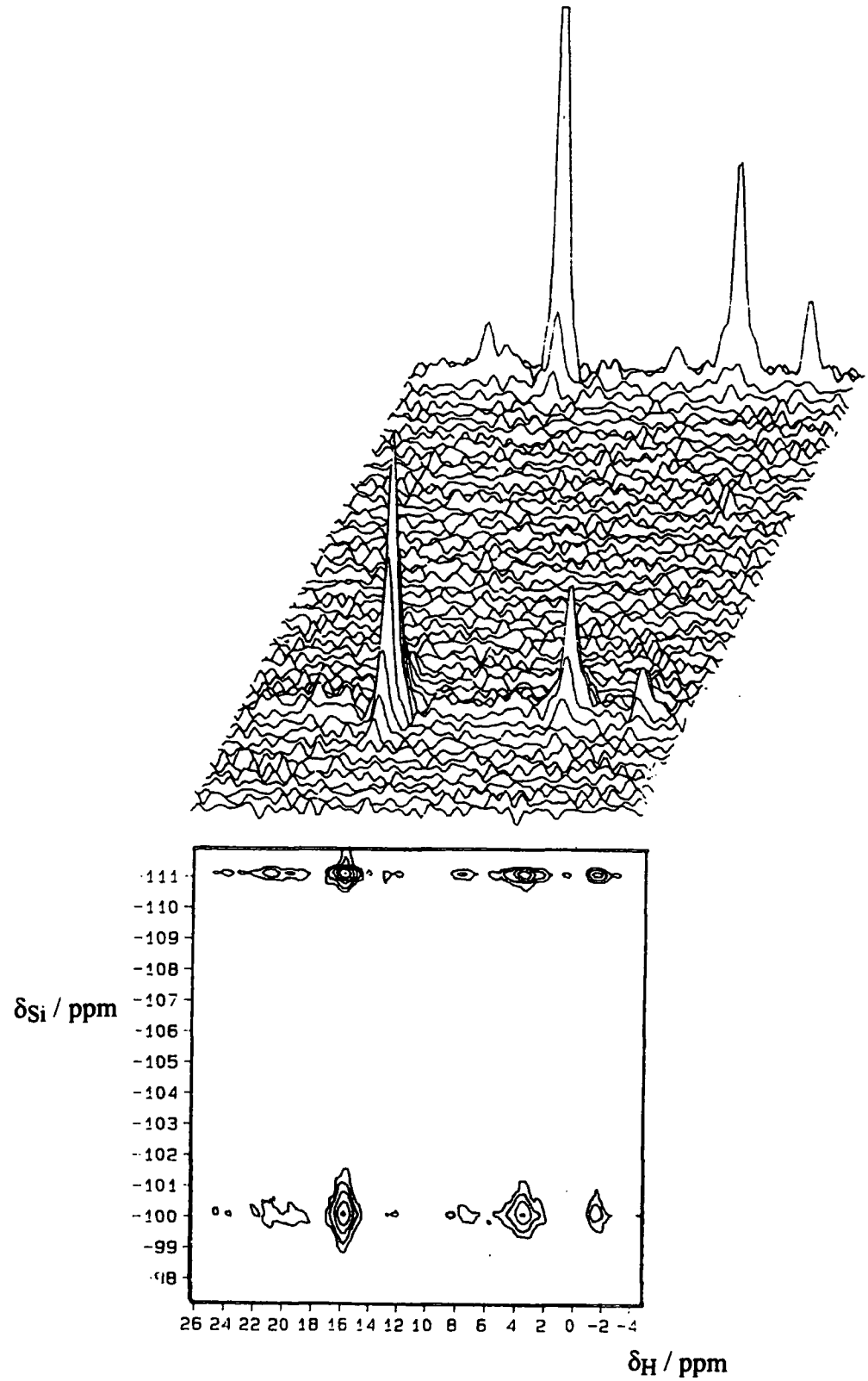

Figure 7.18 The results of a 2-dimensional $^{29}Si,^{1}H$ correlation spectroscopy experiment for octosilicate (sample oca), with a contact time of 8 ms. The results are displayed in stacked-plot and contour-plot mode. Two silicon sites, Q^3 and Q^4, and 2 centre-band proton signals are visible together with some spinning side-bands.

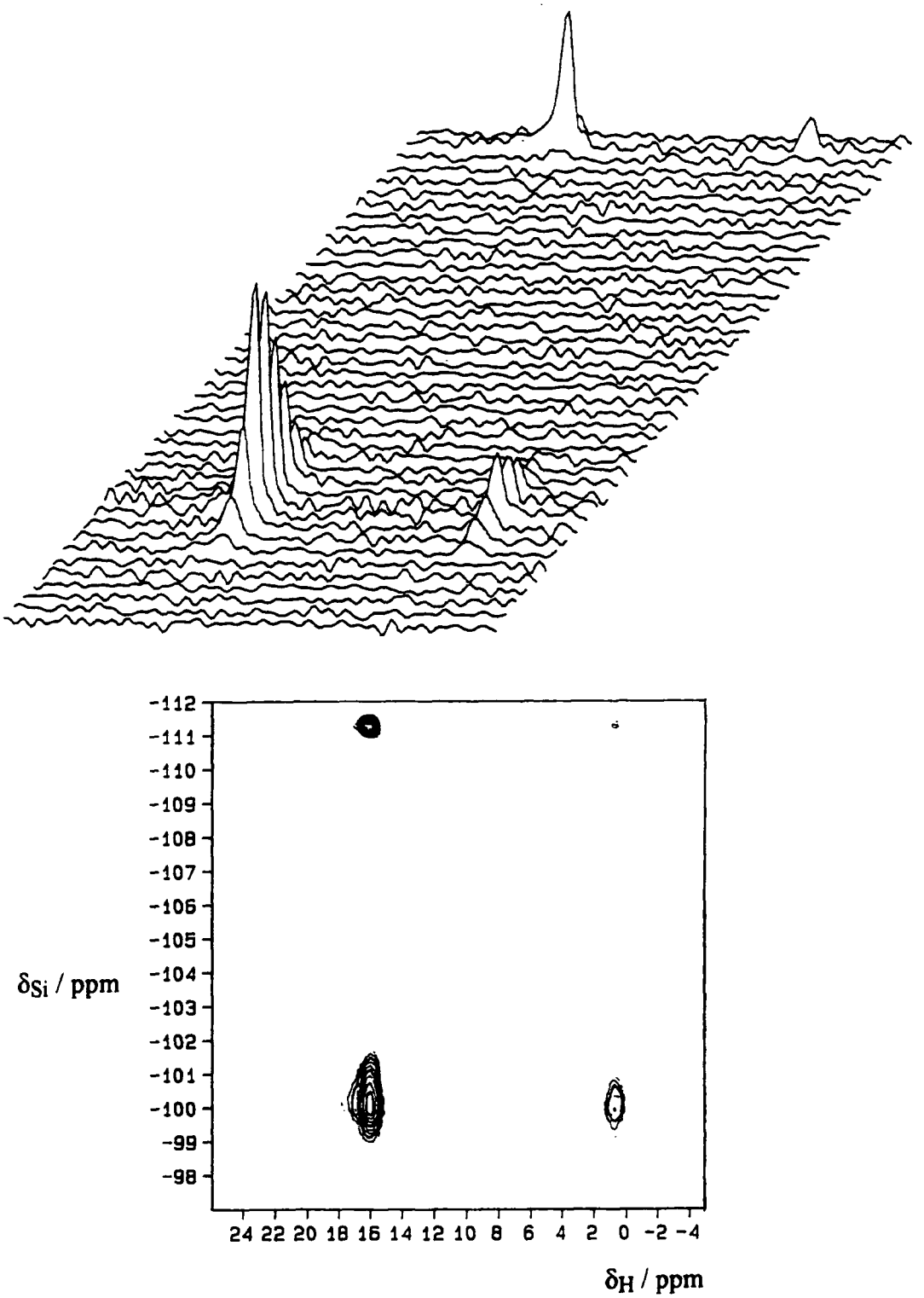

Figure 7.19 The results of a 2-dimensional $^{29}Si,^{1}H$ correlation spectroscopy experiment for octosilicate (sample oca), with a contact time of 1 ms. The results are displayed in stacked-plot and contour-plot mode. Two silicon sites, Q^3 and Q^4, and 1 centre-band proton signal are visible together a spinning side-bands. Further spinning side bands of this proton are observed outside the plot range of this spectrum.

Octosilicate has Q^3 and Q^4 signals in its ^{29}Si CP spectrum and water and H-bonding signals in its ^1H MAS spectrum. The 2-D $^{29}Si,^1H$ spectrum with a contact time of 8 ms contains peaks corresponding to every possible combination of silicon species, protons and proton spinning side-bands. Interestingly, the intensity of the Q^4 peaks is greater than that of the Q^3 lines. This does not necessarily mean that CP to the former is more efficient then to the latter for at least two reasons. Firstly, the volume of the peak rather than the height should be considered and the Q^3 signal is broader in the silicon chemical shift axis direction. Secondly, conclusions regarding CP efficiency should not be drawn from a single contact time experiment. The intensity of the peaks corresponding to H-bonding protons is larger than that corresponding to water protons. Again, predictions about relative cross-polarisation efficiencies are difficult to make with any confidence since the less intense signals are broader in the relevant chemical shift axis direction and the water proton signal intensity is spread over a wider range of spinning side-bands.

The result of the 8 ms $^{29}Si,^1H$ 2-D correlation experiment is inconclusive as there are two possible CP mechanisms which could cause the observed coupling pattern– correlation between both proton types and both silicon sites. Either or both of the proton types could be the source of the cross-polarisation. In the former case, both sites would give signals if chemical exchange or spin-diffusion is significant over the contact time of the experiment. Experiments in section 5.4 have shown that mixing is extensive over a time of 8 ms for octosilicate. Accordingly, any selectivity between the two proton species would be lost. More selective spectra can be obtained if mixing is less extensive. Intuitively, this will be the case with a shorter contact time.

Two contradictory factors affected the choice of the contact time for the repeated $^{29}Si,^1H$ 2-D correlation spectrum. Better signal to noise for the Q^4 peak is obtained with longer contact times, while a shorter value would give less extensive mixing of the proton species. A contact time of 2 ms had been used in a selective $^1H,^{23}Na$ CP correlation experiment for this sample (see section 7.6.2), so an

infinitesimal value was not necessary for selectivity. However, cross-peaks were still evident in a 2-D $^{1}H,^{1}H$ exchange spectrum for this octosilicate sample with a mixing time of only 1 ms. Eventually, the chosen strategy used a contact time of 1 ms, while ten times as many transients as before were acquired.

The 1 ms contact time 2-D $^{29}Si,^{1}H$ correlation spectrum of octosilicate (figure 7.19) consists of only four peaks. These correspond to correlation between the Q^3 and Q^4 silicon sites and the H-bonding proton and a spinning side-band. The peaks for the Q^3 silicon sites are taller and broader than those for the Q^4 sites, probably indicating more efficient cross-polarisation. The important result is that no signals are observed around δ_H 4 in the proton dimension due to correlation with water protons.

The 1 ms $^{29}Si,^{1}H$ correlation spectrum shows that the most efficient ^{29}Si CP mechanism in octosilicate is a transfer of magnetisation from H-bonding protons only to both silicon sites. Coupling between water protons and silicon sites is visible in the 8 ms spectrum. This could be due to direct correlation, $^{1}H_{(Water)} \rightarrow {}^{29}Si$ CP, at a lower efficiency than the main mechanism, or indirect correlation, $^{1}H_{Water} \leftrightarrow {}^{1}H_{H\ bonding} \rightarrow {}^{29}Si$ CP, with chemical exchange or spin-diffusion between the proton species. Further speculation about the true cause of such cross-peaks is unnecessary as the main result of this work is clear: the most efficient mechanism for cross-polarisation in this sample of octosilicate is a transfer of magnetisation from the H-bonding protons to both silicon sites.

7.5.4 Conclusion

Two different strategies have been used for two different samples to show that the ^{29}Si cross-polarisation mechanism for octosilicate is a transfer of magnetisation to both types of silicon site from H-bonding protons only.

7.6 The Mechanism of $^{1}H,^{23}Na$ Cross-Polarisation for Octosilicate

7.6.1 Introduction

The ^{23}Na CP mechanism can be determined using the same methods that were used for the ^{29}Si CP mechanism. Since the potential proton sources for the cross-polarisation are the same as with ^{29}Si CP, selective results should be obtained by using the strategies that have been previously successful. One-dimensional methods can be used which rely on $T_{1\rho}$ rather than T_1, and its indirect measurement will be more likely if variable spin-locked delay ^{23}Na CP experiments are used rather than variable contact times. The 2-dimensional methods are more likely to be selective with short contact times.

7.6.2 A One-Dimensional Method

The experiments were carried out with two octosilicate samples which differed in the number of signals in ^{23}Na SP spectra. Sample occ had two signals, while sample oca had one (figures 5.40a and 5.39a, respectively). Since the difference in the spectra can be attributed to the presence of sodium chloride contamination, and the ^{23}Na CP spectra are practically the same, the two samples should give the same result.

Variable spin-locked delay ^{23}Na CP and ^{1}H MAS experiments for two octosilicate samples were carried out using the CMX200 spectrometer, equipped with a Chemagnetics HX probe and 7.5 mm zirconia Pencil rotors. In each case, spectra were attained at several delay times, τ, while all other parameters were kept constant. Existing pulse sequences were used, t1rhoh for ^{23}Na CP and t1rho for ^{1}H MAS, while a macro was used for automation. Further experimental details are listed in table 7.7.

Sample	Method	Number of Experiments	Number of Transients	Recycle Time / s	Spinning Rate / kHz	Contact Time / ms
occ	^{23}Na CP	16	512	1.5	2.14	2
	^{1}H MAS	32	16	2	4	n/a
oca	^{23}Na CP	24	256	2	2.03	1
	^{1}H MAS	32	32	3	4.02	n/a

Table 7.7 Experimental details for measurements of proton $T_{1\rho}$-values for two octosilicate samples.

For each experiment, all the FID's were given the same baseline-correction, zero-filling, line-broadening, phasing and fourier-transformation routine. The peak intensities of the resultant spectra were fitted to equation 2.13, using non-linear regression. Figures 7.20 to 7.23 are plots of the experimental data together with curves simulated from the fitted values. The results of the statistical analysis are shown in tables 7.8 to 7.11.

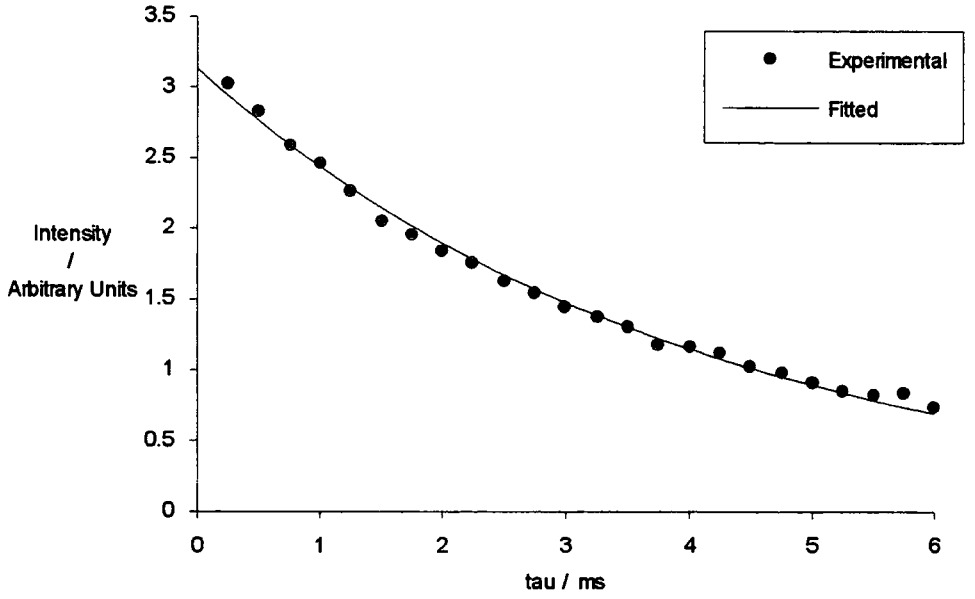

Figure 7.20 The results of a spin-locked delay ^{23}Na CP experiment for octosilicate (sample oca). Filled circles represent the experimental data while the line is the result of a simulation, using values obtained by the fitting routine.

Signal	$T_{1\rho}$ / ms	r^2
Sodium	3.98 ± 0.13	0.99517

Table 7.8 Results of fitting the ^{23}Na CP spin-locked delay experimental data for octosilicate (sample oca) to equation 2.13 using non-linear regression. The quoted errors are 95 % confidence limits and r^2 is a correlation coefficient.

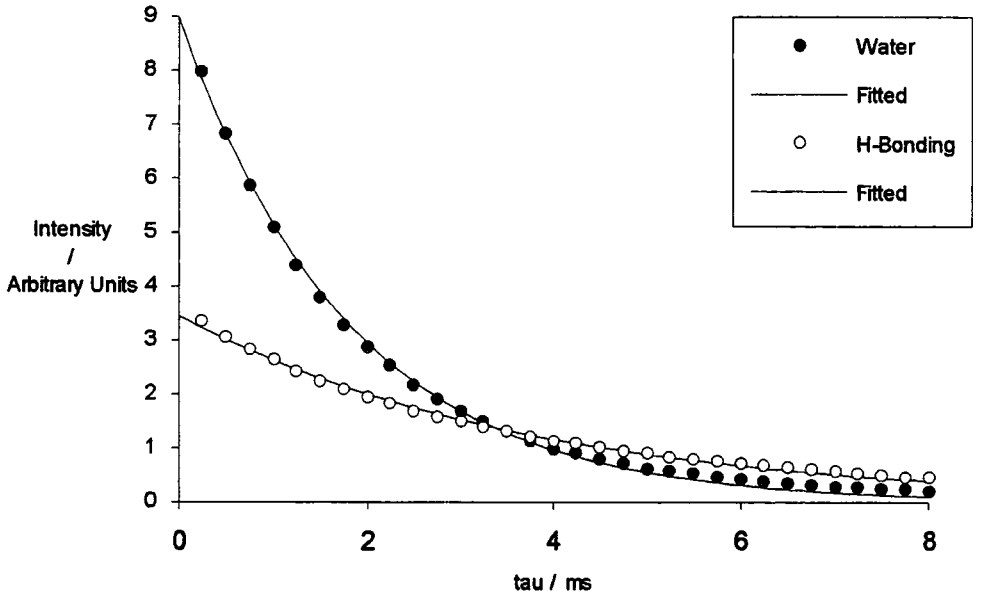

Figure 7.21 The results of a spin-locked delay ^1H MAS experiment for octosilicate (sample oca). Filled and unfilled circles represent the experimental data while the lines are the results of a simulation, using values obtained by the fitting routine.

Signal	$T_{1\rho}$ / ms	r^2
H-Bonding	3.69 ± 0.09	0.99696
Water	1.80 ± 0.04	0.99831

Table 7.9 Results of fitting the ^1H MAS spin-locked delay experimental data for octosilicate (sample oca) to a equation 2.13 using non-linear regression. The quoted errors are 95 % confidence limits and r^2 is a correlation coefficient.

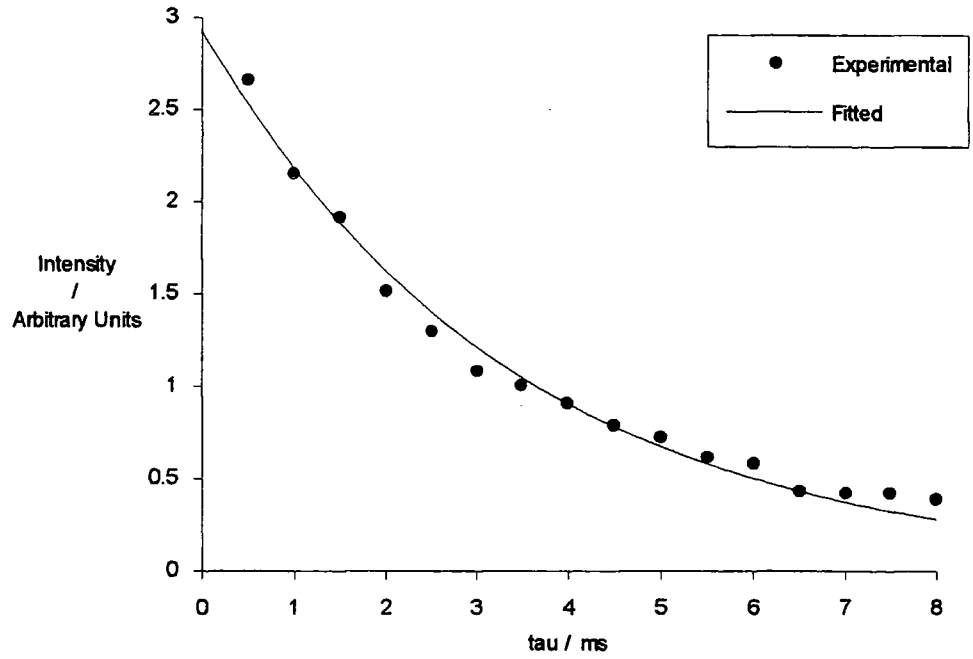

Figure 7.22 The results of a spin-locked delay ^{23}Na CP experiment for octosilicate (sample occ). Filled circles represent the experimental data while the line is the result of a simulation, using values obtained by the fitting routine.

Signal	$T_{1\rho}$ / ms	r^2
Sodium	3.42 ± 0.07	0.98644

Table 7.10 Results of fitting the ^{23}Na CP spin-locked delay experimental data for octosilicate (sample occ) to equation 2.13 using non-linear regression. The quoted errors are 95 % confidence limits and r^2 is a correlation coefficient.

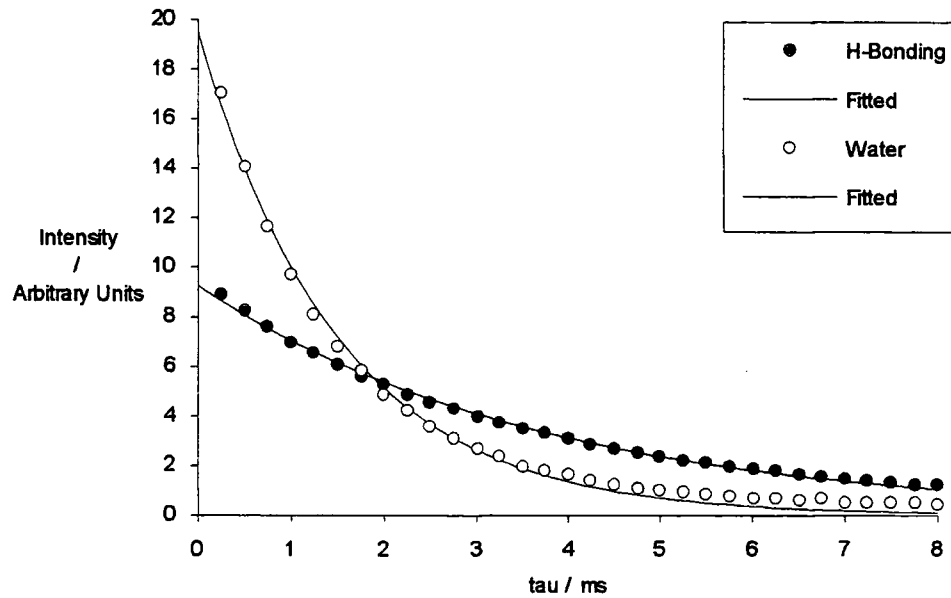

Figure 7.23 The results of a spin-locked delay ^1H MAS experiment for octosilicate (sample occ). Filled and unfilled circles represent the experimental data while the lines are the results of a simulation, using values obtained by the fitting routine.

Signal	$T_{1\rho}$ / ms	r^2
H-Bonding	3.69 ± 0.07	0.99796
Water	1.50 ± 0.06	0.99474

Table 7.11 Results of fitting the ^1H MAS spin-locked delay experimental data for octosilicate (sample occ) to equation 2.13 using non-linear regression. The quoted errors are 95 % confidence limits and r^2 is a correlation coefficient.

With both samples, the rotating frame spin-lattice relaxation time that has been obtained through the cross-polarisation experiments is closer to the value for the H-bonding proton. However, with each sample, there is some significant deviation between the H-bonding and ^{23}Na CP values for $T_{1\rho}$, at 95 % confidence. This is likely to be due to imperfect statistical modelling of the experimental data. If a perfect model was used, only random deviations would be observed and the confidence limits would be a good measure of this deviation and the precision of the fitted value. In this case, there are several possible sources of systematic error, so the confidence limits are a poor measure of precision. Firstly, previous experiments have shown that there is some mixing of the proton species over the time-scale of this experiment. If the mixing is caused by spin-diffusion, the differences in relaxation rate will be averaged over the course of the decay. The averaging will not necessarily be constant, as the rate of spin-diffusion will be affected by the changing spin-temperatures of the two sites, and the decay will not be perfectly exponential– a systematic error. Secondly, sample heating might cause deviations from exponential behaviour. High powers are necessary for spin-locking; because long cross-polarisation contact times (> 30 ms, say) can cause probe damage it is likely that spin-lock times of up to 8 ms can cause some sample heating. Variations in temperature changes will affect the rate of relaxation at each value of the delay, giving systematic errors in the determination of $T_{1\rho}$. Finally, the measured ^{1}H MAS peak intensities are not exact measures of the magnetisation of the aqueous and H-bonded species. Contributions from the probe background and the rotor are included in the peak intensities and these decay at different rates to the octosilicate proton species. Since there are several potential causes of systematic deviations from the model equation, the 95 % confidence limits are not an adequate measure of the precision of the fitted values. The apparently significant deviations in rotating frame spin-lattice relaxation times measured by ^{1}H MAS and ^{23}Na CP are understandable and the result of the experiment is clear. The mechanism for ^{23}Na cross-polarisation is a transfer of magnetisation from the H-bonding protons to the sodium sites in both samples.

7.6.3 A Two-Dimensional Method

The 2-dimensional $^{23}Na,^{1}H$ correlation spectroscopy experiment was carried out for octosilicate (oca) using the CMX200 spectrometer. A pulse sequence was written for the purpose, simply by adding an incremental delay period between the proton 90° pulse and the contact time of a standard CP pulse program. No changes were made to the phasing variations of the original sequence, so hyper-complex data were not collected– 2-dimensional fourier-transformation gave a symmetrised spectrum, that was reflected in the proton transmitter frequency. The 2-dimensional data-set was made up of 128 FID's of 256 points with a dwell-time in t_1 of 30 μs. Each FID consisted of 128 transients with a recycle time of 3 s. The contact time was 2 ms and the spinning rate was kept constant at (4000 ± 10) Hz using the speed controller facility of the spectrometer. One half of the spectrum is shown in figure 7.24.

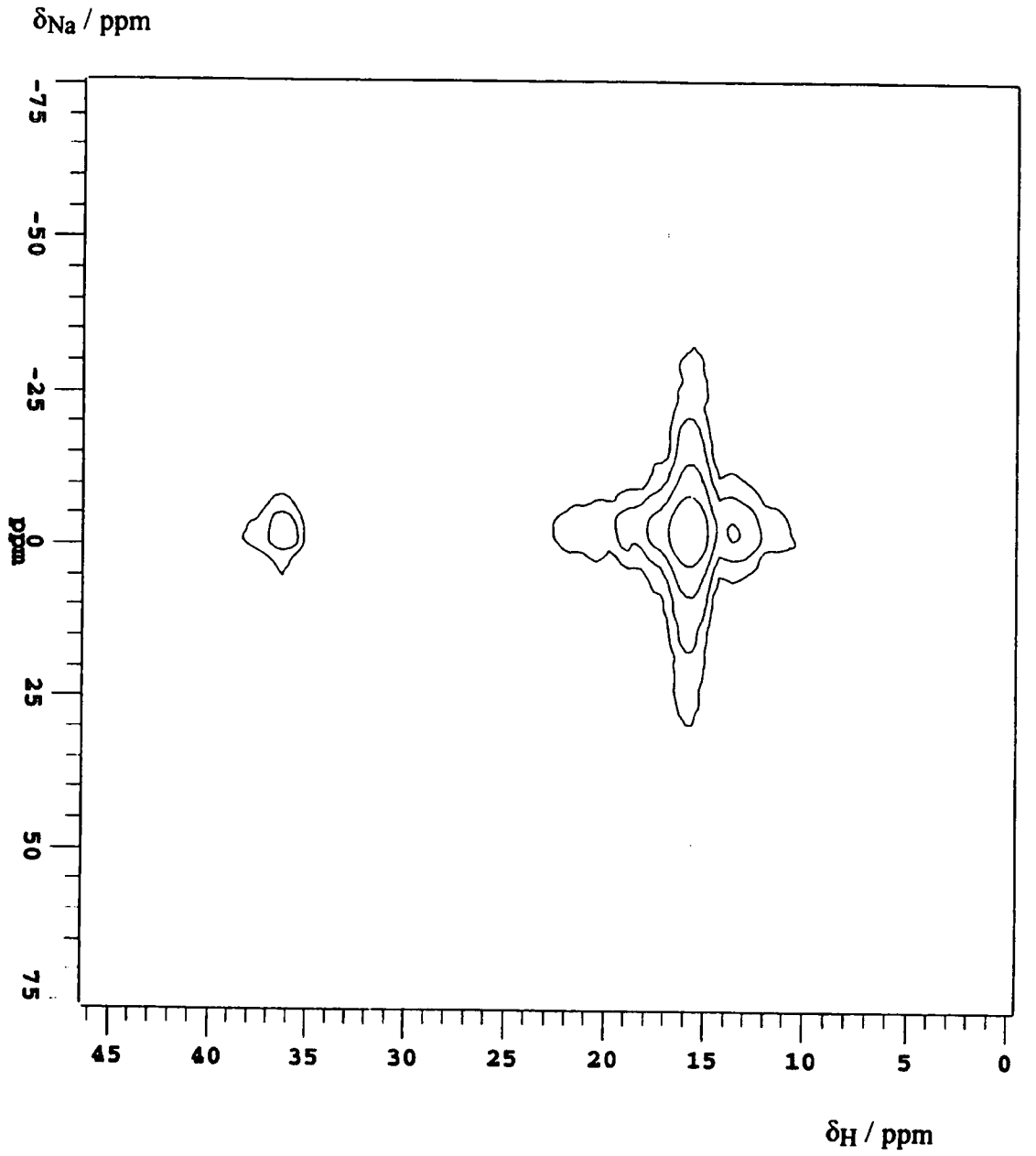

Figure 7.24 The results of a 2-dimensional $^{23}Na,^{1}H$ correlation spectroscopy experiment for octosilicate (sample oca).

The 2-dimensional $^{1}H,^{23}Na$ correlation spectrum for octosilicate consists of a single peak at δ_{Na} for the single observable signal and δ_{H} for the H-Bonding protons, only. Therefore, the mechanism for ^{23}Na CP in this sample of octosilicate is clear. Cross-polarisation occurs *via* a transfer of magnetisation from the hydrogen-bonding protons only to the single sodium site.

7.6.4 Conclusions

Two experiments have been used for two samples to show that ^{23}Na CP occurs *via* a transfer of magnetisation from the hydrogen-bonding protons only to the single observable sodium site in the CP spectrum.

7.7 The Mechanism of ^{29}Si and ^{23}Na Cross-Polarisation in Magadiite

7.7.1 Introduction

Cross-polarisation mechanisms for octosilicate were deduced using 1- and 2-dimensional methods. Similar methods have been considered for magadiite. There are three Q^4 signals and one Q^3 signal in ^{29}Si spectra of magadiite and a single line in ^{23}Na CP spectra, while ^1H spectra have peaks corresponding to strongly hydrogen-bonded and aqueous protons. The work in this section will show which of the proton species is the source of magnetisation for cross-polarisation for each of the silicon and sodium sites.

7.7.2 One-Dimensional Methods

The viability of 1-dimensional methods of determining cross-polarisation mechanisms depends on the determination of distinct relaxation times for the proton species. With octosilicate, the proton species are well-resolved at achievable spinning rates, thus T_1 and $T_{1\rho}$ can be measured precisely. A difference in $T_{1\rho}$ for the two proton species meant that mechanisms for ^{23}Na and ^{29}Si CP could be ascertained. With magadiite, the proton species are poorly resolved and have very similar T_1-values (see sections 5.2.5 and 5.3.2). It is possible that a difference in $T_{1\rho}$-values would allow the determination of mechanisms for ^{29}Si or ^{23}Na cross-polarisation.

A ^1H MAS variable spin-locked delay experiment was carried out for magadiite (sample mga) using the CMX200 spectrometer equipped with a Chemagnetics HX probe. The sample was packed in 7.5 mm Pencil rotors with kel-F end-caps. Under these conditions there is also a considerable background contribution in all spectra; this is displayed in figure 7.25a. Several spectra were acquired with different values for the delay, τ. This was achieved using an existing pulse program, t1rho, and a macro for automation. Eighteen FID's were acquired consisting of 64

transients with a recycle time of 2 s; the spinning rate was 4 kHz. The spectra were subjected to the same zero-filling, baseline correction, apodisation, fourier-transformation and phasing routine. A representative spectrum is shown in figure 7.25b.

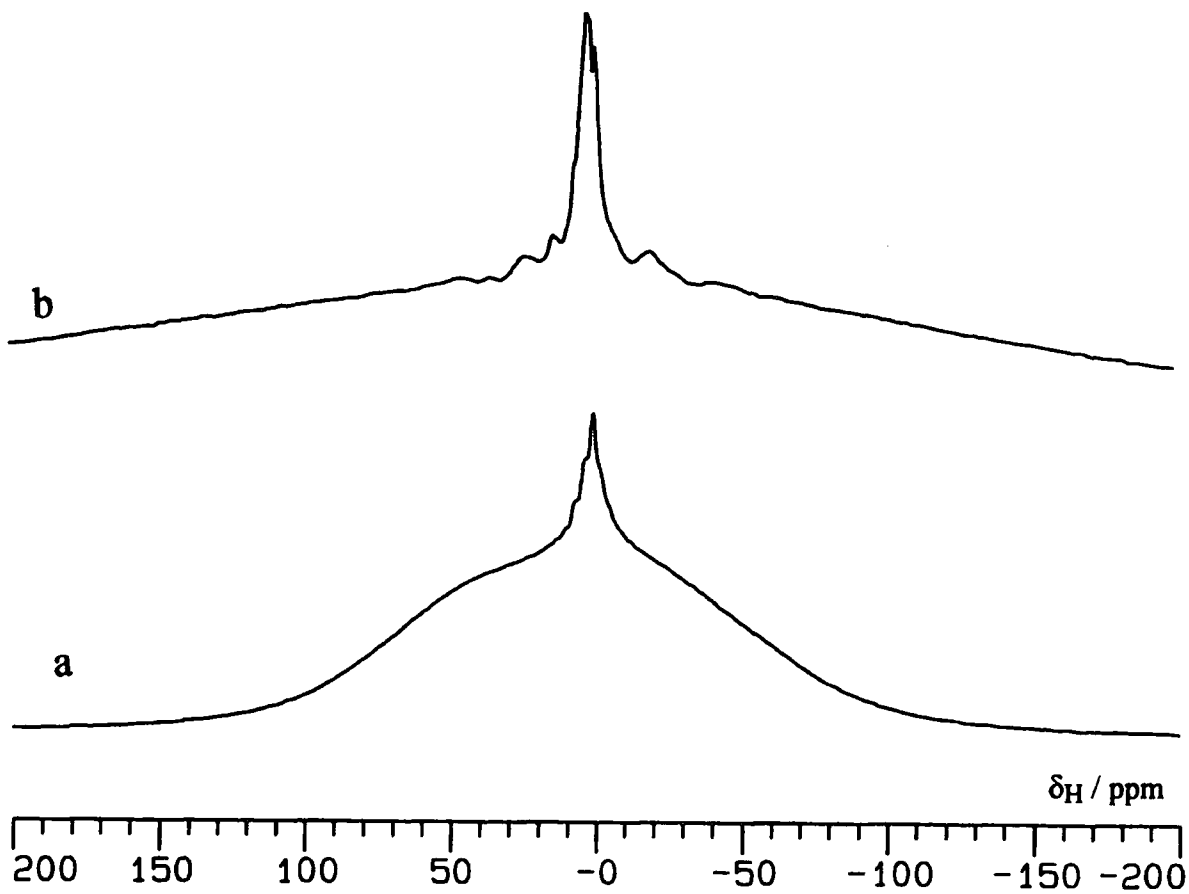

Figure 7.25 a) A typical background ^{1}H MAS spectrum for the Chemagnetics probe and 7.5 mm rotor used in the magadiite (sample mga) variable spin-locked decay experiment. b) A representative spectrum from the magadiite (sample mga) variable spin-locked delay experiment. In this case the delay time was 0.1 ms.

Three lines can be resolved in the magadiite spectrum at δ_H 15, δ_H 5 and δ_H 1. These can be assigned to hydrogen-bonded, water and probe background protons, respectively. Intensities for the two magadiite peaks were fitted to mono- and bi-exponential equations using non-linear regression. Figures 7.26a and 7.26b are plots of the experimental data together with curves simulated from the fitted values. The results of the statistical analysis are shown in tables 7.12 and 7.13.

Signal	$T_{1\rho}$/ ms	r^2
H-Bonding	0.63 ± 0.04	0.99047
Water	0.85 ± 0.05	0.99354

Table 7.12 Non-linear regression results from fitting the magadiite (sample mga) ^{1}H MAS spin-locked delay results to a single exponential (equation 2.11). The quoted errors are 95 % confidence limits and r^2 is a correlation coefficient.

Signal	Faster $T_{1\rho}$ / ms	Slower $T_{1\rho}$ / ms	M_0(Fast) / Arb. Units	r^2
H-Bonding	0.28 ± 0.03	0.98 ± 0.07	0.64 ± 0.06	0.99986
Water	0.35 ± 0.04	1.18 ± 0.06	1.0 ± 0.1	0.99993

Table 7.13 Non-linear regression results from fitting the magadiite (sample mga) ^{1}H MAS variable spin-locked delay to a bi-exponential equation (equation 7.25). The quoted errors are 95 % confidence limits and r^2 is a correlation coefficient. The units of M_0(Fast) are arbitrary but consistent for both signals. The two components were labelled faster and slower on the basis of the rate of relaxation, *after* the fitting procedure.

$$M_t = M_0^{(1)} \exp\left(-t / T_{1\rho}^{(1)}\right) + M_0^{(2)} \exp\left(-t / T_{1\rho}^{(2)}\right) \qquad \text{Eq. 7.25}$$

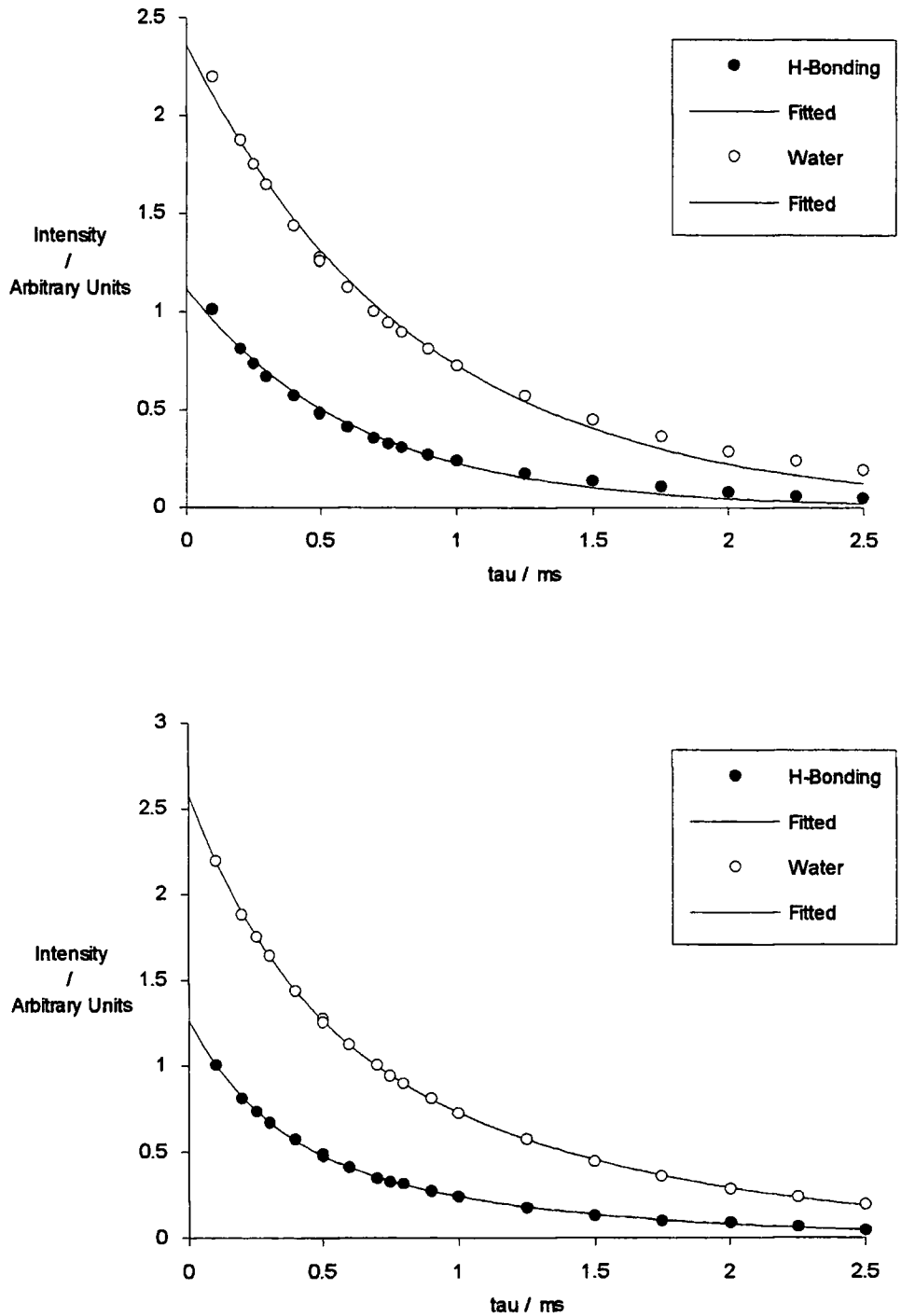

Figure 7.26 The results of a ^{1}H MAS variable spin-locked decay experiment for magadiite (sample mga). Filled and unfilled and circles represent the experimental data; this is the same in both plots. Curves are simulations from value obtained by linear regression to: a) a mono-exponential equation; and b) a bi-exponential equation.

A major problem in this experiment is the significant contribution of background signals in ^1H MAS spectra of magadiite. Octosilicate has sharp intense peaks, so the background had little effect on the viability of relaxation time measurement. The ^1H MAS signals in magadiite are broader and less intense, so the contribution of the background is more significant. Figure 7.25a shows that the background spectrum consists of a broad signal and a sharper more intense one. The spectra of magadiite can therefore be deconvoluted into four overlapping signals: water, H-bonded protons and the two background signals. Though, the intensities of the H-bonding and water protons can be measured, it must be remembered that the intensity will contain a contribution from overlapping species, particularly the broad background absorption.

The variable spin-locked delay experimental data were fitted to exponential equations with one or two components (equations 2.13 and 7.25, respectively). The bi-exponential fitting proved to be a better model for the data: this can be seen by inspection of the plots (figures 7.26a & b) or by comparison of the correlation coefficients. The bi-exponential fitting resolves the relaxation curves into rapidly and slowly decaying components. The rapidly decaying component can be assigned to the broad background absorption. The M_0(Fast) values show that the background makes a larger contribution to the measured water proton intensity– this is consistent with it being centred at around 5 ppm. It has a rotating frame spin-lattice relaxation time of about 300 μs, while the water and H-bonding protons have values of 1.2 ms and 1.0 ms, respectively. These results show that there is a small difference between the $T_{1\rho}$ values of the magadiite water and H-bonding protons. However, to compare these values with any obtained *via* CP would require more faith in these fitting procedures than is really valid.

In summary, one-dimensional determination of the mechanism for CP is not possible for magadiite. The ^1H MAS signals are broad and weak compared to background signals with which there is considerable overlap. This makes the determination of accurate relaxation times very difficult.

7.7.3 A Two-Dimensional Method for Determining the Mechanism of ^{29}Si CP

Two-dimensional $^{29}Si,^{1}H$ correlation spectroscopy can be used to determine the CP mechanism for magadiite. As, with octosilicate, a consideration of proton mixing, chemical exchange or spin-diffusion, is necessary for a full understanding of the results. Drying of the magadiite sample was necessary to provide a full mechanism for ^{29}Si CP.

Two-dimensional $^{29}Si,^{1}H$ correlation spectra for magadiite (sample mga) were acquired using the VXR300 spectrometer, equipped with a Doty MAS probe and 7 mm zirconia rotors. The pulse-sequence was based on that of Fyfe *et al.*[9] Contact times of 8 ms and 0.5 ms were used for an undried sample of magadiite, while the same sample was analysed with a contact time of 8 ms after extensive drying. The experimental details are listed in table 7.14, while the spectra are displayed in figures 7.28, 7.29, and 7.30. One-dimensional spectra of the undried sample are shown in figure 7.27; these were obtained with similar conditions to the 2-D experiment. Spectra for the dried material are fairly similar.[15]

Sample	Undried	Undried	Dried
Contact Time / ms	8	1	8
No. of FID's	64	64	128
No. of Data Points	256	256	512
No. of Transients	800	1400	432
Recycle Time / s	0.5	0.5	0.5
Spinning Rate / kHz	4.96	4.46	4.87
Spectral Width (Si) / kHz	5.87	5.56	5.97
Spectral Width (H) / kHz	16.7	16.7	25.0

Table 7.14 Experimental details for the 2-dimensional $^{29}Si,^{1}H$ correlation spectroscopy experiments with magadiite (sample mga)

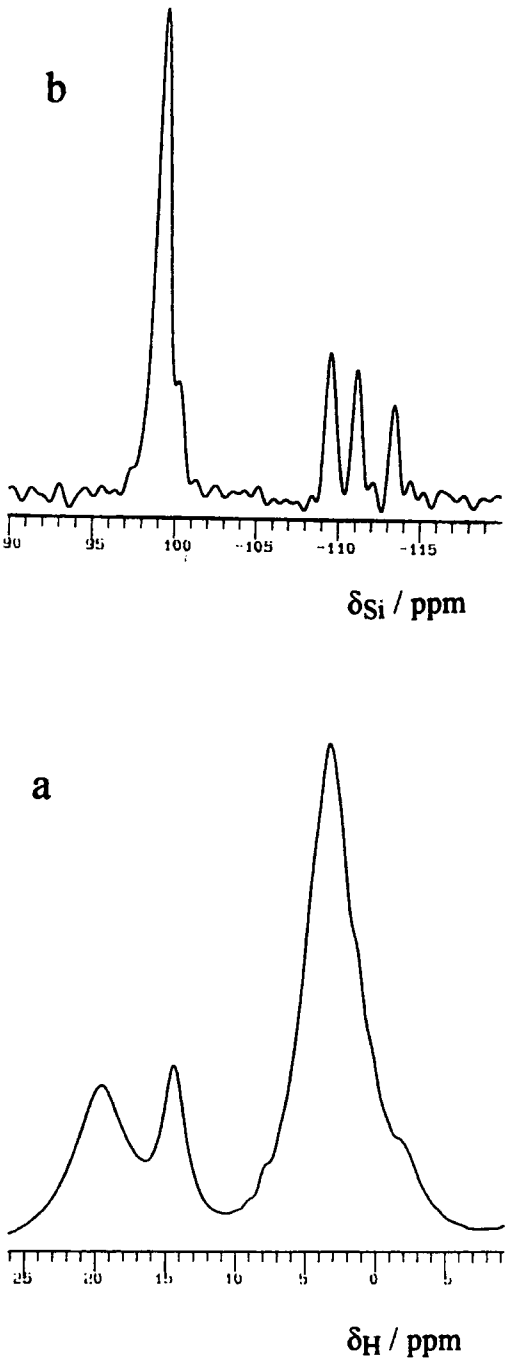

Figure 7.27 One dimensional spectra for magadiite (sample mga): a) ^{1}H MAS; and b) ^{29}Si CP. These were obtained using similar conditions to those for the 2-D spectrum with a contact time of 8 ms for the ^{29}Si spectrum.

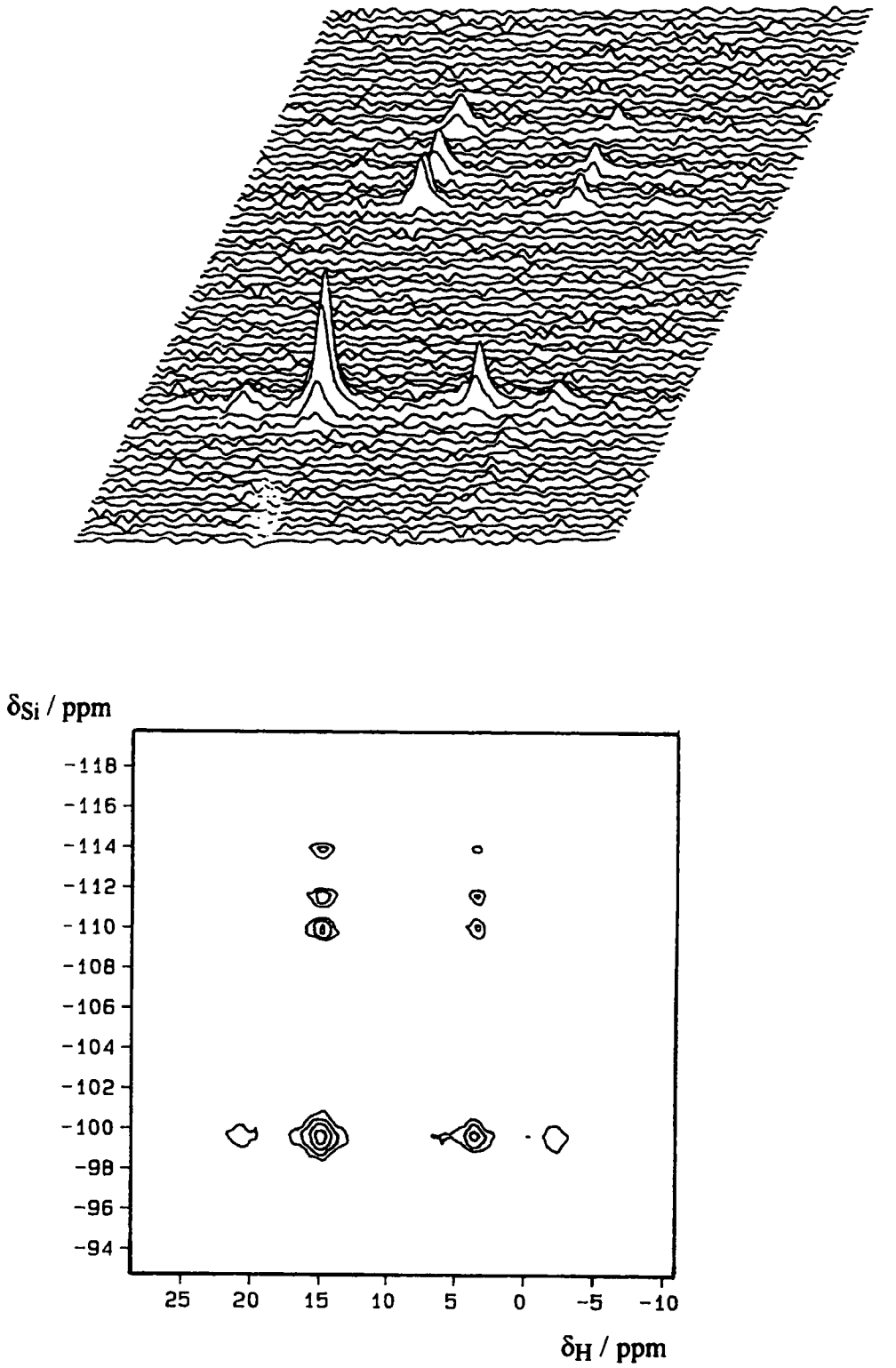

Figure 7.28 A $^{29}Si,^{1}H$ correlation spectrum for undried magadiite (sample mga) with a contact time of 8 ms: a) stacked plot; and b) contour mode.

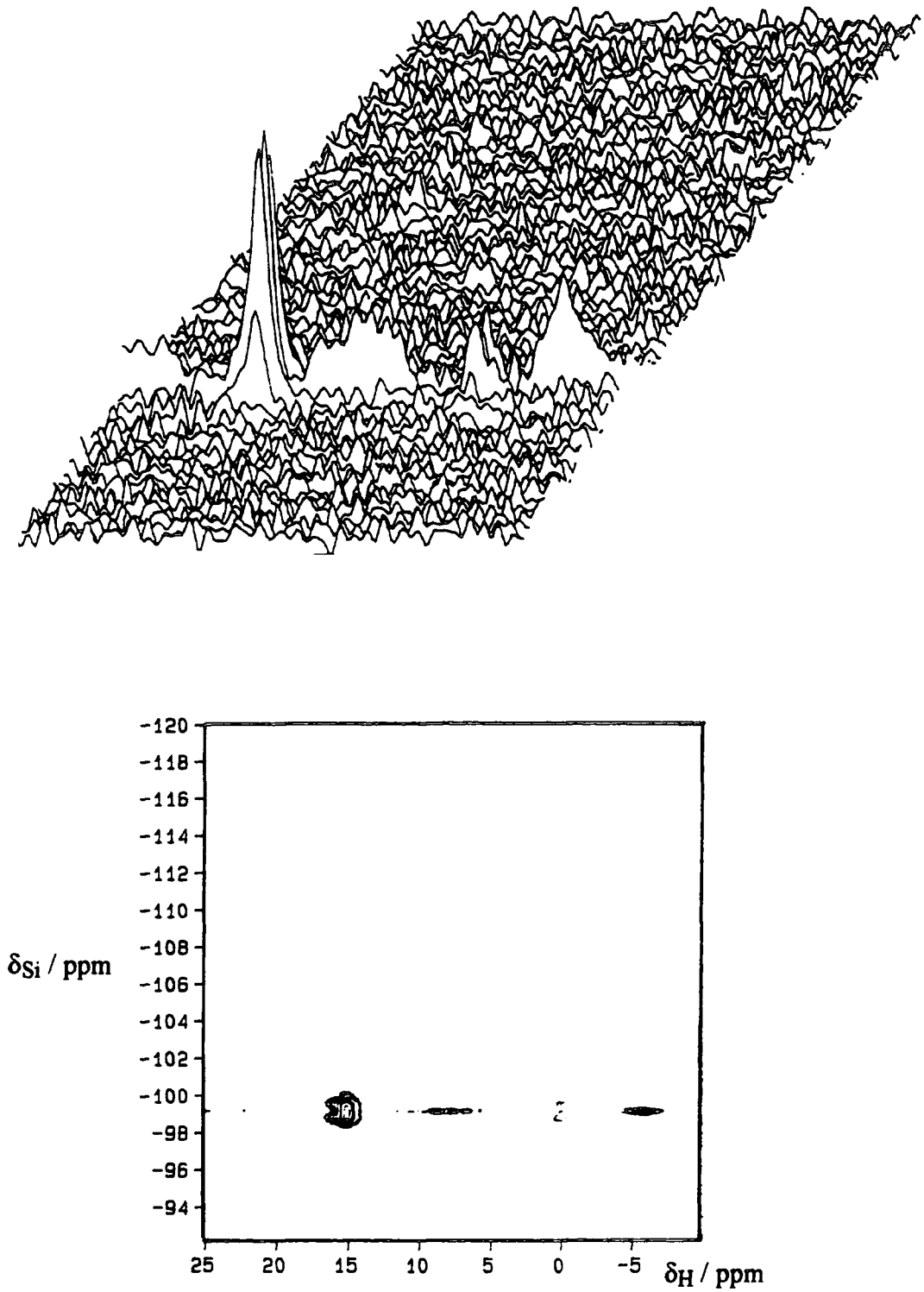

Figure 7.29 A $^{29}Si,^{1}H$ correlation spectrum for undried magadiite (sample mga) with a contact time of 1 ms: a) stacked plot; and b) contour mode. The appearance of the spectrum is spoilt by the presence of artefacts through δ_{Si} -99. However, clear conclusions may still be drawn.

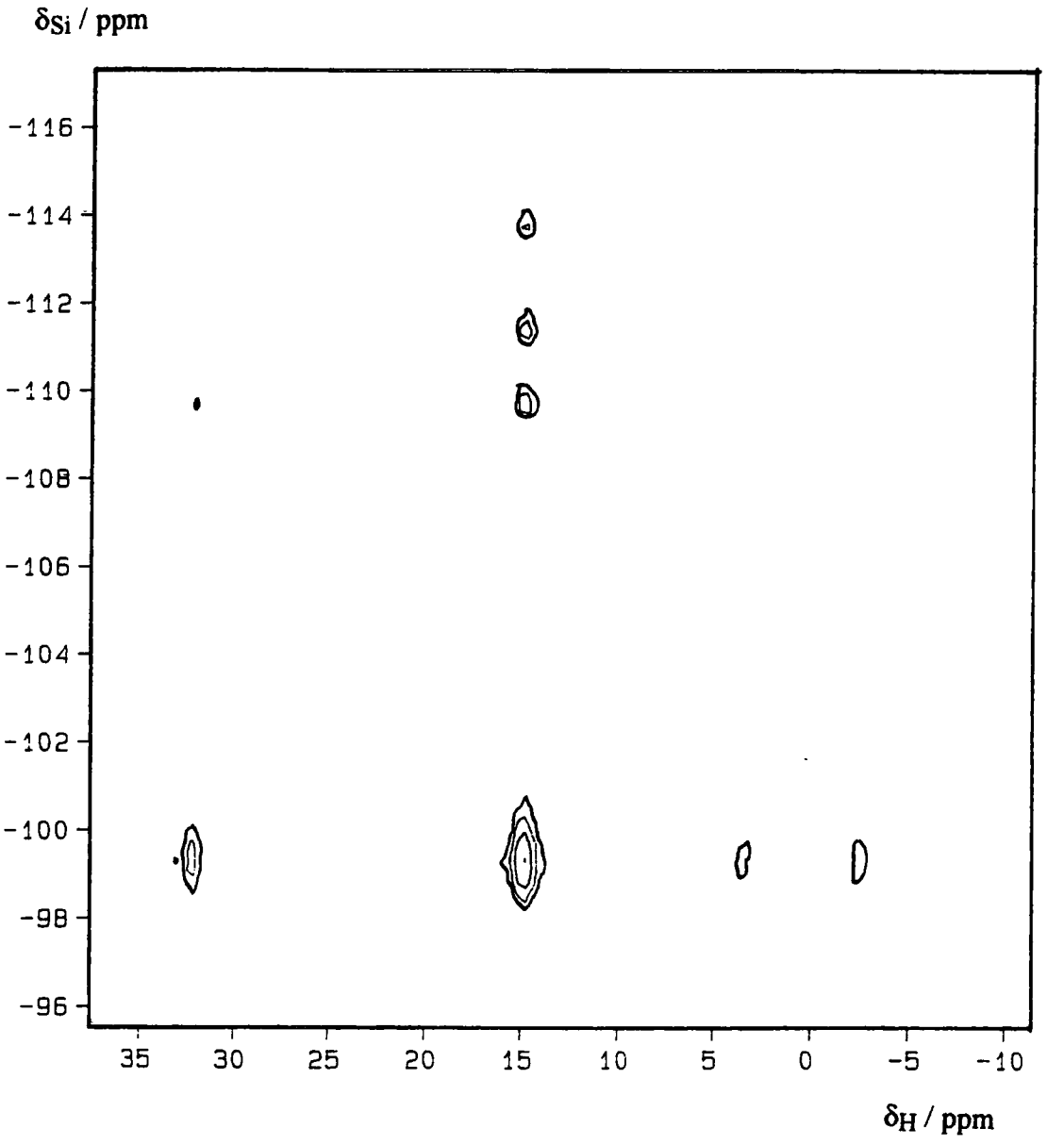

Figure 7.30 A $^{29}Si,^{1}H$ correlation spectrum (contour mode) for magadiite (sample mga) after extensive drying with a contact time of 8 ms.

No selectivity is observed in the 8 ms contact time 2-dimensional $^{29}Si,^{1}H$ correlation spectrum for the undried sample (figure 7.27). Figure 7.26 shows that magadiite spectra contain four silicon signals and two proton signals. Cross-peaks can be seen for all combinations of these; there are also some contributions from correlation between proton spinning side-bands and Q^3 ^{29}Si sites. Previous $^{1}H,^{1}H$ exchange experiments have shown that there is considerable mixing between magadiite protons species over a time of 8 ms (see section 5.4). Therefore, no conclusions can be made concerning the mechanism for ^{29}Si cross-polarisation as this mixing would prevent the observation of selective results.

Two further $^{29}Si,^{1}H$ correlation spectra were obtained at conditions where less mixing would be expected. A 1 ms contact time gives less time for the exchange to occur, but the intensity of Q^4 ^{29}Si signals would be very low. In section 5.4, sample-drying has been shown to reduce the extent of mixing. Thus a contact time of 8 ms might allow a selective result for the Q^4 signals. With less water in the system, the rate of chemical-exchange should be slower by the law of mass-action, while the strength of the homonuclear dipolar interaction (and hence rate of spin-diffusion) would be reduced.

The 1 ms contact time $^{29}Si,^{1}H$ spectrum (figure 7.29) only has signals for the Q^3 silicon sites. No Q^4 signals are seen at this short contact time due to inefficient CP. The cross peaks are only observed at chemical shifts corresponding to the H-bonding proton and a spinning side-band– no coupling is observed between the Q^3 silicon site and the water protons. This spectrum provides half of the mechanism for ^{29}Si CP– cross-polarisation to the Q^3 sites occurs *via* a transfer of magnetisation from the H-bonding protons, only.

Drying the sample provides the complete mechanism. The 2-D $^{29}Si,^{1}H$ correlation spectrum of dried magadiite (figure 7.30) gives a selective result, at a contact time which is large enough for adequate Q^4 signal detection (8 ms). The spectrum contains seven peaks, including five from centre-band proton signals. The intensity of H-bonding signals is much greater than the water proton signals. CP is

therefore more efficient from H-bonding protons. Some mixing would be expected with the dried sample: this probably explains the presence of the small peak in the $^{29}Si,^{1}H$ spectrum corresponding to coupling between the Q^3 silicon atom and the water protons.

7.7.4 A Two-Dimensional Method for Determining the Mechanism of ^{23}Na CP

The mechanism of ^{23}Na cross-polarisation in magadiite can be determined by 2-dimensional $^{23}Na,^{1}H$ correlation spectroscopy. Since the optimum contact time for a magadiite ^{23}Na CP spectrum is *ca.* 2 ms, sample drying should not be necessary for selective $^{1}H,^{23}Na$ correlation results.

The 2-dimensional $^{23}Na,^{1}H$ correlation spectroscopy experiment was carried out for magadiite (sample mga), using the CMX200 spectrometer, equipped with a Chemagnetics HX probe and 7.5 mm zirconia Pencil rotors. The pulse sequence was the same as had been used for similar experiments with octosilicate, so the data were not hyper-complex– 2-dimensional fourier-transformation gives a symmetrised spectrum, that was reflected in the proton transmitter frequency. The 2-dimensional data-set was made up of 95 FID's of 256 points with a dwell-time in t_1 of 20 μs. Each FID consisted of 200 transients with a recycle time of 3 s. The contact time was 2 ms and the spinning rate was 4 kHz. The spectrum is shown in figure 7.31.

The ^{23}Na SP spectrum of sample mga has two lines– one from magadiite and one from NaCl contamination (see figure 5.40b).

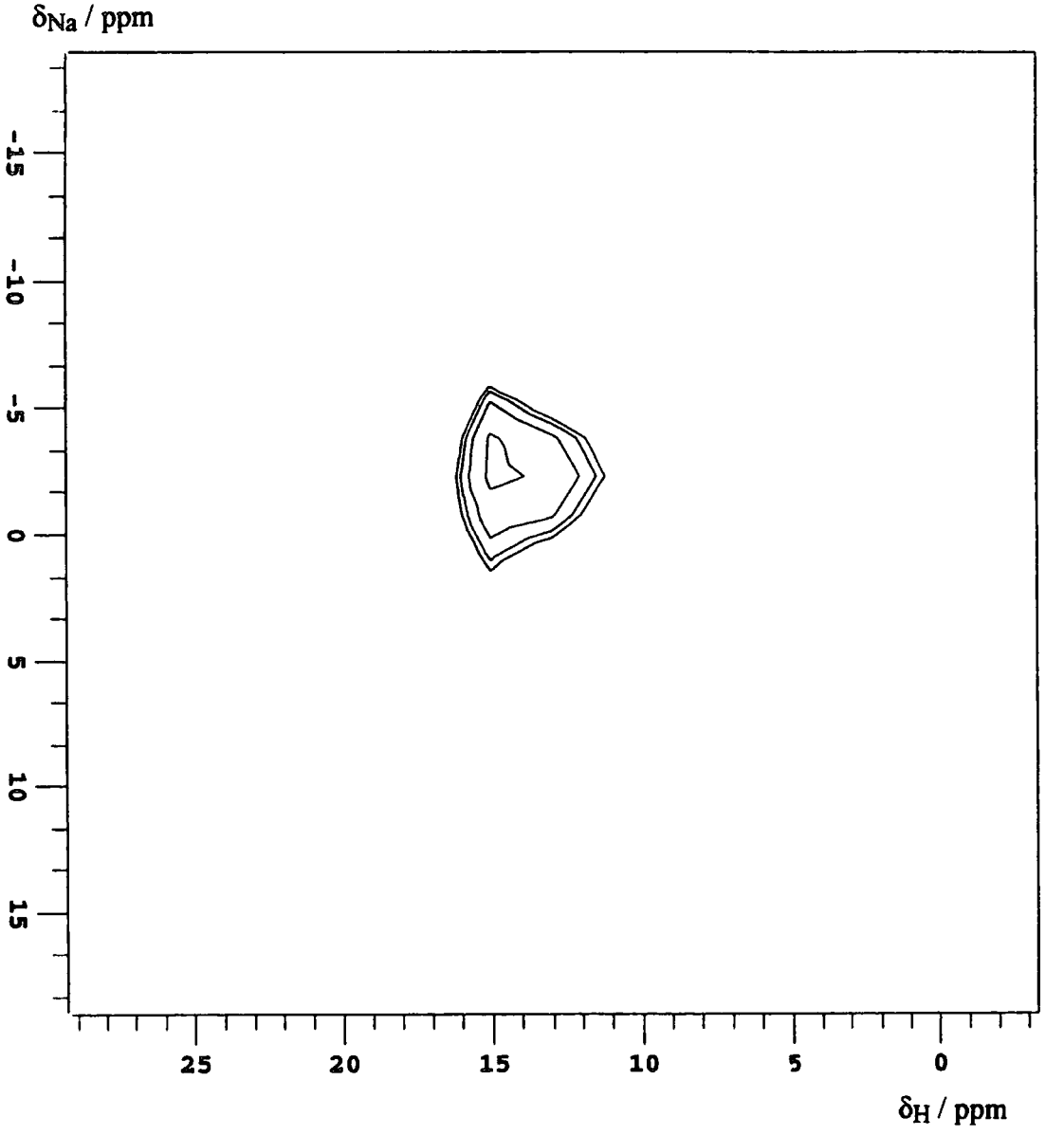

Figure 7.31 The results of a 2-dimensional $^{23}Na,^{1}H$ correlation spectroscopy experiment for Magadiite (sample mga).

The 2-dimensional $^{1}H,^{23}Na$ correlation spectrum contains a single peak at δ_{Na} for the single observable signal and δ_{H} for the H-Bonding protons. Therefore, the mechanism for ^{23}Na CP in magadiite is clear. Cross-polarisation occurs *via* a transfer of magnetisation from the hydrogen-bonding protons only to the single sodium site.

7.7.5 Conclusions

The mechanisms for ^{29}Si and ^{23}Na CP have been deduced using 2-dimensional methods, only. The 1-dimensional strategy which was successful with octosilicate was not feasible with magadiite. Broad lines in the ^{1}H MAS spectrum meant that resolving the water and H-bonding signals of magadiite from the background absorptions was difficult. The data from an experiment to determine $T_{1\rho}$ was fitted to two components, to account for the background, but the difference in relaxation times was barely significant. This similarity might indicate that the rate of spin-diffusion or chemical-exchange in magadiite is larger than in octosilicate.

The 2-dimensional methods were successful, at conditions where the extent of spin-diffusion was not significant. Using a short contact time, as with octosilicate, provided the ^{29}Si CP mechanism for the Q^3 peak, while drying the sample showed that the same mechanism was valid for all silicon signals. Cross-polarisation to both ^{29}Si signals occurs through a transfer of magnetisation from the H-bonding protons only. A short contact time was adequate for deducing the ^{23}Na CP mechanism. Cross-polarisation to the lone ^{23}Na CP signal occurs *via* a transfer of magnetisation from the hydrogen-bonding protons only.

References

1 (a) M. Mehring, *High-Resolution NMR in Solids*, Springer-Verlag, Berlin, 1983, 151-153; (b) R. Challoner, Ph.D. Thesis, University of Durham, 1989.

2 R.A. Komorovski in R.A Komorovski (Ed.), *High-Resolution NMR Spectroscopy of Synthetic Polymers in Bulk*, VCH Publishers, Florida, 1986, 42.

3 K.L. Walther, A. Wokaun and A. Baiker, *Molecular Physics*, 1990, **71**, 769-780.

4 A. Pines, M.G. Gibby and J.S. Waugh, *J. Chem. Phys.*, 1973, **59**, 569-590.

5 E.O. Stejskal, J. Schaefer and J.S. Waugh, *J. Magn. Reson.*, 1977, **28**, 105.

6 J. Kümmerlen, L.H. Merwin, A. Sebald and H. Keppler, *J. Phys. Chem.*, 1992, **96**, 6405-6410.

7 L. Müller, A. Kumar, T. Baumann and R.R. Ernst, *Phys. Rev. Lett.*, 1974, **32**, 1402-1406.

8 A.J. Vega, *J. Am. Chem. Soc.*, 1988, **110**, 1049-1054.

9 C.A. Fyfe, Y. Zhang and P. Aroca, *J. Am. Chem. Soc.*, 1992, **114**, 3252-3255.

10 K. Schmidt-Rohr, J. Clauss and H.W. Spiess, *Macromolecules*, 1992, **25**, 3273-3277.

11 J.P. Yesinowski, H. Eckart and G.R. Rossman, *J. Am. Chem. Soc.*, 1988, **110**, 1367-1375.

12 C.A. Fyfe, Y. Feng, H. Gies, H. Grondley and T.T. Kokotailo, *J. Am. Chem. Soc.*, 1990, **112**, 3264-3270.

13 W. Kolodziejski, P.J. Barrie, H. He and J. Klinowski, *J. Chem. Soc., Chem. Commun.*, 1991, 961-962.

14 R.V. Hosur, K.V.R. Chary and M. Ravi Kumar, *Chem. Phys. Lett.*, 1985, **116**, 105.

15 G.G. Almond, R.K. Harris and P. Graham, *J. Chem. Soc., Chem. Commun.*, 1994, 851-852.

Chapter Eight Structural Conclusions, Summary and Future Work

8.1 Structural Conclusions

8.1.1 The Structure of Kanemite

The structure of makatite is known.[1] Nesbitt proposed that the structure of kanemite was similar with the addition of more water molecules in the interlayer space.[2] This proposal was based on the similarity between ^{29}Si NMR spectra of the two silicates– both contained two resolved Q^3 signals in apparently similar intensity ratios. In this work, a makatite ^{29}Si CP spectrum has been acquired with four resolved lines, while most kanemite spectra have a single line.[3,4] Additionally, strongly hydrogen-bonded protons have been detected for kanemite, only. Therefore, it is unlikely that the structure of kanemite is so similar to that of makatite.

Hydrogen-bonded proton signals are observable in the ^1H MAS spectrum of $KHSi_2O_5$, which also has a single ^{29}Si NMR signal, at δ_{Si} -90. The multiplicity of Q^3 signals and the presence of hydrogen-bonded protons are connected. In a system with silanol protons and a counter-ion, such as Na^+ or K^+, there are two types of Q^3 silicon atom: silanol, $(SiO)_3Si\text{-}OH$, and siloxide, $(SiO)_3Si\text{-}O^-$. These are resolvable in the ^{29}Si NMR spectrum of makatite. In a system with hydrogen-bonded protons, a symmetrical -O···H···O- bond means that there is only one type of Q^3 silicon atom (figure 8.1).

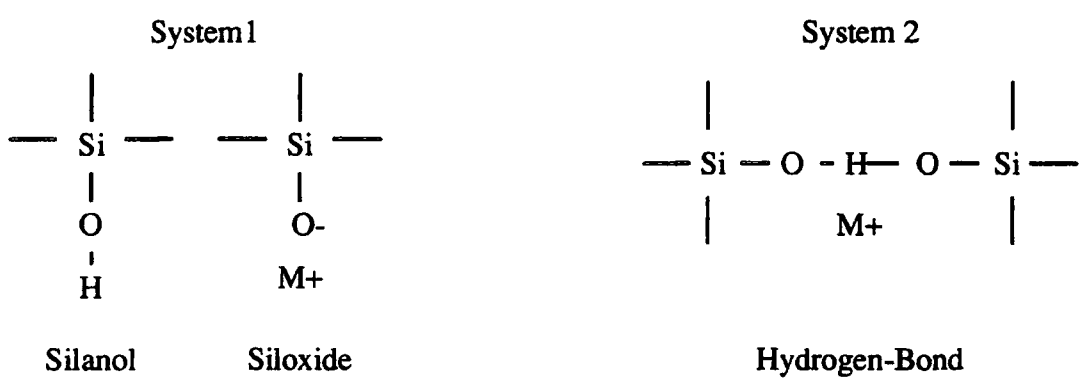

Figure 8.1 In a system with no hydrogen bonds (1), there will be two types of Q^3 silicon atom, whereas a system with a symmetrical H-bond (2) can contain just one type.

In $KHSi_2O_5$, the hydrogen-bonds are situated between single silicate sheets (see figure 3.8).[5] There is no reason to believe that the conformation in kanemite is substantially different. A model structure for kanemite can be formed by replacing the potassium ions in $KHSi_2O_5$ with hydrated sodium ions (figure 8.2). A less puckered silicate layer might be expected for kanemite as there are additional water molecules in the interlayer space. This is also predicted by ^{29}Si NMR data: the chemical shift for $KHSi_2O_5$, -90 ppm, is considerably different to that of kanemite, -97 ppm, and part of the disparity can be explained by changes in bond angles.

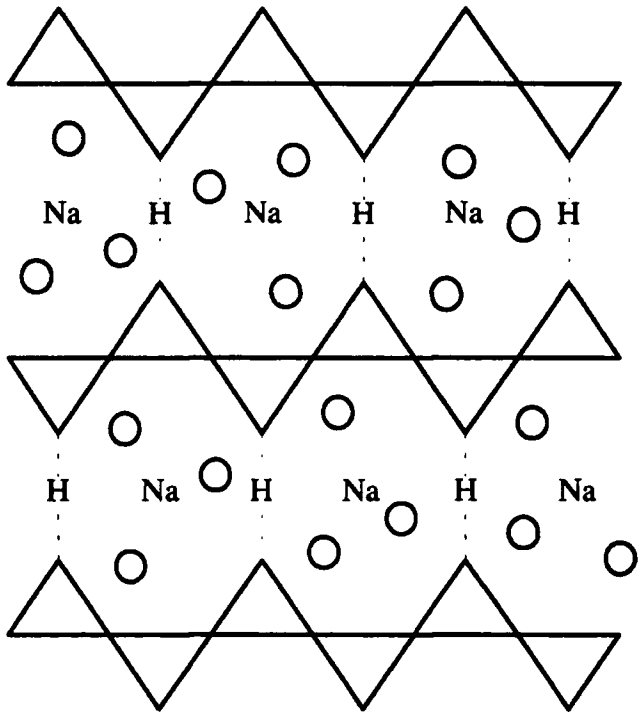

Figure 8.2 A plausible model structure for kanemite: single silicate sheets linked by hydrogen-bonds, and an interlayer space containing hydrated sodium ions. Triangles represent SiO_4 tetrahedra, while water molecules are shown as unfilled circles.

A single kanemite sample (kna) contains extra signals in ^{29}Si CP and ^{1}H MAS spectra. These signals could correspond to stacking faults in the model structure, which would prevent the formation of hydrogen bonds, leaving silanol groups, ≡Si-OH. Such protons would be expected to have signals around δ_H 1, while the chemical shift of the silicon atom would also be different. In the schematic diagram in figure 8.3, the interlayer space consists solely of silanol protons. This is similar to the expected structure of H-kanemite and could arise from partial exchange of sodium for protons. This occurs readily with kanemite and can be achieved by simply washing the sample with water.[6]

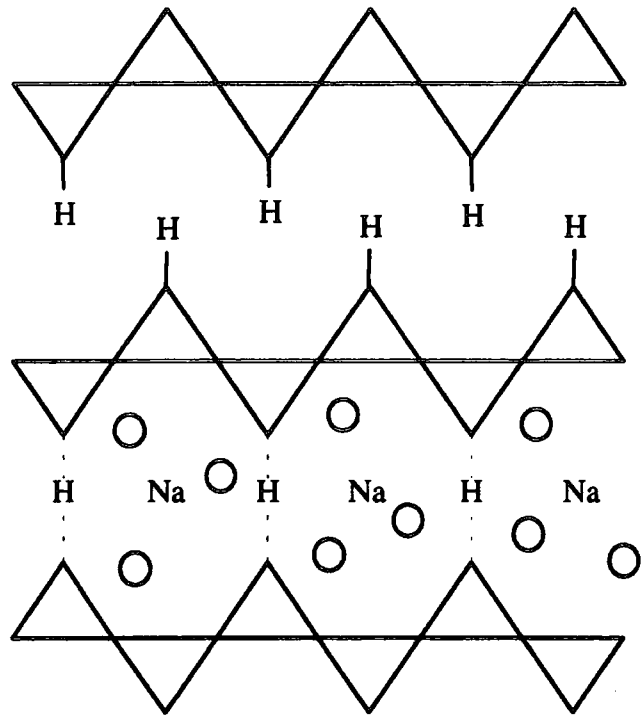

Figure 8.3 A schematic diagram to show how the presence of stacking faults can explain the presence of extra ^{29}Si CP and ^{1}H MAS signals in a single kanemite sample.

8.1.2 The Interlayer Space

Octosilicate, magadiite and kenyaite all contain a single Q^3 ^{29}Si NMR signal and a high-frequency ^1H MAS signal. Therefore, it is possible that the interlayer space for these silicates is similar to that which has been proposed for kanemite. The simplicity of such a model is also suggested by the presence of only one layered sodium polysilicate hydrate signal in ^{23}Na SP spectra. The diagram in figure 8.4 is a plausible model for the interlayer space in kanemite, octosilicate, magadiite and kenyaite. Cross-polarisation correlation experiments indicate that the hydrogen-bonding protons are rigidly-held, while the water molecules are more mobile. The mobility of the water molecules can also be inferred from ^1H MAS spectra, where spinning side-bands are observed. This new model can be compared with that of Rojo *et al.*,[14] which has no H-bonding protons and two types of sodium ion.

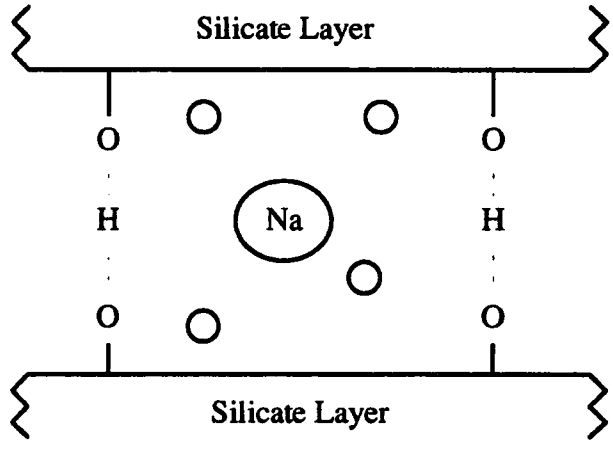

Figure 8.4 A schematic diagram of the interlayer space for kanemite, octosilicate, magadiite and kenyaite. Unfilled circles represent an uncertain number of water molecules.

8.1.3 The Silicate Layer Structure of Octosilicate

Since octosilicate contains silicon atoms of types Q^3 and Q^4 in equal proportions a double-sheet silicate layer is likely. Piperazine silicate (EU19) has such a silicate layer, with a Q^4:Q^3 ratio of 2:1.[7] Figure 8.5 shows that the EU19 structure can be modified to give a Q^4:Q^3 ratio of 1:1, resulting in a simple potential structure for octosilicate.

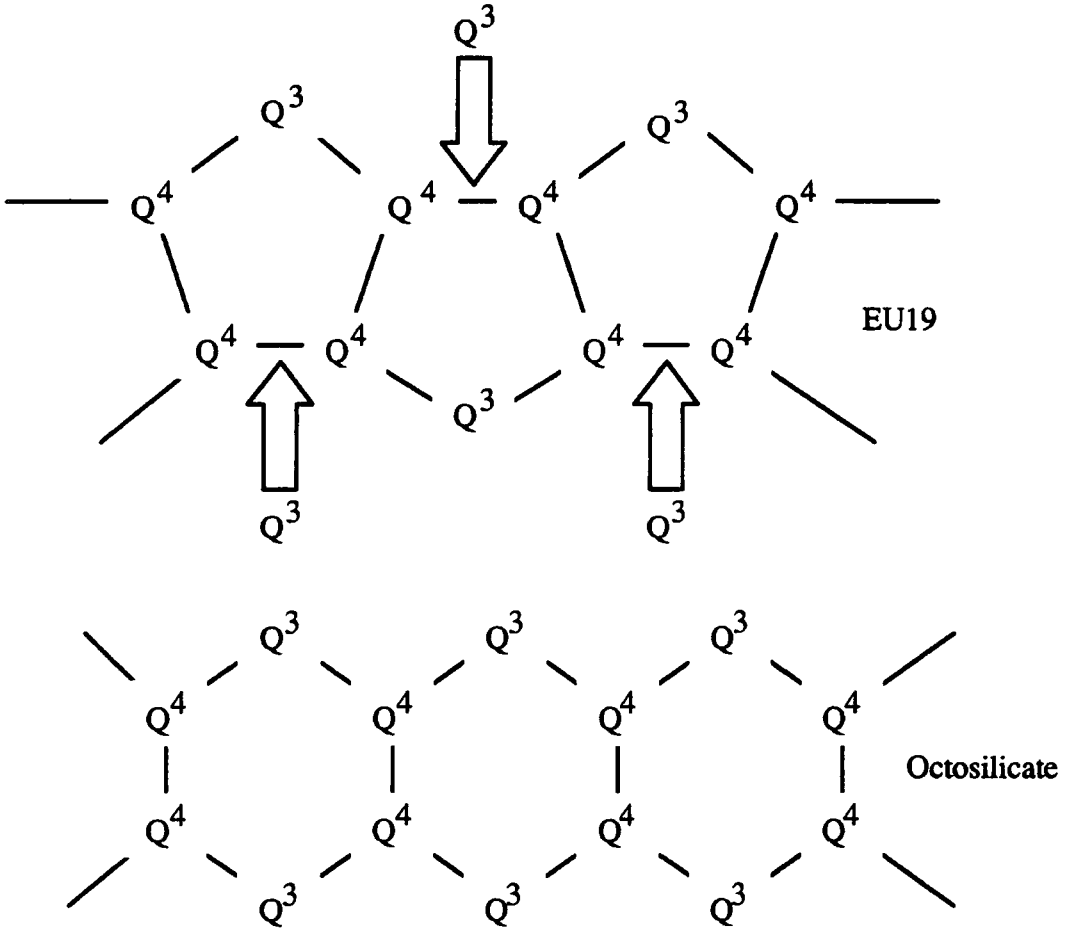

Figure 8.5 By inserting Q^3 silicon atoms into the structure of EU19 (see figure 3.9), a plausible octosilicate structure can be made.

Alternatively, Nesbitt[2] and Schwieger *et al.*[8] have shown that a silicate layer with a Q^3:Q^4 ratio of 1:1 can be made by condensing two makatite sheets. Figure 8.6 compares the two models.

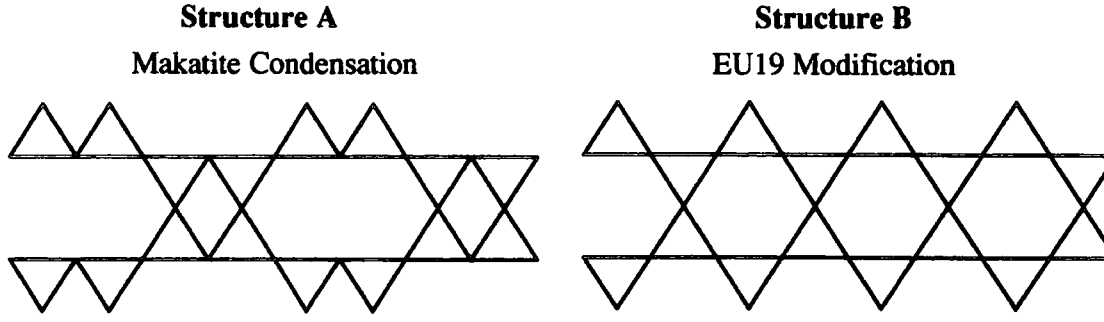

Figure 8.6 Comparison of two hypothetical models for the silicate layer of octosilicate. Triangles represent SiO_4 tetrahedra. Structure A (from figure 3.13) can be built from a repeat unit of eight silicon atoms, whereas structure B can be built up of a four-atom repeat unit.

The ^{29}Si NMR spectrum of octosilicate contains two lines, which are very sharp ($\Delta_{1/2} \approx 20$ Hz). This suggests a very simple silicate layer structure. On this basis, the modified EU19 structure is more likely to be an accurate model for an octosilicate layer than the condensed makatite structure.

8.1.4 Silicate Layers for Magadiite and Kenyaite

Several pieces of information should be remembered when forming hypothetical silicate layers for magadiite and kenyaite. Firstly, powder X-ray diffraction provides a value for the basal spacing: this is equivalent to the combined width of the silicate layer and the interlayer space. Schwieger *et al.* reported values of 15.8 Å and 19.7 Å for the basal spacings in magadiite and kenyaite, respectively.[8] Secondly, Borbély *et al.* reported that the magadiite could be prepared by Soxhlet extraction of octosilicate with water.[11] Therefore, it is likely that the structures are related. Finally, an accurate Q^4:Q^3 ratio of *ca.* 3 has been determined for magadiite,[9] and work in this thesis indicates that the value for kenyaite is *ca.* 5. Scholzen *et al.* noted that these values are related to the structural formulae, particularly the soda:silica ratios.[10] Magadiite and kenyaite contain hydrogen-bonded and water

protons only. The number of moles of sodium ions is equivalent to half the number of moles of Q^3 silicon atoms. Therefore, a Q^4:Q^3 ratio, r, corresponds to a soda:silica ratio, Na_2O:SiO_2, of $[4(r+1)]^{-1}$. Thus, soda:silica ratios can be calculated for magadiite, Na_2O:$16SiO_2$, and kenyaite, Na_2O:$24SiO_2$. There is clearly a disagreement between these ratios and the formulae which are generally quoted for magadiite, Na_2O:$14SiO_2$, and kenyaite, Na_2O:$20SiO_2$. Over-estimation of the sodium-content would be likely in samples which are contaminated with NaCl; perhaps this is responsible for the discrepancy.

Octosilicate is expected to consist of silicate layers with double-sheets. A more condensed layer can be formed by either increasing the number of sheets, or by increasing the proportion of Q^4 silicon atoms in each sheet. Figure 8.7 shows hypothetical silicate layers for magadiite and kenyaite which were made by using both strategies. The double-sheet magadiite model is similar to that of Pinnavaia *et al.*[3]

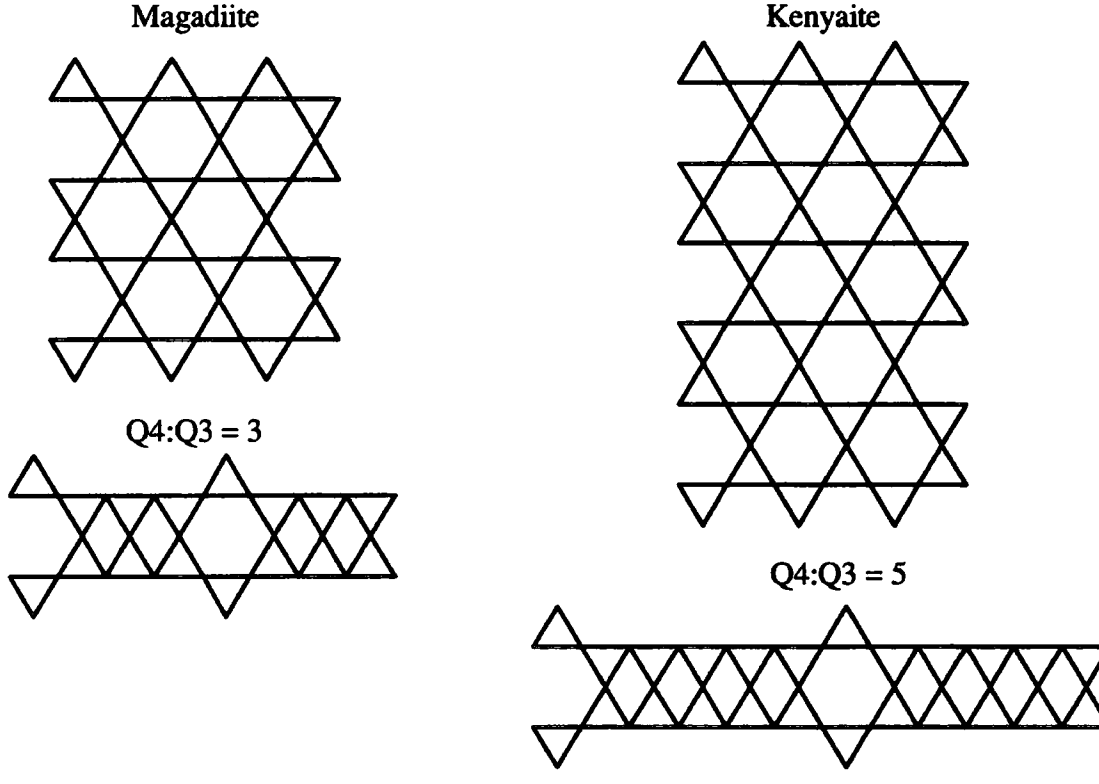

Figure 8.7 Schematic diagrams of hypothetical silicate layer structures for magadiite and kenyaite. Triangles represent SiO_4 tetrahedra.

There are several factors which suggest that the multi-sheet layers are good models for magadiite and kenyaite. Firstly, they explain the increase in basal spacings from octosilicate to magadiite to kenyaite. In this work, ^{1}H MAS and ^{23}Na SP spectra indicate that the three silicates share a common interlayer space: this is also consistent with these models. The regular nature of these structures is similar to that of tridymite, which has ^{29}Si NMR signals at similar chemical shifts to the Q^4 signals in magadiite. Finally, the conversion of octosilicate to magadiite is easy to visualise with these models– two octosilicate layers can condense to form magadiite. However, there is an apparently insoluble problem with the multi-sheet layers of magadiite and kenyaite in that they are much thicker than the observed basal spacings. Deducing exact layer thicknesses is not possible, because different degrees of puckering are feasible. However, a value for the thickness of a single silicate sheet can be calculated from the known crystal structure of makatite. Brandt *et al.* reported that this was *ca.* 5 Å.[12,13] Therefore, the thickness of quadruple-sheet magadiite layers and sextuple-sheet kenyaite layers are expected to be 20 Å and 30 Å, respectively– much larger than the basal spacings. This is a general problem with the hypothetical models of the layered sodium polysilicate hydrates that were proposed by Schwieger *et al.*,[8] Nesbitt,[2] and Brandt *et al.*[12] Their models appeared plausible because they were based on smaller values of the Q^4:Q^3 ratio.

The double-sheet layer models are unlikely to be larger than the basal spacings. They are also simpler, which fits better with the small number of resolved signals in ^{29}Si NMR spectra. However, they do not explain why basal spacings increase in going from octosilicate to magadiite to kenyaite; they have different interlayer spaces; and a facile conversion of octosilicate to magadiite is not easy to visualise– it would involve intralayer condensation.

Overall, none of the models in figure 8.7 is perfect. A combination of the two strategies might provide the most plausible model, *i.e.* a multi-sheet layer containing single sheets with an excess of silicon atoms of type Q^4. The hypothetical structure of Brandt and co-workers for kenyaite (figure 3.16) is a good example.

8.2 Summary

The layered sodium polysilicate hydrates contain four nuclei which are active towards NMR spectroscopy. This work contains example of spectra for three: ^{29}Si, ^{1}H and ^{23}Na. Low nuclear abundance and gyromagnetic ratio made the acquisition of ^{17}O NMR spectra impractical for these samples. Many previous authors have reported ^{29}Si NMR spectra. Nevertheless, new information has been obtained in this work. Makatite contains four crystallographically distinct silicon atoms, and these have probably been detected by ^{29}Si NMR for the first time. Recent authors have confirmed Q^3:Q^4 ratios of 1:1 and 1:3 in octosilicate and magadiite, respectively. These conclusions were formed with the aid of lengthy ^{29}Si inversion-recovery experiments to ensure that quantitative spectra could be acquired. A less rigorous method has been used here to indicate that the Q^3:Q^4 ratio in kenyaite might be 1:5. Proton NMR studies of the layered sodium polysilicate hydrates had previously been restricted to uninformative static and CRAMPS spectra.[2,14] In this work, well-resolved ^{1}H MAS spectra have been recorded. Sharp lines are obtained, particularly for octosilicate and dried samples of kanemite and magadiite. Two types of proton species can be detected in kanemite, octosilicate, magadiite and kenyaite. Aqueous protons, $\underline{H_2}O$, might have been predicted, but strongly hydrogen-bonded protons, -O-$\underline{H}$···O- are an interesting discovery. These are not apparent in makatite or silicic acids. Spin-diffusion or chemical exchange between the two types of protons has been detected in several samples and an approximate rate for this mixing has been determined for octosilicate. The main conclusion from ^{23}Na NMR spectra is in contradiction to a previous finding. Two authors had detected two sodium signals in magadiite or kenyaite and assigned different structural locations for them.[2,14,15] However, one of the peaks has now been shown to come from sodium chloride contamination.

Adequate quantities of kanemite, octosilicate and magadiite were available for the preparation of the corresponding silicic acids. These were analysed by ^{29}Si CP

NMR, thermogravimetric analysis, powder X-ray diffraction and ^{1}H MAS NMR. As had been predicted by Beneke and Lagaly,[16] the H-kanemite sample proved to be a disilicic acid, $H_2Si_2O_5$. The H-octosilicate and H-magadiite samples proved to be more interesting, as in each case two sorts of silicic acid were prepared. Hydrated forms contained molecular water and had larger basal spacings and more negative ^{29}Si chemical shifts than the anhydrous forms.

Interactions between protons in the layered sodium polysilicate hydrates and silicon or sodium nuclei have been investigated with many cross-polarisation experiments. The results for makatite provided further evidence that four crystallographically distinct silicon sites were being detected in ^{29}Si cross-polarisation spectra. Most kanemite samples, octosilicate and magadiite share the same mechanism for ^{29}Si CP: a transfer of magnetisation from H-bonding protons only to all the silicon sites. The H-bonding protons also provide the source for efficient cross-polarisation to the ^{23}Na sites in octosilicate and magadiite. This indicates that these protons are more suitable for CP than water protons on the basis of rigidity, rather than separation. This fits the conclusion from some of the ^{1}H MAS experiments, which indicated that the water molecules are mobile. Determining these mechanisms necessitated a consideration of the extent of mixing between proton species through spin-diffusion or chemical exchange. Generally, selective results were seen where this mixing could be minimised by sample drying or by the use of a short mixing time. The presence of spin-diffusion or chemical exchange meant that the dynamics of cross-polarisation for octosilicate and magadiite were difficult to deduce from variable contact times. As reported by Müller *et al.*[17] and Walther *et al.*,[18] oscillatory curves of signal intensity with time are seen for such systems. Accurate measurement of the rate of ^{29}Si CP was possible for a few silicic acid samples. The value of T_{IS} depends on the distance between the relevant silicon and proton species. Thus, the three Q^4 signals in H-magadiite could be tentatively assigned on this basis. The ^{29}Si CP behaviour of the high-frequency signal for a single kanemite sample with two lines was anomalous– an

irregular variable contact time curve was consistent with a cross-polarisation mechanism involving a transfer of magnetisation from three types of proton.

8.3 Future Work

After three years of research, many more feasible NMR experiments on these samples are still possible. The connectivity of the four resolved ^{29}Si NMR signals in magadiite could be deduced from a $^{29}Si,^{29}Si$ connectivity experiment. Such an experiment would be easier with a sample that is enriched in silicon-29. However, the necessarily small scale of the synthesis and the high cost of the starting material would make experiments at natural-abundance more attractive– these could be possible, with cross-polarisation to reduce recycle times and J-scaling.[19,20]

A deeper study of the ^{23}Na NMR spectroscopy of the layered sodium polysilicate hydrates might be interesting (*e.g.* using DAS or DOR). During this research, such work was side-tracked by the apparently interesting presence of two vastly different signals in the ^{23}Na SP spectra of some octosilicate, magadiite and kenyaite samples.

Thermogravimetric analysis has been successfully used in this work to identify two types of proton species. The results indicate that changes that occur up to *ca.* 300 °C are reversible. Therefore, a variable-temperature NMR study would be possible over a wide temperature range. Such work might be especially interesting for the two types of silicic acid from octosilicate and magadiite. The silicic acids in general are particularly suitable for any further study involving ^{29}Si cross-polarisation since spectral intensities are greater than those of the parent sodium-forms.

Octosilicate spectra contain two sharp ^{29}Si signals and two well-resolved ^{1}H MAS signals with many spinning side-bands. Because the spectra can be obtained quickly, octosilicate is potentially useful as a model sample for use in new exotic experiments or for testing existing ones.

References

1 H. Annehed, L. Fälth and F.J. Lincoln, *Zeitschrift für Kristallographie*, 1982, **159**, 203-210.

2 G.J. Nesbitt, Ph.D. Thesis, University of Durham, 1986.

3 T.J. Pinnavaia, I.D. Johnson and M. Lipsicas, *J. Solid State Chem.*, 1986, **63**, 118-121.

4 T. Yanagisawa, K. Schimizu, K.Kuroda and C. Kato, *Bull. Chem. Soc. Japan*, 1990, **63**, 988-992.

5 M.T. Le Bihan, A. Kalt and R. Wey, *Bull. Soc. Fr. Minéral. Cristallogr.*, 1971, **94**, 15.

6 K. Beneke and G. Lagaly, *Am. Mineral.*, 1977, **62**, 763-771.

7 S.J. Andrews, M.Z. Papiz, R. McMeeking, A.J. Blake, K.R. Franklin, B.M. Lowe, J.R. Helliwell and M.M. Harding, *Acta. Cryst.*, 1988, **B44**, 73-77.

8 W. Schwieger, D. Heidemann and K.-H. Bergk, *Rev. Chim. Minérale*, 1985, **22**, 639-650.

9 J.S. Dailey and T.J. Pinnavaia, *Journal of Inclusion Phenomena and Molecular Recognition in Chemistry*, 1992, **13**, 47-61.

10 G. Scholzen, K. Beneke and G. Lagaly, *Z. anorg. allg. Chem.*, 1991, **597**, 183-196.

11 G. Borbély, H.K. Beyer and H.G. Karge, *Clays and Clay Minerals*, 1991, **39**, 490-497.

12 A. Brandt, W. Schwieger and K.-H. Bergk, *Rev. Chim. Minérale*, 1987, **24**, 564-571.

13 A. Brandt, W. Schwieger and K.-H. Bergk, *Cryst. Res. Technol.*, 1988, **23**, 1201-1203.

14 J.M. Rojo, E. Ruiz-Hitzky and J. Sanz, *Inorg. Chem.*, 1988, **27**, 2785-2790.

15 R.K. Harris and G.J. Nesbitt, *J. Magn. Reson.*, 1988. **78**, 245.

16 K. Beneke and G. Lagaly, *Am. Mineral.*, 1977, **62**, 763-771.

17 L. Müller, A. Kumar, T. Baumann and R.R. Ernst, *Phys. Rev. Lett.*, 1974, **32**, 1402-1406.

18 K.L. Walther, A. Wokaun and A. Baiker, *Molecular Physics*, 1990, **71**, 769-780.

19 W. Kolodziejski, P.J. Barrie, H. He and J. Klinowski, *J. Chem. Soc., Chem. Commun.*, 1991, 961-962.

20 R.V. Hosur, K.V.R Chary and M. Ravi Kumar, *Chem. Phys. Lett.*, 1985, **116**, 105.

Appendix

Publication

A Study of the Layered Alkali metal Silicate, Magadiite, by One- and Two-Dimensional ^{1}H and ^{29}Si NMR Spectroscopy,
G.G. Almond, R.K. Harris and P. Graham, *J. Chem. Soc., Chem. Commun.*, 1994, 851-852.

Oral Presentations

A High-Resolution Solid-State NMR Study of Layered Alkali Metal Silicates, Eleventh International Meeting on NMR Spectroscopy, University College of Swansea, 4-9 July, 1993.

A Solid-State NMR Study of Layered Sodium Polysilicate Hydrates, North-East Universities Postgraduate Chemistry Symposium 1994, University of Northumbria, Newcastle, 12 April 1994.

Poster Presentations

A Multinuclear NMR Study of Layered Alkali Metal Silicates, ICI Poster Competition, University of Durham, December 1992.

Silicon-Proton Coupling in Layered Alkali Metal Silicates, British Radiofrequency Spectroscopy Group Conference on NMR in Solids, University of St. Andrews, 14-15 September 1993.

Colloquia, Lectures and Seminars from Invited Speakers

An asterisk denotes attendance.

1991

October 17	Dr. J. A. Salthouse, University of Manchester Son et Lumiere - a demonstration lecture.
October 31	Dr. R. Keely, Metropolitan Police Forensic Science Modern Forensic Science.
November 6	Prof. B. F. G. Johnson, University of Edinburgh* Cluster-Surface Analogies.
November 7	Dr. A. R. Butler, St. Andrews University Traditional Chinese Herbal Drugs.
November 13	Prof. D. Gani, St. Andrews University The Chemistry of PLP Dependant Enzymes.
November 20	Dr. R. More O'Ferrall, Dublin* Some Acid-Catalysed Rearrangements in Organic Chemistry.
November 28	Prof. I. M. Ward, Leeds University The Science & Technology of Orientated Polymers.
December 4	Prof. R. Grigg, Leeds University* Palladium Catalysed Cyclisation and Ion Capture Processes.
December 5	Prof. A. L. Smith, ex Unilever Soap Detergents and Black Puddings.
December 11	Dr. W. A. Cooper, Shell Research Colloid Science, Theory, and Practice.

1992

January 16	Dr. N. J. Long, University of Exeter Metallocenophanes-Chemical sugar-tongs.
January 22	Dr. K. D. M. Harris, University of St. Andrews* Understanding the Properties of Solid Inclusion Compounds.
January 29	Dr. A. Holmes, University of Cambridge* Cycloaddition Reactions in the Service of the Synthesis of Piperidine and Indolizidine Natural Products.
January 30	Dr. M. Anderson, Sittingbourne Research Centre, Shell Research Recent Advances in the Safe and Selective Chemical Control of Insect Pests.
February 12	Dr. D. E. Fenton, University of Sheffield* Polynuclear Complexes of Molecular Clefts as Models for Copper Biosites.
February 13	Dr. J. Saunders, Glaxo Group Research Limited Molecular Modelling in Drug Discovery.
February 19	Prof. E. J. Thomas, University of Manchester Application of Organo-Stannanes to Organic Synthesis.
February 20	Prof. E. Vogel University of Cologne

	The Musgrave Lecture: Porphyrins, Molecules of Interdisciplinary Interest.
February 25	Prof. J. F. Nixon, University of Sussex Phosphoalkylenes, New Building Blocks in Inorganic and Organometallic Chemistry.
February 26	Prof. M. L. Hitchman, University of Strathclyde* Chemical Vapour Deposition.
March 5	Dr. N. C. Billingham, University of Sussex Degradable Plastics- Myth or Magic?
March 11	Dr. S. E. Thomas, Imperial College London Recent Advances in Organoiron Chemistry.
March 12	Dr. R. A. Hann, ICI Image Data Electronic Photography - An Image of the Future
March 18	Dr H. Maskill, University of Newcastle* Concerted or stepwise fragmentation in a deamination-type reaction.
April 7	Prof. D.M. Knight, Philosophy Department, University of Durham Interpreting experiments: the beginning of electrochemistry.
May 13	Dr. J.-C. Gehret Ciba Geigy, Basel Some aspects of Industrial Agrochemical Research.
October 15	Dr. M. Glazer, Oxford University, & Dr. S. Tarling, Birbeck College, London It Pays to be British! - The Chemist's Role as an Expert Witness in Patent Litigation
October 20	Dr. H. E. Bryndza, Du Pont Central Research Synthesis, Reactions and Thermochemistry of Metal (Alkyl) Cyanide Complexes and Their Impact on Olefin Hydrocyanation Catalysis
October 22	Prof. A. Davies, University College London The Ingold-Albert Lecture: The Behaviour of Hydrogen as a Pseudometal
October 28	Dr. J. K. Cockcroft, University of Durham* Recent Developments in Powder Diffraction
October 29	Dr. J. Emsley, Imperial College, London The Shocking History of Phosphorus
November 4	Dr. T. P. Kee, University of Leeds Synthesis and Co-ordination Chemistry of Silylated Phosphites
November 5	Dr. C. J. Ludman, University of Durham Explosions, A Demonstration Lecture
November 11	Prof. D. Robins, Glasgow University Pyrrolizidine Alkaloids: Biological Activity, Biosynthesis and Benefits
November 12	Prof. M. R. Truter, University College, London Luck and Logic in Host-Guest Chemistry
November 18	Dr. R. Nix, Queen Mary College, London* Characterisation of Heterogeneous Catalysts
November 25	Prof. Y. Vallee. University of Caen Reactive Thiocarbonyl Compounds
November 25	Prof. L. D. Quin, University of Massachusetts, Amherst* Fragmentation of Phosphorous Heterocycles as a Route to Phosphoryl Species with Uncommon Bonding

November 26 Dr. D. Humber, Glaxo, Greenford
AIDS- The Development of a Novel Series of Inhibitors of HIV

December 2 Prof. A.F. Hegarty, University College, Dublin
Highly Reactive Enols Stabilised by Steric Protection

December 2 Dr. R. A. Aitken, University of St. Andrews*
The Versatile Cycloaddition Chemistry of $Bu_3P.CS_2$

December 3 Prof. P. Edwards, Birmingham University
The SCI Lecture: What is Metal?

December 9 Dr. A. N. Burgess, ICI Runcorn
The Structure of Perfluorinated Ionomer Membranes

1993

January 20 Dr. D. C. Clary, University of Cambridge*
Energy Flow in Chemical Reactions

January 21 Prof. L. Hall, Cambridge*
NMR- Window to the Human Body

January 27 Dr. W. Kerr, University of Strathclyde
Development of the Pauson-Khand Annulation Reaction: Organocobalt Mediated Synthesis of Natural and Unnatural Products

January 28 Prof. J. Mann, University of Reading
Murder, Magic and Medicine

February 3 Prof. S. M. Roberts, University of Exeter
Enzymes in Organic Synthesis

February 10 Dr. D. Gillies, University of Surrey*
NMR and Molecular Motion in Solution

February 11 Prof. S. Knox, Bristol University
The Tilden Lecture: Organic Chemistry at Polynuclear Metal Centres

February 17 Dr. R. W. Kemmitt, University of Leicester
Oxatrimethylenemethane Metal Complexes

February 18 Dr. I. Fraser, ICI Wilton
Reactive Processing of Composite Materials

February 22 Prof. D. M. Grant, University of Utah
Single Crystals, Molecular Structure, and Chemical-Shift Anisotropy

February 24 Prof. C. J. M. Stirling, University of Sheffield*
Chemistry on the Flat-Reactivity of Ordered Systems

March 10 Dr. P. K. Baker, University College of North Wales, Bangor
'Chemistry of Highly Versatile 7-Coordinate Complexes'

March 11 Dr. R.A.Y. Jones, University of East Anglia
The Chemistry of Wine Making

March 17 Dr. R.J.K. Taylor, University of East Anglia
Adventures in Natural Product Synthesis

March 24 Prof. I. O. Sutherland, University of Liverpool
Chromogenic Reagents for Cations

May 13 Prof. J. A. Pople, Carnegie-Mellon University, Pittsburgh, USA
The Boys-Rahman Lecture: Applications of Molecular Orbital Theory

May 21 Prof. L. Weber, University of Bielefeld
Metallo-phospha Alkenes as Synthons in Organometallic Chemistry

June 1	Prof. J. P. Konopelski, University of California, Santa Cruz Synthetic Adventures with Enantiomerically Pure Acetals
June 2	Prof. F. Ciardelli, University of Pisa Chiral Discrimination in the Stereospecific Polymerisation of Alpha Olefins
June 7	Prof. R. S. Stein, University of Massachusetts Scattering Studies of Crystalline and Liquid Crystalline Polymers
June 16	Prof. A. K. Covington, University of Newcastle Use of Ion Selective Electrodes as Detectors in Ion Chromatography
June 17	Prof. O. F. Nielsen, H.C. Ørsted Institute, University of Copenhagen Low-Frequency IR- and Raman Studies of Hydrogen Bonded Liquids
September 13	Prof. Dr. A.D. Schlüter, Freie Universität, Berlin, Germany Synthesis and Characterisation of Molecular Rods and Ribbons
September 13	Dr. K.J. Wynne, Office of Naval Research, Washington, USA Polymer Surface Design for Minimal Adhesion
September 14	Prof. J.M. DeSimone, University of North Carolina, Chapel Hill, USA Homogeneous and Heterogeneous Polymerisations in Environmentally Responsible Carbon Dioxide
September 28	Prof. H. Ila, North Eastern Hill University, India Synthetic Strategies for Cyclopentanoids via Oxoketene Dithioacetals
October 4	Prof. F.J. Feher, University of California, Irvine, USA Bridging the Gap between Surfaces and Solution with Sessilquioxanes
October 14	Dr. P. Hubberstey, University of Nottingham Alkali Metals: Alchemist's Nightmare, Biochemist's Puzzle and Technologist's Dream
October 20	Dr. P. Quayle, University of Manchester Aspects of Aqueous ROMP Chemistry
October 21	Prof. R. Adams, University of South Carolina, USA Chemistry of Metal Carbonyl Cluster Complexes: Development of Cluster Based Alkyne Hydrogenation Catalysts
October 27	Dr. R.A.L. Jones, Cavendish Laboratory, Cambridge Perambulating Polymers
November 10	Prof. M.N.R. Ashfold, University of Bristol* High Resolution Photofragment Translational Spectroscopy: A New Way to Watch Photodissociation
November 17	Dr. A. Parker, Rutherford Appleton Laboratory, Didcot* Applications of Time Resolved Resonance Raman Spectroscopy to Chemical and Biochemical Problems
November 24	Dr. P.G. Bruce, University of St. Andrews* Structure and Properties of Inorganic Solids and Polymers
November 25	Dr. R.P. Wayne, University of Oxford The Origin and Evolution of the Atmosphere
December 1	Prof. M.A. McKervey, Queen's University, Belfast Synthesis and Applications of Chemically Modified Calixarenes
December 8	Prof. O. Meth-Cohn, University of Sunderland* Friedel's Folly Revisited- A Super Way to Fused Pyridines
December 16	Prof. R.F. Hudson, University of Kent Close Encounters of the Second Kind

1994

January 26	Prof. J. Evans, University of Southampton* Shining Light on Catalysts
February 2	Dr. A. Masters, University of Manchester Modelling Water Without Using Pair Potentials
February 9	Prof. D. Young, University of Sussex Chemical and Biological Studies on the Coenzyme Tetrahydrofolic Acid
February 16	Prof. K.H. Theopold, University of Delaware, USA Paramagnetic Chromium Alkyls: Synthesis and Reactivity
February 23	Prof. P.M. Maitlis, University of Sheffield* Across the Border: From Homogeneous to Heterogeneous Catalysis
March 2	Dr. C. Hunter, University of Sheffield* Noncovalent Interactions between Aromatic Molecules
March 9	Prof. F. Wilkinson, Loughborough University of Technology* Nanosecond and Picosecond Laser Flash Photolysis
March 10	Prof. S.V. Ley, University of Cambridge New Methods for Organic Synthesis
March 25	Dr. J. Dilworth, University of Essex Technetium and Rhenium Compounds with Applications as Imaging Agents
April 28	Prof. R.J. Gillespie, McMaster University, Canada The Molecular Structure of some Metal Fluorides and Oxofluorides: Apparent Exceptions to the VSEPR Model
May 12	Prof. D.A. Humphreys, McMaster University, Canada Bringing Knowledge to Life